Summer 9-1-2014

Plasmonic Paper as a Novel Chem/Bio Detection Platform

Limei Tian
Washington University in St. Louis

WASHINGTON UNIVERSITY IN ST. LOUIS

School of Engineering & Applied Science

Department of Mechanical Engineering & Materials Science

Dissertation Examination Committee:

Srikanth Singamaneni, Chair

Parag Banerjee

Katharine M. Flores

Guy Genin

Jeremiah Morrissey

Baranidharan Raman

Plasmonic Paper as a Novel Chem/Bio Detection Platform

by

Limei Tian

A dissertation presented to the

Graduate School of Arts and Sciences

of Washington University

in partial fulfillment of the

requirements for the degree

of Doctor of Philosophy

August 2014

Saint Louis, Missouri

Table of Contents

Acknowledgements

First and foremost, I would like to thank my advisor Dr. Srikanth Singamaneni. None of this would be possible without him. I am indebted to him for taking me into this group, and teaching me how to appreciate science, perform research, communicate ideas, and have a vision for the future. He is not only an excellent mentor, but also a valuable moral support on the personal front. He always encouraged me to think independently and look at the bright side. The strong scientific foundation that he has given me will continue to guide and inspire me in my future career. I would also like to thank my committee members: Dr. Parag Banerjee, Dr. Kathy Flores, Dr. Guy Genin, Dr. Jeremiah Morrissey, and Dr. Baranidharan Raman for their time and insightful comments.

I am especially grateful to my previous and current colleagues in soft nanomaterials Laboratory: Dr. Abdennour Abbas, Dr. Chang Lee, Dr. Naveen Gandra, Dr. Ramesh Kattumenu, Ms. Saide Nergiz, Ms. Sirimuvva Tadepalli, Mr. Keng-Ku Liu, Mr. Qisheng Jiang, Mr. Max Fei, Mr. Christopher Portz, Mr. Sang Hyun Park, Mr. Andrew Brimer, and Mr. Enze Chen for their valuable discussions and research assistance.

Special thanks to my parents for giving me a life to experience pain and happiness in such a wonderful world, and thank my other family members for their support and encouragement on realizing my dream. Thank my friends Yanxin Liu, Yanli Liu, and Zhenjiang Yu for words of encouragement.

This work has been supported by Washington University's faculty startup funds, the Office of Congressionally Directed Medical Research Programs and Army Research Office. I would like to thank NanoResearch Facility (NRF), a member of the National Nanotechnology Infrastructure Network (NNIN), for providing access to electron microscopy facilities.

Limei Tian

Washington University in St. Louis

August 2014

Dedicated to my mom, Xueping Li, who believed in me, taught me the value of faith, and encouraged me all the way to get here today

ABSTRACT OF THE DISSERTATION

Plasmonic Paper as a Novel Chem/Bio Detection Platform

by

Limei Tian

Doctor of Philosophy in Mechanical Engineering

Washington University in St. Louis, 2014

Dr. Srikanth Singamaneni, Chair

The time varying electric field of electromagnetic (EM) radiation causes oscillation of conduction electrons of metal nanoparticles. The resonance of such oscillation, termed localized surface plasmon resonance (LSPR), falls into the visible spectral region for noble metals such as gold, silver and copper. LSPR of metal nanostructures is sensitive to numerous factors such as composition, size, shape, dielectric properties of surrounding medium, and proximity to other nanostructures (plasmon coupling). The sensitivity of LSPR to the refractive index of surrounding medium renders it an attractive platform for chemical and biological sensing. When the excitation light is in resonance with the plasmon frequency of the metal nanoparticle, it radiates a characteristic dipolar radiation causing a characteristic spatial distribution in which certain areas show higher EM field intensity, which is manifested as electromagnetic field enhancement. Surface enhanced Raman scattering (SERS) involves dramatic enhancement of the intensity of the Raman scattering from the analyte adsorbed on or in proximity to a nanostructured metal surface exhibiting such strong EM field enhancement. Both LSPR and SERS have been widely investigated for highly sensitive and label-free chemical & biological sensors.

Most of the SERS/LSPR sensors demonstrated so far rely on rigid planar substrates (e.g., glass, silicon) owing to the well-established lithographic approaches, which are routinely employed for either fabrication or assembly of plasmonic nanotransducers. In many cases，their rigid nature results in low conformal contact with the sample and hence poor sample collection efficiency. We hypothesized that paper substrates are an excellent alternative to conventional rigid substrates to significantly improve the (multi-)functionality of LSPR/SERS substrates, dramatically simplify the fabrication procedures and lower the

cost. The choice of paper substrates for the implementation of SERS/LSPR sensors is rationalized by numerous advantages such as (i) high specific surface area resulting in large dynamic range (ii) excellent wicking properties for rapid uptake and transport of analytes to test domains (iii) compatibility with conventional printing approaches, enabling multi-analyte plasmonic sensors (iv) significant reduction in cost (v) smaller sample volume requirement (vi) easy disposability.

In this work, we have introduced novel SERS and LSPR substrates based on conventional filter paper decorated with plasmonic nanostructures, called plasmonic paper. A flexible SERS substrate based on common filter paper adsorbed with gold nanostructures allows conformal contact with real-world surfaces, enabling rapid trace detection. To realize multifunctional SERS substrates, paper substrates were cut into star-shaped structures and the fingers were differentially functionalized with polyelectrolytes that allows separation and pre-concentration of different components of a complex sample in a small surface area by taking advantage of the properties of cellulose paper and shape-enhanced capillary effect. Plasmonic paper can also serve as a novel LSPR biosensing platform by decorating the paper substrate with biofunctionalized nanostructures. Furthermore, calligraphy approach was employed to create well-isolated test domains on paper substrates using functionalized plasmonic nanostructures as ink for multiplexed chemical sensing and label-free biosensing. These plasmonic paper substrates exhibit excellent sample collection efficiency and do not require complex fabrication processes. This class of substrates is expected to have applications not only to first responders and military personal but also to several areas of medical, food analysis, and environmental research.

Chapter 1 Introduction

1.1 Background

1.1.1 Plasmonic sensors based on Localized surface plasmon resonance (LSPR)

Localized surface plasmon resonance (LSPR) of metal nanostructures, which involves collective coherent oscillation of dielectrically confined conduction electrons, is sensitive to numerous factors such as composition, size, shape, surrounding dielectric medium, and proximity to other nanostructures.[1-4] The sensitivity of LSPR to local changes in dielectric environment renders it an attractive transduction platform for chemical and biological sensing.[5-10] LSPR of metal nanostructures has been shown to be sensitive enough to differentiate inert gases with refractive index contrast (δn) on the order of 3×10^{-4}, probe the conformational changes of biomacromolecules, detect single biomolecule binding events, monitor the kinetics of catalytic activity of single nanoparticles, and even optically detect single electron.[11-15] Detection of various biomolecules such as proteins[3, 16-19] and DNA,[20-22] have been demonstrated in the past few years making the transduction platform promising for the development of simple, highly sensitive, label-free, and cost-effective diagnostics.

The amplitude of electromagnetic (EM) near-field decays rapidly from metal surface along the direction perpendicular to the interface into the metal and dielectric, which gives rise to the evanescent wave character to EM near-field.[2, 23-25] The decay of the evanescent EM field can be described as characteristic EM decay length, which depends on the composition, shape, and size of nanostructures.[26] LSPR transducer response can be maximized by optimizing the refractive index sensitivity, and EM decay length of nanostructures, which describes the sensing depth for LSPR sensors. EM decay length has been extensively investigated for gold and silver nanotriangle by Van Duyne and co-workers.[27-29] The EM decay length for these LSPR nanosensors was estimated to be 5-15 nm depending on the size, shape, and composition of the nanostructures. Sutherland and coworkers estimated the EM decay length of gold nanorings to be 12nm, which closely matched with discrete dipole approximation (DDA) calculations.[30] The EM decay length of some other nanostructures such as gold nanocrescent and nanoisland were found to increase with the size of nanostructures.[31] These studies underscore the importance of optimizing the size and shape of a nanotransducer for maximizing the sensitivity for a give pair of analytes and capture molecules.

1.1.2 Plasmonic sensors based on surface enhanced Raman scattering (SERS)

Raman scattering involves the inelastic scattering of light that forms the molecular vibrational fingerprint. Raman spectroscopy is one of the techniques that is well-suited for the identification and characterization of unknown targets both hazardous and benign.[32-44] It is particularly advantageous as it (i) does not suffer from interferences from water, (ii) requires little to no sample preparation, (iii) is robust and can be used in numerous environments, (iv) is relatively insensitive to the wavelength of excitation employed and (v) produces a narrow-band spectral signature unique to the molecular vibrations of the analyte. All of these advantages contribute to Raman spectroscopy's capability to perform sample characterization, identification and quantification. Despite such advantages, Raman spectroscopy has remained a marginalized technique for trace detection of hazardous materials, mainly due to the extremely low scattering cross sections characteristic to many hazardous materials. Surface enhanced Raman scattering (SERS) is a technique that overcomes this shortcoming by greatly enhancing Raman scattering, which has been reported to detect a single molecule under ideal conditions.[45, 46] Compared to conventional Raman scattering, the SERS enhancement has been reported to be six to eight orders of magnitude. [47-49] The SERS phenomenon observed is mainly attributed to two main mechanisms (i) the electromagnetic field generated at or near nanostructured surfaces (electromagnetic enhancement) and (ii) the physical or chemical adsorption of the analyte to a surface (chemical enhancement). Generally, the contribution from EM enhancement is significantly higher (4-6 orders magnitude) compared to the chemical enhancement.

With all the advantages offered by SERS, there is a strong need to explore novel designs and methods that allow the fabrication and use of highly sensitive, reproducible, uniformly enhancing SERS substrate.[50] Colloids were some of the first types of commonly employed SERS substrates due primarily to ease of preparation and large SERS signal enhancement.[51-58] However, the challenges with stability and reproducibility in potentially changing environmental conditions have given rise to more directed types of SERS architectures. Some of the newer techniques to address these challenges include film-over-nanostructures (FONs), assembly and lithographic techniques.[26, 59-66] In particular, film-over-nanostructure (FON) based SERS architecture is one of the common types of SERS substrates available.[67-74] Briefly, FON-based substrates are fabricated by depositing a layer of nanoparticles

typically silica or polystyrene onto a rigid platform. These nanoparticles can then be over-coated with the desired metal of choice (typically silver or gold). The advantages of these types of SERS substrate architectures include increased stability as compared to colloids, ease of fabrication, low cost, rapid fabrication, some tailoring of substrate architecture (shape, size and coinage metal) to match plasmon bands with irradiation source, and good detection of analytes of interest commonly seen with silver-coated substrates. The disadvantages of these types of SERS substrates include a rigid architecture resulting in low conformal contact with the sample and hence poor sample collection efficiency. Significant efforts have been made in using multilayer gold and silver coated biologically compatible substrates with high SERS signal enhancements.[68, 75-77] However, these substrates like most FONs still have the challenges of rigid scaffolding and reproducibility to overcome.

Lithographically produced SERS substrates can be tailored by varying size, shape and precise positioning of nanostructures on various support materials.[43, 65, 78] These lithographically produced substrates are characterized as being highly reproducible and repeatable arrayed nanostructure surfaces within a given area, allowing for increased quantifiable (and in some cases) highly sensitive SERS measurements. However, using this type of fabrication process is not cost-efficient, requires a great deal of effort, time and skill for fabrication, has a low sample collection efficiency and does not necessarily result in a large uniform SERS active sensing area. These considerations clearly highlight need for a novel SERS substrate that is flexible, amenable for conformal contact with solid surfaces, easy fabricate and use and cost-effective.

1.2 Motivation and Rationale

SERS is emerging as a powerful technique for the trace level detection of various biological and chemical species and is believed to make a huge impact in life sciences, environmental monitoring, and homeland security.[60, 63, 79-83] Most of the SERS-based chemical and biological sensors demonstrated so far rely on rigid planar substrates (e.g., glass, silicon) owing to their compatibility with well-established lithographic approaches, such as electron beam lithography and nanosphere lithography, which are routinely employed for either fabrication or assembly plasmonic nanotransducers.[4, 28] In many cases，their rigid nature results in low conformal contact with the sample and hence poor sample collection efficiency. Furthermore, most of the existing SERS substrates involve individual plasmonic

nanostructures or lithography fabricated periodic patterns, which provide limited EM field enhancement, directly resulting in limited SERS enhancement from these substrates. In addition to the abovementioned issues, lack of multifunctionality and chemical selectivity plague the progress of SERS to real-world. The above considerations clearly suggest the need for multiplexed SERS substrates, which enable chemically selective detection of two or more target analytes from a complex chemical mixture, are highly attractive for chemical detection in real-world settings.

LSPR is an attractive transduction platform for label-free biological sensing due to its high sensitivity to local changes in dielectric environment.[5-10] LSPR transducer response can be maximized by optimizing the refractive index sensitivity, and EM decay length of nanostructures, which describes the sensing depth for LSPR sensors. EM decay length has been extensively investigated for lithography fabricated gold and silver nanotriangle by Van Duyne and co-workers, however, the design rule of LSPR biosensors based on individual gold nanoparticles remains elusive. Therefore, the importance of rational design of plasmonic nanotransducers in maximizing the sensitivity and optimizing the performance of the nanobiosensor cannot be overstated. The fabrication of most of the LSPR sensors demonstrated so far rely on labor-, time- and/or resource-intensive patterning techniques such as lithographic approaches. This clearly highlights the need for a simple and biofriendly technique that enables multi-marker biochips for resource-limited settings.

We hypothesized that paper substrates are an excellent alternative to conventional rigid substrates to significantly improve the (multi-)functionality of LSPR/SERS substrates, dramatically simplify the fabrication procedures and lower the cost. Compared to those conventional substrates, the choice of paper substrates for the implementation of chem/biosensor is driven by numerous advantages such as (i) high specific surface area resulting in large dynamic range (ii) excellent wicking properties making it suitable for dip-stick diagnostics (iii) flexibility for efficient collection of analytes by swabbing (iv) compatibility with conventional printing approaches (v) significant reduction in cost per test (vi) smaller sample volume requirement and (vii) easy disposability (by incineration). The synergism of paper-based diagnostics and LSPR/SERS transduction is expected to be truly transformative by opening up novel avenues in chem/biosensing for low-cost, point of care and non-invasive diagnostics.

1.3 Goals and objectives

The goal of the research is to design and develop a novel flexible plasmonic paper for label-free detection of trace amounts of chemical and biological analytes, such as toxic industrial chemicals, explosives and disease biomarkers, based on LSPR and SERS. Plasmonic paper, a novel chem/biosensing platform, involves common filter paper adsorbed with functionalized metal nanostructures, which act as optical nanotransducers.

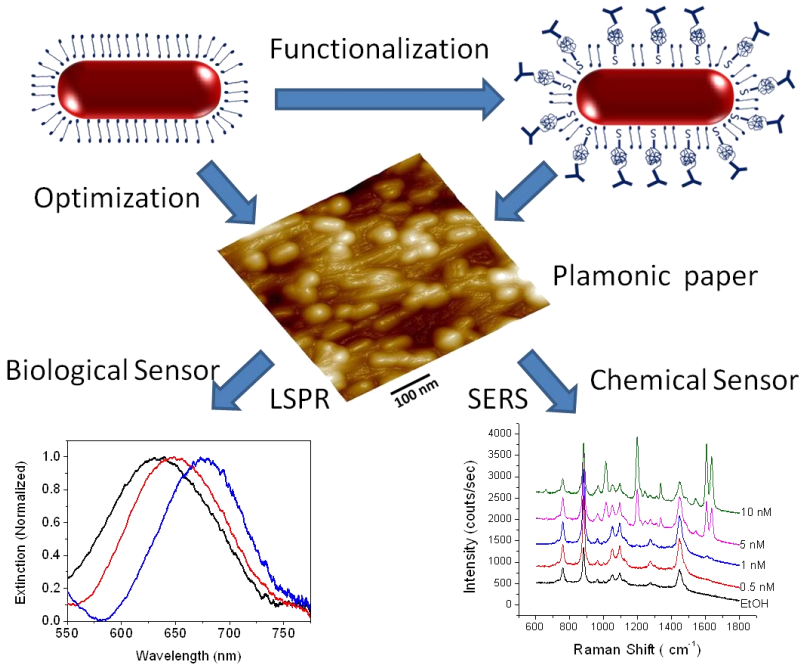

Fig. 1: Illustration outlining the specific tasks of the proposed research project

The key technical objectives are summarized as follows:

● Design and synthesize size- and shape-controlled plasmonic nanostructures with desired surface chemistry and optical properties, such as Au nanospheres, nanorods, nanobipyramids and core-shell nanostructures with intrinsic electromagnetic hotspots.

● Fabricate and test plasmonic paper-based multifunctional SERS substrate that enables separation, pre-concentration and detection of different components of a complex chemical sample.

● Investigate the relationship between electromagnetic decay length and size of the nanostructures and establish design rules for rational selection of metal nanostructures for LSPR-based biosensors, and fabrication of plasmonic paper-based biosensor and probing its sensitivity and specificity.

● Demonstrate plasmonic calligraphy approach for creating well-isolated test domains on paper substrates using functionalized plasmonic nanostructures as ink for multiplexed chemical sensing and label-free biosensing.

1.4 Overview

The current chapter (**Chapter 2**) describes the goals and specific technical objectives of the work discussed in the dissertation. It also provides an overview and organization of the dissertation.

Chapter 3 describes a novel SERS substrate based on common filter paper adsorbed with gold nanorods, which allows conformal contact with real-world surfaces, enabling rapid trace detection. One of the important but often overlooked considerations in the design of SERS substrates for trace detection is the efficiency of sample collection. Conventional designs based on rigid substrates such as silicon, alumina, and glass resist conformal contact with the surface under investigation, making the sample collection inefficient. We demonstrate a novel SERS substrate based on common filter paper adsorbed with gold nanorods, which allows conformal contact with real-world surfaces, thus dramatically enhancing the sample collection efficiency compared to conventional rigid substrates. We demonstrate the detection of trace amounts of analyte (140 pg spread over 4 cm^2) by simply swabbing the surface under investigation with the novel SERS substrate. The hierarchical fibrous structure of paper serves as a 3D vasculature for easy uptake and transport of the analytes to the electromagnetic *hot spots* in the paper. Simple yet highly efficient and cost effective SERS substrate demonstrated here brings SERS based trace detection closer to real-world applications.

Improving on the preliminary paper-based SERS substrate discussed in Chapter 3, **Chapter 4** discusses the synthesis of plasmonic nanorattles for highly efficient SERS-based chemical sensing. Individual plasmonic nanostructures offer limited EM field enhancement, which directly results in limited SERS enhancement from these nanostructures. Plasmonic nanorattles synthesized in this study are comprised of gold nano-octahedra as cores and cubic porous gold shells using a combination of seed-mediated synthesis and galvanic replacement reaction. Plasmonic coupling between the solid core and porous shell of the nanorattles results in a large enhancement in the electromagnetic (EM) field at the interior of the nanorattles, making them excellent candidates for SERS. The porous nature of the outer shell facilitates the diffusion of the analytes into pre-designed electromagnetic hotspots within each of these

nanostructures. A flexible SERS substrate fabricated through the uniform adsorption of nanorattles on filter paper exhibited remarkable sensitivity with a limit of detection below 10 pM of 2-napthalenethiol (2-NT). The inherent EM hotspot within each of the nanostructures obviates the need for the conventional methods of controlled aggregation or assembly of solid nanostructures to form EM hotpsots that are critical for SERS substrates exhibiting high sensitivity.

Chapter 5 describes a plasmonic paper-based analytical platform with functional versatility and sub-attomolar ($< 10^{-18}$ M) detection limit using optimally designed paper-based SERS substrate. In this design, the microfluidic paper-based analytical device (μPAD) is made with a lithography-free process by a simple cut and drop method. Complex samples are separated by surface chemical gradient created by differential polyelectrolyte coating of the paper. The μPAD with a star-like shape is designed to enable liquid handling by lateral flow without microchannel patterning. This design generates a rapid capillary-driven flow capable of dragging liquid samples as well as gold nanorods into a single cellulose microfiber, thereby providing an extremely pre-concentrated and optically active detection spot.

Chapter 6 describes a new approach called plasmonic calligraphy that involves the formation of chemically selective test domains on paper substrates using functionalized plasmonic nanostructures as ink in a regular ballpoint pen. Multiplexed SERS substrates, which enable chemically selective detection of two or more target analytes from a complex chemical mixture, are highly attractive for chemical detection in real-world settings. We demonstrate selective detection of positively and negatively charged analytes (rhodamine 6G and methyl orange) from complex chemical mixtures using polyelectrolyte-coated gold nanorods as SERS medium. The approach demonstrated here obviates the need for complex patterning techniques such as photolithography to create isolated test domains on paper substrates for multiplexed chemical detection. Plasmonic calligraphy can be easily extended to other shape-controlled nanostructures with different surface functionalities and potentially automated by implementing with a robotic arm.

Chapter 7 describes the design rules for rational selection of metal nanostructures for LSPR-based biosensing applications. Owing to the facile tunability of the LSPR and large refractive index sensitivity, gold nanorods (AuNR) are of high interest as plasmonic nanotransducers for label-free biological sensing. We investigate the influence of gold nanorod dimensions on distance-dependent LSPR sensitivity and EM

decay length using electrostatic layer-by-layer (LbL) assembly of polyelectrolytes. The electromagnetic decay length was found to increase linearly with both the nanorod length and diameter, although to variable degrees. The rate of EM decay length increase with nanorod diameter is significantly higher compared to that of the length, indicating that diameter is a convenient handle to tune the EM decay length of gold nanorods. The ability to precisely measure the EM decay length of nanostructures enables the rational selection of plasmonic nanotransducer dimensions for the particular biosensing application.

Chapter 8 describes a novel biosensing platform based on paper substrate adsorbed with biofunctionalized nanorods. In particular, we demonstrate that bioplasmonic paper enables rapid urinalysis for the detection of kidney cancer biomarkers in artificial urine down to a concentration of 10 ng/ml. Compared to conventional rigid substrates, bioplasmonic paper offers numerous advantages such as high specific surface area (resulting in large dynamic range), excellent wicking properties (naturally microfluidic), mechanical flexibility, compatibility with conventional printing approaches (enabling multiplexed detection and multi-marker biochips), and significant cost reduction.

Chapter 9 describes bioplasmonic calligraphy, a novel approach for realizing multiplexed label-free bioassays. Printable multimarker biochips that enable simultaneous quantitative detection of multiple target biomarkers in point-of-care and resource-limited settings are a holy grail in the field of biodiagnostics. However, preserving the functionality of biomolecules, which are routinely employed as recognition elements, during conventional printing approaches remains challenging. Biofriendly plasmonic calligraphy approach serves as a facile method to miniaturize the test domain size to few mm^2, which significantly improves the sensitivity of the plasmonic biosensor compared to bioplasmonic paper fabricated using immersion approach. Furthermore, plasmonic calligraphy also serves as a simple and efficient means to isolate multiple test domains on a single test strip, which facilitates multiplexed biodetection and multi-marker biochips. Plasmonic calligraphy, which can be potentially automated by implementing with a robotic arm, serves as an alternate path forward to overcome the limitations of conventional ink-jet printing.

Chapter 2 Experimental Details

This chapter describes a general overview of the experimental techniques, procedures, and equipment that were utilized throughout the work presented in the dissertation. Specific experimental techniques are detailed in each of the individual chapters. After describing general sample preparation procedures, we provide an overview of the characterization equipment and procedures.

2.1 Synthesis and Fabrication

2.1.1 Synthesis of Gold nanorods

Gold nanorods had been synthesized using a seed-mediated approach. [84, 85] Seed solution was prepared by adding 1 mL of an ice-cold solution of 10 mM sodium borohydride into magnetically stirred 10 mL of 0.1 M cetyltrimethylammonium bromide (CTAB) and 2.5×10^{-4} M $HAuCl_4$ aqueous solution at room temperature. The color of the seed solution changed from yellow to brown. Growth solution was prepared by mixing 95 ml of 0.1 M CTAB, 1 ml of 10 mM silver nitrate, 5 ml of 10 mM $HAuCl_4$, and 0.55 ml of 0.1 M ascorbic acid in the same order. The solution was homogenized by gentle stirring. To resulting colorless solution, 0.12 ml of freshly prepared seed solution was added and set aside in dark for 14 hours. The solution turned from colorless to violet brown with most of the color change happening in the first hour. Prior to use, the gold nanorod solution was centrifuged at 13,000 rpm for 10 min to remove excess CTAB and redispersed in nanopure water (18.2 MΩ-cm). The procedure was repeated twice.

2.1.2 Absorption of gold nanorods on paper and planar silicon substrates

AuNRs are loaded in a laboratory filter paper (Whatman No. 1 grade) by immersing a 1 cm^2 paper in 2.5 mL of AuNR solution for two days. Upon removing from the solution, the paper was gently rinsed with nanopure water and then blow-dried under a stream of dry nitrogen. Planar silicon substrates for comparison were fabricated by modifying the silicon substrate with poly(2-vinyl pyridine) (P2VP) by exposing the piranha cleaned silicon surface to 4% P2VP solution in ethanol. After rinsing the silicon substrate with ethanol it was exposed to gold nanorod solution to enable adsorption of the gold nanorods. Finally, the substrate was rinsed with water to remove the loosely bound nanorods leaving a highly dense layer of nanorods on the surface.

2.1.3 AuNR-IgG conjugates preparation

To a solution of heterobifunctional polyethylene glycol (SH-PEG-COOH) in water (37.5 µl, 20 µM, Mw=5000 g/mol, Jenkem Technology), 1-Ethyl-3-(3-dimethylaminopropyl) carbodiimide (EDC, Thermo Scientific) and N-hydroxy succinimide (NHS, Thermo Scientific) with the same molar ratio as SH-PEG-COOH were added followed by shaking for 1 h. The pH of the above reaction mixture was adjusted to 7.4 by adding 10x concentrated phosphate buffered saline (PBS), followed by the addition of Rabbit Immunoglobulin G (IgG) (10 µl, 75 µM, Mw=150 kDa, Thermo Scientific). The reaction mixture was incubated for 2 h, and then filtered to remove any byproduct during the reaction using a 50 kDa filter. The final SH-PEG-IgG conjugates solution (0.75 µM) was obtained after washing with PBS buffer (pH 7.4) twice. AuNR-IgG conjugates solution was prepared by adding 50 µl SH-PEG-IgG conjugates solution to 1 ml twice centrifuged AuNR solution with incubation for 1 h. The amount of SH-PEG-IgG was optimized to obtain maximum coverage of IgG on AuNR surface (Fig. S6.4 in Appendix 6).

2.2 Characterization techniques

2.2.1 Scanning electron microscopy (SEM)

Scanning electron microscope (SEM) images were obtained using a FEI Nova 2300 Field Emission SEM at an accelerating voltage of 10 kV. Unless mentioned otherwise, the sampled were sputtered with gold for 60 sec prior to SEM imaging.

2.2.2 Transmission electron microscopy (TEM)

Transmission electron microscopy (TEM) micrographs were recorded on a JEM-2100F (JEOL) field emission instrument. Typically TEM samples were prepared by drying a drop of the solution on a carbon-coated grid, which had been previously made hydrophilic by glow discharge.

2.2.3 Atomic force microscopy (AFM)

Atomic force microscopy (AFM) images were obtained using Dimension 3000 (Digital instruments) AFM in light tapping mode.[86] Standard AFM probe featuring pyramidal silicon tip with resonance frequency ~325 kHz and force constant ~40 N/m was typically used to perform imaging.

2.2.4 UV-vis spectroscopy

Extinction spectra from paper substrates were collected using a CRAIC microspectrophotometer (QDI 302) coupled to a Leica optical microscope (DM 4000M) with 100x objective in the range of 450-800 nm

with 10 accumulations and 0.8 sec exposure time in reflection mode. The spectral resolution of the spectrophotometer is 0.2 nm. Shimadzu UV-1800 spectrophotometer was employed for collecting UV-vis extinction spectra from solution and glass samples.

2.2.5 Raman spectroscopy

Raman spectra were measured using a Renishaw inVia confocal Raman spectrometer mounted on a Leica microscope with 20X objective (NA = 0.40) in the range of 100 – 3200 cm^{-1} with one accumulation and 10 s exposure time. A 785 nm wavelength diode laser (0.5 mW) coupled to a holographic notch filter with a grating of 1200 lines mm^{-1} was used to excite the sample. The following expression was used to approximate the laser spot size (1.2 µm in diameter)[87]

$$w_0 = \frac{0.61 \times \lambda}{NA} \qquad (2)$$

where w_0 is the minimum waist diameter for a laser beam of wavelength λ focused by an objective with a numerical aperture NA. The focal volume (τ) was approximated from the following expressions[88, 89]

$$\tau = \left(\frac{\pi}{2}\right)^{1.5} w_0^2 z_0 \qquad (3)$$

$$z_0 = \frac{2\pi w_0^2}{\lambda} \qquad (4)$$

where z_0 is the focal depth.

Chapter 3 Paper Based SERS Swab for Rapid Trace Detection on Real-world Surfaces

3.1 Introduction

Surface enhanced Raman scattering (SERS) is emerging as a powerful technique for the trace level detection of various biological and chemical species and is believed to make a huge impact in life sciences, environmental monitoring, and homeland security.[60, 63, 79-83] Numerous SERS substrates from roughened noble metal surfaces to e-beam patterned metal nanostructures with enhancement factors ranging from 10^4 to 10^{10} have been demonstrated over the last two decades.[3, 50, 90, 91] Very high enhancement factors (> 10^9) have been reported for SERS substrates fabricated from top-down and bottom-up approaches such as e-beam lithography, colloidal lithography, on-wire lithography and self- and directed-assembly, which enable precise control over the size, shape, and organization of the metal nanostructures.[64, 65, 92-94] On the other hand, 3D SERS substrates such as photonic crystal fibers and porous alumina membranes decorated with nanoparticles and periodic nanohole arrays also offer large SERS enhancements (10^6 - 10^9) owing to the large surface area within the source laser footprint and efficient light-matter interaction compared to the 2D counterparts.[95-97]

Although most of these studies clearly demonstrate that SERS substrates hosting closely separated metal nanostructures and/or sharp tips result in large enhancements, an important practical consideration apart from the cost, which is often overlooked, is the ease and efficiency of the sample collection. In real-world applications such as explosive detection, the efficiency of sample collection becomes a decisive factor. For example, in the case of explosives such as trinitrotoluene (TNT), which inherently have low vapor pressure (~10 ppb_v at room temperature), intentional packaging further lowers the actual vapor concentration by more than an order of magnitude.[98] For detection of such explosives, it is extremely important to collect particulates (few µg), that are invariably present on the surface of objects exposed to the explosive. Physical swabbing, puffer systems (aerodynamic), and direct vapor sniffing are recognized as efficient methods to collect trace amounts of analytes. In particular, swabbing the surface under investigation with a soft and flexible substrate (swab) is a highly practical and efficient method to maximize the sample collection from a real-world surface. In fact, this strategy is being extensively employed for passenger screening at airports using ion mobility spectroscopy.[99] On the contrary, conventional SERS substrates based on silicon, glass, and porous alumina, which are conceived for

homeland security applications, are not compatible with such efficient sample collection process due to their non-conformal, rigid and brittle nature.

Herein, we demonstrate the fabrication of a simple yet highly efficient paper based SERS substrate by loading gold nanorods (AuNR) in a commercially available laboratory filter paper. The SERS substrate demonstrated here can be used by simply swabbing the surface of an object suspected of exposure to a hazardous material. We demonstrate the detection of less than 140 pg of 1,4-benzenedithiol (1,4-BDT) residue spread over 4 cm^2 surface by swabbing the AuNR loaded paper on the surface. Previous attempts employing filter paper exhibited limited sensitivity possibly due to the thin metal films (thermally evaporated or sputtered) or poor control over the size and shape of the metal nanostructures employed in these designs.[100, 101] Apart from the large enhancement, the uniform decoration of the nanorods demonstrated here preserves the favorable attributes such as flexibility, conformal nature and capillarity of the paper. To our knowledge, this study presents the first SERS swab for rapid and efficient sample collection from real-world surfaces with unprecedented sensitivity.

3.2 Experimental section

For the dipping test, we evaluated the performance of detecting a trace amount of 1,4-BDT by dipping the SERS substrate in various concentrations of 1,4-BDT in ethanol for 20 minutes, followed by light rinsing with ethanol and drying with compressed nitrogen gas before the Raman measurements. Six Raman scans were performed for each substrate with each scan representing a different spot within the same substrate. The Raman data were averaged and normalized against 1058 cm^{-1} band.

For the swabbing test, 100 µL of 1 µM to 1 nM 1,4-BDT (corresponding to ~ 14 µg to 14 pg) in ethanol was pipetted on the surface of a glass slide, which immediately spread over 4 cm^2 area. Evaporation of ethanol left residue of 1,4-BDT. We placed a drop of ethanol on a 0.5 × 1 cm SERS substrate to wet, and then swabbed the surface of the glass slide to pick up the residue of 1,4-BDT. We collected Raman spectra of the swabbed SERS substrate on six different spots. The Raman spectra were averaged and normalized against 1058 cm^{-1} band.

3.3 Results and discussion

3.3.1 Gold nanorods paper fabrication and characteration

Gold nanorods were synthesized using a previously reported seed-mediated approach using cetyltrimethylammonium bromide (CTAB) as a capping agent (see experimental section).[84, 85] The nanorods were found to be ~80 nm long and ~20 nm in diameter, making the aspect ratio to be nearly four. Exposing the filter paper to CTAB-capped gold nanorod solution resulted in uniform adsorption of the nanorods on the surface of the paper and a color change from white to purple (Figure 3.1A). A significant decrease in the intensity of the purple color of the AuNR solution was observed after removing the paper from the solution (see Figure 3.1A), which corresponded to nearly 50% decrease in extinction intensity. This significant change in the intensity of the color of the solution following the filter paper exposure is in accordance with the high density of nanorods on the surface of the paper and deep purple color of the paper. UV-vis extinction spectra of the AuNR solution showed the two characteristic peaks at ~ 530 nm and 650 nm corresponding to the transverse and longitudinal plasmon resonances of the nanorods, respectively (see Figure 3.1B).[102] AuNR loaded paper exhibited similar extinction spectrum with both transverse and longitudinal plasmon slightly blue shifted compared to the solution. The blue shift observed can be attributed to the change in the dielectric ambient (from water to air + substrate) with an effective decrease in the refractive index. The blue shift of the longitudinal plasmon peak (34 nm) was found to be slightly higher compared to the transverse band (12 nm), which can be attributed to the higher sensitivity of the longitudinal plasmon resonance to the changes in the dielectric ambient compared to the transverse band.[103]

Cellulose is biodegradable, renewable, and abundant in nature thus cellulose (or paper) based products can be inexpensively produced and recycled.[104] Due to numerous advantages such as significant reduction in cost, high specific surface area, excellent wicking properties, and compatibility with conventional printing approaches (enabling multiplex detection and easy disposability) paper is gaining increased attention as a substrate in diagnostic and tissue engineering applications.[105-109] Figure 3.2A shows the hierarchical fibrous morphology of the filter paper with cellulose nanofibers braided into microfibers (average diameter of ~ 0.4 μm). The RMS surface roughness of the paper was found to be 72 nm over 5 × 5 μm^2 area, which indicates the large surface area of the paper substrates. Raman

spectra obtained from six different areas of the pristine filter paper with 1 inch diameter exhibited excellent compositional (spectral) homogeneity, which is extremely important for its application as a SERS substrate (see Appendix 1, Figure S1.1). It is well known that uniform and high density adsorption of CTAB (cationic surfactant) capped AuNR to polymer surfaces is a significant challenge.[110, 111] We observed that once the AuNR loaded paper was dried, even under vigorous rinsing with water or alcohol, no noticeable change in the AuNR density was observed, suggesting the stability of these substrates for deployment in liquid environments. Cellulose has a large number of hydroxyl groups, which are accessible for attaching positively charged species. [112] The uniform, irreversible, and high density adsorption of the AuNR is possibly due to the electrostatic interaction between the positive charged nanorods and the filter paper.

AFM imaging revealed a uniform and dense adsorption of nanorods on the surface of the paper without any signs of large scale aggregation of the nanorods (Figure 3.2B). Higher magnification AFM images show the nanorods decorating the fibers of the paper and a partial local alignment of the nanorods along the nanofibers (Figure 3.2C, 3.2D). From numerous AFM images collected at different areas of the substrate, the number density of the nanorods was found to be 98 ± 22 / μm^2. High magnification SEM image shows the uniformly adsorbed gold nanorods on the paper (Figure 3.2E). Energy dispersive X-ray spectra (EDX) confirmed the presence of gold on the surface apart from the carbon and oxygen rich cellulose fibers (inset of Figure 3.2E).

3.3.2 SERS performance of gold nanorods paper

1,4-Benzenedithiol (1,4-BDT) is widely employed as a model analyte for SERS owing to its ability to readily adsorb on gold or silver particles and its distinct Raman fingerprint. The Raman spectrum of 1,4-BDT in neat solid state exhibits strong bands at 740, 1058, 1093, 1186, and 1573 cm^{-1}. Three prominent bands: 1058 cm^{-1} due to the combination of the phenyl ring breathing mode, CH in-plane bending, and CS stretching, 1181 cm^{-1} due to CH bending, and 1562 cm^{-1} due to phenyl ring stretching are commonly employed as characteristic peaks for evaluating the performance of SERS substrates.[87, 113, 114] We utilized 1058 cm^{-1} band to test the performance of our SERS substrate in detecting trace amounts of 1,4-BDT in ethanol. The pristine SERS substrate (AuNR loaded paper) does not show any peak in this region (see Appendix 1, Figure S1.2).

As a planar rigid substrate for comparison, we employed a highly dense (number density: 220 ± 14 /μm^2) layer of gold nanorods bound to silicon substrate modified with poly(2-vinyl pyridine) (Figure 3.3). Figure 3.4A shows the Raman spectra obtained from the planar AuNR control sample and AuNR loaded paper both exposed to 1 mM of 1,4-BDT, followed by rinsing with ethanol. While the Raman spectra obtained from the AuNRs on silicon substrate exhibits weak Raman bands of 1,4-BDT, the AuNR loaded paper exhibited much stronger (~ 250 times) Raman bands. These Raman spectra obtained from the SERS substrates exhibited small shifts in frequency of the vibrational bands compared to the bulk 1,4-BDT (i.e. 1185 cm^{-1} for bulk BDT, and 1180 cm^{-1} for SERS substrate), possibly due to the orientation change of 1,4-BDT molecules adsorbed on to the AuNR.[115]

To investigate the trace detection ability of the paper based SERS substrate, Raman spectra were collected from substrates exposed to 1,4-BDT down to concentrations of 0.1 nM. All the characteristic bands of the 1,4-BDT exhibited a monotonous decrease in intensity with decreasing concentration (Figure 3.4B). Figure 3.4C shows the higher resolution spectra of the smoothed 1058 cm^{-1} band, which is clearly distinguishable (signal to noise ratio of 3) down to a concentration of 0.1 nM (17 ppt) (see Appendix 1, Figure S1.3 shows higher resolution spectra). Semi-log plot of the concentration vs. 1058 cm^{-1} peak intensity shows a monotonic increase in the Raman intensity with increasing concentration of the analyte (Figure 3.4D). Data from Figure 3.4D can be plotted as the inverse of the fractional coverage (taken as a ratio of intensity, I_{max}/I) with respect to the inverse of the concentration (1/c), which exhibits a linear relationship, reflecting the expected Langmuir adsorption isotherm of 1,4-BDT to gold nanorods (inset of Figure 3.4D). [116]

The following expression was used to calculate the enhancement factor (EF) of SERS substrate at 1058 cm^{-1} band:

$$EF = I_{SERS} \times N_{bulk} / I_{bulk} \times N_{SERS} \qquad (1)$$

where I_{SERS} (N_{SERS}) and I_{bulk} (N_{bulk}) are the intensities (the number of 1,4-BDT molecules probed) for the SERS and bulk spectra, respectively. N_{SERS} was estimated by assuming a complete monolayer of 1,4-BDT on the nanorods for SERS substrates exposed to 1 mM concentration, which ensures that the enhancement factor is not overestimated. Based on numerous AFM images, the areal coverage of the AuNR was estimated to be ~ 23% and N_{SERS} was calculated to be 4.9 × 10^5 molecules. I_{bulk} and N_{bulk}

were determined from the Raman spectra of a 0.1 M of 1,4-BDT in 12 M $NaOH_{(aq)}$ (see experimental for details). Using the SERS intensity of the 1058 cm^{-1} band, the enhancement factor was calculated to be ~ 5×10^6. The enhancement factor observed here is high considering the absence of any resonance contribution, the use of gold nanostructures as opposed to silver nanostructures, which result in higher enhancement at the expense of poor long-term stability, absence of any intentionally formed hot spots (dimers or controlled aggregates) and the simplicity of the fabrication approach.[117]

One of the important considerations in the fabrication of paper based SERS substrates is the effect of the exposure time of the paper substrates to the metal nanostructure solution. The extinction spectra of the paper substrates exposed to gold nanorod solution for different amounts of time show that the intensity of both transverse and longitudinal plasmon bands increase with the exposure time, indicating the progressive increase in the density of the nanorods adsorbed on the paper surface (see Appendix 1, Figure S1.4). It was also noted that the paper substrates progressively become darker overtime with adsorption of nanorods. SERS intensity of the paper substrates exposed to AuNR solution for different amount of time increased rapidly for the first 10-15 hours, followed by a small increase for subsequent exposure (Figure S1.4). This trend closely agrees with the intensity variation of the extinction spectra obtained from the paper substrates exposed to AuNR solution for different durations. The number of nanorods adsorbed on the paper substrates rapidly increases for the first 10-15 hours followed by a saturation of the density of the adsorbed nanorods subsequently.

In order to understand the source of spatial variation in the SERS intensity (heterogeneity) of the paper substrate, we performed confocal Raman mapping following the exposure to non-resonant analyte. 1,4-BDT employed for these studies is also widely employed as a model analyte for SERS owing to its ability to readily adsorb on gold or silver particles and its distinct Raman fingerprint. The Raman spectrum of 1,4-BDT in neat solid state exhibits strong bands at 740, 1058, 1093, 1186, and 1573 cm^{-1}. The optical micrograph of the region of the paper where the mapping was performed is characterized by porous and fibrous morphology (Figure 3.5A). Figure 3.3B shows the SERS intensity map of 1058 cm^{-1} band. In general, the map shows a homogenous SERS intensity with maximum difference between the brightest and darkest regions being close to 80%.

There are several interesting features that can be noted from Raman map. A close comparison between the optical image and the Raman map reveals that the variations in the Raman intensity are primarily related to the roughness of the paper substrates (Figure 3.5A, B). The brighter regions (indicated by square c) correspond to the areas where the incident laser was focused below the surface while the darker regions (indicated by square a) correspond to the areas where the laser was focused slightly above the surface. The regions which were in focus exhibited intermediate intensity between these two extreme cases. Figure 3.5C shows average spectra obtained from different regions (a, b, and c) marked in the optical image and the SERS map, quantitatively showing the variation in SERS intensity discussed above. Figure 3.3D shows the intensity of the 1058 cm^{-1} band along the length of a microfiber identified by the dotted line in the optical image. It can be seen that the variation in SERS intensity along the length of the fiber is within ±15%. The variation even along the fiber is primarily due to the small variations in focus along the length of the microfiber suggesting the high level uniformity of the adsorption of gold nanorods on paper surface. This observation clearly suggests that optimization of the paper morphology (i.e. smoother surface) can significantly improve the homogeneity of the SERS intensity. Raman spectra obtained using larger laser spot would enable spatial averaging of the focal variations and result in enhanced homogeneity across the substrate.

3.3.3 Swabbing test

One of the distinct advantages of the paper based SERS substrate is the ability to collect trace amount of analytes from real-world surfaces by swabbing across the surface. We demonstrate this unique ability of the paper substrates by swabbing a slightly wetted (in ethanol) paper on surface of a glass with trace quantities of analyte deposited on the surface (see Figure 3.6A). Figure 3.6B shows the Raman spectra (averaged over 6 different spots) obtained by swabbing the paper across the surface with different amounts of analyte. Again, we used the strongest Raman band at 1058 cm^{-1} to evaluate the efficiency of the SERS swab. It can be seen that the Raman bands of 1,4-BDT can be clearly distinguished down to 140 pg on the surface (Figure 3.6C). Considering that the swabbing of the surface results only a fraction of the analyte to be absorbed into the paper, a detection limit on the order of few tens of picograms on the surface is truly remarkable.

Envisioned and designed as an end-user level SERS substrate, proper handling of paper SERS substrate becomes an important issue as they contain metal nanostructures, which could be potentially harmful to humans and the environment. Toxicity of gold nanoparticles is still debated even though many reports indicate that gold nanoroparticles are essentially nontoxic. In a recent perspective, Alkilany et al. suggested that the toxicity and cell uptake of gold nanorods can be controlled to a point that they would not pose a serious harm by functionalizing the surface of gold nanorods with biocompatible ligands.[118, 119] Similar approach i.e. tailoring the surface chemistry of the metal nanostructures can be employed to make the paper SERS substrates bio-friendly.

3.4 Conclusions

We have demonstrated highly efficient SERS substrate based on common filter paper filled with gold nanorods, which exhibited more than two orders of magnitude higher SERS enhancement compared to the silicon based SERS substrate. Numerous favorable traits of the paper such as flexibility, conformability, efficient uptake, and transport of the analytes from liquid and solid media to the surface of metal nanostructures due to hierarchical vasculature and high specific surface area make the paper based SERS substrates demonstrated here an excellent candidate for trace chemical and biological detection. The paper based SERS substrates also offer cost-effective platform for SERS detection and opens up a new venue for other biological and chemical detection. The process demonstrated here can be easily scaled up for batch fabrication of SERS swabs. Furthermore, the paper based SERS substrate introduces a novel platform for integrating conventional chromatography, microfluidics and biological assays (e.g Western blot analysis) with SERS, imparting chemical specificity to these techniques. Similar to microfluidic devices, paper SERS based multiplexed detection of analytes from a complex real-world sample can be a very powerful approach, which is a subject of our future investigation.[120] We also see electrospinning of polymer fibers as a potential method for realizing flexible SERS substrates. Electrospun polymer mats possess a hierarchical fibrous structure similar to that of paper, and the use of different types of polymers in electrospinning can bring better control (fiber diameter, alignment, surface chemistry) and multi-functionality to the SERS design and applications.

3.5 Supporting information

Supporting information for chapter 3 is provided in appendix 1.

Figures

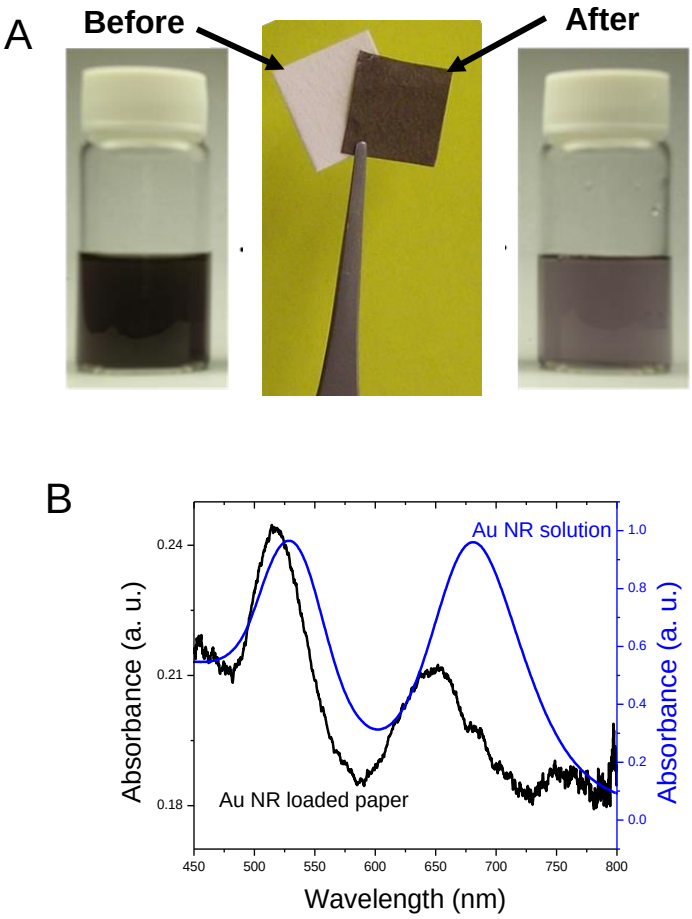

Figure 3.1 (A) Photographs of the AuNR solutions and the filter paper before and after exposure showing the strong color change (B) UV-vis extinction spectra of the AuNR solution and the AuNR loaded paper showing the transverse and longitudinal plasmon absorption of the AuNR.

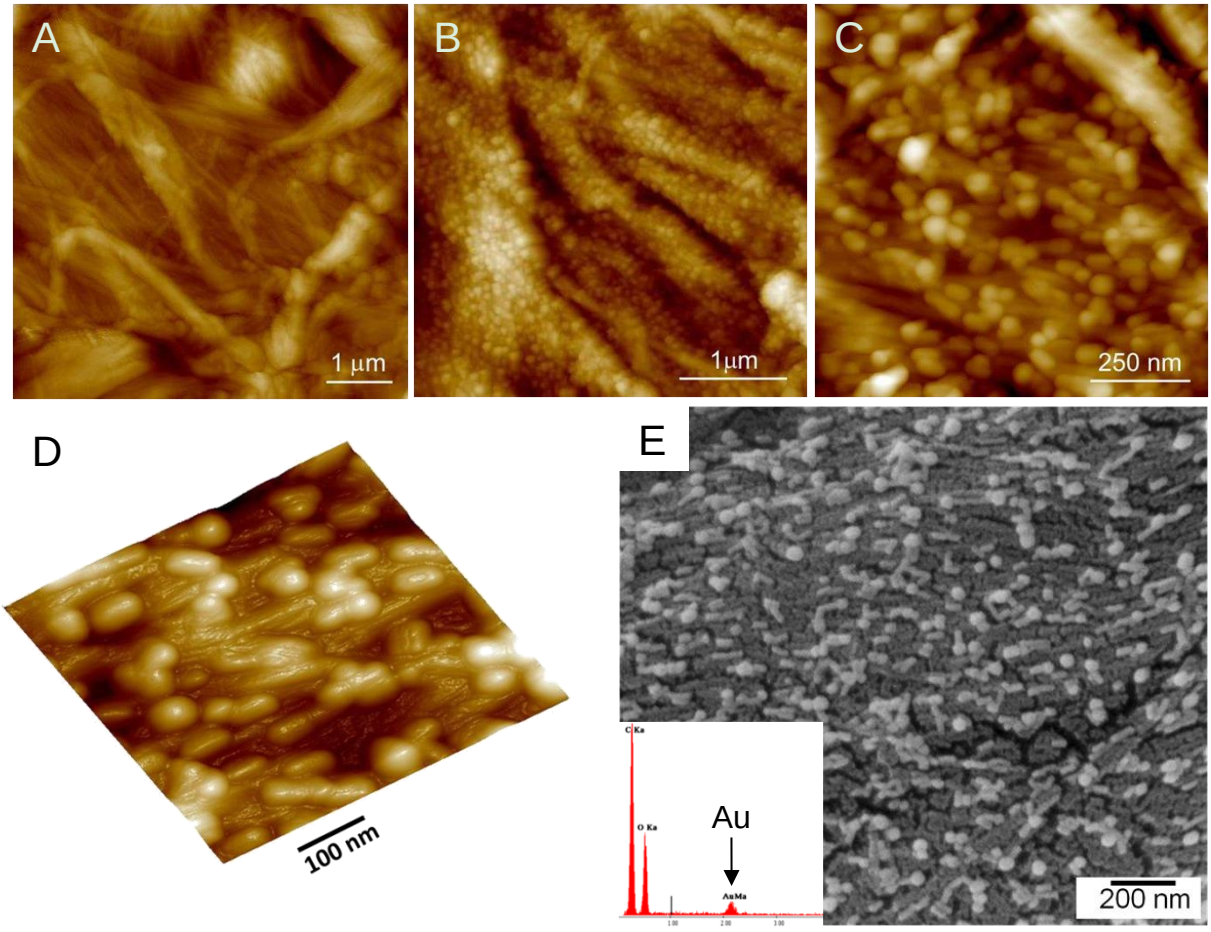

Figure 3.2 AFM images of (A) bare filter paper (B) paper with gold nanorods (C) higher magnification image showing the nanorods uniformly decorating the fibers of the paper (D) 3D AFM image showing the partial local alignment of the nanorods along the fibers (E) SEM showing the large scale uniformity of the gold nanorods adsorbed on the surface of the paper (inset shows the EDX confirming the presence of the gold on the surface of the paper).

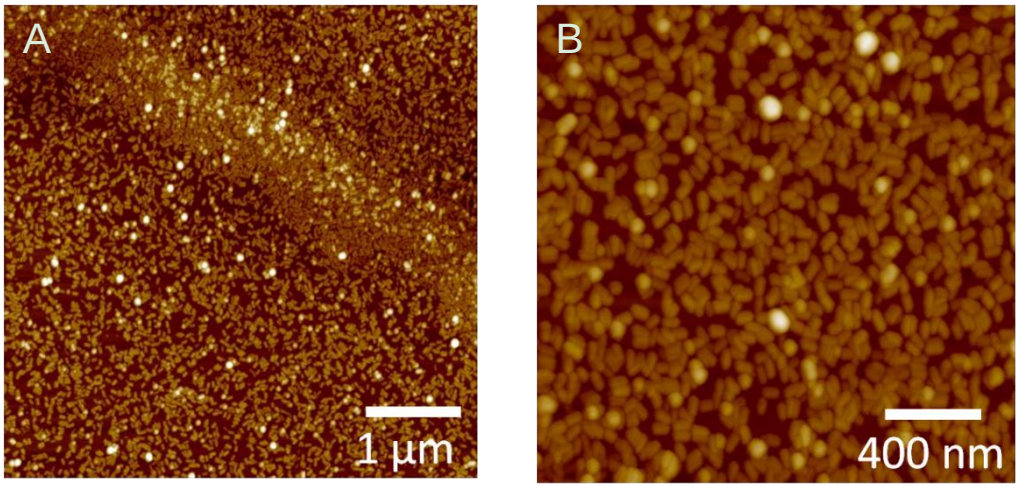

Figure 3.3 AFM images of (A) uniformly and high density array of nanorods on silicon surface modified with poly(2-vinyl pyridine) and (B) higher magnification image showing the gold nanorods shown in (A).

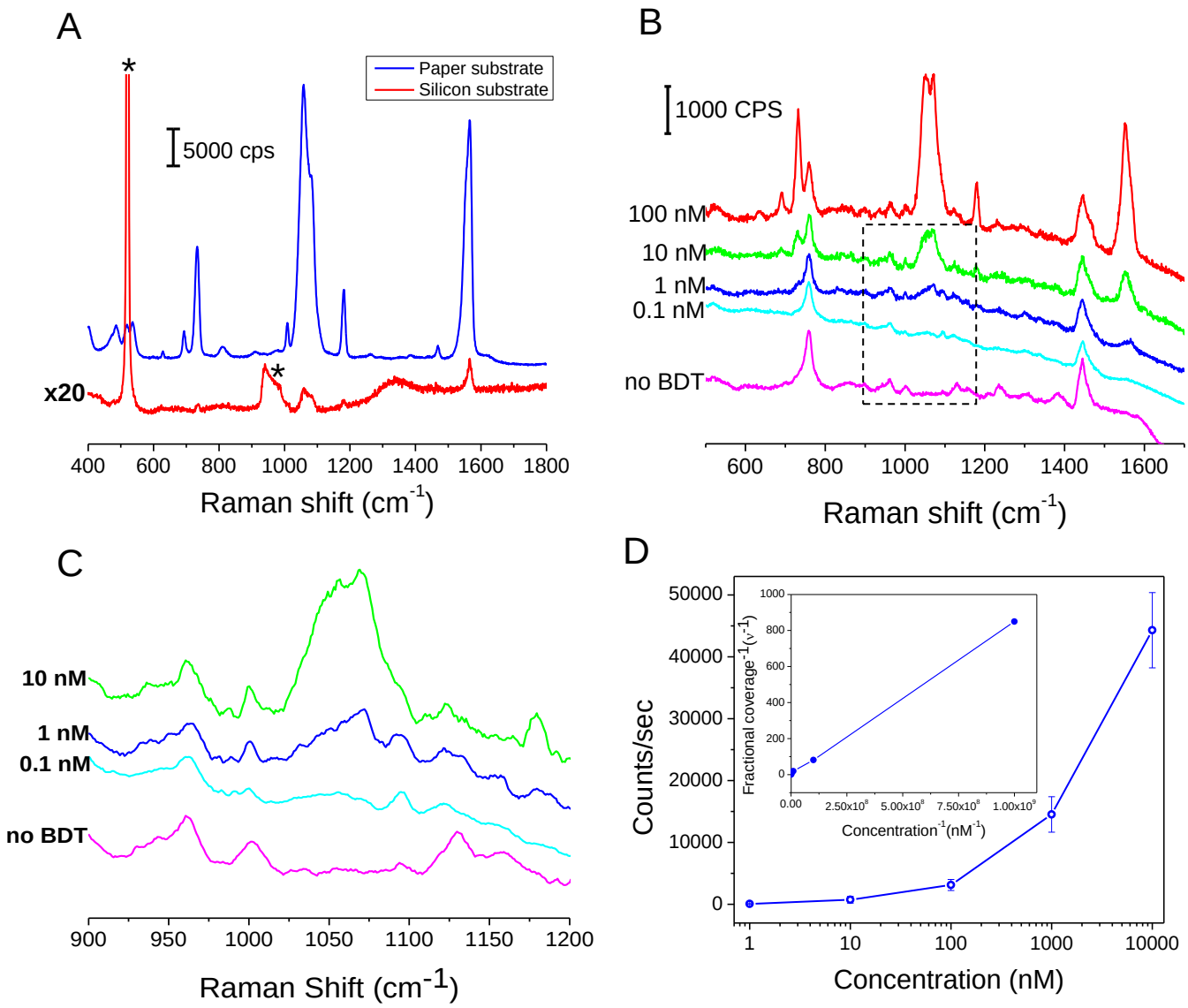

Figure 3.4 (A) Raman spectra collected from AuNR loaded paper and 2D assembly of AuNR, both exposed to 1mM 1,4-BDT; Raman bands indicated with asterisk (*****) correspond to silicon substrate (B) SERS spectra from AuNR loaded paper exposed to different concentrations of 1,4-BDT (C) higher resolution spectra (smoothed) showing 1058 cm^{-1} band, (D) concentration vs. SERS intensity plot showing a monotonous increase in SERS intensity with increasing 1,4-BDT concentration (inset shows the plot of the inverse of the fractional coverage vs. inverse concentration).

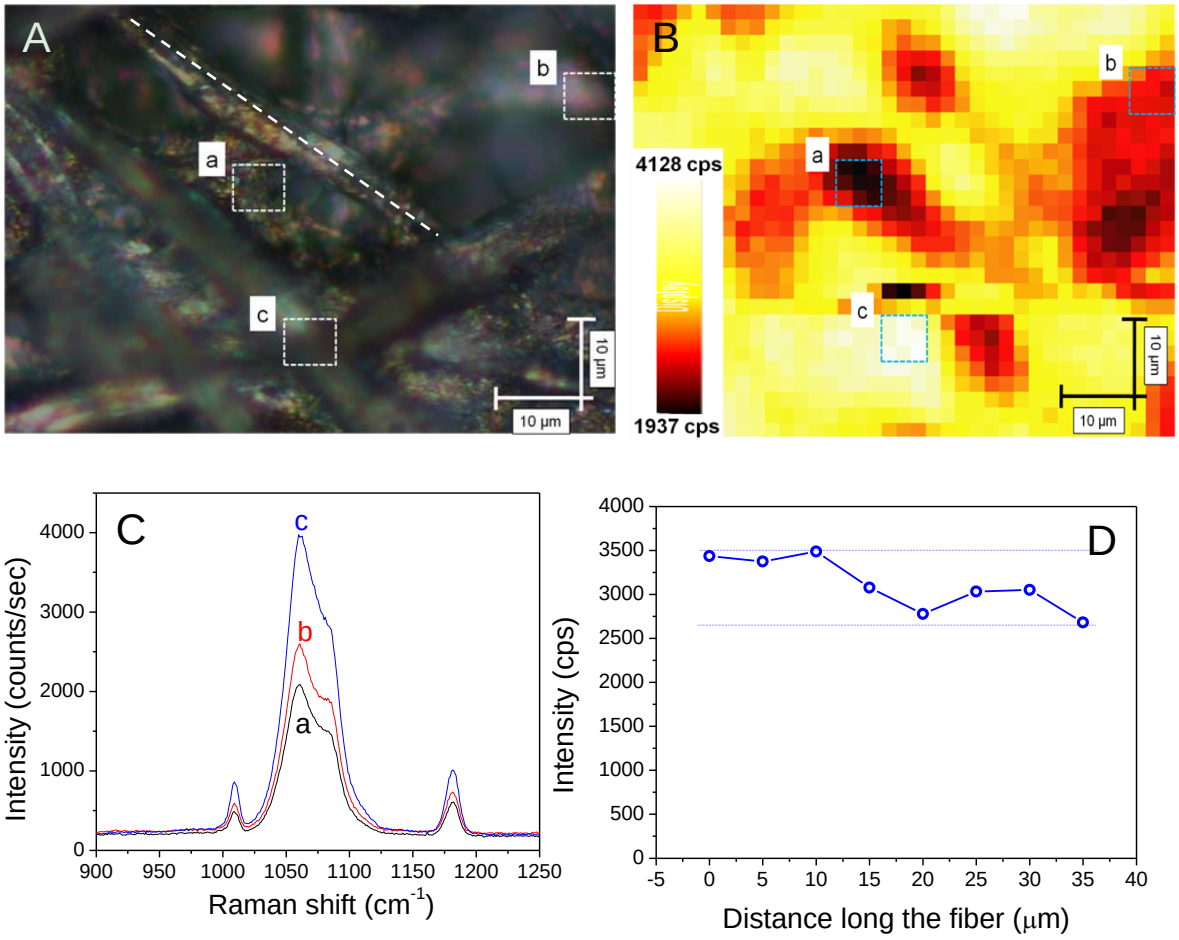

Figure 3.5 Raman mapping of the paper substrate exposed to 1 mM 1,4-BDT (A) optical micrograph showing the region where the Raman mapping was performed (B) Intensity map of 1058 cm^{-1} band within the region shown in (A) (C) Average Raman spectra obtained from regions indicated in (A) (D) Intensity variation along a single fiber shown by the dotted line in (A)

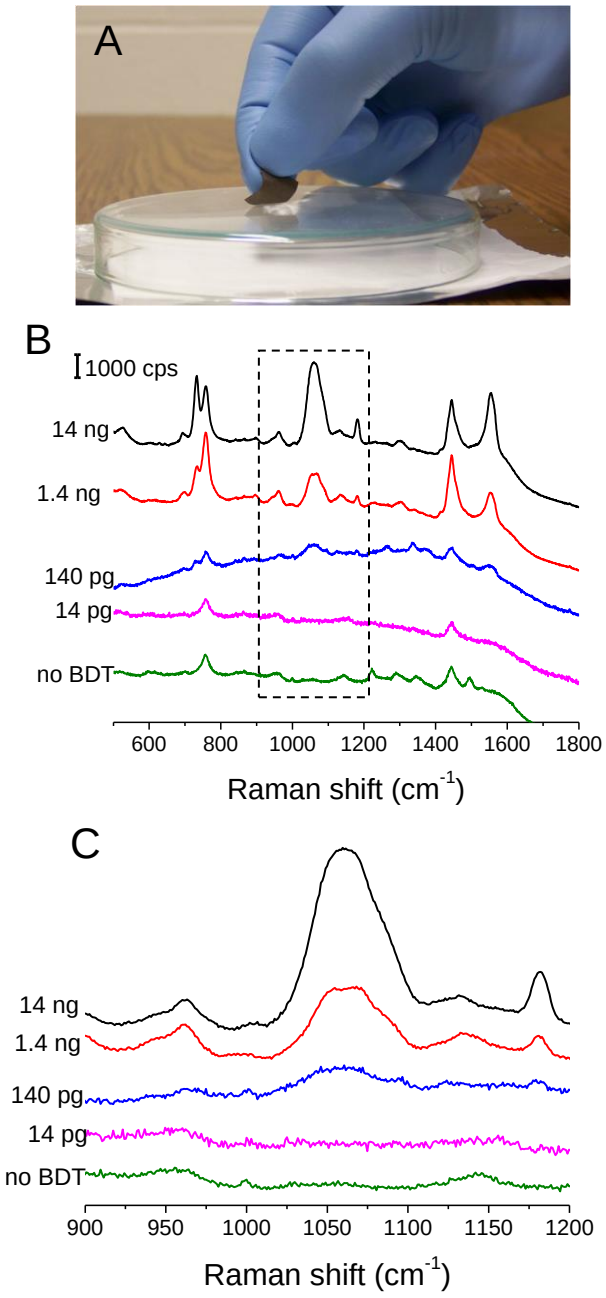

Figure 3.6 (A) photograph showing the SERS substrate being swabbed on the glass surface to collect trace amounts of analyte (B) SERS spectra from AuNR loaded paper swabbed on a glass surface with different amounts of 1,4-BDT (C) higher resolution spectra showing the 1058 cm^{-1} band.

Chapter 4 Plasmonic Nanorattles with Intrinsic Electromagnetic Hot-Spots for Surface Enhanced Raman Scattering

4.1 Introduction

Surface enhanced Raman scattering (SERS) involves the large enhancement of Raman scattering from molecules adsorbed on or in close proximity to nanostructured metal surface.[56, 121] Phenomenal progress in the synthesis of various shape-controlled plasmonic nanostructures over the past decade has led to the emergence of SERS as a powerful analytical and trace detection platform.[79, 122-126] Numerous SERS substrates from roughened metal films to highly ordered nanostructure assemblies fabricated using e-beam lithography have been designed and tested for the trace level monitoring of chemical and biological analytes.[50] 1D SERS substrates, which include nanoparticle and nanodisk strings, [127-131] and 2D SERS substrates comprised of densely-packed nanoparticles and their periodic arrays obtained by nanosphere lithography and Langmuir-Blodgett assembly have been extensively investigated as SERS substrates. [132-135]

Most of the SERS substrates based solely on individual nanostructures offer modest SERS enhancement. On the other hand, interstices between assembled or lightly aggregated nanostructures, often termed as electromagnetic hot spots, offer large SERS signal enhancements, enabling single molecule detection under ideal conditions.[50, 136-138] Although the assemblies of nanostructures are highly SERS-active, the SERS response is very sensitive to the assembly state, thus making it challenging to realize uniform and reproducible SERS substrates with high density of EM hot spots based on such traditional assemblies.[139, 140] Furthermore, fabrication of SERS substrates based on controlled assemblies of nanostructures involves either complex chemical methods or expensive lithographic techniques.[141-145] Therefore, it is desirable to engineer nanostructures with inherent EM hot spots, which can significantly enhance the EM field and enable sensitive detection of analytes using SERS.[146]

In this communication, we report on the synthesis and SERS properties of gold nanorattles comprised of Au nanooctahedron as core and porous gold cube as shell. The nanorattle structure results in the formation of an electromagnetic hotspot between the core and the shell. We demonstrate that the nanorattle structures offer significantly higher SERS enhancement as compared to other solid nanostructures of similar size (e.g., Au nanocubes). Inherent hotspots within the nanostructures obviate

the need for controlled aggregation or assembly of nanostructures to realize electromagnetic hot-spots that are critical for ultrasensitive SERS-based chemical detection.

4.2 Experimental section

Materials: Chloroauric acid ($HAuCl_4$), silver nitrate ($AgNO_3$), cetyltrimethylammonium bromide (CTAB), sodium borohydride ($NaBH_4$), ascorbic acid, poly(vinyl pyrrolidone) (MW =29,000 g/mol), poly (allyl amine) hydrochloride (PAH), 2-naphthalene thiol (2-NT) was purchased from Sigma-Aldrich and used as received without further purification. Nanopure water (>18 MΩ cm) was used for all experiments.

Synthesis of Au nanorattles: Au octahedron particles were synthesized following a seed-mediated growth process.[147, 148] The seed solution was prepared by mixing 7.5 mL aqueous CTAB solution (0.1 M) and 2.5 mL of $HAuCl_4$ (1 mM) in a 20 mL scintillation vial, followed by the rapid addition of 0.6 mL of ice-cold $NaBH_4$ (10 mM) under vigorous stirring to yield a brown colored seed solution. The seed solution was diluted 100 times for the growth of Au octahedrons after 3 h of aging. Growth solution was prepared by adding 7.7 mL of $HAuCl_4$ (0.05 mM) and 0.6 mL of ascorbic acid (0.1 M) to 1.6 mL of CTAB (0.1 M) and under vigorous stirring. To the growth solution 120 µL of the diluted seed was added and the reaction mixture was left undisturbed for about 12 h after vigorous mixing for 30 sec. For the synthesis of Ag@Au nanoparticles, 0.5 mL of $AgNO_3$ (10 mM) and 2 ml of ascorbic acid (0.1 M) were added to 5 mL of as prepared Au octahedron seed solution under stirring. The solution was kept in an oil bath at 60 ^oC for 20 h to complete the growth, resulting in a yellow color solution.

Au nanorattles were synthesized by performing a galvanic replacement reaction.[149] 6 mL of the as prepared Ag@Au nanoparticles solution were centrifuged at 10,000 rpm for 10 min and suspended in 6 mL of PAH solution (6 mg/mL in 6 mM NaCl), followed by the sonication for 1 h. The resultant solution was centrifuged again at 10,000 rpm for 10 min and dispersed in 90 mM PVP solution used for galvanic replacement reaction. $HAuCl_4$ aqueous solution (0.5 mM) was injected to the above mildly boiled Ag@Au solution at a rate of 0.25 mL/min under vigorous magnetic stirring until blue colored solution appeared. The solution was allowed to stand for about 2 h to precipitate AgCl byproduct. The solution was then centrifuged at 7,000 rpm for 10 min and dispersed in nanopure water for further use.

Synthesis of Au nanocubes: Au nanocubes were synthesized using a seed-mediated growth approach reported by Sisco and Murphy.[150] Seed particles were synthesized by mixing 7.75 mL of CTAB (0.1 M)

and 0.25 mL of $HAuCl_4$ (10 mM), followed by the addition of 0.6 mL of ice cold $NaBH_4$ (10 mM) solution under vigorous stirring. The resultant seed solution was stirred for 2 min and aged for one hour before use. Growth solution was prepared by adding 2.5 µL of 10 times diluted seed solution to a mixture of 4.5 mL of $HAuCl_4$ (0.225 mM), 0.4 mL of 0.2 M CTAB, and 0.6 mL of ascorbic acid (0.1 M) under stirring. After overnight aging, the Au nanocubes solution was centrifuged twice at 10000 rpm for 10 min and dispersed in nanopure water before use.

Electromagnetic Modelling: The modeling of the electromagnetic field distribution around plasmonic nanorattles and nanocubes was performed using three-dimensional finite-difference time-domain (FDTD) technique with commercially available software (EM Explorer). FDTD simulations exploit the time and position dependence of Maxwell's equations to model electromagnetic waves in rectangular 3D cells of finite volume called Yee cells.[151] A single gold nanorattle of 55 nm in outer width and 7 nm in shell thickness and a single gold nanocube of 55 nm in width are modeled in a simulation domain of 300 nm × 300 nm × 200 nm, respectively. Perfectly matched layer (PML) absorbing boundary conditions were applied in all directions. A high resolution simulation (Yee cell size of 1 nm) was run at the excitation wavelength (λ = 785 nm) using p-polarized incident plane wave for illumination to obtain the electromagnetic field distribution. The complex refractive index of gold at this frequency was set to $n = 0.18+i\ 4.96$,[152] and the refractive index of surrounding medium was set to be 1 as air.

Spectroscopy Measurements: SERS spectra from paper substrates were collected using a Renishaw inVia confocal Raman spectrometer. Spectra were collected using the 785 nm laser, which was focused on the sample using a 20× objective with 10 sec exposure time. The laser power at the sample surface was measured to be approximately 0.7 mW. At least six spectra were collected from different spots across each substrate for statistical analysis. Extinction spectra of solution were recorded using Shimadzu UV-1800 spectrometer. Extinction spectra of gold nanorattles on paper substrates were collected from a 2×2 μm^2 area using a CRAIC microspectrophotometer (QDI 302) coupled to a Leica optical microscope (DM 4000M) with a 20x objective in the range of 450-800 nm with 10 accumulations and 0.1 sec exposure time in reflection mode. The spectral resolution of the spectrophotometer is 0.2 nm. Six spectra were collected from different spots across the paper substrate to obtain the average.

4.3 Results and discussion

4.3.1 Synthesis of plasmonic nanorattles

Synthesis of plasmonic nanorattles involves the formation of Au nano-octahedra followed by the growth of an Ag shell on these structures using seed-mediated growth technique to form Ag@Au nanostructures. Subsequently, the bimetallic core-shell nanostructures are converted to nanorattles by converting the silver shell into a porous gold layer using galvanic replacement reaction (Fig. 4.1). We hypothesize that the coupling between Au octahedra core and external porous gold shell renders the inherent EM hotspots, which are accessible for the analytes of interest through diffusion.

Gold nano-octahedra, employed as cores, were synthesized using a seed-mediated method with cetyl trimethylammonium bromide (CTAB) as the stabilizing agent.[147] Au nano-octahedra were found to be monodisperse with a body length of 36.5 ± 3.2 nm (n>100) as measured from the transmission electron microscope (TEM) images (Fig. 4.2A, S2.1a). A thin silver shell was formed on the nano-octahedra by introducing the as prepared Au nano-octahedra into a silver growth solution comprised of silver precursor ($AgNO_3$), ascorbic acid as the reducing agent and CTAB as the stabilizer following a method described by Fan et al. with some modifications (please see experimental section).[147] Epitaxial growth of the silver shell on the Au cores resulted in the formation of core-shell nanocubes. The synthesized Ag@Au nanocubes were monodisperse with an edge length of 44.5 ± 2.5 nm (n>100) as determined from the TEM images (Fig. 4.2B, S2.1b). It is worth noting that the original Au nano-octahedra employed as cores did not possess sharp corners. However, after the silver shell formation, the nano-octahedra exhibited sharp edges of as evidenced by the TEM images. Since, the as prepared nano-octahedra solution was used for the growth of silver shell, possibly the unreacted Au ions in presence of Ag^+ ions led to the formation of sharp corners (Fig. 4.2C).

A galvanic replacement reaction was carried out in order to create the nanorattle structure where the gold octahedron core remains embedded within the porous Au shell. Prior to the replacement reaction, the capping agent CTAB was replaced with poly(allylamine hydrochloride) (PAH) and the reaction was carried out in presence of poly(vinyl pyrollidone) (PVP). Generally, the galvanic replacement reaction for the formation of an Ag nanocube is conducted in the presence of PVP as the stabilizer.[153] However, in the present case we observed aggregation of the Ag@Au nanoparticles while dispersing the particles in

PVP solution, as evidenced by the change in the shape of the LSPR band of Ag@Au nanoparticle solution and large aggregates of Ag@Au nanoparticles found in the SEM images (Fig. S2.2). In order to overcome this issue, we first exchanged the capping agent, CTAB, with PAH and then performed the galvanic replacement reaction. It is to be noted that if the galvanic replacement was carried out in absence of PVP, the morphology of the template Ag@Au nanoparticles was not preserved (Fig. S2.3). Hence, exchange of CTAB with PAH was necessary to avoid aggregation, while the inclusion of PVP was required to preserve the morphology of the template nanoparticles during the galvanic replacement reaction. The TEM image of Au nanorattles shows the presence of porous cubic Au shell surrounding the intact octahedron Au core, where the vertices of the octahedron touches the faces of the cubic shell structure. From the TEM images, the size of the nanorattles was determined to be 54.6 ± 4.5 nm (n>100) and the wall thickness of the shell was estimated to be ~7 nm (Fig. 4.2D, S2.1c).

The Au nano-octahedra exhibited a localized surface plasmon resonance (LSPR) peak at around 555 nm (Fig. 4.2E). The extinction spectrum of Ag@Au nanoparticles revealed three distinct peaks at 412 nm, 486 nm and 580 nm. The peaks at 412 and 486 nm are consistent with those observed in case of Ag nanocubes, while 580 nm peak is ascribed to the inner Au core particle and coupling between gold and silver at the interface.[154] Galvanic replacement reaction resulted in the disappearance of LSPR peaks corresponding to the Ag shell with concomitant raise of a new higher wavelength band that exhibited progressive red-shift with increase in the amount of Au precursor added to the reaction. The extinction spectrum of the Au nanorattles displayed a major peak at 710 nm and a minor peak corresponding to the Au octahedron core at 555 nm. A photograph of Au core, Ag@Au and Au nanorattles solutions under ambient light clearly demonstrates the distinct extinction characteristics of the nanostructures (Inset of Figure 4.2E).

4.3.2 FDTD simulations of plasmonic nanorattles

As previously mentioned, one of the distinct features of the nanorattle structures as compared to conventional solid plasmonic nanostructures is the plasmonic coupling between the core and porous shell, which results in an electromagnetic hotspot within the nanostructure. To estimate the enhanced EM field intensity in the nanorattle structure compared to solid nanostructure, we have employed finite-difference time-domain (FDTD) simulations (Fig. S2.4). The spatial map of E-field intensity (at λ_{ex}=785 nm) around

nanorattles and nanocubes of same dimensions (side length of 55 nm) with polarization parallel to the sidewall ([100] direction) and along the diagonal ([110] direction) is depicted in Figure 4.3A-E. Au nanocubes exhibited a maximum E-field intensity enhancement of nearly 12 and 45 times for polarization along [100] and [110] directions, respectively. The maximum enhancement was found to be at the sharp corners of the nanocubes (Fig. 4.3C). On the other hand, the maximum field enhancement in the case of the nanorattle structures reached nearly ~2300 and ~3300 times for polarization along [100] and [110] directions, respectively (Fig.4.3F). In the case of nanorattles, the maximum field enhancement occurred at the junction of the solid core and porous shell. The enhancement in the maximum field intensity in the case of nanorattles is nearly two orders magnitude higher compared to that of the solid nanostructures. It important to note that SERS enhancement scales with the square of the field intensity enhancement, which implies a nearly four order higher SERS enhancement from nanorattles compared to solid nanocubes.[50]

4.3.3 SERS performance of plasmonic nanorattles

Plasmonic nanorattles hosting such an intense EM field enhancement can serve as an excellent medium for SERS-based chemical sensing. Furthermore, the porous nature of the outer shell facilitates the uptake of the analytes and their transport to the highly SERS-active regions. To test the performance of the nanorattles as SERS-active nanostructure, nanorattles deposited on a silicon substrate were exposed to a model analyte, 2-naphthalenethiol (2-NT, 1 mM). Raman spectra were collected from individual particles by locating them under dark-field microscopy (Fig. 4.3G). The SERS spectra collected from five different individual particles are depicted in Figure 4.2C. The most prominent peaks were observed at 1066, 1381 and 1625 cm^{-1}, which corresponds to the C-H bend and ring stretch vibrations of 2-NT molecule respectively (Fig. 4.3H).[155, 156] Although variations were observed in the intensity of the SERS spectra, it is worth noting that all the individual nanostructures exhibited clearly distinguishable Raman spectra corresponding to 2-NT (Fig. 4.3H). The SERS intensity of particle-to-particle variation (~40%) is possibly due to the variation in the orientation of the nanorattle structures with respect to the polarization direction of the excitation laser. It is known that SERS activity of the anisotropic nanostructures such as nanocubes exhibit a strong dependence on the orientation with respect to polarization of the excitation source.[157] The SERS activity of nanorattles was compared to that of Ag@Au nanostructures and the

solid gold nanocubes of similar dimensions (see Fig. S2.6 for TEM images of Au nanocubes). Under similar conditions, the SERS spectra of individual Au@Ag nanostructures showed extremely weak but discernable signal with peaks at 1066, and 1381 cm^{-1} while individual Au nanocubes exposed to 2-NT did not exhibit any discernible Raman bands corresponding to 2-NT (Fig. 4.3H). The large SERS signal from individual nanorattles as opposed to Au@Ag nanostructures and Au nanocubes clearly demonstrates their potential as highly promising SERS media.

We further demonstrate the fabrication of a simple and flexible SERS substrate based on these novel plasmonic nanostructures. We and others have previously introduced plasmonic paper, paper substrates adsorbed with plasmonic nanostructures, as a highly sensitive SERS substrate that can be deployed as swab for detection of trace levels of chemical analytes in liquids and on surfaces.[158-163] However, previous demonstrations relied on either individual nanostructures that offered limited SERS enhancement or mildly aggregated nanoparticles with poor uniformity. The SERS substrate was fabricated by immersing the paper substrates into the nanorattle solution that led to the uniform adsorption of the nanostructures on the paper fibers. The inset of Figure 4.4D shows the paper substrate before and after adsorption of the nanorattles demonstrating the intense gray-blue color of the paper substrates adsorbed with nanostructures. SEM images revealed the uniform adsorption of plasmonic nanorattles on paper substrates. The density of nanorattles on paper surface was calculated to be ~40±5 /μm^2 from the SEM image (Fig. 4.4A and see Fig. S2.7 for large area image). The higher magnification image of Au nanorattles on paper surface depicts the tiny pores on the surface of nanorattles that are critical for diffusion of the analytes into EM hotspot regions (inset of Figure 4A, S8). Vis-NIR spectrum obtained from the plasmonic paper depicts the extinction bands corresponding to the plasmonic nanorattles discussed above (inset of Fig. 4.4A). The LSPR bands exhibited a small blue shift as compared to their position in solution due to the effective decrease in the refractive index of surrounding medium upon their adsorption on paper substrates from aqueous solution.

Paper is made up of a biodegradable polymer, cellulose. Cellulose offers a hydroxyl surface enabling the electrostatic adsorption of positively charged Au nanorattles, resulting from the coating of PAH and PVP.[164] Once the nanorattles are adsorbed onto the paper, it can serve as a simple flexible SERS substrate for the detection of chemical analytes. The trace detection capability of the paper based

substrate was investigated by exposing the fabricated substrate to varying concentrations of 2-NT in ethanol (Fig. 4.4C). The Raman spectrum of the bulk 2-NT molecule is shown in Figure S2.9 (see support information). Similar to those observed in case of single particle SERS, the Raman bands corresponding to the C-H bending mode at 1083 cm^{-1} in the bulk normal Raman spectrum shifts to 1069 cm^{-1} in all the SERS spectra indicating the binding of 2-NT to the metal surface.[156] The Raman band at 1381 cm^{-1} was used to monitor the trace detection ability of the fabricated substrate. The semi-log plot of the concentration of the analyte vs 1381 cm^{-1} peak intensity showed increase in the intensity of the Raman band with increasing concentration of the analyte (Figure 4.4D). Distinguishable peak (signal to noise ratio >4) was observed down to a concentration of 10 pM. Adsorption of 2-NT observed here can be fit with Freundlich adsorption isotherm given as $\theta = K_F C^{1/n}$ where θ is the fractional coverage taken as the ratio of I/I_{max} for peak at 1381 cm^{-1}, C is the concentration of the analyte and K_F and n are constants.[165-167] The linearity of fractional coverage and concentration on a log-log plot confirms the Freundlich adsorption observed here (inset of Figure 4.4D). The substrate exhibited good homogeneity with standard deviation of around 15%, which is close to that observed for commercial SERS substrates (Fig. S2.10).[168]

4.4 Conclusions

We have demonstrated the synthesis of Au nanorattles structure with an Au nano-octahedron core, where the vertices of the core particle touch a porous cubic Au shell structure. Owing to the large enhancement in the EM field in the interior of the nanostructures, the nanorattles exhibited large SERS enhancement of analyte molecules that diffused through the porous shell into the hotspot regions. Flexible SERS substrate based on the nanorattles exhibited excellent uniformity and sensitivity with a detection limit of ~10 pM of 2-NT. The SERS substrate design suggested overcomes the need for controlled aggregation or assembly of nanostructures for forming EM hotspots.

4.5 Supporting information

Supporting information for chapter 4 is provided in appendix 2.

Figures

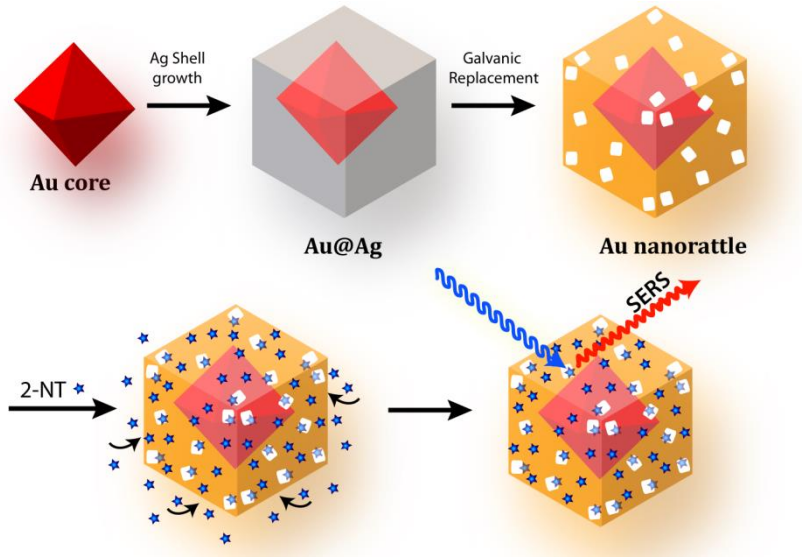

Figure 4.1 Schematic illustration of the synthesis of Au nanorattles.

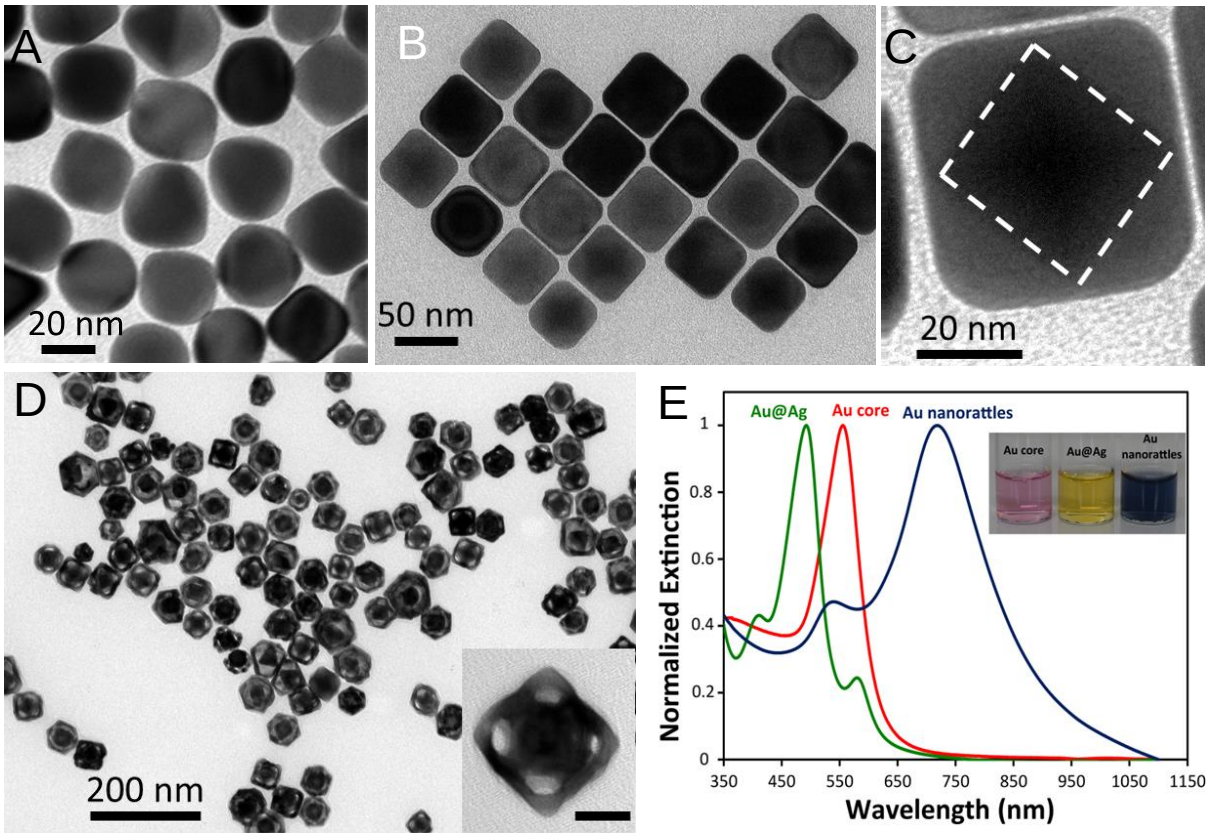

Figure 4.2 Representative TEM images of (A) Au core, (B-C) Ag@Au nanoparticles following the deposition of thin silver shell on Au nanostructures. (D) Au nanorattles with inset showing the magnified view of a single nanorattle (scale bar in the inset image represents 20 nm). (E) Extinction spectra of Au core, Ag@Au and Au nanorattles with inset showing the photograph of the colloidal solutions of various nanostructures described above.

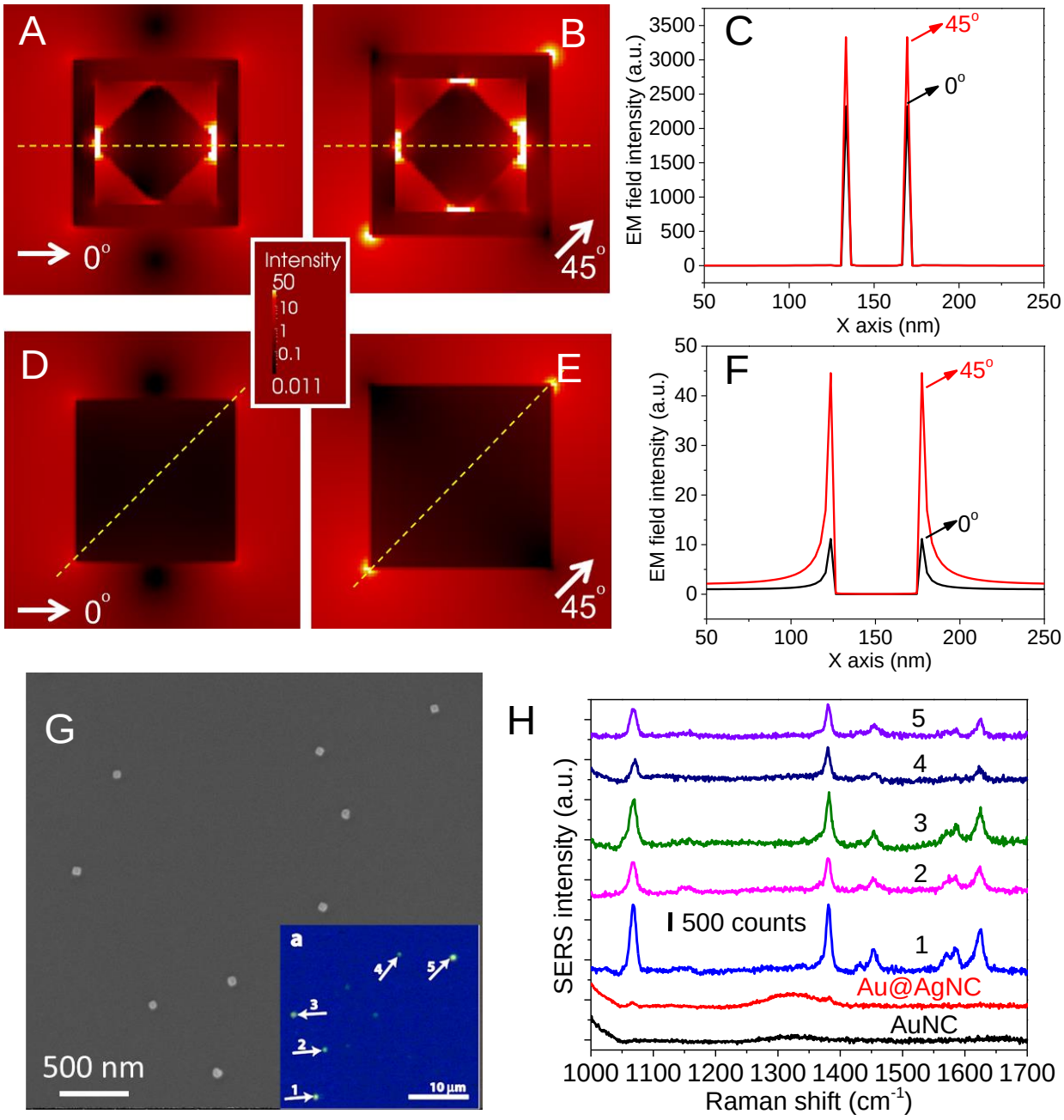

Figure 4.3 FDTD simulations showing the electric field distribution of Au nanorattles in logarithmic scale for electric field polarized along (A) [100] and (B) [110] and (C) corresponding cross-sections along the lines shown in E-field maps. FDTD simulations showing the electric field distribution of Au nanocubes in logarithmic scale for electric field polarized along (D) [100] and (E) [110] and (F) corresponding cross-sections along the lines shown in E-field maps. (G) SEM image and dark field optical image (inset) of the isolated Au nanorattles adsorbed on a silicon substrate. (H) SERS spectra obtained from the individual

nanorattles as marked in (G), individual Ag@Au nanocubes (Ag@AuNC) and Au nanocubes (AuNC) for comparison.

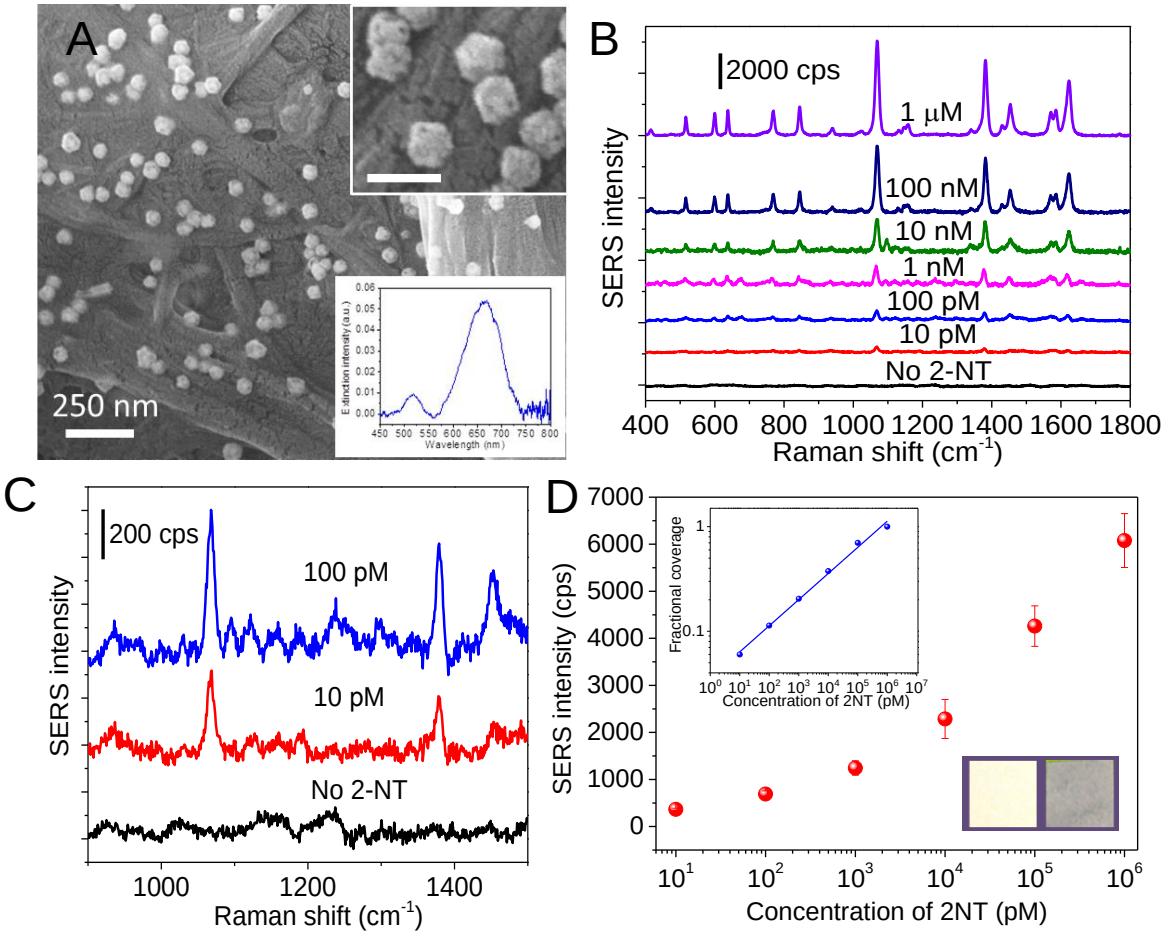

Figure 4.4 (A) SEM image showing the uniform adsorption of Au nanorattles on a paper substrate with an inset of magnified SEM image showing nanorattles with tiny pores on the surface (scale bar: 100 nm) and an inset Vis-NIR extinction spectra obtained from paper substrates adsorbed with Au nanorattles (bottom panel). (B) SERS spectra obtained from plasmonic paper substrate after exposing it to varying concentration of 2-NT in ethanol, and (C) zoomed spectra at low concentrations. (D) Semi-log plot showing the concentration vs intensity of the 1069 cm^{-1} Raman band demonstrating monotonic increase in the peak intensity with concentration. Inset shows the photograph of the paper substrate before and after adsorption of Au nanorattles. concentration vs. SERS intensity plot showing a monotonous increase in SERS intensity with increasing 1,4-BDT concentration (inset shows the plot of the fractional coverage vs. concentration on log-log scale).

Chapter 5 Multifunctional Analytical Platform on a Paper Strip: Separation, Pre-concentration and Sub-Attomolar Detection

5.1 Introduction

Paper is a versatile and common material that finds many uses in consumer oriented products because its source (cellulose) is abundant in nature, renewable, inexpensively produced and recycled.[104] Paper is also biodegradable, biocompatible, and has ability to easily wick and absorb fluids.[169] Paper has gained much interest in recent years as a low-cost and ideal platform for building portable miniature diagnostic devices suitable for developing countries, resource-limited environments, and point-of-care settings.[170, 171] Paper-based chemical and biological sensing has emerged as an attractive analytical and detection platform with a potential of becoming the best trade-off between cost/time-efficiency, simplicity and detection abilities. The detection is traditionally performed by fluorescence, chemiluminescence or electrochemical sensing,[172-174] and mostly directed towards labelling methods using antibodies or colorogenic reactions.[175, 176] The last few years have witnessed the integration of microfluidic paper-based analytical devices (μPADs) with electrically or optically active nanomaterials such as carbon nanotubes[175] and graphene.[177]

We and others have recently introduced a highly sensitive paper-based surface enhanced Raman scattering (SERS) substrate, which involves uniform adsorption of metal nanostructures onto common filter paper.[159, 178-180] SERS enables label-free detection of a wide variety of chemical and biological analytes. However, current paper-based SERS substrates lack key functionalities such separation, chemical selectivity, and pre-concentration, which are critical to realize a versatile lab-on-chip platform. In other words, for these sensors to be able to analyse complex samples, separation abilities need to be integrated into the paper. While increasing efforts have been focused in extending functionality of the paper substrate,[172, 181-185] these developments usually involved lithographic processes or multi-layer fabrication,[184, 186-188] which is achieved at the expense of the simplicity of the paper device.

The challenge is then to design and develop a highly sensitive label-free analytical platform that does not require any lithographic or microfabrication steps, while providing a multifunctional platform. The second challenge addressed in this work is to significantly lower the detection limit beyond the nanomolar or part per billion (ppb) levels reported in recent literature for different μPAD configurations (ESI, Supplementary

Table S1).[171-174, 189-193] We seek a versatile system that allows separation and preconcentration of the different components of a complex sample in a small surface area and a label-free optical detection, by taking advantage of the properties of cellulose paper: the capillary effect that is attracting increasing interest among the lab-on-a-chip community,[170, 179, 182, 194] the microfibrous structure and the suitability for nanoparticle adsorption by a simple immersion or drop-casting.

5.2 Experimental section

Reagents and Materials: The chemicals rhodamine 6G (R6G), fluorescein isothiocyanate (FITC) and 2-naphtalenethiol, poly(allylamine hydrochloride) (PAH) and poly(sodium 4-styrenesulfonate) (PSS) were all obtained from Sigma-Aldrich (St. Louis, MO, USA). PAH (2%) and PSS (2%) solutions were prepared by dissolving 20 mg of PAH or PSS powder in 1 mL deionized water. These solutions were diluted to prepare 1 %, 0.5 % and 0.25 % polyelectrolyte solutions. Chlorophyll mixture was obtained by the extraction of spinach concentrate.

Surface and materials characterization: Surface enhanced Raman scattering (SERS) spectra were collected using a *Renishaw inVia* confocal Raman spectrometer mounted on a Leica microscope with 50X objective (NA = 0.90) in the range of 100–3200 cm^{-1}. A diode laser of 785 nm wavelength (0.5 mW) was used for sample excitation. Optical and fluorescence images of the µPAD were obtained with a Leica optical microscope (DM 4000M) coupled with a point-shot microspectrometer using 20X and 50X objectives. Fluorescence spectra were obtained from paper substrates using a CRAIC microspectrophotometer (QDI 302) coupled to the abovementioned optical microscope. Transmission electron microscopy (TEM) images and energy-dispersive X-ray spectroscopy (EDX) maps were obtained using a field emission transmission electron microscope (JEM-2100F, JEOL) operating at an accelerating voltage of 200 kV, and SEM images were collected using a JEOL JSM-7001 FLV field emission SEM at an accelerating voltage of 15kV. Elementary analysis (atomic ratio) of carbon, nitrogen (N1s) and sulfur (S2p) composition of the paper is achieved by X-ray photoelectron spectroscopy (XPS) using M-Probe Surface Science XPS spectrometer.

5.3 Results and discussion

5.3.1 Star shape plasmonic microfluidic paper-based analytical devices (µPADs)

Filter paper employed in this study (Whatman#1) is composed of microscale (~ 10 µm) cellulose fibrous strands interwoven together. Smaller microfibers (average diameter of ~ 0.4 µm) made part of the large fibrous structure with nanofibers braided in between. The RMS surface roughness of the paper was measured to be ~70 nm over 5 × 5 μm^2 area, indicating that the paper offers a large surface area. To keep the device fabrication process simple, filter paper was cut into a star-like geometry with 8 points named fingers (Figure 5.1B). This design obviates the need for lithographic or hydrophobic patterning of the paper while offering an effective liquid handling system using capillary forces. The shape-enhanced capillary forces *i.e.*, the small size of the tips (radius of tips is ~10-20 µm) result in a much faster drying of the solvent at the tips compared to the rest of the paper substrate in turn causing a rapid flow from the wetted surface to the dry area thus concentrating analytes to the tiny test regions. Interestingly, these strong capillary effects make the flow strong enough to drag not only macromolecules but also gold nanorods with a length of ~ 60 nm.

Gold nanorods (AuNR) were employed as plasmonic nanostructures for enabling SERS owing to the facile tunability of the longitudinal plasmon resonance (to fit to the source laser) and sharp corners, which results in electromagnetic hot-spots (Figure 5.1A).[195, 196] Figure 5.1B shows that immersion of the paper into AuNR solution results in a preferential concentration of the nanorods at the finger-tips and edges of the device. Even simple visual inspection clearly indicates such concentration of AuNR at the tips, which appear darker compared to the other regions of the paper (Figure 5.1B). SEM images and EDX maps obtained from different regions of the paper substrates clearly demonstrate this effect (Figure 5.1C). This is of a great importance as the accumulation of the nanorods in a small area increases the number of electromagnetic hot-spots, thus enhancing the sensitivity of the optical detection.[197-199] This enhancement is exploited here using SERS as the transduction method.[191, 200]

In addition to AuNR transport, the capillary-driven flow is also used here to drag and preconcentrate samples at the µPAD tips, thus providing enough analyte in the test spot for detection even at very low sample concentrations. In order to enable analyte preconcentration on paper and at the same time separate complex samples, we explored the possibility of using polyelectrolytes. Each finger of the µPAD was modified with a different concentration of PAH (positively charged) or PSS (negatively charged) (Figure 5.2A). This modification is achieved by exposing the tip of each finger to a droplet of

polyelectrolyte solution (3 µL) with a defined concentration as indicated in Figure 5.2a. The droplet is spontaneously absorbed by the paper and rapidly spread along a single finger without reaching other areas of the platform. As a result, the different polyelectrolyte-coated fingers form a gradient of charges that control the direction and distance of migration of the analytes, depending on their electrostatic interactions with the charged substrate. We hypothesize that complex samples could be separated and directed into different fingers of the µPAD. The chemical surface gradient formed by the differential functionalization of the fingers is confirmed by EDX mapping. The distribution of the polyelectrolytes is monitored by the detection of nitrogen (N) and sulphur (S) atoms in PAH and PSS, respectively (Figure 5.3). The elemental analysis by XPS also confirmed the decrease in S2p and N1s atomic composition, reflecting the different concentration of PSS and PAH on different fingers.

5.3.2 Separation and preconcentration of a complex mixture

The first example demonstrating the effect of the chemical gradient is shown in Figure 5.2B using fluorescein. Depending on the charge and concentration of the polyelectrolyte coating, fluorescein forms a distinct band or completely migrates to the finger tip. Specifically, we observed that fluorescein tends to concentrate at the fingertip coated with 2%PSS. On the other hand, it forms a distinct band at the entrance of the finger coated with 2%PAH. Considering that fluorescein is negatively charged in water, it tends to strongly bind to the positively charged PAH, resisting any capillary-driven motion to the tips. On the other hand, in the case of the PSS coated fingers, the capillary forces drag the fluorescein along the finger and concentrate them at the tips. This observation clearly hints that (*i*) potentially different molecules can migrate into different fingers which provide the most electrostatically compatible surface and (*ii*) can be concentrated at the tip, thus providing an extremely high concentration in a very small surface area. To further demonstrate the separation ability of this platform, we have analysed a mixture of rhodamine and fluorescein. Rhodamine is known to bear positive charge, while fluorescein is known to be negatively charged in water. Distinct electrostatic interaction with different fingers enables spatially isolating the two dyes on the µPAD as demonstrated in Figure 5.4A. Furthermore, using similar principle, a more complex sample composed of chlorophyll a, chlorophyll b, carotene and xanthophyll, obtained from spinach concentrate can also be separated using such differential functionalization of the paper substrates (Figure 5.4B). The identification of the different separated components is confirmed by

their emission spectra under a fluorescence microscope.

A more complex matrix was prepared by mixing 100 µM R6G with a one-time diluted spinach concentrate. This sample is used to demonstrate two important points: the first is that the µPAD is able to separate and pre-concentrate R6G molecules from the other chromophores contained in the spinach concentrate as shown in Figure 5.5A and B. The distribution of R6G demonstrates a preferential concentration at the fingertips functionalized with PAH. Secondly, one of the components of spinach concentrate (chlorophyll b) exhibits fluorescence emission in the same wavelength range as R6G. As a result fluorescence spectroscopy is not sufficient to clearly distinguish between these two components. Figure 5.5B shows that SERS spectroscopy enables one to specifically identify R6G molecules, thus demonstrating the productive complementarity of SERS and fluorescence techniques and the advantages provided by plasmonic paper platforms.

Once we have established the ability to separate and preconcentrate the analytes from a complex mixture to predetermined locations of the µPAD, we turn our attention to trace detection capabilities of this novel analytical platform. To evaluate the detection limit of the µPAD and the advantages offered by the capillarity-driven preconcentration at the finger-tips, we attempt to detect different concentrations of R6G (Figure 5.6A). The results indicate a remarkable detection limit down to attomolar level (100 aM). This limit can be further lowered by concentrating the analyte in a micrometric surface area, corresponding to a single cellulose microfiber at the very tip of the finger (Figure 5.6B and ESI, Supplementary Figure S3.1a). The pre-concentration factor can be estimated from the paper properties, the initial concentration and data obtained by SERS measurement. The concentration of 100 aM in 100 µL sample corresponds to around $6x10^6$ molecules. As indicated by fluorescence images, most of these molecules can be pre-concentrated at the paper fingertip into a surface area smaller than $1mm^2$ (paper thickness is 180 µm). Knowing that filter paper (Whatman#1) has a water absorbance of 1.8 ± 0.2 $\mu L/cm^2$ as determined experimentally, the final sample concentration at the fingertip is estimated to be 0.5 nM, which gives a remarkable pre-concentration factor of 10^9. This factor can be further enhanced by working with a single cellulose microfiber where the sample can be concentrated into an extremely tiny volume i.e., fiber of 50 µm length (Supplementary Figure S3.1b). Figure 6C shows the increase in the SERS intensity when the Raman laser spot is focused on to the fingertip region labelled “b”. The SERS measurement on the

microfiber tip provides an additional 10X improvement in the detection limit.

To further verify this result, we prepared paper substrates with tips ending by a single cellulose microfiber of around 20 µm in diameter. Two different analytes, namely, fluorescein and napthalenethiol, were tested. The test domains exhibited a detection limit of ~100 aM for fluorescein, while no characteristic band was observed when the detection was performed outside the microfiber (Figure 5.7A and B). Even better performance was noted for naphtalenethiol (due to its strong affinity to gold) that showed a remarkable detection limit of 500 zM (signal to noise ratio (SNR) equal to 3). This detection limit is also the result of the thiol binding of the molecule to AuNRs, offering an optimal distance for SERS. However, this performance has a very limited dynamic range going from 500 zM to 10 µM. This is expected as higher concentrations rapidly saturate the micrometric detection spot. To verify he applicability of this platform on a real world sample, 2-naphtalenethiol (1 µM) was added to tap water and the obtained solution is introduced to the paper platform for separation and detection. Interestingly, Figure S3.2A shows a visible separation and accumulation of the different water ions (K, Na, Ca, Mg, Cl,.) at the paper fingers functionalized with PSS. This unexpected accumulation makes the migration of the target molecules in other fingers easier by reducing the molecular crowding. As depicted in Figure S3.2B, the platform can be effectively used to detect 2-naphtalenethiol and other aromatic contaminants in tap water. The studies reported here with R6G and FTIC represent the lowest detection limit reported for µPADs. It is interesting to note that this performance is only limited by the size of the laser spot in the Raman instrument and the available sample volume. In other words, a concentration of 100 zM (10^{-19} M) corresponds to only 6 molecules in the test solution volume (100 µL). Therefore, beyond the attomolar level, higher sample volume is needed to ensure the presence of the molecule in the detection spot. Future efforts are aimed to shorten the migration time of the molecule to the detection spot and improve the separation abilities by exploring a variety of polymers as well as silica nanoparticles for a column chromatography-like separation.

5.4 Conclusions

In summary, we demonstrate a plasmonic paper-based analytical platform that combines chromatographic separation abilities with preconcentration and detection functionalities on a single level µPAD. The use of capillary forces by shaping the paper substrate overcomes the need of active

microfluidics and the associated microfabrication process. The generation of charge gradient on the paper substrate through polyelectrolyte coating is shown to exhibit remarkable separation abilities of complex samples. The results also show that capillary-driven flow could be used for the transport and preconcentration of both analytes and metal nanoparticles in a very small detection area and even on a single cellulose microfiber. The combination of this concept with surface enhanced Raman scattering analysis pushes the detection limit down to the attomolar level, placing microfluidic paper-based analytical devices in a competitive stand with the traditional sensors and without scarifying their simplicity.

5.5 Supporting information

Supporting information for chapter 5 is provided in appendix 3.

Figures

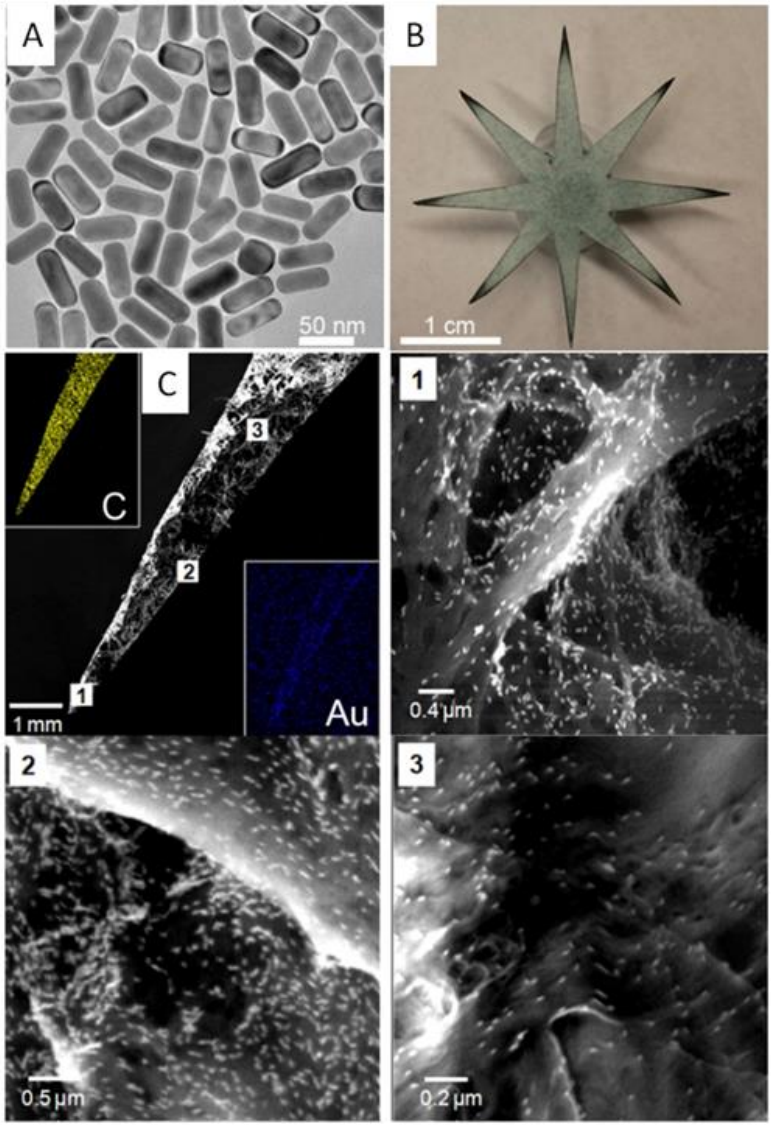

Fig. 5.1 (A) TEM image of the AuNR employed for the fabrication of SERS µPAD. (B) Designed µPAD with eight fingers showing the accumulation of AuNRs at the tips (dark edges). (C) SEM images of the µPAD tips. The insets represent EDX maps of carbon (C) and gold (Au) distribution. A zoom at the fingertip shows nanorods distribution at three different spots labeled 1, 2 and 3 as a result of lateral flow concentration.

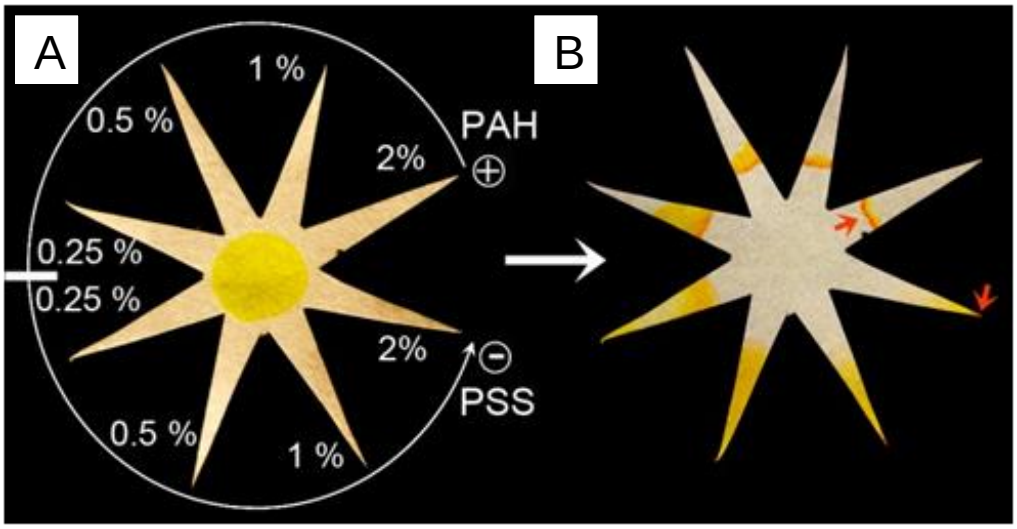

Fig. 5.2 Separation by surface charge gradient. (A) Charge gradient obtained by different concentrations of PAH and PSS polyelectrolytes. The yellow spot at the center is caused by fluorescein droplet as deposited. (B) Migration of fluorescein into different fingers. The red arrows indicate the concentration at which fluorescein form either a band or concentrates at the tip.

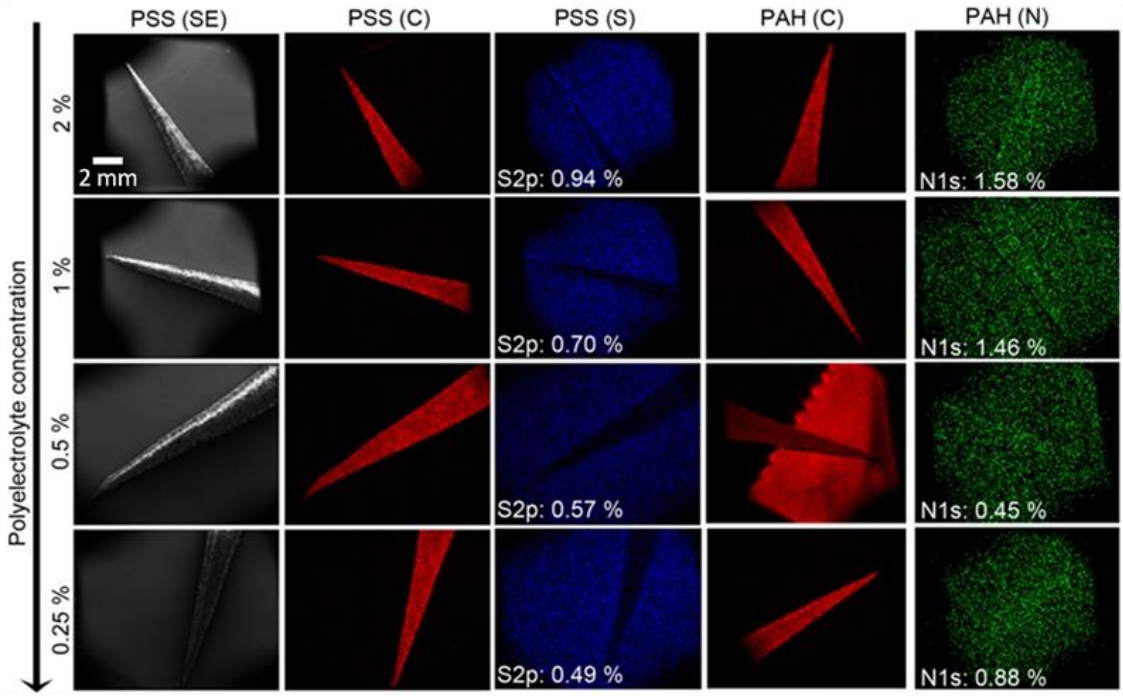

Fig. 5.3 EDX mapping and XPS elementary analysis of the surface charge gradient generated by differential polyelectrolyte coating. The panel PSS (SE) represents secondary electrons (SE)-SEM micrographs of the μPAD fingers coated with PSS. Panels “PPS (C)” and “PAH(C)” are EDX mapping of carbon atoms on PSS and PAH coated fingers respectively. These two panels are showed to indicate the position of the fingers in the images and facilitate comparison. Panels “PSS (S)” and “PAH (N)” represent EDX mapping of sulphur (S) and nitrogen (N) atoms in PSS and PAH coated fingers respectively. The percentage numbers indicated in the images represent the composition ratio of sulphur (S2p) and nitrogen (N1s) obtained by XPS elementary analysis.

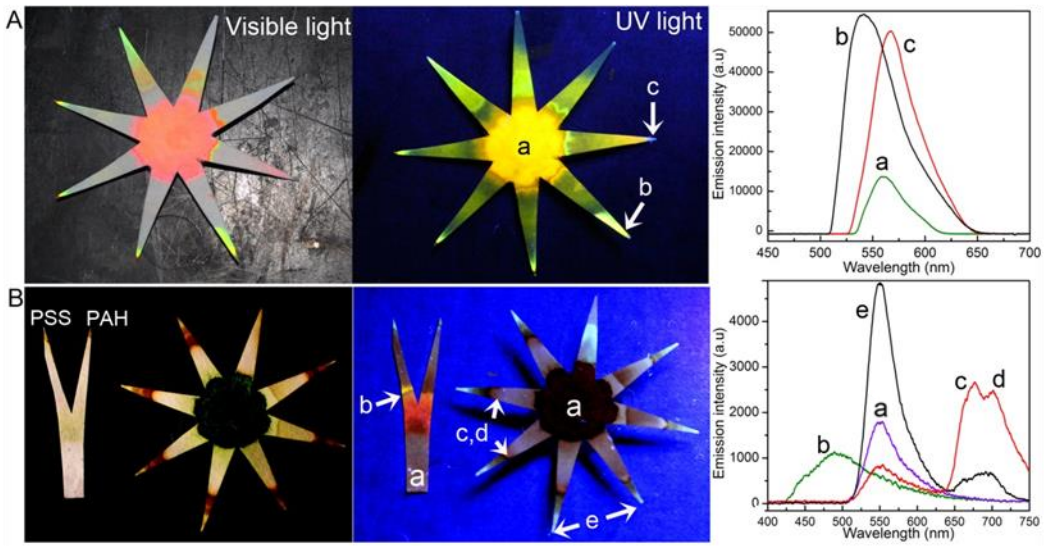

Fig. 5.4 Separation of complex samples by electrostatic gradient charge and capillary forces. Images from the left to the right show the µPAD under visible light, under UV light and the emission spectra obtained using a fluorescence microscope. (A) Separation of (a) a mixture of two molecular dyes. (b) and (c) are respectively fluorescein and R6G dyes. (B) Separation of spinach concentrate (a). The lower case letters (b-e) in panel B represent respectively carotene, xanthophyll, chlorophyll a and chlorophyll b.

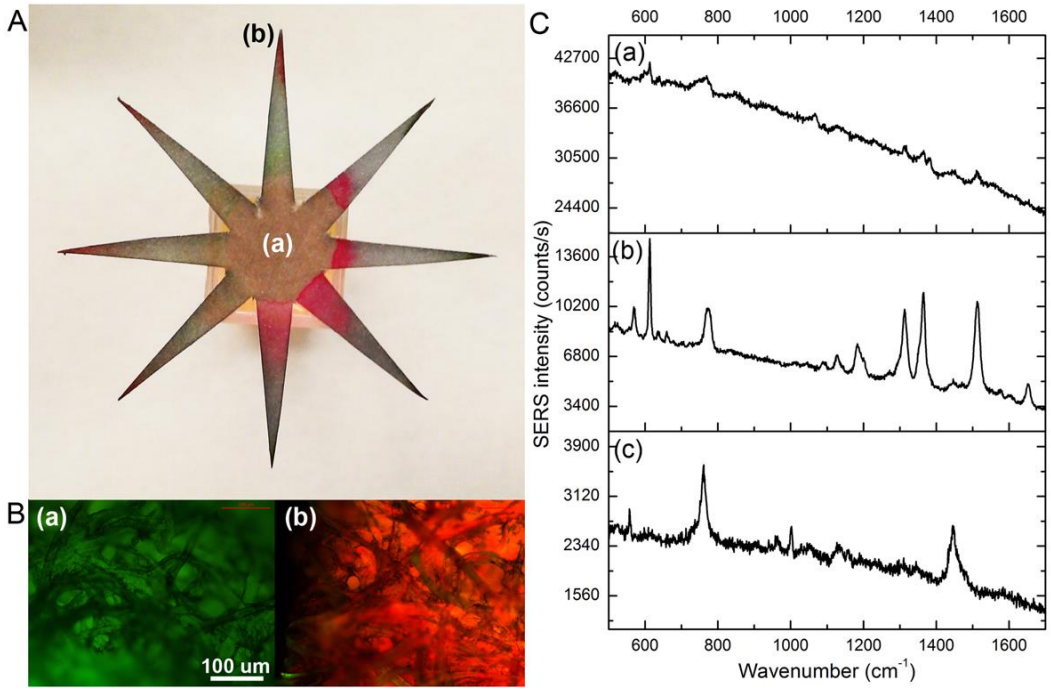

Fig. 5.5 Separation and SERS detection of R6G in a mixture containing spinach concentrate. A) Optical image of the paper platform at the end of the separation step. B) Fluorescence images obtained with a I3 filter at the center and fingertip of the platform. C) Surface enhanced Raman scattering analysis. (a), (b) refer respectively to data collected at the center and at the fingertip of the platform. (c) shows the SERS spectrum of a control (nanorods-functionalized paper).

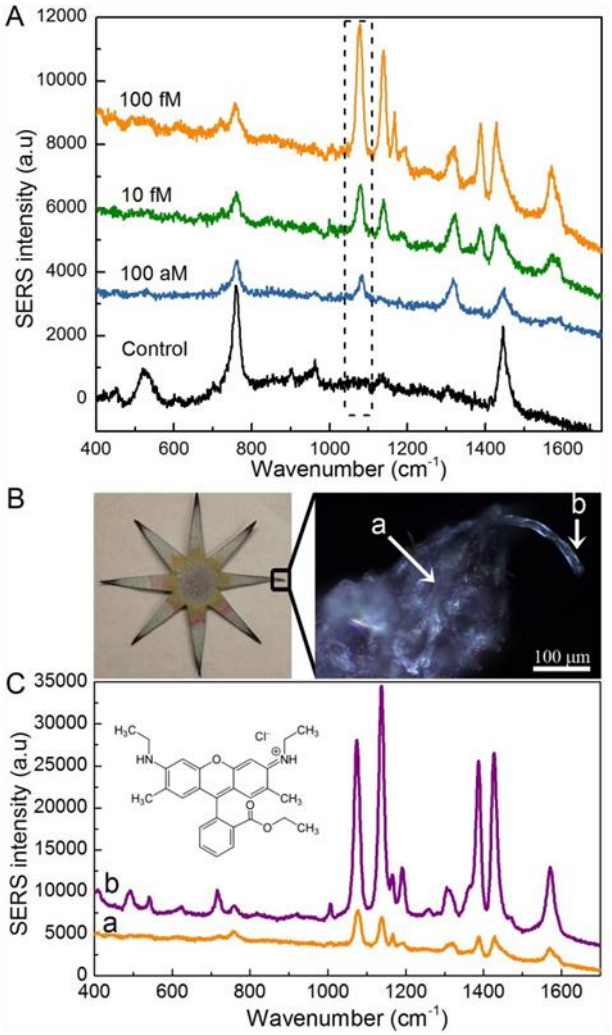

Fig. 5.6 Surface enhanced Raman scattering analysis of R6G (λ=785 nm). (A) Detection of different concentrations of R6G. (B) Optical image of the µPAD. The zoom shows a dark field image of the tip, where (a) and (b) show the position of the laser spot used to collect the R6G spectra shown in Figure 5C.

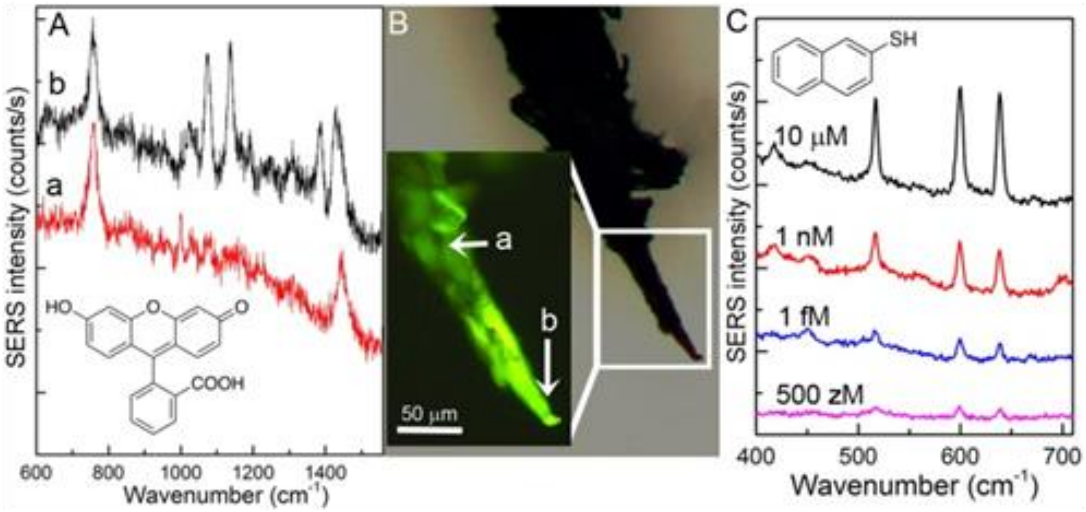

Fig. 5.7 SERS Detection limit on a single cellulose microfiber. (A) Detection of 100 attomolar of fluorescein. (a) and (b) represent SERS spectra collected at the positions indicated in panel B. The bands at 1075 cm^{-1}, 1138 cm^{-1} and 1385 cm^{-1} are assigned to fluorescein. (B) Optical and fluorescence image of the μPAD tip. C) Detection of 2-naphthalene thiol. The peaks at 516 cm^{-1}, 600 cm^{-1}, 638 cm^{-1} are assigned to ring deformation and twist.

Chapter 6 Multiplexed Charge-Selective Surface Enhanced Raman Scattering based on Plasmonic Calligraphy

6.1 Introduction

Surface enhanced Raman scattering (SERS) involves the dramatic enhancement (under ideal conditions $>10^{10}$ times) of Raman scattering signal (vibrational molecular fingerprint) from molecules adsorbed on or in close proximity to a nanostructured metal surface.[56, 121] SERS is a highly promising transduction platform for the detection of trace levels of both known and unknown chemical and biological species with applications spanning from life sciences, environmental monitoring, to homeland security.[79, 122-126] Remarkable progress in the synthesis of shape-controlled plasmonic nanostructures over the last 15 years has led to numerous SERS substrates. However, most of these efforts were focused on achieving large and uniform SERS enhancement across the substrate.[46, 123, 201-211] To transform SERS into a viable chemical detection method in real-world settings, one of the challenges that must be overcome is the inherent poor chemical selectivity of plasmonic nanostructures to capture target analytes in complex chemical environment.[79] To date there have only been a few studies focusing on improving the selectivity of SERS substrates.[212-215] A multiplexed SERS substrate, enabling the detection of multiple target analytes on the same surface is a powerful means for real-world chemical detection. To achieve chemical selectivity from a complex mixture, selective coatings on SERS-active surfaces have been employed to promote the adsorption of analytes and prevent the adsorption of unwanted species. [79, 215, 216]

Paper-based technologies have emerged as attractive analytical and detection platforms owing to the many advantages of paper substrates, such as high specific surface area, excellent wicking properties, compatibility with conventional printing approaches, significant cost reduction, flexibility and easy/cheap disposal.[217-221] We have recently successfully demonstrated a highly sensitive paper-based SERS substrate, which involves uniform adsorption of metal nanostructures onto common filter paper by immersion approach.[222-224] Despite the inherent morphological heterogeneity, paper-based SERS substrates exhibited excellent homogeneity in optical properties and SERS enhancement. However, immersion approach precludes spatial multiplexing (*i.e.*, realizing multiple test domains for the detection

of two or more analytes on the same substrate) as it results in uniform adsorption of metal nanoparticles over the entire paper substrate.

Here, we introduce a simple yet powerful approach, namely, plasmonic calligraphy for realizing spatially isolated and chemically-selective test domains. This technique can be potentially automated by implementing with a robotic arm for realizing large scale patterns on paper substrates. It can serve as an alternate path forward to multiplexed paper-based SERS substrates by overcoming the drawbacks of conventional printing approaches, which involve tedious routines for optimizing the nanoparticle ink formulation for ink-jet printing and expensive equipment costs in the case of material printers.[162, 225] Recently we have demonstrated a multiplexed label-free bioassay based on localized surface plasmon resonance using calligraphy of bioplasmonic nanostructures.[226] In the present study, as a proof-of-principle, we demonstrate a chemically-selective multiplexed SERS substrate in which isolated test domain achieved by plasmonic calligraphy are comprised of polyelectrolyte-coated gold nanorods. These plasmonic nanostructures bind to oppositely charged species in a multi-analyte chemical mixture enabling multiplexed charge-selective chemical detection.

6.2 Experimental details

Materials: Cetyltrimethylammonium bromide (CTAB), chloroauric acid ($HAuCl_4$), ascorbic acid, sodium borohydride, rhodamnine 6G (R6G), methyl orange (MO), poly(styrene sulfonate) (PSS) (Mw=70,000 g/mol), and poly(allyl amine hydrochloride) (PAH) (Mw=56,000 g/mol) were purchased from Sigma-Aldrich. Silver nitrate and filter paper (Whatman #1) was purchased from VWR international. All the chemicals have been used as received with no further purification. Paper mate profile retractable ballpoint pens were bought from Amazon.com, Inc. Dove damage therapy intensive repair shampoo was purchased from a supermarket.

Preparation of polyelectrolytes coated gold nanorods (AuNRs) and corresponding plasmonic ink: AuNRs were coated with polyelectrolytes as previously reported.[227] Briefly, 5 ml of twice-centrifuged AuNR solution was added drop-wise to 5 ml of PSS (0.2% w/v) in NaCl aqueous solution (6 mM) under vigorous stirring, followed by stirring for 3 hours. To remove excess PSS, the above solution was centrifuged at 10,000 rpm for 10 min, and the pellet was dispersed in nanopure water after removing the supernatant. To modify AuNRs with PAH, 5ml of PSS coated AuNR solution was added drop-wise to 5

ml of PAH (0.2% w/v) in 6 mM NaCl aqueous solution, followed by stirring for 3 hours. The resultant 1ml of PSS and PAH coated AuNR solution (~1 nM) was centrifuged and concentrated to 10 µl solution as ink, which was injected into a ball point pen refill cleaned with ethanol and nanopure water by sonication.

SERS spectra measurements: A regular laboratory filter paper (Whatman #1) calligraphed with PSS-AuNRs and PAH-AuNRs at distinct regions was employed as the SERS substrate (Fig. 6.3A inset). Each test domain was comprised of five adjacent lines and each line involved two strokes. Repetitive stroke at the same position was employed to increase the density of nanorods while five adjacent strokes were applied to create larger test domains for statistical analysis. The width of each stroke depends on the tip of the ball point pen, which in this case was measured to be around 1 mm (Fig. 6.2A inset). These substrates were exposed to different concentrations of rhodamine (R6G) and methyl orange (MO) for 1 hour followed by thoroughly rinsing with water and allowing them to naturally dry. SERS spectra from paper substrates were collected using a Renishaw InVia Raman microscope and Wire 3.0 software operating on a dedicated computer. Spectra were collected using the 785 nm laser, which was focused on the sample using a 20X objective with 10 sec exposure time. The laser power at the sample surface was measured to be approximately 0.7 mW. At least six spectra were collected from different spots across each substrate.

6.3 Results and discussion

6.3.1 Characterization of oppositely charged AuNRs

AuNRs modified with negatively charged poly(styrene sulfonate) (PSS) and positively charged poly(allylamine hydrochloride) (PAH) were employed as plasmonic ink to achieve charge-selective multiplexed SERS. AuNRs are particularly attractive as SERS medium considering the facile and large tunability of the LSPR wavelength of nanorods with aspect ratio and the electromagnetic (EM) hot-spots at their edges.[139, 221, 228-231] AuNRs, synthesized using a seed-mediated approach, are positively charged with a length of 59.9±3.1 nm and a diameter of 21.6±2.2 nm (TEM image in Figure 6.1A).[232, 233] UV-vis extinction spectra of the AuNRs are characterized by two distinct bands at ~512 nm and 675 nm corresponding to the transverse (lower wavelength) and longitudinal (higher wavelength) oscillation of electrons with incident EM field (Figure 6.1B). Adsorption of PSS on positively charged cetyltrimethylammonium bromide (CTAB) stabilized AuNRs through electrostatic interaction resulted in a

small red shift of ~1 nm in the longitudinal LSPR wavelength of AuNRs due to increase of refractive index of medium around AuNRs. Similarly a further red shift of ~1 nm was observed upon adsorbing a layer of PAH on PSS modified AuNRs. The shape of the LSPR bands of PSS coated AuNRs (called PSS-AuNRs henceforth) and PAH coated AuNRs (called PAH-AuNRs henceforth) is identical to that of the pristine AuNRs solution indicating the absence of aggregation during surface modification (Figure 6.1B).[234] Zeta potential values of CTAB coated AuNRs, PSS-AuNRs, and PAH-AuNRs were measured to be +33 mV, -67 mV, and +48 mV, respectively, which further confirms the successful modification of AuNRs with positively and negatively charged polyelectrolytes (Figure 6.1C).

6.3.2 Characterization of SERS substrates fabricated using plasmonic calligraphy

To achieve SERS test domains with differential functionalization of plasmonic nanostructures on paper substrates, we employ polyelectrolyte coated AuNRs as ink. Such plasmonic ink facilitates one to create test domains comprised of functionalized nanostructures on paper substrates adjacent to each other without cross-contaminating the test domains based on the concept of plasmonic calligraphy as illustrated in Figure 6.2A. The inset depicts the SEM image of the tip of a ballpoint pen with a ball diameter of ~1.5 mm, showing the residue of AuNRs ink left on the ball surface. Ball pens are particularly well-suited for dispensing nanoparticle inks due to their compatibility with liquid and gels.[235] The viscosity of AuNRs ink was measured to be ~1.25 Pa·s, which is close to the optimal viscosity of silver nanoparticle ink reported previously for writing electrically conductive lines on paper surface.[236]

The density of the nanostructures on the paper substrate can be controlled by the number of strokes. The density of the PSS-AuNRs adsorbed on the paper substrate for a single stroke was found to be 35±8/μm^2 from SEM images (Figure 6.2B). Interestingly, some nanorods were observed under the cellulose fiber, possibly from the diffusion of AuNRs during the writing process. However, owing to the porous nature of filter paper, these AuNRs are still accessible to the chemical analytes. Extinction spectra were collected from five different spots (spot size of 2×2 μm^2) of written PSS-AuNRs line and the variation in the extinction intensity of the longitudinal LSPR band, which corresponds to the optical density, was found to be relatively small (relative standard deviation of 10%). Longitudinal LSPR wavelength also exhibited a small standard deviation of ~1 nm, which indicates the absence of uncontrolled aggregation of AuNR (Figure 6.2C). The excellent spectral homogeneity is due to the uniform adsorption of AuNRs on

paper substrates as evidenced by the SEM images (Figure 6.2B, S4.1). The spectral homogeneity observed here is quite remarkable considering the simplicity of the writing process and the inherent heterogeneity of the paper substrates (large surface roughness and hierarchical nature of the fibrous mat). Notably, the adsorption of AuNRs on paper is sufficiently strong to resist desorption from paper surface even after extensive rinsing with water as confirmed by little change in the intensity and shape of extinction spectra collected before and after rinsing.

6.3.3 Charge selective detection of chemical analytes

To demonstrate the charge selective detection of chemical analytes, we chose positively charged rhodamine 6G (R6G) and negatively charged methyl orange (MO) as analytes. We hypothesize that the negatively charged analytes (*i.e.*, MO) preferentially adsorb to the test domain comprised of positively charged PAH-AuNRs and positively charged analytes (*i.e.*, R6G) preferentially adsorb to the test domain comprised of negatively charged PSS-AuNRs, enabling charge-selective detection of the analytes. To test charge selectivity of calligraphed SERS test domains, we wrote two distinct test domains comprised of PSS-AuNRs and PAH-AuNRs on the same strip of filter paper as shown in the top right inset of Figure 3A. Two identical test strips was exposed to separate R6G and MO aqueous solutions (10 μM) and SERS spectra were collected from both test domains (Figure 6.3A). For the test strip exposed to MO solution, SERS spectrum obtained from PAH-AuNR domain revealed characteristic Raman bands of MO at 1117, 1143, and 1392/1422 cm^{-1}, corresponding to Ph-N stretching, C-H deformation, and N=N stretching vibration, respectively (Figure 6.3B).[237] On the other hand, PSS-AuNR test domain did not exhibit any Raman bands corresponding to MO, which indicates the absence of MO due to the electrostatic repulsion. Similarly, for the test strip exposed to R6G solution, SERS spectrum of PSS-AuNRs exhibited strong Raman bands corresponding to R6G at 612, 1311, and 1363/1509 cm^{-1}, which correspond to C-C-C ring in-plane vibration, C-O-C stretching, and aromatic C-C stretching vibration, respectively (Figure 6.3C).[238] In contrast, PAH-AuNRs domain did not exhibit any R6G bands.

To test the selectivity of the SERS test domains from a chemical mixture, a paper strip with PAH-AuNRs and PSS-AuNRs test domains was exposed to a mixture of R6G and MO (concentration of 100 μM each). Following thorough rinsing with nanopure water, SERS spectra were collected from both test domains. The test domain comprised of PSS-AuNR exhibited Raman bands corresponding to R6G while the PAH-

AuNR test domain exhibited Raman bands corresponding to MO (Figure 6.3D and E). These results clearly indicate the charge selectivity of polyelectrolyte-modified AuNRs even from a mixture of chemical compounds. Furthermore, plasmonic calligraphy approach demonstrated here serves a simple and facile tool to create charge-selective SERS test domains.

Next, we set out to probe the trace detection ability and limit of detection (LOD) of the calligraphed charge-selective test domains. Figure 6.4A shows the SERS spectra collected from PAH-AuNRs domain after exposure to different concentrations of MO in water. The spectra clearly reveal the monotonic decrease in the intensity of the characteristic Raman bands of MO with decreasing concentration. The most intense Raman band at 1117 cm^{-1} was used to analyze the trace detection ability of the calligraphed test domains. The Raman band is clearly distinguishable (signal to noise ratio (SNR) > 10) down to 10 nM concentration as seen from the higher resolution spectra compared to PAH-AuNRs control (Figure 6.4B). The plot of the intensity of the 1117 cm^{-1} band vs. concentration of MO collected from PAH-AuNRs region shows a monotonic increase of the intensity with increasing concentrations of MO, in contrast to virtually no signal corresponding to MO from PSS-AuNRs at different concentrations (Figure 6.4C).

As expected, SERS spectra collected from PSS-AuNRs region upon exposure to different concentrations of R6G aqueous solution clearly show the intensity decrease in characteristic Raman bands of R6G with decreasing concentrations (Figure 6.4D). Raman band at 1363 cm^{-1} was employed for probing the trace detection ability of the test domains. The Raman band is clearly distinguishable (SNR > 8) down to 10 nM concentration (Figure 6.4E). The plot of the intensity of the 1363 cm^{-1} band vs. concentration of R6G collected from PSS-AuNRs region shows a monotonic increase of the intensity with increasing concentrations of R6G, in contrast to extremely small signal for various concentrations observed from PAH-AuNRs domain (Figure 6.2F). One would expect stronger SERS signals from PSS-AuNR exposed to R6G compared to PAH-AuNR exposed to MO due to the smaller separation of the analyte from AuNR surface in the case of PSS-AuNR (note that PAH was coated on PSS-AuNR). However, we have observed that the PSS-AuNR exposed to R6G exhibited slightly smaller SERS intensity compared to PAH-AuNR exposed to MO possibly because the affinity between MO and PAH is stronger compared to that between R6G and PSS. The detection limit of SERS substrate can be improved by increasing the density of AuNRs on the paper substrate by applying more strokes.[223] The SERS substrates exhibit

excellent homogeneity with relative standard deviation of ~20%, which is close to the values observed for commercially available microfabricated SERS substrates.[168] This level of homogeneity is remarkable considering the simplicity of the calligraphy approach and inherent heterogeneity of the paper substrates. In fact, the variation in the SERS signals was found to be largely due to the focal variations of the incident laser on the paper substrates as described previously.[223]

6.3.4 Complex real-world chemical mixtures analysis

To elucidate the charge selectivity of polyelectrolyte modified AuNRs with varying chemical and physical environmental conditions, paper strips with calligraphed test domains were exposed to chemically complex media involving many interfering compounds. Shampoo represents a complex mixture of organic chemicals, especially anionic surfactants, such as sodium laureth sulfate, sodium lauryl sulfate, sodium, ammonium, and triethanolammonium (TEA) lauryl sulfates, which serves as a true representation of a real-world sample. Figure 6.5A clearly shows the prominent characteristic Raman bands of MO detected from PAH-AuNRs after exposure to 1 mg/ml of a commercial shampoo solution spiked with MO (1mM), compared to the sample exposed to virgin shampoo solution. On the other hand, no Raman bands of MO were noted in the SERS spectra collected from PSS-AuNRs domain following the exposure to MO spiked shampoo solution (Figure 6.5B).

SERS spectra collected from the PAH-AuNRs region upon exposure to different concentrations of MO shampoo solution clearly demonstrates a decrease in intensity of characteristic MO Raman bands with decreasing concentration (Figure 6.5C). The Raman band is clearly distinguishable (signal to noise ratio > 3) down to 1 µM concentration (Figure 6.5D). The higher detection limit (*i.e.,* lower sensitivity) likely results from the competitive interaction of MO and abundant anions in shampoo with positively charged PAH-modified AuNRs. We have also performed SERS measurements from PSS-AuNRs region upon exposure to different concentration of R6G spiked in shampoo solution (Figure S4.4). We noted similar limit of detection (1 µM) for R6G. These results clearly demonstrate the charge selective SERS based detection of chemical analytes from complex real-world mixtures using plasmonic calligraphy technique.

6.4 Conclusions

In conclusion, we have introduced plasmonic calligraphy as a simple and effective means to achieve multiplexed charge-selective SERS substrate for detection of target chemical analytes from a complex

chemical mixture. Plasmonic calligraphy approach serves as a simple, low-cost tool for creating well-isolated SERS test domains using functionalized plasmonic nanostructures as ink in a regular ballpoint pen. The approach suggested here obviates the need for any complex multi-step process such as formation of hydrophilic test domains and hydrophobic barriers using complex material printing approaches (usually performed using specialized material printers) to achieve multiple test domains on the same strip of paper. Plasmonic calligraphy can be extended to various shape-controlled plasmonic nanostructures with other surface functionalities to achieve arrays of chemically selective domains for analyzing complex real-world chemical mixtures.

6.5 Supporting information

Supporting information for chapter 6 is provided in appendix 4.

Figures

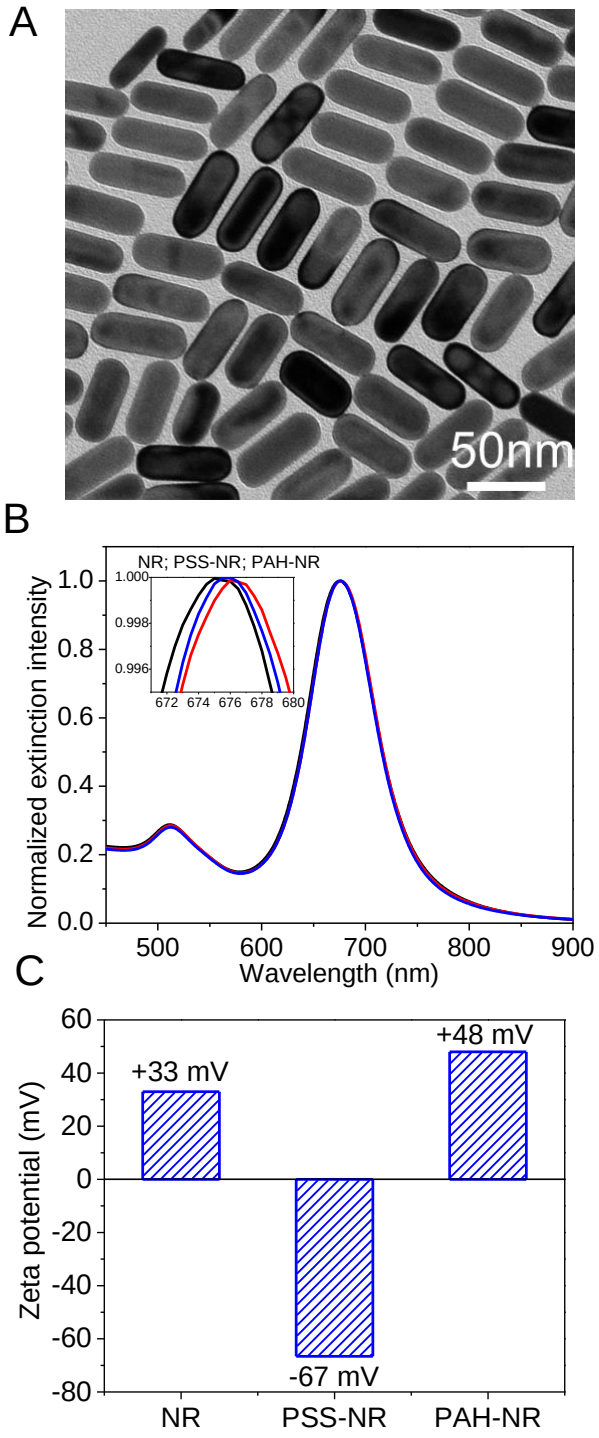

Figure 6.1 (A) Representative TEM image of AuNRs. (B) Extinction spectra and (C) Zeta potential of AuNRs, PSS, and PAH modified AuNRs in aqueous solution.

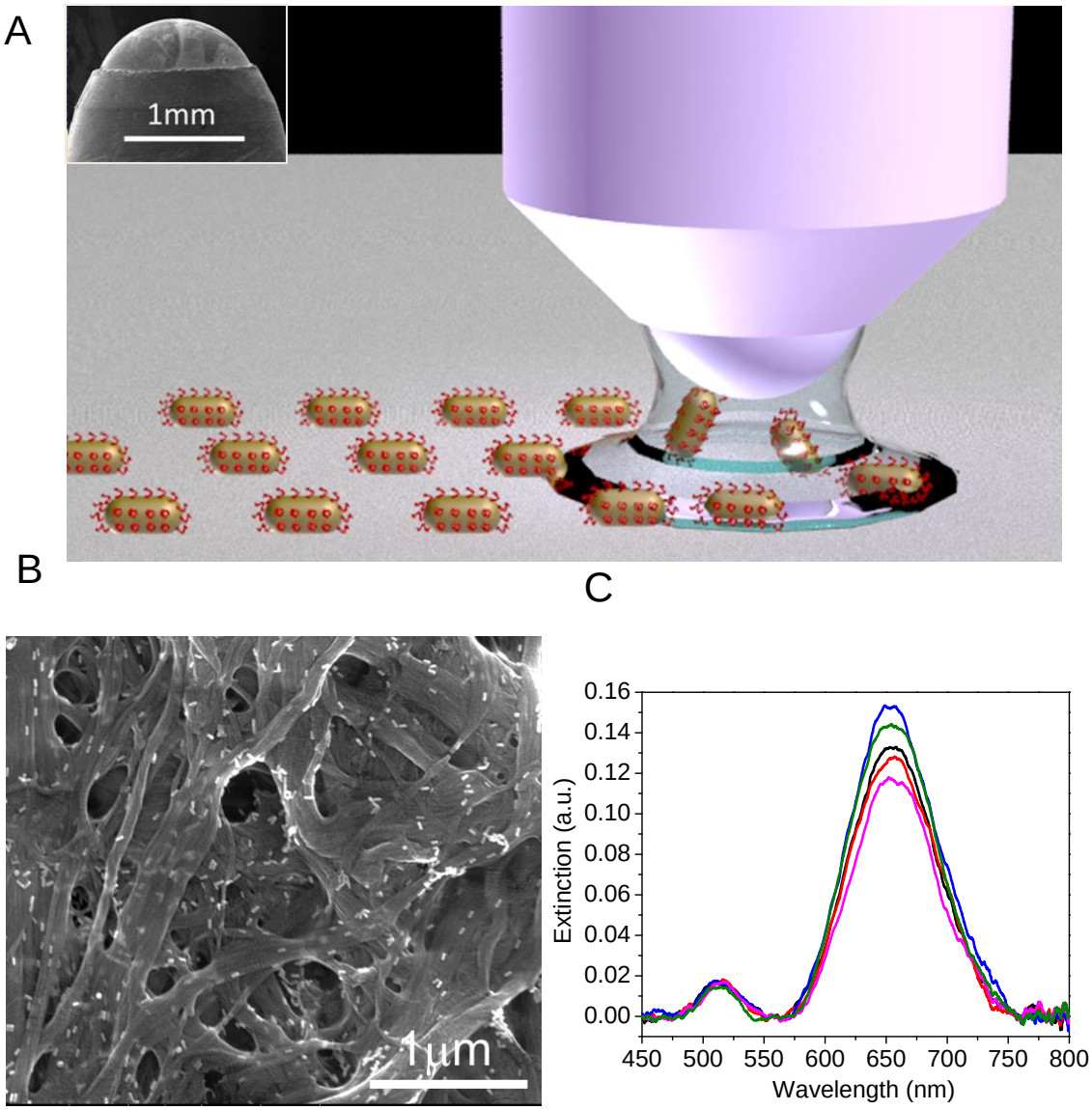

Figure 6.2 (A) Schematic illustration of the concept of plasmonic calligraphy (inset: SEM image of the tip of a ball pen with AuNR ink residue on the surface). (B) SEM images of PSS-AuNRs calligraphed on paper substrates. (C) Extinction spectra measured from five different spots of PSS-AuNRs test domain, showing excellent spectral homogeneity with only small variation intensity.

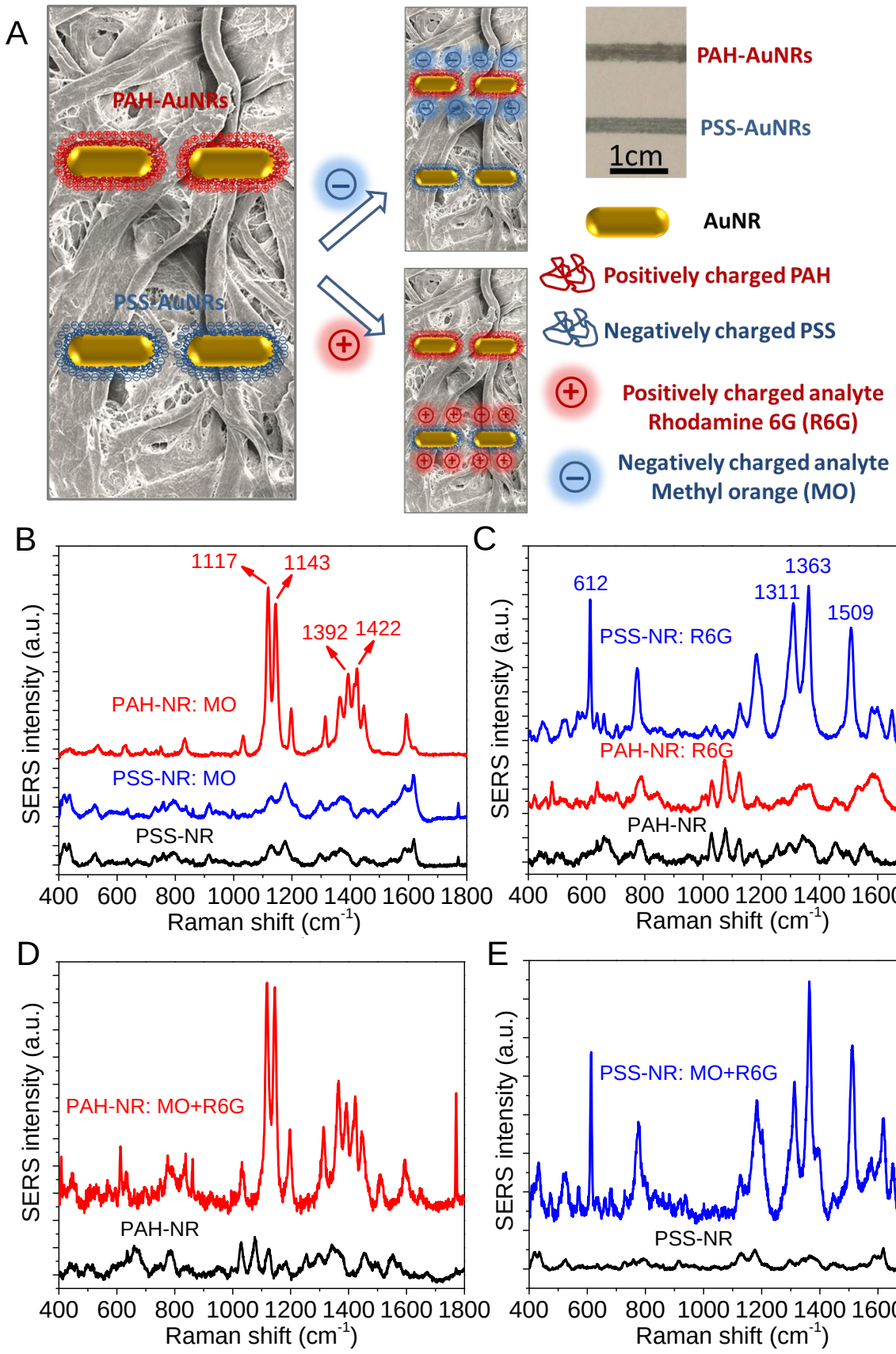
A
PAH-AuNRs
PSS-AuNRs
PAH-AuNRs
PSS-AuNRs
1cm
AuNR
Positively charged PAH
Negatively charged PSS
Positively charged analyte
Rhodamine 6G (R6G)
Negatively charged analyte
Methyl orange (MO)
B
1117
1143
1392
1422
PAH-NR: MO
PSS-NR: MO
PSS-NR
SERS intensity (a.u.)
400 600 800 1000 1200 1400 1600 1800
Raman shift (cm-1)
C
612
1363
1311
1509
PSS-NR: R6G
PAH-NR: R6G
PAH-NR
SERS intensity (a.u.)
400 600 800 1000 1200 1400 1600 1800
Raman shift (cm-1)
D
PAH-NR: MO+R6G
PAH-NR
SERS intensity (a.u.)
400 600 800 1000 1200 1400 1600 1800
Raman shift (cm-1)
E
PSS-NR: MO+R6G
PSS-NR
SERS intensity (a.u.)
400 600 800 1000 1200 1400 1600 1800
Raman shift (cm-1)

Figure 6.3 (A) Schematic illustration of charge-selective multiplexed SERS detection based on plasmonic calligraphy (right top inset: a photograph of PSS-AuNRs and PAH-AuNRs lines written on paper, showing uniform color). (B) SERS spectra collected from PAH-AuNRs and PSS-AuNRs upon exposure to 10 μM of MO aqueous solution compared with PSS-AuNRs without exposure as control. (C) SERS spectra collected from PAH-AuNRs and PSS-AuNRs upon exposure to 10 μM of R6G aqueous solution compared with PAH-AuNRs without exposure as control. SERS spectra collected from (D) PAH-NR and (E) PSS-NR test domains before and after exposure to mixture of R6G and MO, revealing the preferential binding of R6G to PSS-NR and MO to PAH-NR.

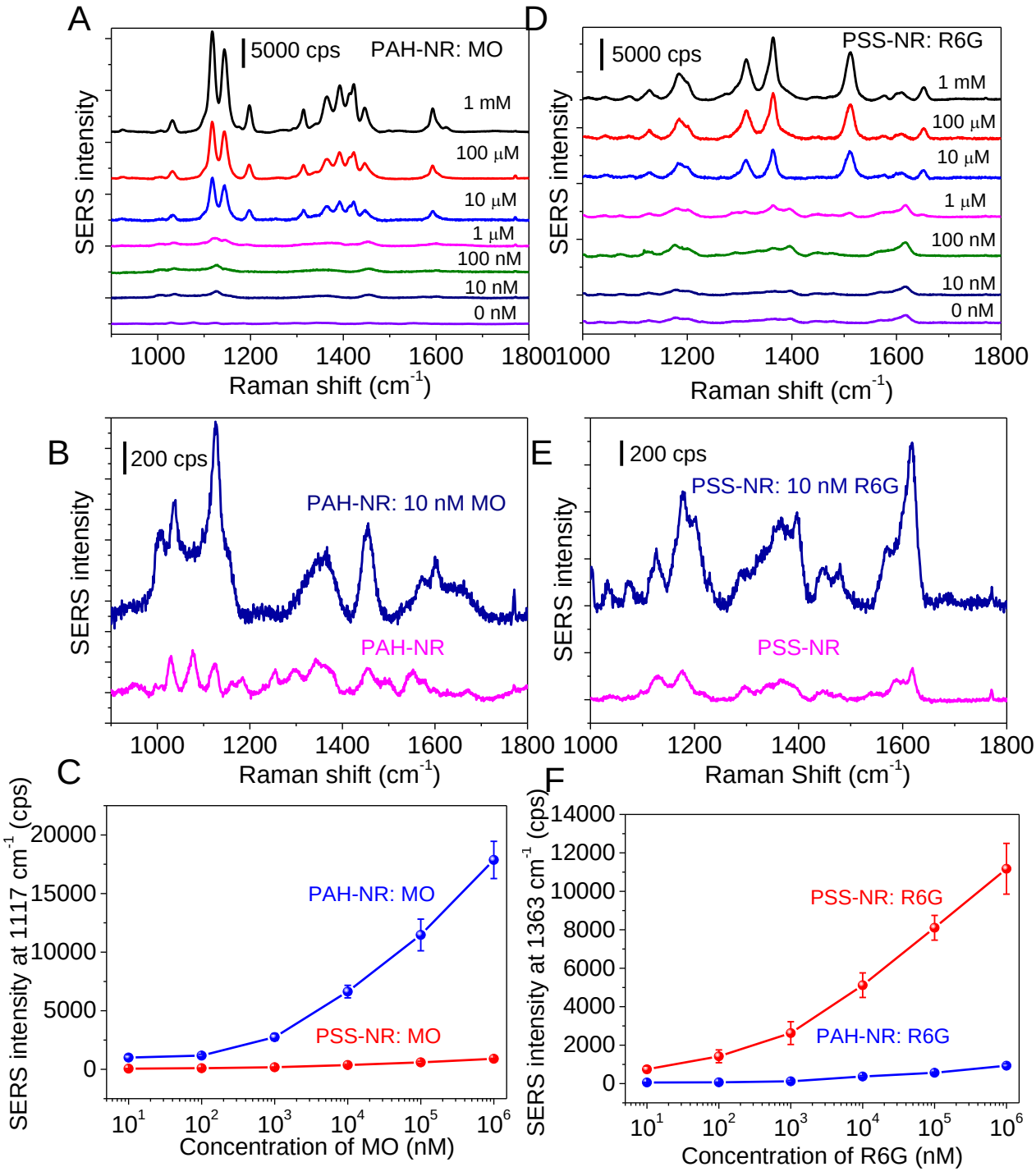

Figure 6.4 (A) SERS spectra obtained from PAH-AuNRs domain upon exposure to different concentrations of MO aqueous solution. (B) Zoom in SERS spectra corresponding to 10 and 0 nM MO

showing the distinct MO Raman bands for the sample exposed to 10 nM of MO. (C) Plot showing the concentration vs. intensity of the 1117 cm^{-1} Raman band of MO collected from PAH-AuNRs and PSS-AuNRs test domains. (D) SERS spectra obtained from the paper substrate adsorbed with PSS-AuNRs after exposure to different concentrations of R6G aqueous solution. (E) Zoom in SERS spectra corresponding to 10 and 0 nM R6G showing distinct R6G Raman bands from the sample exposed to 10 nM of R6G. (F) Plot showing the concentration vs. intensity of the 1363 cm^{-1} Raman band of R6G collected from PAH-AuNRs and PSS-AuNRs test domains.

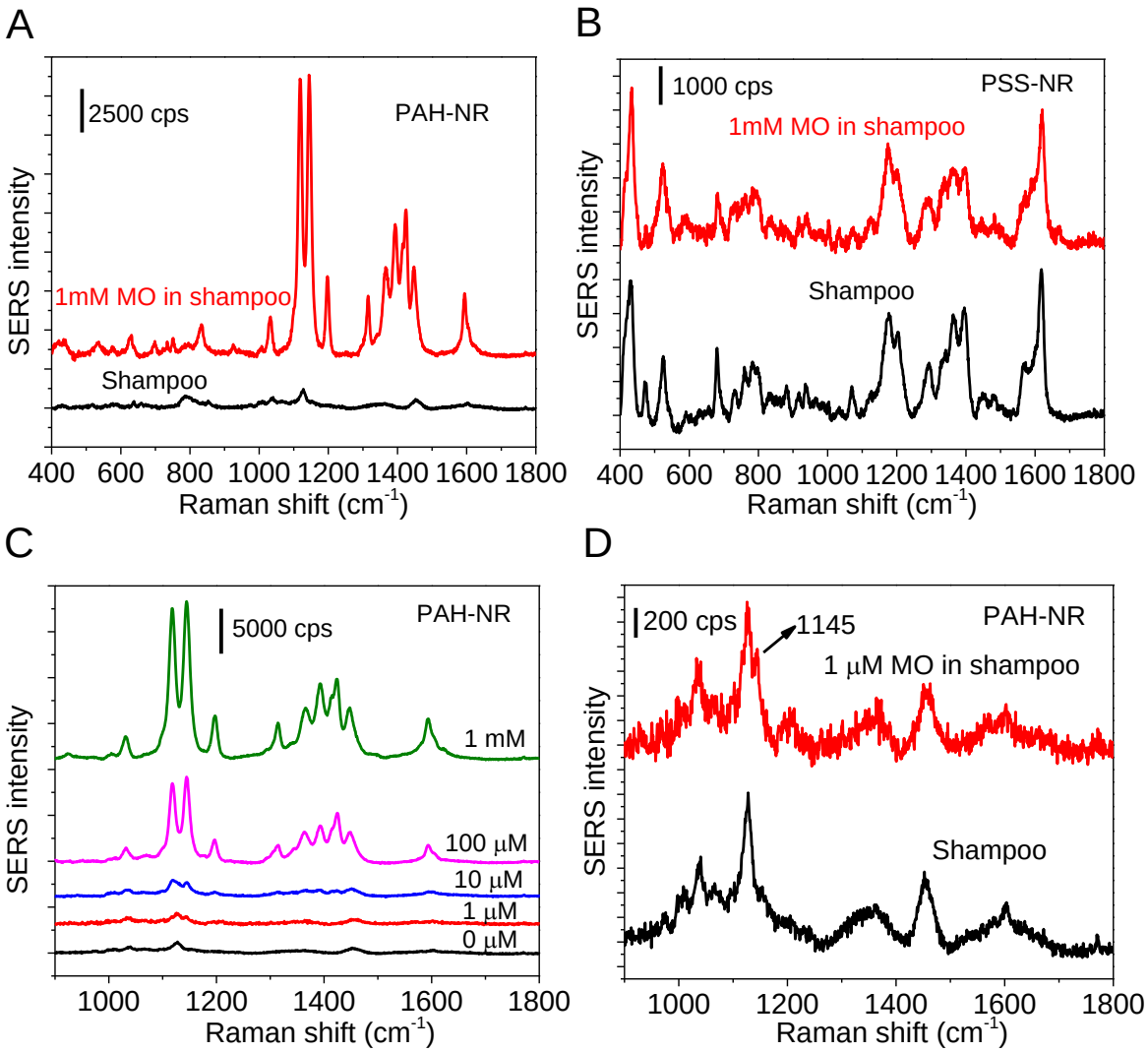

Figure 6.5 SERS spectra obtained from (A) PAH-AuNRs, (B) PSS-AuNRs test domains upon exposure to 1 mg/ml shampoo solution spiked with MO (1 mM) and virgin shampoo solution (C) SERS spectra obtained from PAH-AuNRs test domain after exposure to different concentration of MO in 1 mg/ml shampoo solution (D) Zoom in SERS spectra for low concentration of MO compared with PAH-AuNRs control sample.

Chapter 7 Gold Nanorods as Plasmonic Nanotransducers: Distance-dependent Refractive Index Sensitivity

7.1 Introduction

The time-varying electric field of the electromagnetic (EM) radiation causes collective oscillation of conduction electrons in metal nanoparticles with a resonance frequency, termed localized surface plasmon resonance (LSPR).[239, 240] For noble metals such as gold, silver and copper, this resonance frequency falls into the visible portion of the electromagnetic spectrum. LSPR of metal nanostructures depends on numerous factors such as composition, size, shape, dielectric environment, and proximity to other nanostructures (plasmon coupling).[1, 241] The extremely high sensitivity of LSPR to changes in the dielectric environment around the nanoparticles renders it an attractive transduction platform for chemical and biological sensing. [3, 5-9] LSPR has been shown to be sensitive enough to differentiate various inert gases with a refractive index difference on the order of 3×10^{-4} refractive index units (RIU), probe the conformational changes of individual biomacromolecules, detect single biomolecule binding events, monitor the kinetics of catalytic activity of single NPs and even optically detect single electrons.[11-13, 15]

The amplitude of EM near-field decays rapidly from metal surface along the direction perpendicular to the interface into the metal and dielectric, which gives rise to the evanescent wave character to EM near-field.[2, 23, 24, 242] The decay of the evanescent EM field can be described as characteristic EM decay length, which depends on the composition, shape, and size of nanostructures.[26] LSPR transducer response can be maximized by optimizing the refractive index sensitivity, and EM decay length of nanostructures, which describes the sensing depth for LSPR sensors. EM decay length has been extensively investigated for gold and silver nanotriangle by Van Duyne and co-workers.[27-29] The EM decay length for these LSPR nanosensors was estimated to be 5-15 nm depending on the size, shape, and composition of the nanostructures. Sutherland and coworkers estimated the EM decay length of gold nanorings to be 12nm, which closely matched with discrete dipole approximation (DDA) calculations.[30] The EM decay length of some other nanostructures such as gold nanocrescent and nanoisland were found to increase with the size of nanostructures.[31, 243]

Gold nanorods (AuNR) have been demonstrated to be highly promising class of plasmonic nanostructures for surface enhanced Raman scattering[158, 159, 210], multiplexed biosensors,[244-247] and

nanomedicine[248-253]. Gold nanorods are particularly attractive for plasmonic sensors considering the facile and large tunability of the LSPR wavelength of nanorods with aspect ratio and sharp corners, which form electromagnetic hot-spots.[4, 19, 195, 196, 254] The importance of rational design of plasmonic nanotransducers in maximizing the sensitivity and optimizing the performance of the nanobiosensor cannot be overstated. Towards this end, Chilkoti and co-workers have described the dynamic sensing range of gold nanorods using layer-by-layer assembly of polyeletrolytes.[18] In a subsequent report, the same group has developed an analytical model for the rational design of biosensor based on LSPR shifts of individual gold nanoparticles.[228] Recently, Lu and co-workers have reported a computational study using finite-difference time-domain method, which described the key governing factors for the rational design of gold nanorods as plasmonic nanosensors.[255] In this work, a linear increase in the EM decay length with increase in length and diameter of the AuNRs with similar aspect ratio was observed.

While there are numerous reports, which demonstrate AuNR as plasmonic nanotransducers for biosensing applications, a systematic experimental study to probe the distance-dependent refractive index sensitivity and EM decay length of AuNR and their dependence on absolute dimensions (i.e., length and diameter) of AuNR is still lacking. In this work, the distance-dependent LSPR sensitivity and electromagnetic decay length of AuNR with different diameters and lengths have been investigated using LbL assembly of polyelectrolytes. Knowledge of the distance-dependent sensitivity enables the rational design and fabrication of plasmonic biosensors.

7.2 Experimental section

Materials: Cetyltrimethylammonium bromide (CTAB), chloroauric acid, ascorbic acid, sodium borohydride, poly(styrene sulfonate) (PSS) (Mw=70,000 g/mol), and poly(allyl amine hydrochloride) (PAH) (Mw=56,000 g/mol) were purchased from Sigma-Aldrich. Silver nitrate was purchased from VWR international. Poly(2-vinyl pyridine) (Mw=200,000 g/mol) was obtained from Scientific Polymer Products. H_2O_2 was obtained from J. T. Baker. 1-Ethyl-3-(3-dimethylaminopropyl) carbodiimide (EDC) and N-hydroxy succinimide (NHS), Rabbit IgG and Goat anti-Rabbit IgG (Mw=150kDa) were purchased from Thermo scientific. SH-PEG-COOH was purchased from Jenkem Technology. All the chemicals have been used as received with no further purification.

Synthesis of gold nanorods: Gold nanorods were synthesized using a seed-mediated approach. [84, 85] Seed solution was prepared by adding 0.6 mL of an ice-cold solution of 10 mM sodium borohydride into 10 mL of magnetically stirred 0.1 M CTAB and 2.5×10^{-4} M $HAuCl_4$ aqueous solution at room temperature. The color of the seed solution changed from yellow to brown. Growth solution was prepared by mixing 95 mL of 0.1 M CTAB, 0.2, 0.4, 0.6 or 0.8 mL of 10 mM silver nitrate, 5 mL of 10 mM $HAuCl_4$, and 0.55 mL of 0.1 M ascorbic acid in the same order. The solution was homogenized by gentle stirring. To the resulting colorless solution, 0.12 mL of freshly prepared seed solution was added and set aside in dark for 14 h. In this method, 0.2, 0.4, 0.6 or 0.8 mL of silver nitrate were added to obtain AuNR with the diameters of ~24, 20, 16, and 14 nm, respectively. Prior to use, the AuNR solution was centrifuged at 13,000 rpm for 10 min to remove excess CTAB and redispersed in nanopure water (18.2 MΩ-cm). The centrifugation procedure was repeated twice. AuNR with different lengths but same diameter were obtained by adding 0.1 ml H_2O_2 (30%) to ~59 nm long AuNR solution (0.9 ml) followed by waiting for 10, 30, 60 or 120 min to progressively shorten the length of nanorods to ~55, 45, 37, and 31 nm, respectively.[256]

Adsorption of AuNR on glass surface: The glass substrate deposited with AuNR was fabricated by modifying the substrate with poly(2-vinyl pyridine) (P2VP) by exposing the piranha cleaned glass surface to 4% (w/v) P2VP solution in ethanol. After rinsing the substrate with ethanol, it was exposed to AuNR solution to enable adsorption of the gold nanorods. Finally, the substrate was rinsed with water to remove the loosely bound nanorods, leaving a highly dense layer of nanorods on the surface.

Polyelectrolyte LbL assembly: The substrates adsorbed with AuNR were immersed in 10 mM PSS in 0.1 M NaCl aqueous solution for 15 minutes followed by rinsing with nanopure water for 30 sec and rinsing with 0.1 M NaCl solution for additional 30 sec on each side of glass slides. Then the substrates were immersed in a solution of 10mM PAH in 0.1 M NaCl for 15 minutes followed by rinsing procedure described above. Subsequently, the substrates were dried under a stream of nitrogen before acquiring extinction spectra using UV-vis spectrometer. This procedure was repeated 10 times to deposit a total of 10 bilayers. The thickness of each polyelectrolyte bilayer was measured to be ~2 nm.[25]

SH-PEG-IgG conjugates preparation: To a solution of SH-PEG-COOH in water (37.5 µl, 20 µM, Mw=5000 g/mol, Jenkem Technology), 1-Ethyl-3-(3-dimethylaminopropyl) carbodiimide (EDC, Thermo Scientific) and N-hydroxy succinimide (NHS, Thermo Scientific) with the same molar ratio as SH-PEG-

COOH were added followed by shaking for 1 h. The pH of the above reaction mixture was adjusted to 7.4 by adding 10x concentrated PBS buffer, followed by the addition of Rabbit IgG (10 µl, 75 µM, Mw=150 kDa, Thermo Scientific). The reaction mixture was incubated for 2 h, and then filtered to remove any byproduct during the reaction using a 50 kDa filter. The final SH-PEG-IgG conjugates solution (0.75 µM) was obtained after washing with pH 7.4 PBS buffer twice.

7.3 Results and discussion

7.3.1 Synthesis of gold nanorods (AuNRs) of different dimensions

We have synthesized AuNR with diameters ranging from 14 to 24 nm using seed-mediated approach (Fig. 7.1A).[85, 257] UV-vis extinction spectra of AuNR are characterized by two distinct bands corresponding to the transverse and longitudinal oscillation of electrons with incident EM field. For AuNR with similar length (~50 nm), the transverse plasmon resonance wavelength was found to be at 509, 509.5, 512.5, 514 nm, corresponding to diameters 13.8±0.8, 16.1±1.1, 20.4±1.7, 23.7±1.8 nm, respectively (Fig. 7.1B). Expectedly, a small red-shift and increase in intensity of transverse plasmon band was observed with increase in AuNR diameter. On the other hand, AuNR with varying length and same diameter (~19nm) were obtained by shortening AuNR with a length of 58.6±3.7 nm to lengths of 54.5±3.5, 45.1±3.0, 36.8±3.5, 31.3±3.0 nm (Fig. 7.2A). The longitudinal plasmon resonance wavelength for AuNR exhibited a red-shift with increase in the aspect ratio (length/diameter) (Fig. 7.2B). The longitudinal plasmon band of AuNR is known to be highly sensitive to the aspect ratio of AuNR, which can be understood within the framework of Gans theory, which describes the optical properties of ellipsoid nanoparticles based on dipole approximation.[258] In aqueous solution, the longitudinal plasmon resonance wavelength (λ_{max}) is linearly proportional to the aspect ratio (R) given by the following relationship: [259-261]

$$\lambda_{max} = 95R + 420 \qquad (1)$$

AuNR were adsorbed on poly(2-vinyl pyridine) (P2VP)-coated glass slide by exposing the glass slide to AuNR solution, followed by extensive rinsing with water to remove weakly adsorbed nanorods.[139, 262] The pyridyl groups of P2VP are known to have high affinity for gold, resulting in strong adsorption of

AuNR to P2VP film.[263] AFM images revealed the uniform distribution of AuNR with no signs of aggregation or patchiness (Fig. 7.3A).

7.3.2 Layer-by-layer (LbL) assembly of polyelectrolyte multilayers (PEM)

Layer-by-layer (LbL) assembly of polyelectrolyte multilayers (PEM) involves the alternate adsorption of oppositely charged polyelectrolytes. LbL assembly offers an excellent control over the thickness of the PEM down to ~ 1nm.[25, 264-267] We employed LbL assembly of polyelectrolytes for probing the distance-dependent LSPR sensitivity and EM decay length of AuNR with different dimensions (Fig. 7.3B). Electrostatic LbL assembly was performed by alternate adsorption of negatively charged poly(styrene sulfonate) (PSS) and positively charged poly(allyl amine hydrochloride) (PAH). LbL assembly of PAH and PSS has been extensively studied and is known to result in a linear increase of PEM film thickness with the number of bilayers, consistent with our own studies.[268] AFM scratch test after the deposition of 10 bilayers revealed the thickness of the PEM on the glass surface between AuNR to be ~20 nm, which closely agrees with the value reported previously for PAH-PSS system (Fig. 7.3C).[25] The diameter of AuNR, as measured from AFM images, even after the deposition of 10 bilayers remained virtually unchanged, suggesting the conformal deposition of the polyelectrolyte multilayers on these nanostructures.

7.3.3 Distance-dependent sensitivity and electromagnetic decay length

To probe the distance-dependent sensitivity and electromagnetic decay length of AuNR with different dimensions, extinction spectra were collected following the deposition of each polyelectrolyte bilayer (Fig. 7.4A-D and Fig. 7.5A-E). The spectra revealed a progressive red-shift in LSPR wavelength and a monotonic increase in LSPR intensity with the deposition of each bilayer due to the increase in the refractive index (from air to polymer layer). The longitudinal band of AuNR deposited on glass substrate exhibits a weak shoulder due to the coupling of longitudinal plasmon bands of the nanorods (Fig. 7.4E).[230] Owing to its higher refractive index sensitivity compared to transverse plasmon band, longitudinal plasmon band of AuNR is routinely employed in plasmonic biosensing. We analyzed the longitudinal plasmon band of AuNR to probe the distance-dependent LSPR shift and EM decay length of AuNR. The longitudinal LSPR wavelength was obtained by deconvoluting the extinction band into two Gaussian peaks (Fig. 7.4E). The peak corresponding to the plasmon resonance of the individual

nanorods was used to identify the LSPR wavelength and measure the EM decay length of AuNR. The cumulative LSPR wavelength shift following the deposition of each polyelectrolyte layer for nanorods with different dimensions increases with increase in aspect ratio (Fig. 7.4F and Fig. 7.5F). The incremental LSPR shifts decrease with the addition of polyelectrolyte layers indicating that LSPR sensitivity of AuNR decreases with the increase in the distance from AuNR surface.

Owing to the evanescent nature of the EM field at the surface of the plasmonic nanostructures, the LSPR wavelength shift exhibits a characteristic decay with the increasing distance from the surface of the nanorods (*i.e.* increasing number of layers), given by

$$R = m\Delta\eta\left(1 - \exp\left(-2d/l\right)\right) \qquad (2)$$

where R is LSPR shift, m is the refractive index sensitivity of AuNR, $\Delta\eta$ is the change in the refractive index in RIU, d is the adsorbate layer thickness (thickness of the polyelectrolyte layer in this case) and l is the EM decay length. The refractive index sensitivity (m) and EM decay length (l) of AuNR were calculated by fitting the experimental data of LSPR shift using equation (2).

The variation in the EM decay length of AuNR with varying diameter and similar length of ~50 nm and varying length and constant diameter of ~19 nm is shown in Fig 7.6A and Fig 7.6B, respectively. EM decay length increases linearly as a function of both AuNR length and diameter, which is in agreement with a recent computational study by Lu and co-workers. The increase in the EM decay length with change in diameter (1.29±0.13 nm/nm) was nearly five times higher compared to that of the length (0.23±0.01 nm/nm) indicating that diameter is a more convenient handle to tune the EM decay length of AuNR (Fig. 7.6A and Fig. 7.6B). On the other hand, for the AuNR dimensions studied here, EM decay length does not exhibit any general trend with the aspect ratio of AuNR (Fig. 7.6C). For AuNR of similar aspect ratio (~2.3), larger nanorods of 55×24 nm exhibit higher EM decay length (30.0±0.8 nm) compared to smaller nanorods of 45×19 nm (23.0±0.7 nm). In other words, small nanorods have shorter electromagnetic decay length, which consequently have higher local sensitivity in the vicinity of AuNR surface.

The linear increase in the EM decay length with the increase in length and diameter of AuNR is in agreement with computational study by Lu et al.[255] Furthermore, the computational results also indicate the higher sensitivity of EM decay length to diameter compared to length of AuNR, which is in agreement

with our experimental findings. However, experimentally observed increase in EM decay length with increasing AuNR length (~0.23 nm/nm) is slightly higher compared to that obtained in the computational study (0.17 nm/nm). The discrepancy between experimental and computational results can be mainly attributed to the substrate effect in experiments and the absence of the same in simulations. The PEM film on the glass surface in the immediate vicinity of the nanorods influences the effective refractive index experienced by the nanorods as the thickness of the PEM in these regions becomes comparable to the diameter of the nanorods. Furthermore, in the case of the FDTD simulations, the model was simplified to two dimensions and the refractive index change was administered over the entire surface of the nanorods uniformly.

Recently, Chilkoti et al. have suggested that the molecular detection limit of AuNR can be expressed as an analytical equation as:[228]

$$L_M = \frac{V_S}{V_A \Delta RI} \frac{\sqrt{U_{system}^2 + U_{fit}^2}}{\exp\left(\frac{-2r}{l_d}\right)\left(3S_0\right)} \qquad (3)$$

Where L_M is the molecular detection limit of the system, V_S is the sensing volume, V_A is the analyte volume, ΔRI is the RI difference between the analyte and the surrounding medium, U_{system} is the peak measurement uncertainty, U_{fit} is the peak determination uncertainty, r is the distance from the nanorod surface at which the analyte binds, S_0 is the bulk RI sensitivity, and l_d is the EM decay length. Furthermore, from their experimental observations they suggested that the EM decay length of AuNR can be expressed as a function of aspect ratio:[228]

$$l_d = 228 \times \sqrt{1 - \left(\frac{d}{l}\right)^2} - 176 \qquad (4)$$

Where l_d is the EM decay length, l and d are length and diameter of AuNR, respectively. The analytical expression implies that l_d monotonically increases with an increase in the aspect ratio of AuNR.

However, our experimental findings and previous computational study suggest that the absolute dimensions of AuNR (*i.e.,* length and diameter) determine the EM decay length rather than the aspect ratio of AuNR. In other words, large nanorods (e.g., 54×24 nm) with smaller aspect ratio have higher EM decay length compared with small nanorods (e.g., 50×14 nm) with larger aspect ratio (Fig. 7.6C). Therefore, one has to consider the absolute dimensions of AuNR and not just the aspect ratio in the rational choice of AuNR as nanotransducers.

7.3.4 Maximization of optical response for biosensing

According to equation 2, to maximize the optical response to refractive index changes (e.g., biomolecule binding), one should (i) maximize RIS (*m)* and (ii) match the electromagnetic decay length (*l*) to the dielectric layer thickness (i.e., receptor+analyte layer thickness). This essentially means that the dimensions of the nanorods and hence the EM decay length need to be tuned to match the receptor+analyte layer thickness. We illustrate this point by evaluating the biosensing performance of AuNR with same aspect ratio (~2.7) and different dimensions of 59×22 and 38×14 (Fig 7.7B). We employed Rabbit IgG (capture molecule) and anti-Rabbit IgG (target bioanalyte) as model biomolecules to demonstrate the LSPR biosensor. Figure 7A illustrates the steps involved in the biofunctionalization of AuNR for the detection of target bioanalytes. Thiol-terminated polyethylene glycol (SH-PEG), a nontoxic and hydrophilic polymer, serves as a flexible linker to increase the accessibility of IgG to target biomolecules and forms a stable protective layer around AuNRs to reduce non-specific binding. AuNR were functionalized with SH-PEG-IgG molecules (see experimental section for details). Subsequently, AuNR-IgG conjugates were exposed to Goat anti-Rabbit IgG (anti-IgG henceforth) solution resulting in its specific binding to IgG, which can be detected as a red-shift in the LSPR wavelength of AuNRs (Fig. 7.7C and Fig. 7.7D).

For the typical IgG thickness of 3-4 nm,[269, 270] larger AuNR with EM decay length much higher than thickness of IgG leads to a weaker response considering that the IgG molecules occupies only a small fraction of the sensing volume compared to smaller nanorods. This is confirmed by comparing the LSPR shifts upon appending IgG to AuNR; larger AuNR (59×22 nm) showed smaller red-shift (~26.8 nm) compared to smaller AuNR (38×14 nm), which exhibited significantly higher shift (~39.8 nm). On the

other hand, considering that anti-IgG binding occurs ~4 nm far from AuNR surface, smaller nanorods with lower EM decay length are not ideal as the analyte would lie, at least partially, outside the sensing volume. For this case, larger nanorods are required to ensure that the analyte is within the sensing volume. Upon anti-IgG binding to IgG, larger AuNR (59×22 nm) showed a larger red-shift (~10.5 nm) compared to smaller AuNR (38×14 nm), which exhibited a significantly smaller red-shift (~4.0 nm) (Fig. 7.7E). It is interesting to note that the fraction of the total shift (i.e., IgG+anti-IgG) upon anti-IgG binding in the case of larger AuNR (59×22 nm) is nearly 38%, while it is extremely small (~9%) in the case of smaller nanorods (38×14 nm). Clearly, the absolute dimensions play a critical role in the rational design of AuNR-based plasmonic nanobiosensors.

7.4 Conclusions

In conclusion, we have presented a systematic experimental study on the influence of AuNR dimensions on distance-dependent LSPR sensitivity and EM decay length using electrostatic LbL assembly of polyelectrolytes. Electromagnetic decay length was found to increase linearly with both AuNR length and diameter. The increase in the EM decay length with change in diameter was significantly higher (~1.29nm/nm) compared to that with change in length (~0.23 nm/nm). In contrast to earlier reports, for AuNR dimensions studied here, EM decay length did not exhibit any general trend with the aspect ratio. Knowledge of the EM decay length enables rational choice of plasmonic nanotransducers for maximizing the sensitivity of nanotransducers for a given receptor-analyte pair. The dependence of EM decay length and distance-dependent refractive index sensitivity on nanotransducer dimensions is expected to be relevant to other types of plasmonic nanostructures and LbL forms a powerful to experimentally measure the EM decay length of such nanotransducers.

7.5 Supporting information

Supporting information for chapter 7 is provided in appendix 5.

Figures

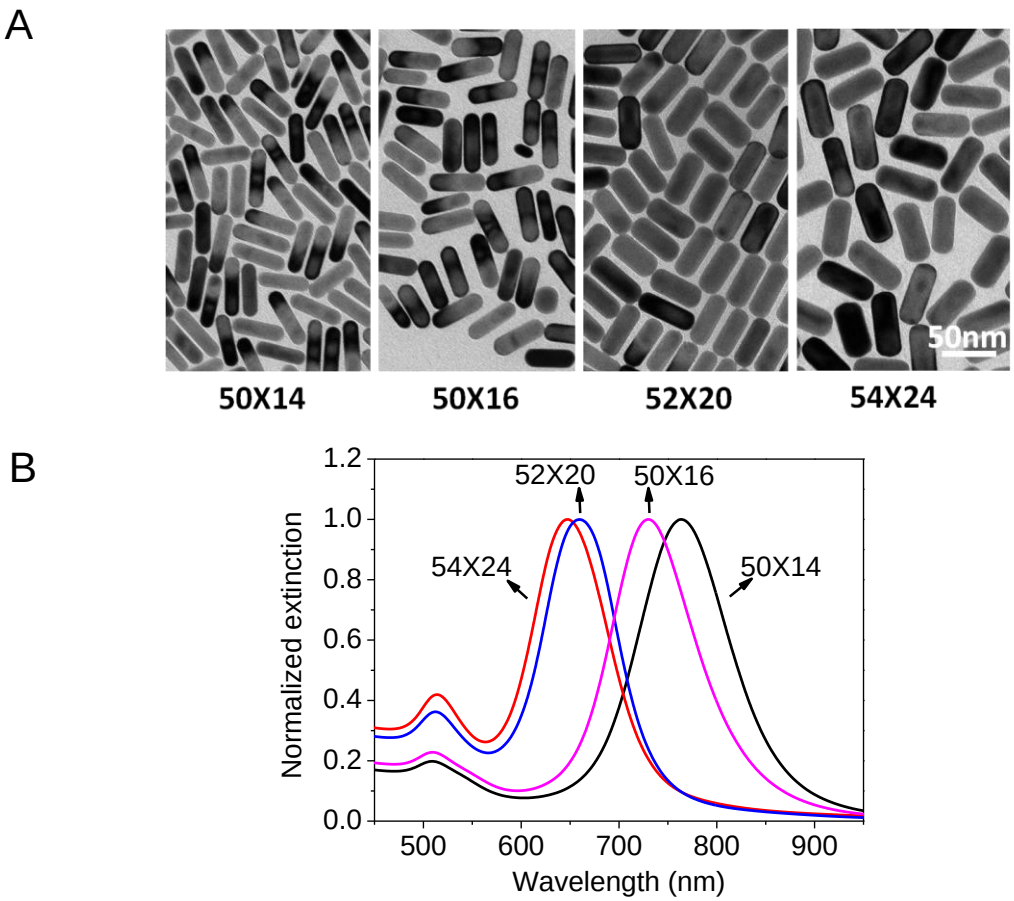

Figure 7.1 (A) Representative TEM images of AuNR with similar length and different diameters. (B) Corresponding extinction spectra of AuNR solution.

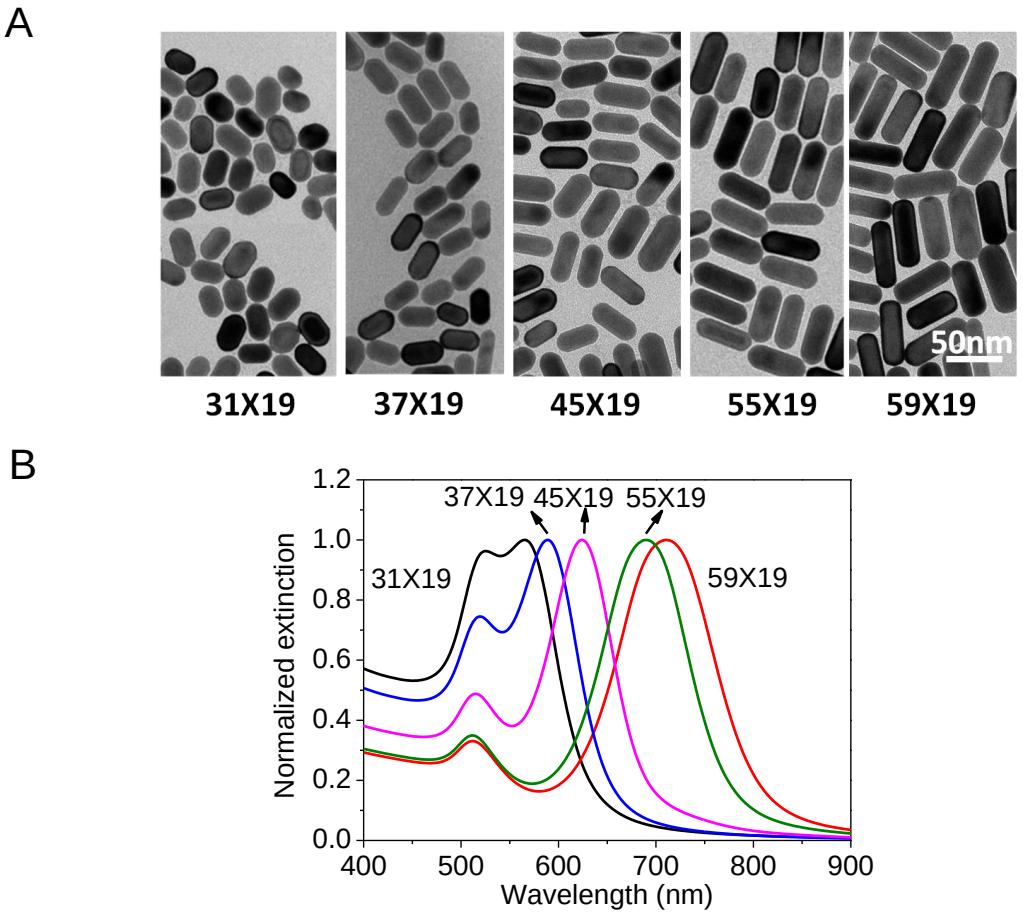

Figure 7.2 (A) Representative TEM images of AuNR with similar diameter and different lengths. (B) Corresponding extinction spectra of AuNR solution.

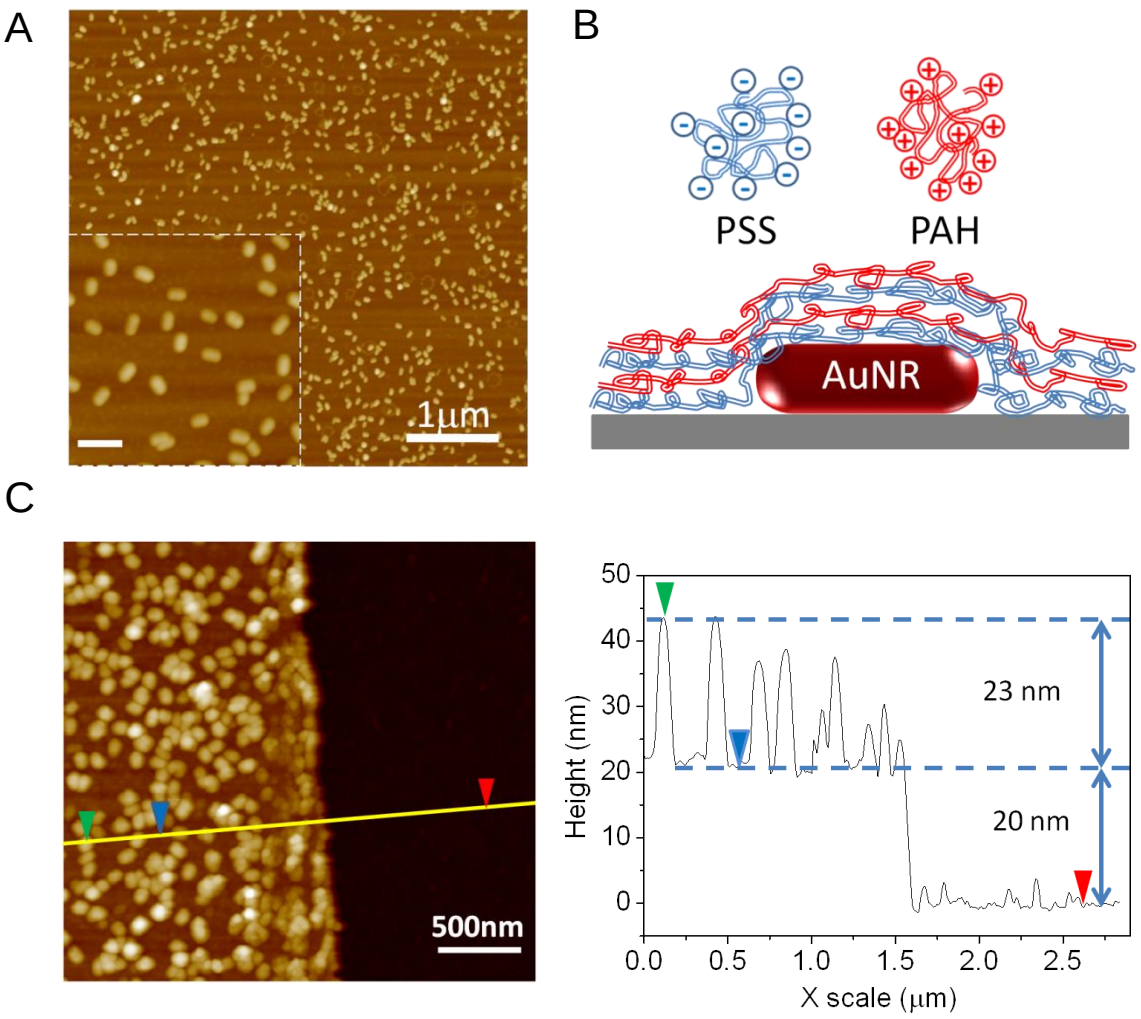

Figure 7.3 (A) AFM showing uniformly adsorbed AuNR on P2VP-modified glass substrate (the inset scale bar is 200 nm, Z scale is 80nm) (B) Schematic of AuNR on a glass substrate covered with polyelectrolyte multilayers. (C) AFM image along the edge of an intentional scratch in PEM film comprised of 10 bilayers deposited on AuNR. Cross-sectional profile shows the thickness of the PEM film on the glass substrate and the conformal deposition of PEM film on AuNR (52×20 nm).

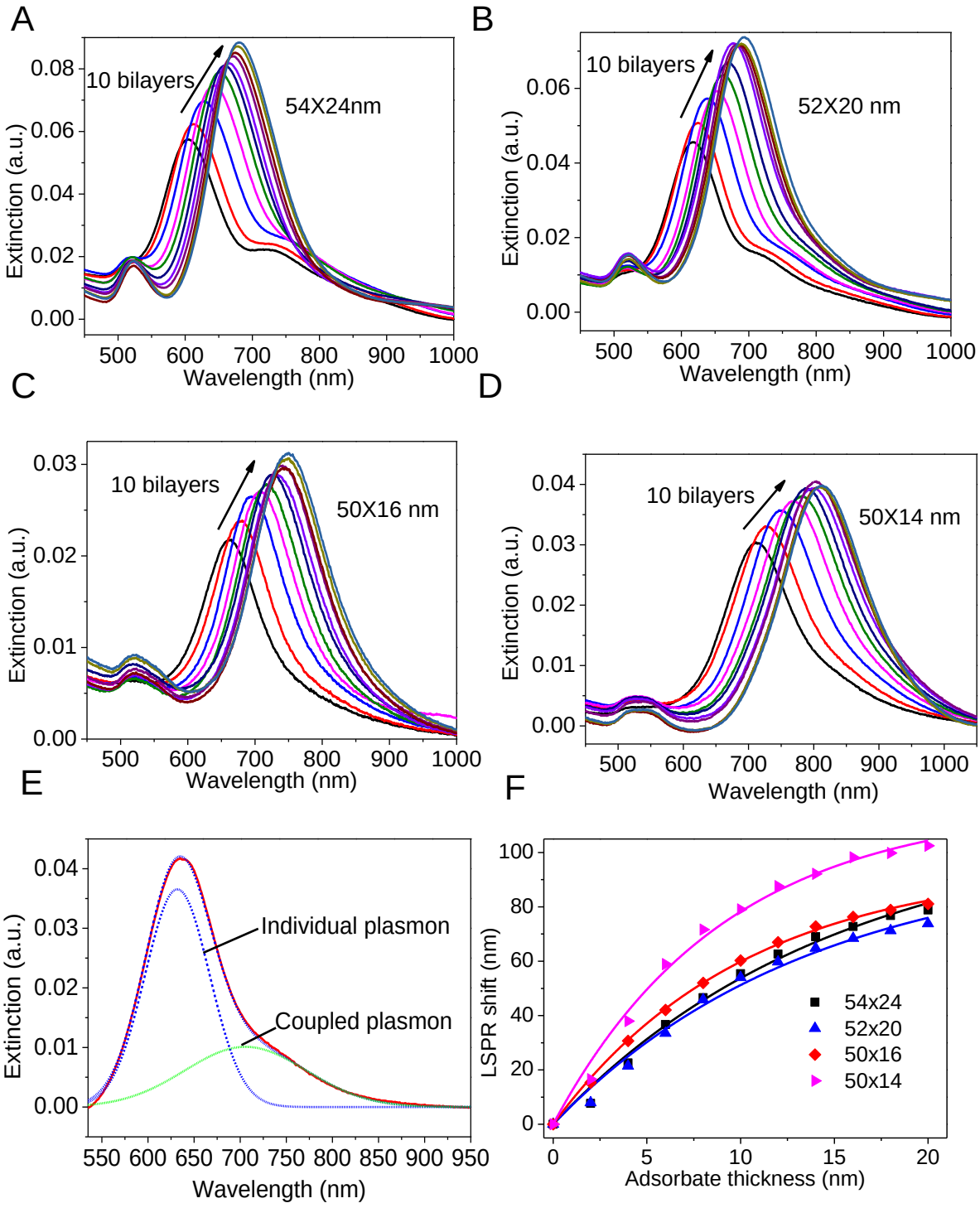

Figure 7.4 (A-D) UV-vis extinction spectra of AuNR with different diameters following the deposition each polyelectrolyte layer showing a progressive red-shift and increase in the intensity of the longitudinal plasmon band. (E) Deconvolution of the longitudinal LSPR band of AuNR adsorbed on glass substrate

into two Gaussian peaks. (F) Plot of cumulative shift of longitudinal plasmon resonance wavelength with the deposition of PEM on AuNR with different diameters.

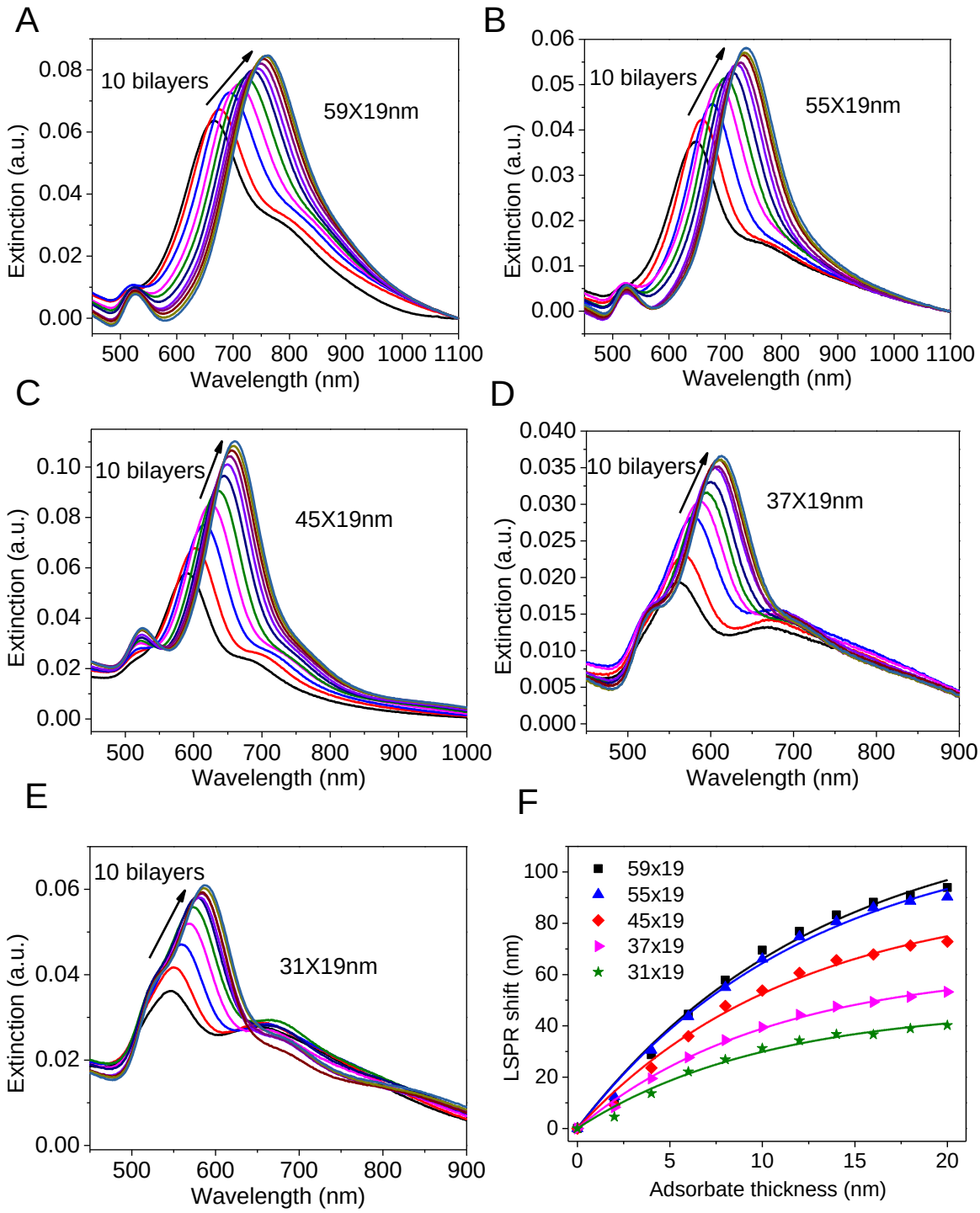

Figure 7.5 (A-E) UV-vis extinction spectra of AuNR with different lengths following the deposition each polyelectrolyte layer showing a progressive red-shift and increase in the intensity of the longitudinal plasmon band. (F) Plot of cumulative shift of longitudinal plasmon resonance wavelength with the deposition of PEM on AuNR with different lengths.

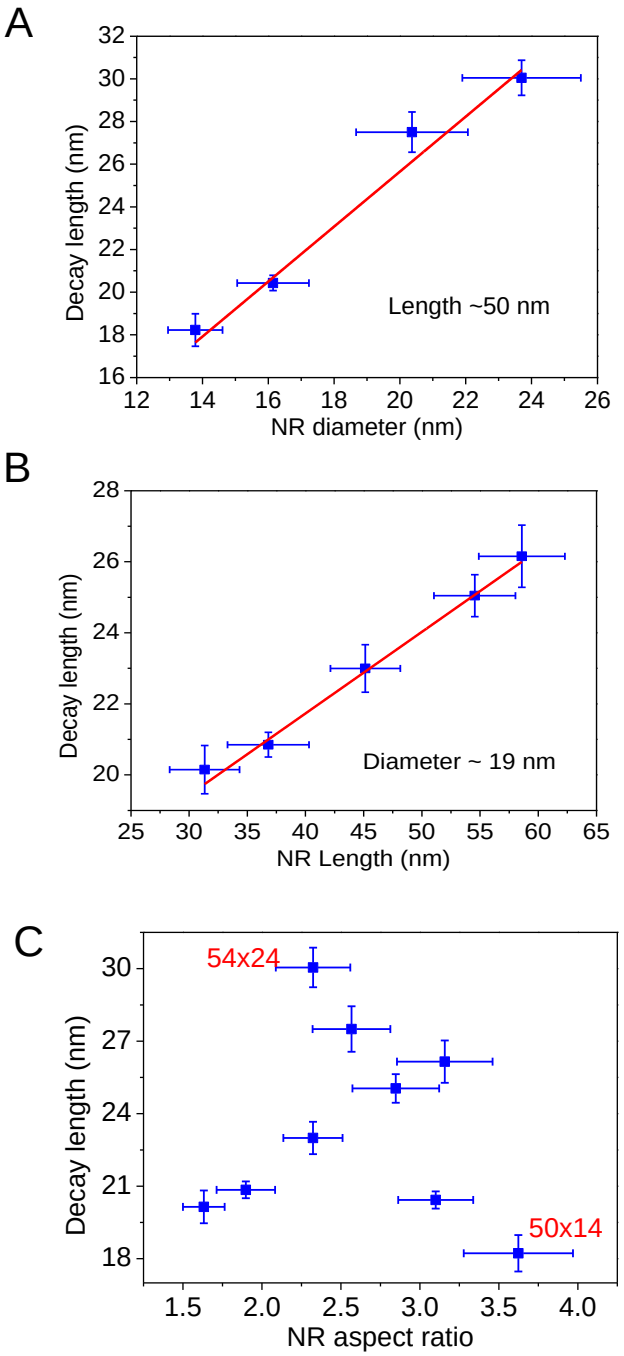

Figure 7.6 Electromagnetic decay lengths of AuNR (A) with different diameters, and (B) with different lengths. (C) Plot showing the EM decay length vs. aspect ratio of AuNR.

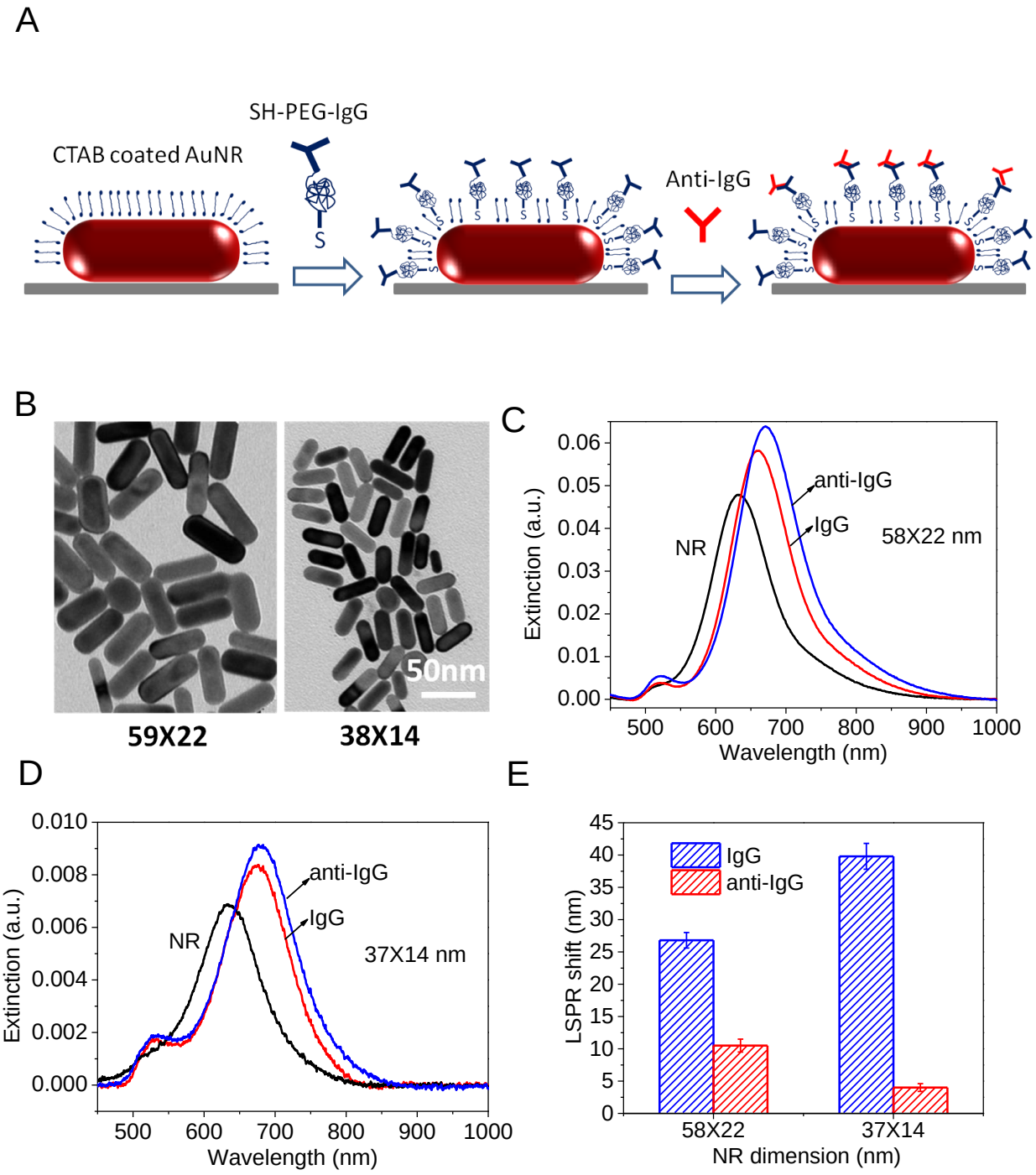

Figure 7.7 (A) Schematic illustration representing the fabrication steps of AuNR-based plasmonic biosensor for anti-IgG detection. (B) Representative TEM images of AuNR with the same aspect ratio but different dimensions. Extinction spectra corresponding to AuNR of different dimensions upon appendage

of SH-IgG and subsequent binding of anti-IgG (C) 58×22nm and (D) 37×14nm. (E) Plot showing the LSPR shift of longitudinal plasmon resonance wavelength corresponding to the fabrication steps of IgG and anti-IgG.

Chapter 8 Bioplasmonic Paper as a Platform for Detection of Kidney Cancer Biomarkers

8.1 Introduction

Renal cancer is generally silent, frequently fatal and accounts for 3% of adult malignancies. It is estimated that in 2012 alone 64,770 new cases will be diagnosed with and 13,570 deaths will occur of cancer of the kidney and renal pelvis.[271] Altogether, this disease represents the sixth leading cause of death due to cancer. In a recent study, it has been demonstrated that the proteins aquaporin-1 (AQP1) and adipophilin (ADFP) in urine form excellent candidates for the non-invasive and early detection of renal cancer carcinoma (RCC).[272] While this study clearly demonstrated the possibility of using these proteins as potential biomarkers for early and non-invasive detection of RCC, an inexpensive and high throughput biodetection platform is required to translate these biomarkers to clinical setting and incorporation into routine health physical. Conventional labeled assays such as enzyme-linked immunosorbent assay (ELISA) are time consuming and expensive, and require tedious labeling procedures making them unsuitable for rapid and routine urinalysis. The above considerations clearly suggest the need for a label-free approach, for rapid and quantitative detection of the proteins in urine at physiologically relevant concentrations (ng/ml).

Localized surface plasmon resonance (LSPR) of metal nanostructures, which involves collective coherent oscillation of dielectrically confined conduction electrons, is sensitive to numerous factors such as composition, size, shape, surrounding dielectric medium, and proximity to other nanostructures.[1-4] The sensitivity of LSPR to local changes in dielectric environment renders it an attractive transduction platform for chemical and biological sensing.[5-10] LSPR of metal nanostructures has been shown to be sensitive enough to differentiate inert gases with refractive index contrast (δn) on the order of 3×10^{-4}, probe the conformational changes of biomacromolecules, detect single biomolecule binding events, monitor the kinetics of catalytic activity of single nanoparticles, and even optically detect single electron.[11-15] Detection of various biomolecules such as proteins[3, 16-19] and DNA,[20-22] have been demonstrated in the past few years making the transduction platform promising for the development of simple, highly sensitive, label-free, and cost-effective diagnostics.

Most of the LSPR sensors demonstrated so far rely on rigid planar substrates (e.g., glass, silicon) owing to their compatibility with various well-established lithographic approaches (e.g., photolithography, e-

beam lithography and nanosphere lithography), which are routinely employed for either fabrication or assembly of plasmonic nanotransducers.[4, 28, 273, 274] Compared to these conventional substrates, paper has numerous advantages such as high specific surface area, excellent wicking properties, compatibility with conventional printing approaches, significant cost reduction and easy disposability. For all these reasons, paper is gaining increased attention as a potential substrate for various applications including biodiagnostics, food quality testing as well as environmental monitoring.[106-109, 275-277] Paper substrates functionalized with inorganic nanoparticles such as gold, silver, and titania have been investigated for a wide range of applications including self-cleaning,[278] disinfection,[279] colorimetric sensing,[280] surface enhanced Raman scattering (SERS) based trace analyte detection,[281],[159],[162] and antimicrobial activity.[282]

Here, we report for the first time a bioplasmonic paper that comprises of a common laboratory filter paper uniformly adsorbed with biofunctionalized plasmonic nanostructures for the detection of target bioanalytes from model physiological fluids. The sensitivity and detection limit of the paper based LSPR substrate is on par or better compared to the conventional rigid substrates using similar plasmonic nanostructures. Furthermore, we demonstrate the deployment of such bioplasmonic paper as a flexible swab to collect and detect trace quantities (few µg spread over cm^2 area) of model bioanalytes on real-world surfaces.

8.2 Experimental section

AuNR and AuNR-IgG conjugates on rigid planar substrates: Glass substrates were cut into approximately 1×2 cm rectangular slides and cleaned in piranha solution (3:1 (v/v) mixture of H_2SO_4 and 30% H_2O_2) followed by extensive rinsing with nanopure water. AuNR or AuNR-IgG conjugates were adsorbed onto glass substrates following the modification of the surface with (3-mercaptopropyl)-trimethoxy-silane (MPTMS) by exposing the glass surface to 5% MPTMS in ethanol for 15 min followed by ultrasonication in ethanol for 30 min and rinsing with water. Subsequently, the glass surface was exposed to AuNR or AuNR-IgG conjugates solution for 1 h, followed by rinsing with water to remove the loosely bound nanorods. Similar approach was employed for biofunctionalization of AuNR with anti-AQP1 (Sigma), which were employed for the detection of AQP1 (Origene) from artificial urine (Surine, Cerilliant).

Plasmonic paper substrates preparation: Adsorption of AuNR-IgG conjugates on paper substrate was achieved by immersing a 1×1 cm^2 paper in AuNR-IgG conjugates solution (2 ml) for 12 h. After removing from the solution, the paper was thoroughly rinsed with water, and then exposed to SH-PEG solution to block non-specific binding. LSPR measurements were performed by exposing the plasmonic paper to various concentrations of anti-Rabbit IgG (Thermo Scientific) in PBS for 1 h, followed by thorough rinsing with PBS and water and drying with a stream of nitrogen. Six UV-Vis extinction spectra were collected for each substrate before and after anti-IgG exposure. Each spectrum represented a different spot within the same substrate.

8.3 Results and discussion

8.3.1 Fabrication and characterization of bioplasmonic paper

Laboratory filter paper (Whatman # 1) employed as a plasmonic substrate in this study is characterized by cellulose fibers with a diameter of ~10μm (Supporting information, Fig. S6.1). AFM images revealed the hierarchical fibrous morphology of the filter paper with cellulose nanofibers braided into microfibers (average diameter of ~ 400 nm) (Fig. S6.1). The root mean square (RMS) surface roughness of the paper was found to be 72 nm over 5 × 5 μm^2 area, which indicates the large surface area of the paper substrate available for adsorption of biofunctionalized plasmonic nanostructures.

We employed Goat Rabbit IgG (IgG henceforth) as model capture biomolecule and Goat anti-Rabbit IgG (anti-IgG) as model target bioanalyte demonstrate the LSPR biosensor. Bioplasmonic paper, which serves as a LSPR biosensor, is comprised of biofunctionalized gold nanorods (AuNRs) adsorbed on the filter paper. Figure 8.1 illustrates the steps involved in the fabrication and deployment of bioplasmonic paper as a LSPR sensor for the detection of target bioanalytes. Thiol-terminated polyethylene glycol (SH-PEG), a hydrophilic polymer, serves as a flexible linker to increase the accessibility of IgG to target biomolecules and forms a stable protective layer around AuNRs to reduce non-specific binding. AuNR-IgG conjugates were prepared by functionalizing AuNRs with SH-PEG-IgG molecules (see experimental section for details). Subsequently, AuNR-IgG conjugates were adsorbed onto paper substrate by exposing the paper substrates to AuNR-IgG conjugate solution followed by thorough rinsing with water to remove the weakly adsorbed nanorods. Following the adsorption of the AuNR-IgG conjugates, the paper substrates were exposed to SH-PEG solution to block non-specific binding. Exposure to anti-IgG solution

resulted in its specific binding to IgG, which can be detected as a spectral shift of the LSPR wavelength of AuNRs.

AuNRs are particularly attractive as plasmonic nanotransducers considering the large refractive index sensitivity of longitudinal LSPR, facile and large tunability of the LSPR wavelength of nanorods with aspect ratio and the electromagnetic (EM) hot-spots at the edges.[228] AuNRs, synthesized using a seed-mediated approach,[283],[284] are positively charged with a length of 55.8±3.6 nm and a diameter of 22.0±2.1 nm (TEM image in Fig. 8.2A). UV-vis extinction spectra of the AuNRs are characterized by two distinct bands corresponding to the transverse (lower wavelength) and longitudinal (higher wavelength) oscillation of electrons with incident EM field. The longitudinal plasmon band of AuNRs, which is known to be more sensitive to the refractive index change of the surrounding medium compared to the transverse band, exhibited a red shift of ~8.5 nm and an increase in extinction intensity upon SH-PEG-IgG appendage (Fig. 8.2B). The red shift and increase in intensity correspond to the increase in the refractive index around the AuNRs with SH-PEG-IgG binding. SERS spectra collected from AuNRs and AuNR-IgG conjugates also confirm the biofunctionalization of AuNRs (Fig. 8.2C). The successful bioconjugation of IgG is evidenced by the Raman bands at 831 cm^{-1} and 852 cm^{-1} , 1004 cm^{-1} and 1031 cm^{-1} , 1230 cm^{-1} , and 1685 cm^{-1} corresponding to tyrosine, phenylalanine, amide III, and amide I, respectively.

The average hydrodynamic diameter of AuNR and AuNR-IgG measured using dynamic light scattering (DLS) was found to be ~25.0 and ~35.0 nm, respectively (Fig. 8.2D). The increase in hydrodynamic diameter of AuNR can be primarily attributed to the successful appendage of IgG (Mw=150 KDa) to AuNR surface. Only a small increase of ~0.2 nm was observed for the conjugation of SH-PEG (Mw=5 KDa) (see Fig. S6.2). Figure 8.2E shows the AFM images of the AuNR and AuNR-IgG adsorbed on silicon surfaces. Apart from indicating the stability of AuNR-IgG in solution (absence of any large scale aggregates), a small increase in the average diameter (~ 3nm) of nanorods was observed following SH-PEG-IgG functionalization, which closely corresponds to the size of IgG (Fig. 8.2F).[269],[285] The discrepancy between the DLS and AFM measurements can be attributed to two factors: (i) AFM imaging was performed in dry state as opposed to DLS measurements, which reveals the hydrodynamic radius of

AuNR (ii) possible deformation (compression under AFM tip) of the biomolecules and polymer during AFM imaging although the imaging was performed in light tapping mode.

An important consideration in the design of bioplasmonic paper substrates is the optical homogeneity of the substrate. The homogeneity determines the noise floor of the spectral shift, which in turn determines the resolution of the bioplasmonic paper. SEM images revealed highly uniform distribution of AuNR-IgG conjugates on paper surface with no signs of aggregation or patchiness on the substrate (Fig. 8.3A). Higher magnification image reveals the preferential alignment of AuNR-IgG conjugates along cellulose fibers. The surface density of the AuNR-IgG conjugates adsorbed on the paper substrate was found to be 351±11/μm^2, which can be controlled by incubation time (Fig. 8.3B). SERS spectra were collected from AuNRs and AuNR-IgG conjugates paper to confirm the preservation of IgG conjugation during incubation process (Fig. S6.5).

Longitudinal LSPR wavelength of AuNR-IgG conjugates adsorbed on paper substrate exhibited a significant blue shift (~17nm) compared to that in solution due to the change in the refractive index of the surrounding medium (aqueous to air+substrate) (Fig. 8.3C).[286] The extinction spectrum from the paper substrate was collected from a 2×2 μm^2 area using a microspectrometer mounted on an optical microscope, which corresponds to ~1400 nanorods. The narrow and symmetric extinction band (FWHM of 115 nm) corresponding to the longitudinal LSPR of AuNR indicates the absence of AuNR aggregates on paper surface, which is in agreement with the SEM images discussed above. Extinction spectra collected across 0.5×0.5 cm^2 area revealed excellent optical uniformity of the bioplasmonic paper substrate. LSPR wavelength measured from six different spots over such large area exhibited a small standard deviation of ~1 nm (Fig. 8.3D). The excellent spectral homogeneity is due to the highly uniform adsorption of AuNR-IgG conjugates as evidenced by the SEM images. The spectral homogeneity observed here is quite remarkable considering the simplicity of the fabrication process and the inherent heterogeneity of the paper substrates (large surface roughness and hierarchical nature of the fibrous mat).

The biosensing capability of the paper substrates is demonstrated by using anti-IgG as a model bioanalyte, which is known to exhibit strong and specific binding the heavy chains of IgG.[287] Extinction spectra were obtained from paper substrates adsorbed with bare AuNRs, AuNR-IgG conjugates with SH-PEG (for blocking non-specific binding) and subsequently exposed to 24 µg/ml of anti-IgG (Fig. 8.4A).

LSPR wavelength exhibited a ~17 nm red shift with the partial replacement of CTAB layer with AuNR-IgG conjugates and SH-PEG molecules, and a further red shift of ~23 nm upon specific binding of anti-IgG (24 µg/ml) to IgG. On the other hand, a small red shift of ~2 nm was observed upon exposure to bovine serum albumin (BSA) (24 µg/ml), which indicates small non-specific binding of the biofunctionalized nanorods (Fig. 8.4B).

The extinction spectrum was deconvoluted by fitting the extinction spectrum with two Gaussian peaks, from which the longitudinal LSPR wavelength of AuNRs was employed to monitor the biomolecule binding (Fig. 8.4C). A semi-log plot of the longitudinal LSPR wavelength shift for different concentrations of anti-IgG revealed that LSPR shift monotonically increases with increase in the concentration of anti-IgG. The plot also reveals extremely small non-specific binding of BSA for various concentrations (Fig. 8.4D). Conventional glass substrates exhibited smaller shift (20 nm) compared to the bioplasmonic paper (24 nm) under similar conditions (Fig. S6.3). The larger shift in the case of paper substrate compared to glass substrate is possibly due to the 3D porous structure of paper substrate, which enables better uptake and transport of the bioanalytes to the plasmonic nanostructures. A detection limit of 24 pg/ml (~0.16 pM) was noted in the case of bioplasmonic paper, which is on par with that observed in the case of other rigid substrates.[4]

8.3.2 Detection of renal cancer carcinoma biomarker

Similar approach was employed to detect AQP1, a biomarker for RCC in urine. We employed AuNR appended with anti-AQP1 as biofunctionalized transducers for the detection of AQP1 in artificial urine. Figure 8.5A shows the shift in the longitudinal LSPR of AuNR upon binding of AQP1 (4.67 µg/ml) from artificial urine sample (Fig. 8.5A). A monotonic increase in the LSPR shift is observed with increasing the concentration of AQP1 in artificial urine (Fig. 8.5B). The measured LSPR shift for 10 ng/ml (0.35 nM) of AQP1 is ~1.1 nm. This shift is significantly higher than the noise floor of the bioplasmonic paper (~0.6 nm). The detection limit matches with the lower limit of the range of AQP1 in patients with RCC.[288] The detection limit of AQP1 is higher than anti-IgG, which is possibly due to: (i) the molecular weight of AQP1 is 28.3 kDa, much smaller than model bioanalyte anti-IgG 150 kDa, causing a smaller change in refractive index; and (ii) limited binding sites accessible to AQP1 compared to that available for anti-IgG, which

binds to the heavy chain of IgG. The detection limit can be lowered by optimizing the ratio of SH-IgG and AuNRs, and selecting nanostructures or their organized assemblies with higher LSPR sensitivity.

8.3.3 Swabbing test using bioplasmonic paper

One of the distinct advantages of the bioplasmonic paper is the ability to collect trace amount of bioanalytes from real-world surfaces by simply swabbing across the surface. To demonstrate such unique ability, 12 µg of anti-IgG was deposited on a tomato as purchased from a grocery store. A slightly wet (in PBS buffer) bioplasmonic paper substrate was swabbed on the surface of the tomato to collect the bioanalytes (Fig. S6.6A). The longitudinal LSPR wavelength exhibited a red shift (~21 nm) upon specific binding of anti-IgG, which was collected from six different spots in the center of the plasmonic paper (Fig. S6.6B). The inset photographs of Figure 8.6B shows that the color of the bioplasmonic paper turned from blue to grey upon binding of the target biomolecules to the biofunctionalized nanorods. A control experiment was performed by swabbing a slightly wetted plasmonic paper on the surface of as purchased tomato (*i.e.,* no prior cleaning). Longitudinal LSPR wavelength exhibited a ~3 nm red shift, which can be attributed to the surface contaminants non-specifically adsorbing to AuNR on the unwashed tomato (Fig. S6.6C). Considering that the swabbing of the surface results in only a fraction of the biomolecules being absorbed onto the paper, the much higher LSPR shift upon specific binding of anti-IgG on the surface clearly indicates the plasmonic paper substrate to be excellent candidate for collecting trace amount of bioanalytes from real-world surfaces as LSPR biosensors.

8.4 Conclusions

In conclusion, we have demonstrated a bioplasmonic paper for the rapid and label-free detection of AQP1, a biomarker for early detection of RCC. Bioplasmonic paper exhibited excellent spectral homogeneity, sensitivity, dynamic range and selectivity, comparable to or better than the conventional rigid LSPR substrates. Furthermore, owing to its unique flexible and conformal nature, bioplasmonic paper enables simultaneous collection and detection of trace amount of bioanalytes from real-world surfaces. Paper based LSPR substrates offer numerous advantages such as low cost, easy storage, transport and disposability, which lead to simple, inexpensive plasmonic biochips for point-of-care diagnostics. Besides being highly cost-effective and environmental-friendly, the use of paper-based LSPR substrates when transformed into printable microfluidic devices will enable the detection of multiple bioanalytes in complex

physiological fluids. The synergism of paper-based microfluidics and LSPR based biosensing is expected to be truly transformative by opening up novel avenues in multi-analyte biological detection.

8.5 Supporting information

Supporting information for chapter 8 is provided in appendix 6.

Figures

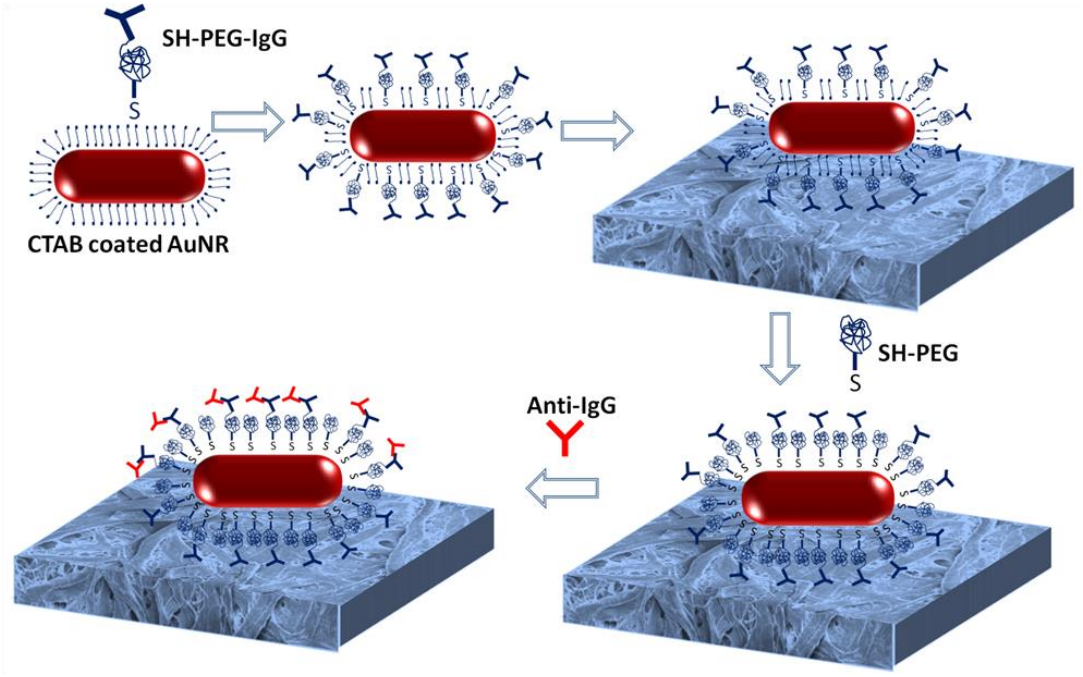

Figure 8.1: Schematic illustration representing the fabrication steps involved in the fabrication of bioplasmonic paper for anti-IgG detection.

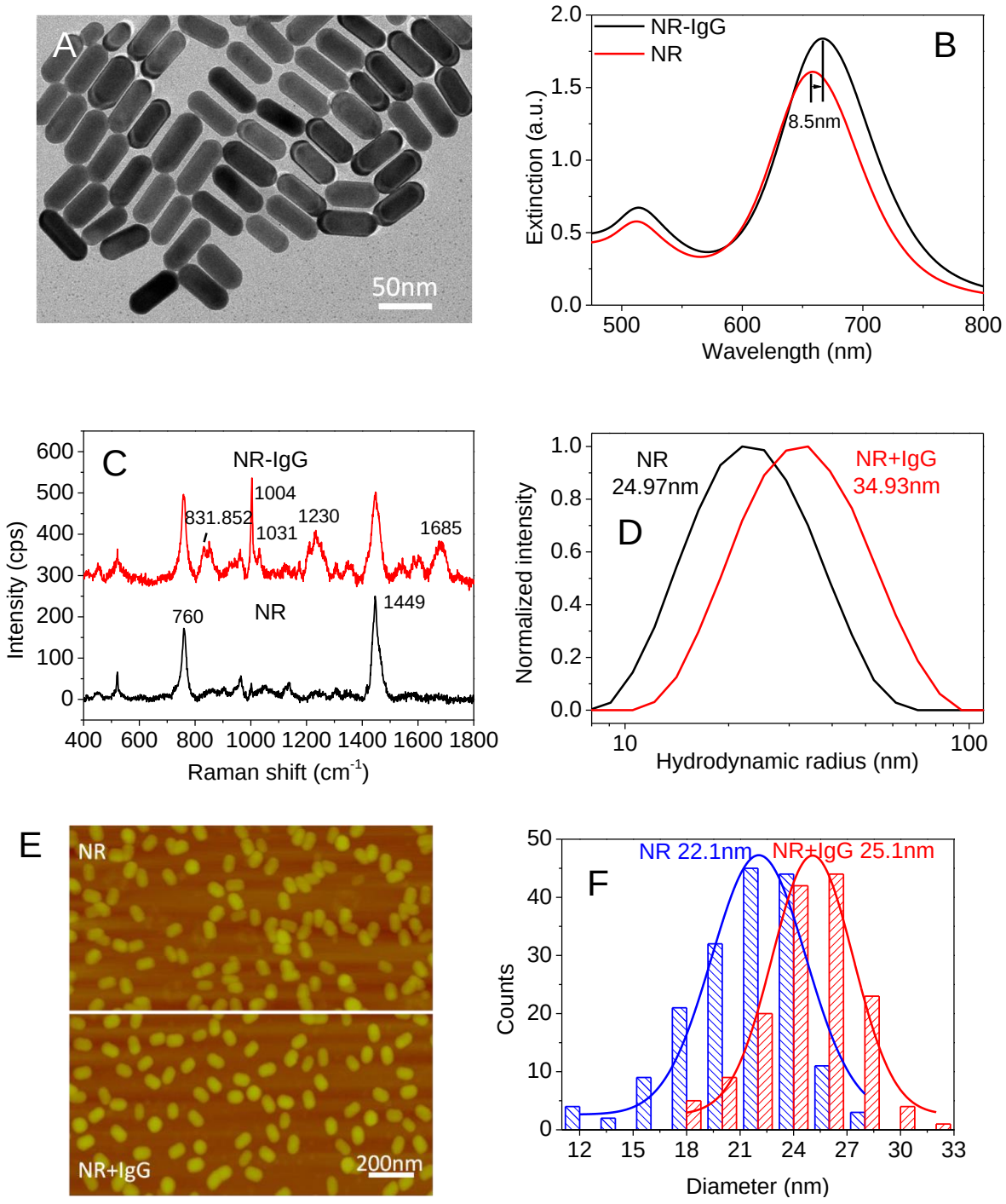

Figure 8.2: (A) TEM image of AuNRs. (B) UV-vis extinction spectra confirming AuNR and SH-PEG-IgG conjugation. The UV-vis extinction spectrum of 56×22 nm AuNRs shows a longitudinal LSPR wavelength of 658 nm (AuNRs, red). After incubation with SH-PEG-IgG, the λ_{max} red shifts 8.5 nm (AuNR-IgG,

black). (C) Hydrodynamic diameters obtained from DLS show that the average hydrodynamic diameter increased by 10nm following IgG conjugation. (D) Surface enhanced Raman spectra before and after the conjugation of antibody on gold nanorods reveal the Raman bands corresponding to IgG. (E-F) AFM images of AuNRs and AuNR+IgG conjugates, revealing the increase in the average diameter of the nanorods following the bioconjugation.

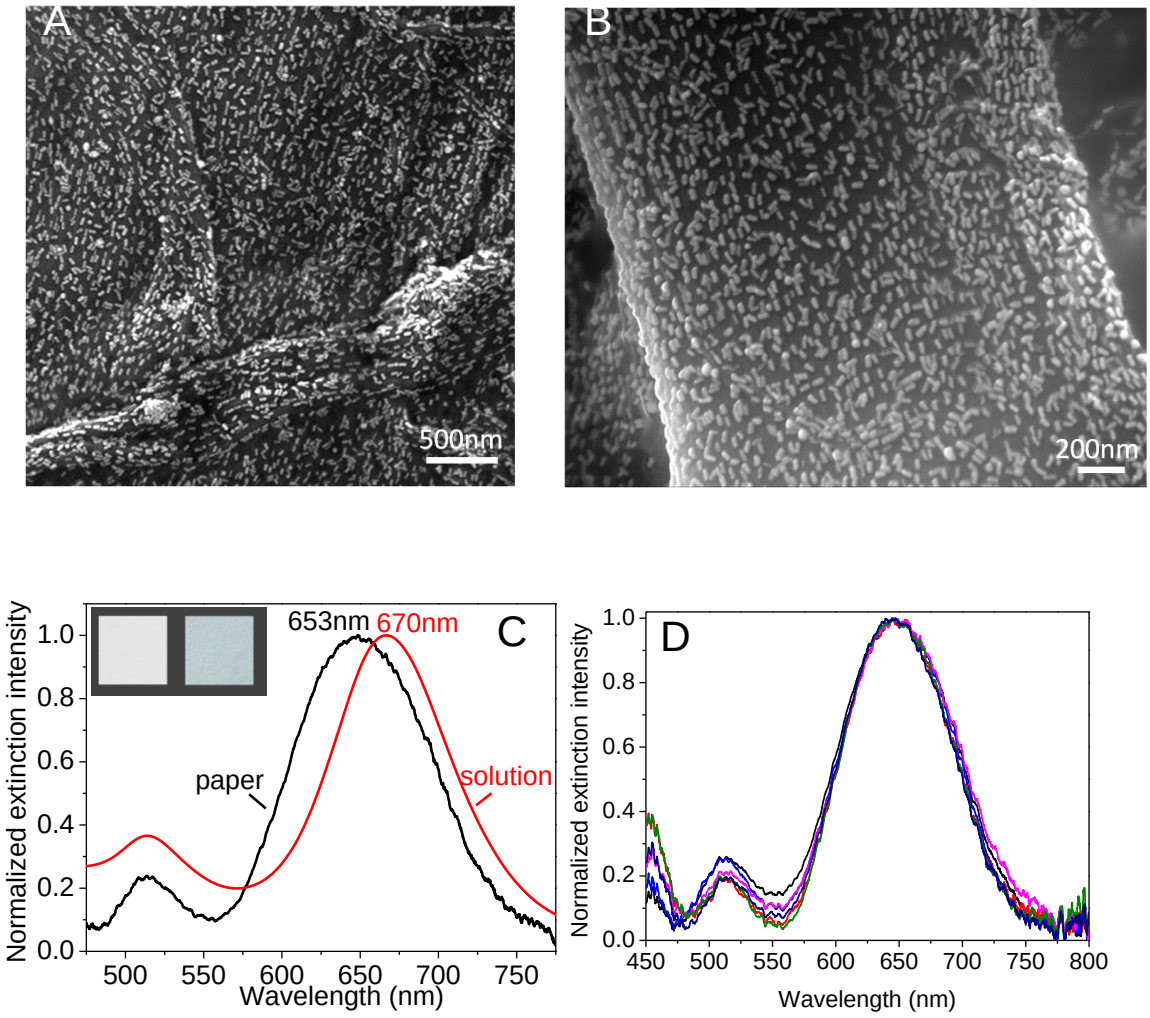

Figure 8.3: (A-B) SEM images of paper adsorbed with AuNR-IgG conjugates. (C) Extinction spectra of AuNR-IgG conjugates in solution and on paper (inset: shows photographs of the bare filter paper (left) and filter paper after adsorption of AuNR+IgG conjugates (right)). (D) Six extinction spectra collected from different spots on a plasmonic paper of 0.5×0.5 cm^2 area showing the remarkable spectral homogeneity of bioplasmonic paper.

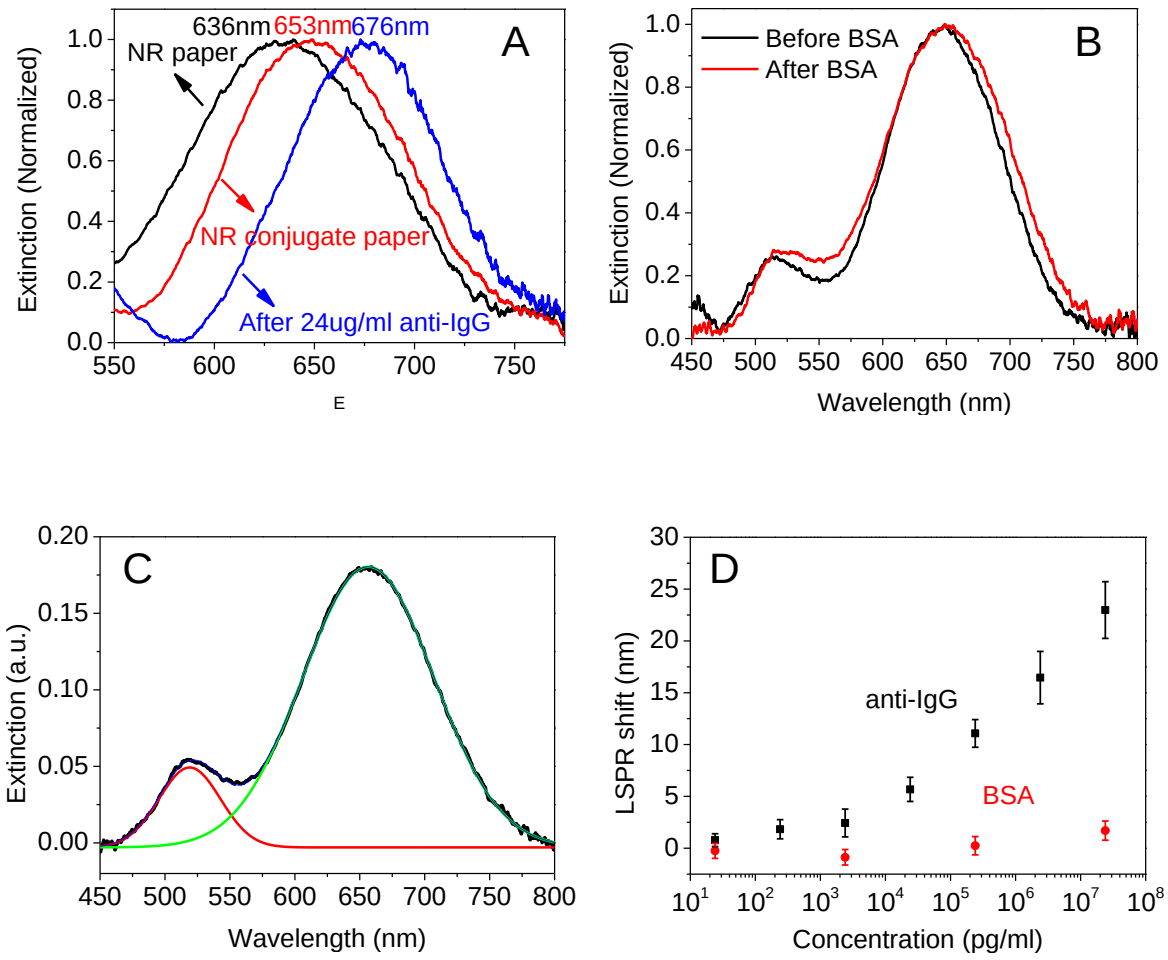

Figure 8.4: (A) Extinction spectra of AuNR paper substrate (black), AuNR-IgG conjugates on the paper substrate before (red) and after binding of anti-IgG (blue). (B) Control experiment showing the small non-specific binding of BSA on bioplasmonic paper substrate. (C) LSPR spectra deconvoluted using two Gaussian peaks. (D) Plot showing the LSPR peak shift of bioplasmonic paper for various concentrations of anti-IgG and BSA.

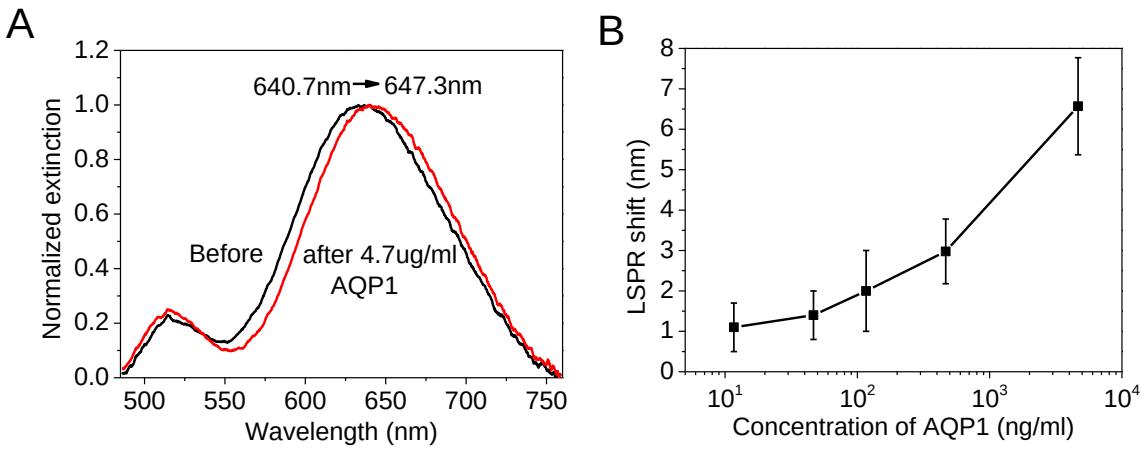

Figure 8.5: (A) Extinction spectra of AuNR appended with anti-AQP1 adsorbed on a paper substrate before (black) and after exposing to 4.7µg/ml AQP1 in artificial urine (red) (B) Plot showing the LSPR peak shift of bioplasmonic paper for various concentrations of AQP1.

Chapter 9 Bioplasmonic Calligraphy for Multiplexed Label-free Biodetection

9.1 Introduction

Owing to numerous advantages such as high specific surface area, excellent wicking properties, compatibility with conventional printing approaches, significant cost reduction and easy disposability, paper substrates are gaining increased attention in biodiagnostics, food quality testing, environmental monitoring, flexible energy and electronic devices.[159, 219, 220, 281, 289-296] Recent surge in the activity related to paper-based diagnostic devices is primarily focused on realizing microfluidic paper-based analytical devices (μPADs) for point-of-care assays and inexpensive diagnostic tools for resource-limited environments.[220, 297] Most of these developments rely on labor-, time- and/or resource-intensive patterning techniques such as photolithography, wax printing, inkjet printing of polydimethylsiloxane (PDMS), to create fluidic pathways and/or different functional regions for site-selective adsorption of the biochemical reagents. [163, 291, 298-304] Moreover, implementing ink-jet printing with biomolecules results in loss of recognition functionality due to the inherent temperature variations associated with inkjet printing process. These considerations clearly highlight the need for a simple and biofriendly technique that enables multi-marker biochips for point-of-care and resource-limited settings.

The refractive index sensitivity of localized surface plasmon resonance (LSPR) of plasmonic nanostructures renders it an attractive transduction platform for chemical and biological sensing.[224, 305-316] We have recently demonstrated plasmonic paper comprised of biofunctionalized gold nanorods (AuNRs) uniformly adsorbed on paper substrates.[294] The bioplasmonic paper enabled the detection of aquaporin-1, a kidney cancer biomarker in artificial urine down to a concentration of 10 ng/ml. Bioplasmonic paper, fabricated by immersing a paper substrate into biofunctionalized AuNRs solution, facilitates the detection of one specific target protein in the analyte solution (e.g., urine). Perceivably, this immersion approach hinders spatial multiplexing (*i.e.*, realizing multiple test domains for the detection of more than one target biomolecule on the same substrate) as it results in uniform adsorption of the bioconjugated nanorods over the entire paper surface.

Here, we demonstrate a simple yet powerful plasmonic calligraphy approach for realizing multiplexed label-free bioassays using a regular ballpoint pen filled with gold nanorods or biofunctionalized gold nanorods as (bio)plasmonic ink. Plasmonic calligraphy offers two distinct advantages over plasmonic

paper substrates obtained by immersion method as reported previously. Firstly, plasmonic calligraphy serves as a facile method to miniaturize the test domain size to few mm^2, which significantly improves the sensitivity of the plasmonic biosensor compared to bioplasmonic paper fabricated using immersion approach.[294] Secondly, plasmonic calligraphy using bioplasmonic ink enables simple and efficient multiplexed biodetection on paper substrates thus leading to multi-marker biochips. In this study, we demonstrate these two aspects using gold nanorods as plasmonic nanotransducers.

9.2 Experimental section

Materials: Cetyltrimethylammonium bromide (CTAB), chloroauric acid, ascorbic acid, sodium borohydride, poly(styrene sulfonate) (PSS) (Mw=70,000 g/mol), and poly(allyl amine hydrochloride) (PAH) (Mw=56,000 g/mol) were purchased from Sigma-Aldrich. Silver nitrate and filter paper (Whatman #1) was purchased from VWR international. 1-Ethyl-3-(3-dimethylaminopropyl) carbodiimide (EDC) and N-hydroxy succinimide (NHS), Rabbit IgG, Goat anti-Rabbit IgG, Human IgG, Goat anti-human IgG, Mouse IgG, and Goat anti-mouse IgG were purchased from Thermo scientific. SH-PEG-COOH (Mw=5,000 g/mol) was purchased from Jenkem Technology. All the chemicals have been used as received with no further purification. Paper mate profile retractable ballpoint pens were bought from Amazon.

Preparation of polyelectrolytes coated gold nanorods (AuNRs): AuNRs were modified with polyelectrolytes as previously reported.[317] Briefly, 1 ml of twice centrifuged AuNRs solution was added drop-wise to 0.5 ml of PSS solution (0.2% w/v) in 6 mM NaCl aqueous solution under vigorous stirring, followed by shaking for 3 h. To remove excess PSS, the above solution was centrifuged at 10,000 rpm for 10 min, and the pellet was dispersed in nanopure water after removing the supernatant. To modify AuNRs with PAH, 1ml of PSS coated AuNRs solution was added drop-wise to 0.5 ml of PAH (0.2% w/v) solution in 6 mM NaCl, followed by gentle shaking for 3 h. The resultant 1ml of PAH coated AuNRs solution was centrifuged and concentrated to 10 µl and employed as ink to write on paper substrates. The surface charge of CTAB stabilized AuNRs, PSS and PAH coated AuNRs were estimated by measuring the zeta potential of corresponding solution (Fig. S7.3).

Bioplasmonic paper substrates preparation: A regular laboratory filter paper (Whatman™ # 1) was immersed into a 1% (w/v) BSA in PBS buffer (pH 7.5) for 1 h as a pretreatment step to prevent nonspecific binding (Fig. S7.5A). We noted ~30% improvement in plasmonic biosensor response (i.e.,

longitudinal LSPR shift of AuNRs) for BSA-blocked paper compared to pristine paper (Fig. S7.5B, S7.5C). Plasmonic ink was prepared by concentrating 1 ml of twice centrifuged as synthesized AuNRs to 10 µl after twice centrifugation. Bioplasmonic ink was concentrated from 1 ml of NR-IgG conjugates solution by centrifugation at 3,000 rpm for 20 min. The plasmonic ink was injected into an empty ball point pen refill cleaned with ethanol and nanopure water by sonication. The adsorption of AuNRs-IgG conjugates on paper was achieved by direct writing with bioplasmonic ink filled pen, or exposing written AuNRs paper in SH-PEG-IgG conjugates solution for 30 min, followed by thorough rinsing with buffer and nanopure water. Bioplasmonic paper was exposed to various concentrations of anti-IgG in PBS for 1 h, followed by thorough rinsing with PBS and water and drying with a stream of nitrogen.

Extinction Spectra Measurements: Extinction spectra from paper substrates were collected using a CRAIC microspectrophotometer (QDI 302) coupled to a Leica optical microscope (DM 4000M) with 20x objective in the range of 450-800 nm with 10 accumulations and 0.1 sec exposure time in reflection mode. The spectral resolution of the spectrophotometer is 0.2 nm. Several UV-Vis extinction spectra (~ 10) were collected for each substrate before and after anti-IgG exposure. Each spectrum represented a different spot within the same substrate. Shimadzu UV-1800 spectrophotometer was employed for collecting UV-vis extinction spectra from solution.

9.3 Results and discussion

9.3.1 Characterization of Plasmonic Calligraphed Paper

Plasmonic calligraphy using a ball point pen to form sensing islands on paper offers a unique advantage in that the volume of ink deposited can be well-controlled by a altering the viscosity of the ink and 'finesse' of the ball used for writing. On the other hand, a more conventional approach of micropipette-based deposition of sensing elements (*i.e.*, biofunctionalized AuNR) on paper surface results in fuzzy boundaries and non-uniform drying patterns due to uncontrolled evaporation on heterogeneous paper surface. Gold nanorods are particularly attractive as plasmonic transducers considering the high refractive index sensitivity of longitudinal LSPR, facile and large tunability of the LSPR wavelength with aspect ratio and the electromagnetic (EM) hot-spots at the tips.[228, 318, 319] AuNRs, synthesized using a seed-mediated approach, are positively charged with a length of 56.3±3.7 nm and a diameter of 22.4±1.8 nm (TEM image in Fig. 9.1A).[232, 320] Figure 9.1B depicts plasmonic calligraphy on a laboratory filter

paper (Whatman # 1) using a regular ballpoint pen with AuNRs ink, which yields continuous and clearly defined lines visible to even un-aided eye. Ball pens are particularly well suited for dispensing nanoparticle inks due to their compatibility with liquid and gels.[235] The viscosity of AuNRs ink was measured to be ~1.25 Pa·s, which is close to the optimal viscosity for silver nanoparticle ink reported previously.[236] The left inset image of Figure 9.1B shows the logo of Washington University in St. Louis, a complex pattern, drawn on a laboratory filter paper using cetyltrimethylammonium chloride (CTAC) stabilized gold nanospheres (AuNPs, red region) and cetyltrimethylammonium bromide (CTAB) stabilized gold nanorods (AuNRs, green region). The right inset image of Figure 9.1B depicts the SEM image of the tip of a ballpoint pen with a ball diameter of ~1.5 mm, showing the residue of AuNRs ink left on the ball surface. Extinction spectra collected from several locations of red and green region of the university logo drawn with AuNPs and AuNRs ink revealed excellent optical uniformity of the plasmonic paper substrate (Fig. 9.1C). UV-vis extinction spectrum obtained from AuNRs region is characterized by two distinct bands corresponding to the transverse (lower wavelength) and longitudinal (higher wavelength) oscillation of electrons with the incident EM field (Fig. 9.1C).

The extinction spectrum of AuNRs was deconvoluted by fitting the extinction spectrum with two Gaussian peaks to obtain the longitudinal LSPR wavelength of AuNRs, which was used to monitor the binding of target proteins to AuNRs (Fig. 9.1D). It is known that longitudinal LSPR of AuNRs is more sensitive to the refractive index change of the surrounding medium compared to its transverse band and LSPR of AuNPs.[292, 294] Longitudinal LSPR wavelength measured from ten different spots of the green region of the university logo exhibited a small standard deviation of ~1 nm (Fig. 9.1C). The excellent spectral homogeneity is due to the uniform adsorption of AuNRs on paper substrates as evidenced by the SEM images (Fig. 9.1E, 9.1F). The spectral homogeneity observed here is quite remarkable considering the simplicity of the writing process and the inherent heterogeneity of the paper substrates (large surface roughness and hierarchical nature of the fibrous mat). The density of the nanostructures on the paper substrate can be controlled by the number of strokes. The density of the AuNRs adsorbed on the paper substrate for a single stroke was found to be 31±9/μm^2 determined using SEM micrographs. Notably, the adsorption of AuNRs on paper is sufficiently strong to resist desorption from paper surface even after extensive rinsing with water or buffer as confirmed by little change in the intensity and shape of extinction

spectra collected before and after rinsing. In addition to AuNRs, various shape-controlled nanostructures stabilized with different ligands, including gold nanospheres stabilized with citrate ions, gold nanoshells capped with poly(vinyl pyrrolidone) (PVP), can be written on paper with no sign of aggregation or patchiness (Fig. S7.1).

9.3.2 Significant Improvement on Sensitivity of Bioassays

First, we set out to demonstrate that the plasmonic calligraphy approach serves as a simple and powerful tool to miniaturize the test domain size, which leads to dramatic improvement in plasmonic paper-based biosensor performance compared to previous immersion method. Capillary-driven flow of the analyte solution across the test domain written on paper is employed to maximize the target analyte interaction with the recognition elements on the plasmonic nanostructures.[321] To visually demonstrate the concept of capillary-driven flow-based sensing, AuNRs modified with positively charged poly(allylamine hydrochloride) (PAH@AuNRs) was written on the stem portion of a paper substrate cut in the shape of a badminton racket with a head of 4.3 cm diameter and a stem of 4×0.6 cm^2 (Fig. 9.2A). The head portion serves as a wicking pad or collection reservoir and the bottom end of the stem is immersed in the analyte solution of a predefined volume. The model analyte solution comprised of negatively charged fluorescein molecules was deposited at the lower end of the stem (Fig. 9.2B). The capillary-driven flow results in the transport of fluorescein from the tip of the stem to the wicking pad. In the case of paper substrate without PAH@AuNRs line, most of the fluorescein is collected at the neck of the substrate as indicated by the strong green fluorescence from the neck region under UV illumination (Fig. 9.2C). On the other hand, reduced fluorescence was observed at the neck region of the substrate with PAH@AuNRs line as most of the negatively charged fluorescein was bound to the positively charged PAH@AuNRs line (Fig. 9.2C). Absence of strong fluorescence from the PAH@AuNRs line is possibly due to the non-radiative quenching of fluorescence by the plasmonic nanostructures (Fig. 9.2C).[322, 323]

In most of sensing systems, miniaturization of the test domain size results in improved sensitivity and lower limit of detection while adversely affecting the dynamic range. In the case of plasmonic sensors, individual nanostructures and even specific parts of individual nanostructures have been employed for chemical and biological detection, which exhibit remarkable sensitivities but limited dynamic range.[14, 324] Most of these demonstrations involve complex and tedious fabrication methods (e.g., e-beam lithography)

and/or signal collection and processing methods (e.g., dark-field scattering spectroscopy). Plasmonic calligraphy approach serves as a facile tool to optimize the test domain size for achieving a balance between sensitivity and dynamic range (e.g., covering physiological and pathological concentration of a protein biomarker). The test domain size can be controlled by simply cutting the paper substrates to vary the feature size written on the paper substrate using plasmonic ink. Figure 9.3A shows AuNRs line was written at the bottom end of the stem portion of a test strip followed by functionalization of AuNR with rabbit immunoglobulin G (IgG) (see experimental section for details). A predefined volume of the target protein solution (100 µl of 24 ng/ml anti-rabbit IgG) was transported from the bottom of the stem to wicking pad across test domains of different sizes using capillary force. The approach adapted here ensures the analyte to pass through test domain, overcoming one of the drawbacks of miniaturizing the test domain *i.e.*, low probability for the analyte molecules to 'find and bind' to the test domain. The LSPR wavelength shift was observed to be 13.3 nm when the domain size was reduced to 3×1.5 mm^2 compared to 8.4 nm for a test domain of 6×1.5mm^2 upon exposure to 24 ng/ml of anti-IgG (Fig. 9.4B, 9.3C). The increase in LSPR shift by about 58%, indicates an improvement in sensitivity by reducing the test domain size (Fig. 9.3D). Plasmonic calligraphy in combination with "paper cutting" forms a powerful tool to dial in the required sensitivity or dynamic range of a paper-based biosensor.

9.3.3 Multiplexed Biosensing based on Bioplasmonic Calligraphy

Multi-marker plasmonic biochips using paper substrates that enable multiplexed biosensing will be an extremely powerful tool to facilitate the detection and quantification of multiple prognostic biomarkers using the same substrate. To achieve such a multi-marker biochip, individual test domains should be comprised of plasmonic nanostructures with differential functionalization specific to target biomarkers. To realize the differential functionalization of test domains on paper substrates, we employ biofunctionalized nanostructures as ink (called bioplasmonic ink henceforth) rather than biofunctionalization after creating the test domains as described above (Fig. 9.3A). Such bioplasmonic ink facilitates one to write with distinct biofunctionalized nanostructures on paper substrates adjacent to each other without cross-contaminating the test domains based on the concept of bioplasmonic calligraphy as illustrated in Fig. 9.4A. SEM images revealed highly uniform distribution of gold nanorods modified with rabbit IgG (NR-rabbit IgG) conjugates on paper surface with no signs of aggregation or patchiness on the substrate (Fig.

9.4B). Higher magnification image reveals the preferential alignment of AuNRs-rabbit IgG conjugates along the cellulose fibers (Fig. S7.2). Extinction spectra were obtained from paper substrates calligraphed with NR-rabbit IgG and subsequently exposed to 24 μg/ml of anti-rabbit IgG (Fig. 9.4C). LSPR wavelength exhibited a red shift of ~17 nm upon specific binding of anti-rabbit IgG to rabbit IgG appended on the AuNRs. A semi-log plot of the longitudinal LSPR wavelength shift for different concentrations of anti-rabbit IgG revealed that LSPR shift monotonically increases with increase in the concentration of anti-rabbit IgG. An extremely small LSPR shift (~1 nm) was noted for relatively high concentration of BSA (24 μg/ml) due to non-specific binding (Fig. 9.4D). Detection limit was determined to be of 24 pg/ml (~0.16 pM), which is on par with that observed in the case of other rigid substrates.[314] It is worth noting that the biomolecules appended to the nanostructure preserve their recognition capabilities confirming that the simple bioplasmonic calligraphy approach suggested here is "biofriendly" and can be potentially employed for multiplexed biodetection as demonstrated below.

To test capability of multiplexed detection, we wrote two distinct test domains comprised of AuNRs with human IgG and mouse IgG, and then obtained the LSPR shift upon exposure to the different combination of target proteins (goat anti-human IgG, and goat anti-mouse IgG) (Fig. 9.5A and inset of Fig. 9.5B). Goat anti-human IgG and goat anti-mouse IgG are affinity-purified secondary antibodies with well-characterized specificity for human IgG and mouse IgG, respectively, which have been tested by ELISA and/or solid-phase adsorbed to ensure minimal cross-reaction with each other. Extinction spectra of AuNRs functionalized with human IgG (NR-human IgG) showed LSPR shift of ~17.1 nm and AuNRs functionalized with mouse IgG (NR-mouse IgG) showed extremely small LSPR shift (~1.0 nm) upon exposure to 24 μg/ml of anti-human IgG (Fig. 9.5B). On the other hand, upon exposure to 24 μg/ml of anti-mouse IgG, NR-human IgG line showed extremely small shift (~ 1.1 nm) while LSPR shift of NR-mouse IgG was measured to be ~14.5 nm (Fig. 9.5B). Upon exposure to a mixture of anti-human IgG and anti-mouse IgG (24 μg/ml each), NR-human IgG showed ~17.6 nm of LSPR shift and NR-mouse IgG showed ~12.3 nm. The spectral response of the two lines upon exposure to the mixture closely corresponds to the LSPR shift measured for exposure to individual target biomolecules. This multiplexed bioassay was also challenged with exposure to a mixture of anti-mouse IgG of different concentrations and anti-human IgG of a fixed concentration (Fig. 9.5C). A monotonic increase in the LSPR shift of NR-

mouse IgG band was observed with increasing the concentration of anti-mouse IgG while NR-human IgG band exhibited a stable ~8 nm LSPR shift corresponding to the fixed concentration of anti-human IgG (7.5 µg/ml) in the mixture. A detection limit of 750 pg/ml of anti-mouse IgG was noted even in the presence of a constant interfering 7.5 µg/ml of anti-human IgG. These results clearly show the capability of multiplexed biosensing based on bioplasmonic calligraphy approach. The approach suggested here obviates the need for any complex multi-step process such as formation of hydrophilic test domains and hydrophobic barriers to achieve label-free multiplexed biodetection.

9.4 Conclusions

Plasmonic calligraphy approach serves as a simple and powerful tool to miniaturize test domain size by controlling the calligraphed feature size and simply cutting the paper to desired dimensions, which results in dramatic improvement in sensitivity and lowering limit of detection. We introduced a low-cost novel approach for fabricating multiplexed label-free biosensing on paper substrates in the form of bioplasmonic calligraphy. The calligraphy approach allows one to create well-isolated test domains on paper substrates using biofunctionalized plasmonic nanostructures as ink. We have demonstrated here the feasibility of such an approach for multiplexed biosensing using two target proteins. Bioplasmonic calligraphy can serve as a powerful tool enabling the synergism of paper-based microfluidics and plasmonic biosensing, which is expected to be truly transformative by opening up novel possibilities to realize the fabrication of multi-marker paper-based biochips.

9.5 Supporting information

Supporting information for chapter 9 is provided in appendix 7.

FIGURES

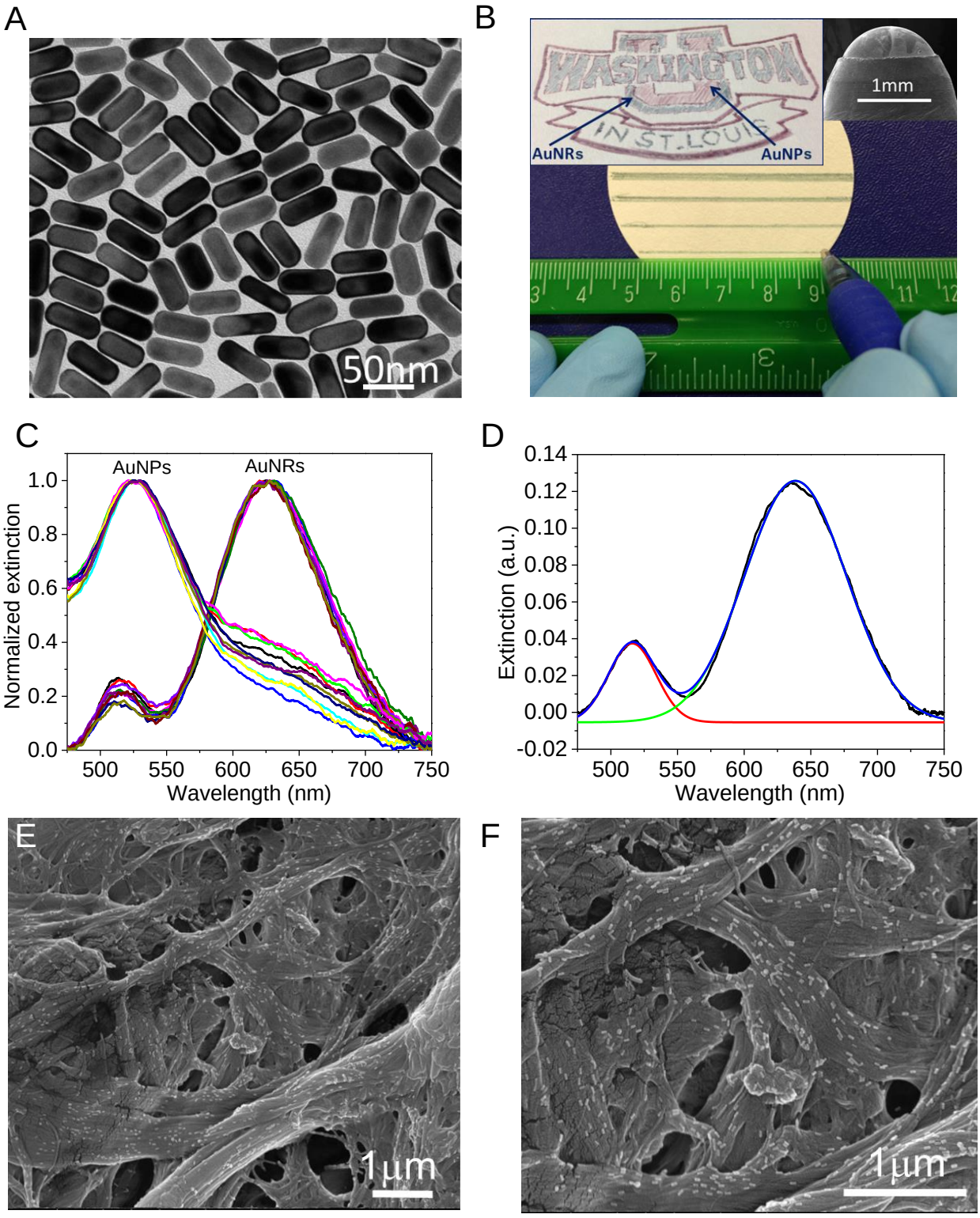

Figure 9.1 (A) TEM image of AuNRs. (B) Demonstration of writing AuNRs on paper substrate (Left inset:

the logo of Washington University in St. Louis drawn using gold nanospheres (AuNPs, red region) and gold nanorods (AuNRs, green region). Right inset: SEM image of the tip of a ball pen with AuNRs ink residue on the surface). (C) Extinction spectra measured from ten spots of the red and green region of the university logo, showing excellent spectral homogeneity. (D) A representative LSPR spectrum of AuNRs deconvoluted using two Gaussian peaks (E-F) SEM images of AuNRs adsorbed on paper substrates by plasmonic calligraphy approach.

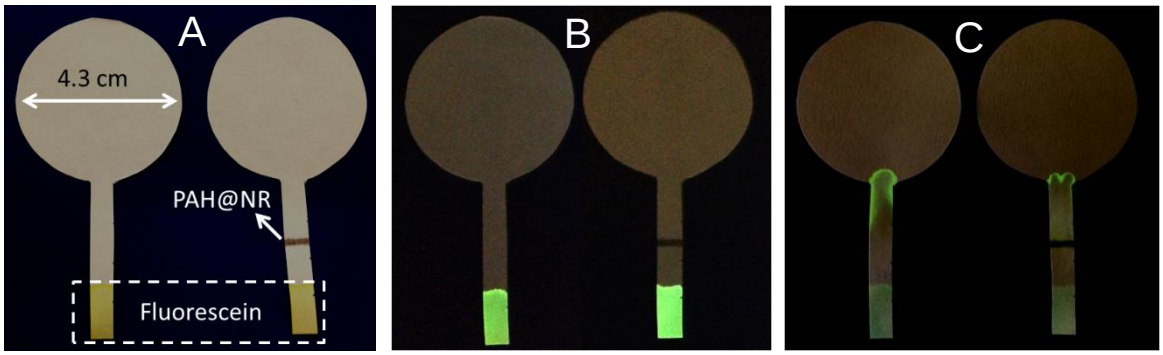

Figure 9.2 (A) Optical and (B) fluorescence images of paper strips with 10 µl of 10 mM fluorescein molecules adsorbed at the bottom of strip under visible light and UV light. (C) Transport of the fluorescein molecules toward wicking pad with 50 µl of water, showing the adsorption capability of negatively charged fluorescein molecules on positively charged PAH @AuNRs band.

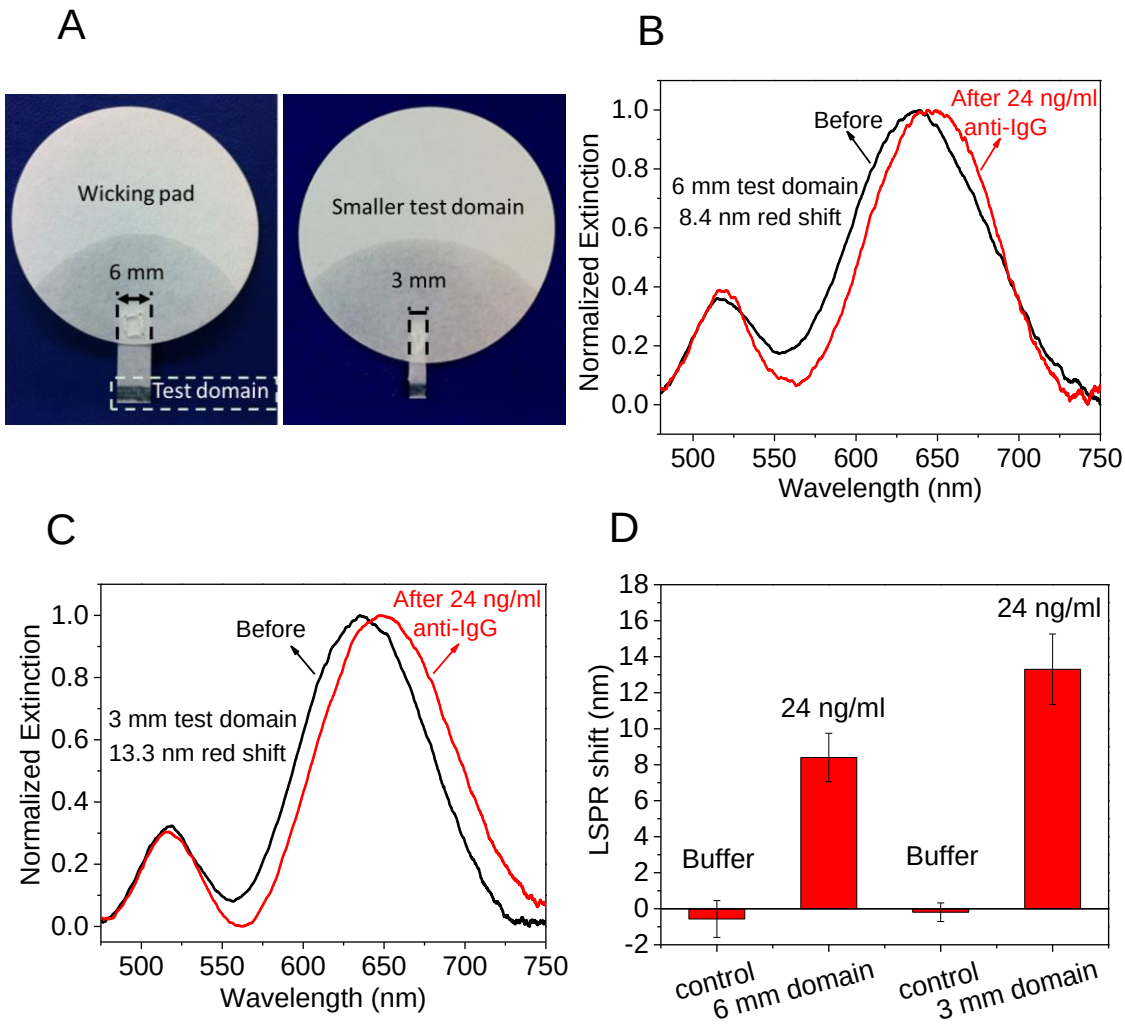

Figure 9.3 (A) Images of paper strips with different size of test domains (B-C) Extinction spectra of AuNRs paper upon 24 ng/ml of anti-IgG binding corresponding to different test domain size. (D) Comparison of LSPR shifts for different test domain size of bioassays.

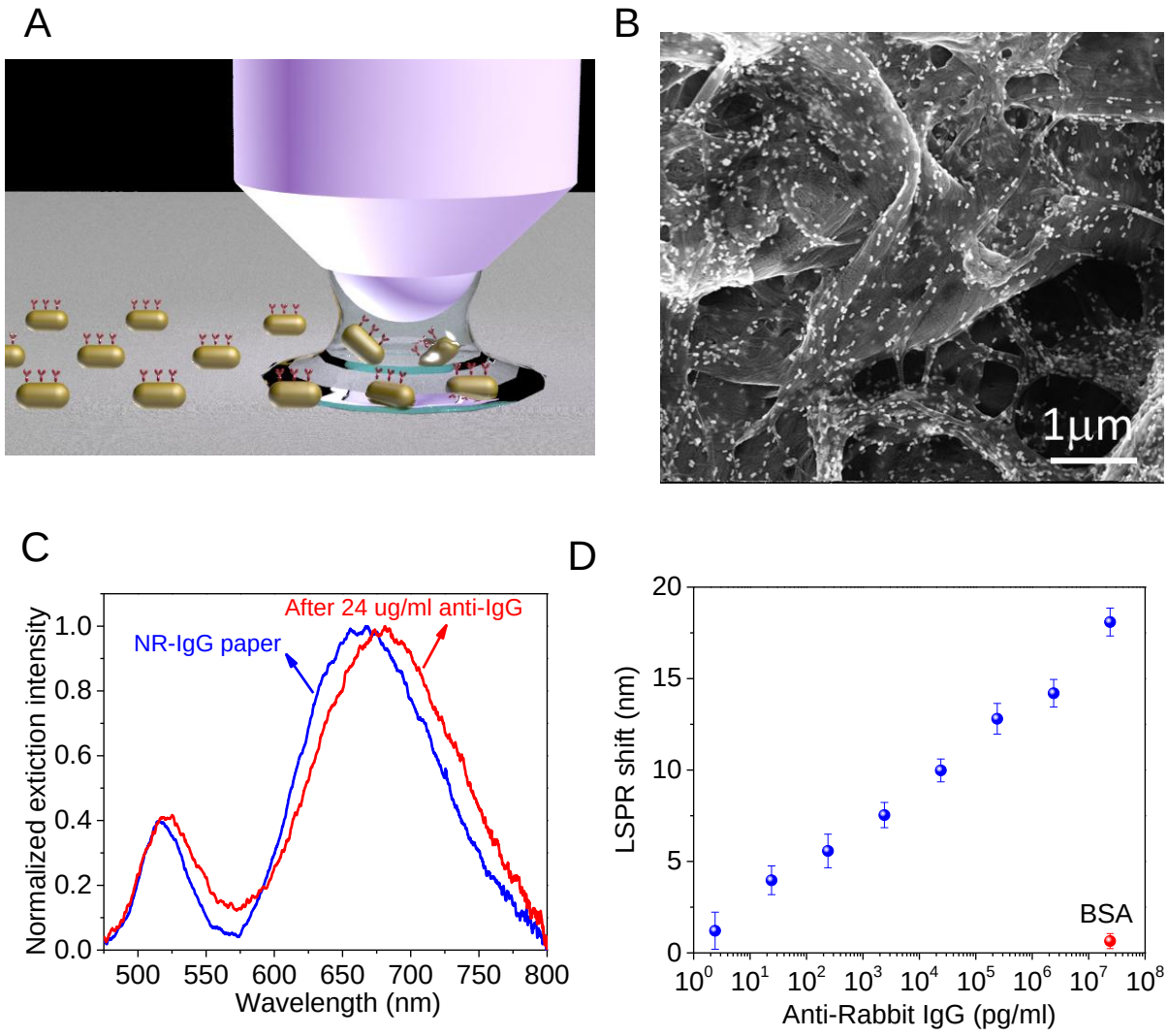

Figure 9.4 (A) Schematic illustration of the concept of bioplasmonic calligraphy. (B) SEM images of NR-IgG conjugates adsorbed on paper substrates by bioplasmonic calligraphy approach. (C) Extinction spectra of AuNRs-IgG conjugates on the paper substrate before (blue) and after binding of anti-IgG (red). (D) Plot showing the LSPR peak shift of bioplasmonic paper for various concentrations of anti-IgG and BSA.

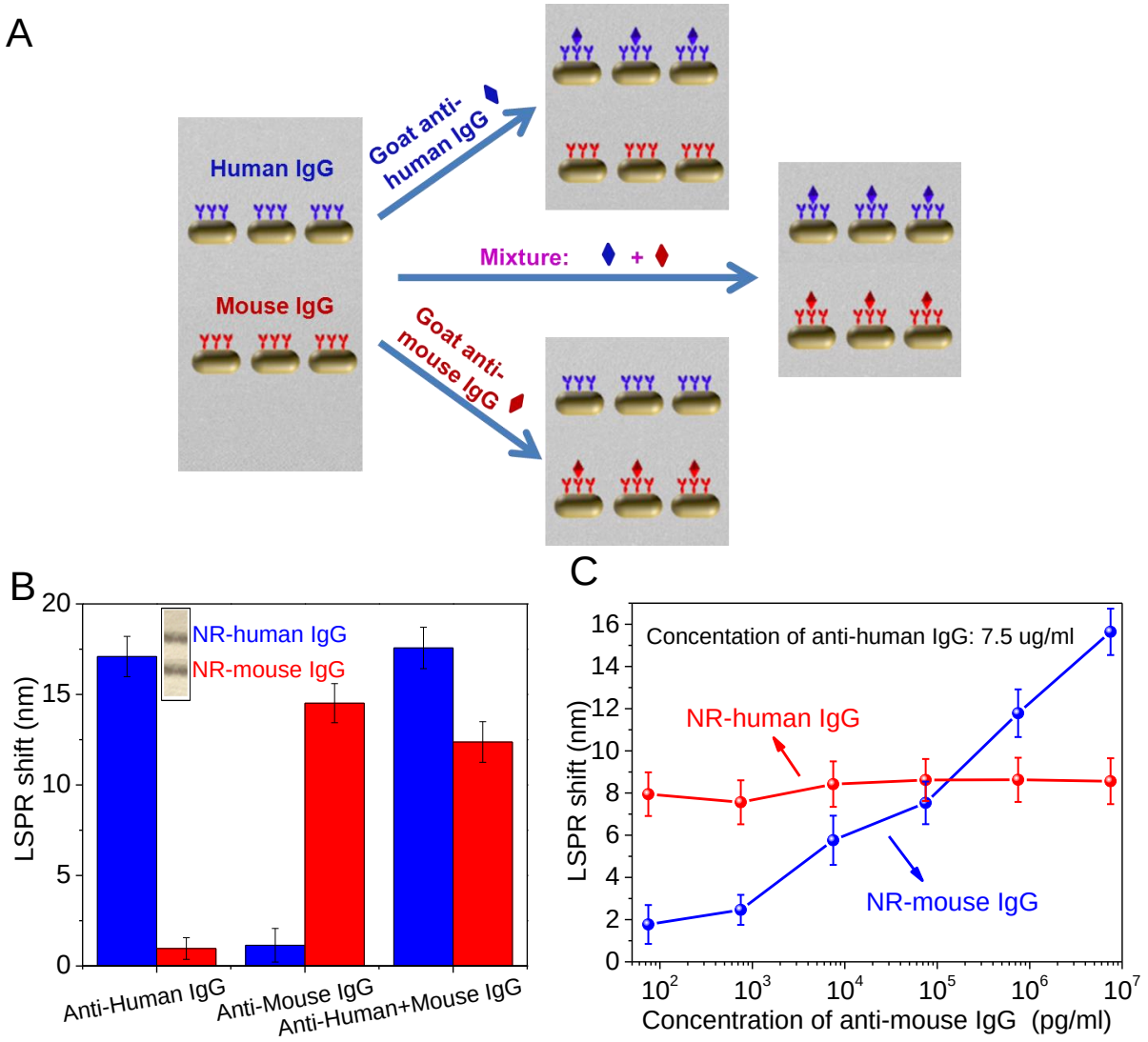

Figure 9.5 (A) Schematic illustration of multiplexed detection based on bioplasmonic calligraphy. (B) Longitudinal LSPR wavelength shift of AuNRs functionalized with human IgG and mouse IgG corresponding to exposure the bioassay to goat anti-human IgG, goat anti-mouse IgG, and the mixture of both (Inset: image of NR-human IgG and NR-mouse IgG written on paper). (C) Longitudinal LSPR wavelength shift of NR-human IgG and NR-mouse IgG corresponding to exposure the bioassay to the mixture of different concentrations of goat anti-mouse IgG and the constant concentration of goat anti-human IgG.

Chapter 10 General Conclusions and Outlook

10.1 General conclusions

Most of the conventional SERS substrates and LSPR sensors are based on rigid and brittle surfaces such as glass, silicon and alumina. Clearly, this bias is due to the compatibility of such substrates with common micro- and nanofabrication technologies (*e.g.*, photolithography and e-beam lithography) and well-established surface modification procedures (*e.g.*, self-assembled monolayers, adsorbed ultrathin polymer layers) for anchoring the chemically synthesized plasmonic nanostructures on surfaces. Apart from high fabrication and processing cost, such substrates preclude applications that require flexibility *e.g.*, swabbing the substrate on a surface of interest to make conformal contact with surface for efficient sample collection. Beyond flexibility, compared to these conventional substrates, paper has numerous advantages such as high specific surface area, excellent wicking properties, compatibility with conventional printing approaches, significant cost reduction and easy disposability. For all these reasons, paper is gaining increased attention as a potential substrate for various applications including sensing, biodiagnostics, food quality testing as well as environmental monitoring.

In this work, we have introduced a novel SERS and LSPR substrate based on conventional filter paper decorated with plasmonic nanostructures. Pre-synthesized shape-controlled nanostructures such as AuNRs, which offer facile tunability of LSPR wavelength, were uniformly adsorbed on paper substrates by immersing the paper substrates in nanostructure solution followed by extensive rinsing to remove weakly adsorbed nanostructures. Plasmonic paper substrates exhibited excellent uniformity as evidenced by SEM imaging, LSPR spectra and SERS spectra obtained across the substrate. The relative standard deviation in SERS intensity following the exposure of plasmonic paper (1×1 cm^2) to model analytes such as 1,4-benzenedithiol (1,4-BDT) and trans-1,2-bis(4-pyridyl)ethene (BPE) was found to be ~15%, which is remarkable considering the heterogeneous nature and inherent roughness of the paper substrates. Apart from exhibiting sub-nM limit of detection (LOD), the plasmonic paper substrates could be employed as swabs to collect and detect trace amounts of analyte from real-world surfaces. Conformal contact and high SERS efficiency of plasmonic paper enabled the detection of ~100 pg of 1,4-BDT spread over 2×2 cm^2.

Typically individual plasmonic nanostructures offer limited EM field enhancement, which directly results in limited SERS enhancement from these nanostructures. Plasmonic nanorattles synthesized in this work are comprised of gold nano-octahedra as cores and cubic porous gold shells using a combination of seed-mediated synthesis and galvanic replacement reaction. Plasmonic coupling between the solid core and porous shell of the nanorattles results in a large enhancement in the electromagnetic (EM) field at the interior of the nanorattles, making them excellent candidates for SERS. The porous nature of the outer shell facilitates the diffusion of the analytes into pre-designed electromagnetic hotspots within each of these nanostructures. A flexible SERS substrate fabricated through the uniform adsorption of nanorattles on filter paper exhibited remarkable sensitivity with a limit of detection below 10 pM of 2-napthalenethiol (2-NT). The inherent EM hotspot within each of the nanostructures obviates the need for the conventional methods of controlled aggregation or assembly of solid nanostructures to form EM hotpsots that are critical for SERS substrates exhibiting high sensitivity.

Paper-based SERS substrates discussed above lack key functionalities such as separation, chemical selectivity, and pre-concentration, which are critical to realize a versatile lab-on-chip platform. In other words, for these sensors to be able to analyse complex samples, separation abilities need to be integrated into the paper. While increasing efforts have been focused in extending functionality of the paper substrate, these developments usually involve lithographic processes or multi-layer fabrication, which is achieved at the expense of the simplicity of the paper device. We sought out to design and develop a highly sensitive label-free analytical platform that does not require any lithographic or microfabrication steps, while providing a multifunctional platform. We have demonstrated a versatile approach that allows separation and pre-concentration of the different components of a complex sample in a small surface area by taking advantage of the properties of cellulose paper and shape-enhanced capillary effect. As a proof-of-principle demonstration, paper substrates were cut into star-shaped structures and the fingers were differentially functionalized with polyelectrolytes that led to the separation of charged analytes on the surface of the paper. Furthermore, the vertices of the star-shaped paper, owing to enhanced capillary effect, served as pre-concentration sites for analytes deposited at the center of the star-shaped plasmonic paper substrates. A remarkable sub-attomolar detection of a model analyte (2-napathalenethiol) was noted at the micrometric detection spot *i.e.*, fine tips of the paper.

We have presented a systematic experimental study on the influence of AuNR dimensions on distance-dependent LSPR sensitivity and EM decay length using electrostatic LbL assembly of polyelectrolytes. Electromagnetic decay length was found to increase linearly with both AuNR length and diameter. The increase in the EM decay length with change in diameter was significantly higher (~1.29nm/nm) compared to that with change in length (~0.23 nm/nm). In contrast to earlier reports, for AuNR dimensions studied here, EM decay length did not exhibit any general trend with the aspect ratio. Knowledge of the EM decay length enables rational choice of plasmonic nanotransducers for maximizing the sensitivity of nanotransducers for a given receptor-analyte pair. The dependence of EM decay length and distance-dependent refractive index sensitivity on nanotransducer dimensions is expected to be relevant to other types of plasmonic nanostructures and LbL forms a powerful to experimentally measure the EM decay length of such nanotransducers.

Bioplasmonic paper which involves filter paper adsorbed with biofunctional AuNR, was employed for the rapid and label-free detection of aquaporin-1 (AQP1), a biomarker for early detection of renal cancer carcinoma (RCC). Bioplasmonic paper exhibited excellent spectral homogeneity, sensitivity, dynamic range and selectivity, comparable to or better than the conventional rigid LSPR substrates. Furthermore, owing to its unique flexible and conformal nature, bioplasmonic paper enables simultaneous collection and detection of trace amount of bioanalytes from real-world surfaces. Besides being highly cost-effective and environmental-friendly, the use of paper-based LSPR substrates when transformed into printable microfluidic devices will enable the detection of multiple bioanalytes in complex physiological fluids. The synergism of paper-based microfluidics and LSPR based biosensing is expected to be truly transformative by opening up novel avenues in multi-analyte biological detection.

We introduced plasmonic calligraphy approach that serves as a simple, low-cost tool for creating well-isolated test domains using functionalized plasmonic nanostructures as ink in a regular ballpoint pen. The approach suggested here obviates the need for any complex multi-step process such as formation of hydrophilic test domains and hydrophobic barriers using complex material printing approaches (usually performed using specialized material printers) to achieve multiple test domains on the same strip of paper. Plasmonic calligraphy can be extended to various shape-controlled plasmonic nanostructures with other surface functionalities to achieve arrays of chemically selective domains for analyzing complex real-world

chemical mixtures. Calligraphy approach was employed to create well-isolated test domains on paper substrates using functionalized plasmonic nanostructures as ink for multiplexed chemical sensing and label-free biosensing. Plasmonic calligraphy can serve as a powerful tool enabling the synergism of paper-based microfluidics and plasmonic chemi/biosensing, which is expected to be truly transformative by opening up novel possibilities to realize the fabrication of multi-marker paper-based biochips.

10.2 Significance and Outlook

Taken together, we believe that plasmonic paper will rapidly emerge as a highly promising analytical platform for trace detection of chemical and biological analytes. Simplicity in fabrication and usage combined with versatility in function and performance makes this a highly promising platform for numerous applications ranging from homeland security, point-of-care diagnostics, environmental monitoring, forensics, and industrial safety. The combination of plasmonic paper and handheld Raman or UV-vis spectrometers is expected to make SERS and LSPR powerful and field-deployable trace detection platforms.

References

[1] N. L. Rosi, C. A. Mirkin, *Chem Rev* **2005**, *105*, 1547.
[2] S. A. Maier, H. A. Atwater, *J Appl Phys* **2005**, *98*.
[3] J. N. Anker, W. P. Hall, O. Lyandres, N. C. Shah, J. Zhao, R. P. Van Duyne, *Nat Mater* **2008**, *7*, 442.
[4] K. M. Mayer, J. H. Hafner, *Chem Rev* **2011**, *111*, 3828.
[5] B. Sepulveda, P. C. Angelome, L. M. Lechuga, L. M. Liz-Marzan, *Nano Today* **2009**, *4*, 244.
[6] A. J. Haes, R. P. Van Duyne, *J Am Chem Soc* **2002**, *124*, 10596.
[7] J. C. Riboh, A. J. Haes, A. D. McFarland, C. R. Yonzon, R. P. Van Duyne, *J Phys Chem B* **2003**, *107*, 1772.
[8] C. R. Yonzon, E. Jeoungf, S. L. Zou, G. C. Schatz, M. Mrksich, R. P. Van Duyne, *J Am Chem Soc* **2004**, *126*, 12669.
[9] A. J. Haes, L. Chang, W. L. Klein, R. P. Van Duyne, *J Am Chem Soc* **2005**, *127*, 2264.
[10] M. Svedendahl, S. Chen, A. Dmitriev, M. Kall, *Nano Lett* **2009**, *9*, 4428.
[11] C. Novo, A. M. Funston, P. Mulvaney, *Nat Nanotechnol* **2008**, *3*, 598.
[12] J. M. Bingham, J. N. Anker, L. E. Kreno, R. P. Van Duyne, *J Am Chem Soc* **2010**, *132*, 17358.
[13] W. P. Hall, J. Modica, J. Anker, Y. Lin, M. Mrksich, R. P. Van Duynet, *Nano Lett* **2011**, *11*, 1098.
[14] K. M. Mayer, F. Hao, S. Lee, P. Nordlander, J. H. Hafner, *Nanotechnology* **2010**, *21*.
[15] C. Novo, A. M. Funston, A. K. Gooding, P. Mulvaney, *J Am Chem Soc* **2009**, *131*, 14664.
[16] R. V. Olkhov, J. D. Fowke, A. M. Shaw, *Anal Biochem* **2009**, *385*, 234.
[17] G. J. Nusz, S. M. Marinakos, A. C. Curry, A. Dahlin, F. Hook, A. Wax, A. Chilkoti, *Anal Chem* **2008**, *80*, 984.
[18] S. M. Marinakos, S. H. Chen, A. Chilkoti, *Anal Chem* **2007**, *79*, 5278.
[19] K. M. Mayer, S. Lee, H. Liao, B. C. Rostro, A. Fuentes, P. T. Scully, C. L. Nehl, J. H. Hafner, *Acs Nano* **2008**, *2*, 687.
[20] T. Sannomiya, C. Hafner, J. Voros, *Nano Lett* **2008**, *8*, 3450.
[21] S. Schultz, D. R. Smith, J. J. Mock, D. A. Schultz, *P Natl Acad Sci USA* **2000**, *97*, 996.
[22] C. Sonnichsen, B. M. Reinhard, J. Liphardt, A. P. Alivisatos, *Nat Biotechnol* **2005**, *23*, 741.
[23] C. Girard, C. Joachim, S. Gauthier, *Rep Prog Phys* **2000**, *63*, 893.
[24] L. S. Jung, C. T. Campbell, T. M. Chinowsky, M. N. Mar, S. S. Yee, *Langmuir* **1998**, *14*, 5636.
[25] B. Liedberg, I. Lundstrom, E. Stenberg, *Sensor Actuat B-Chem* **1993**, *11*, 63.
[26] K. A. Willets, R. P. Van Duyne, *Annu Rev Phys Chem* **2007**, *58*, 267.
[27] A. J. Haes, S. L. Zou, G. C. Schatz, R. P. Van Duyne, *J Phys Chem B* **2004**, *108*, 6961.
[28] A. J. Haes, S. L. Zou, G. C. Schatz, R. P. Van Duyne, *J Phys Chem B* **2004**, *108*, 109.
[29] A. V. Whitney, J. W. Elam, S. L. Zou, A. V. Zinovev, P. C. Stair, G. C. Schatz, R. P. Van Duyne, *J Phys Chem B* **2005**, *109*, 20522.
[30] E. M. Larsson, J. Alegret, M. Kall, D. S. Sutherland, *Nano Lett* **2007**, *7*, 1256.
[31] R. Bukasov, T. A. Ali, P. Nordlander, J. S. Shumaker-Parry, *Acs Nano* **2010**, *4*, 6639.
[32] M. E. Hankus, D. N. Stratis-Cullum, P. M. Pellegrino, "Towards advanced biological detection using surface enhanced raman scattering (SERS)-based sensors", 2010.
[33] E. L. Holthoff, D. N. Stratis-Cullum, M. E. Hankus, "Xerogel-based molecularly imprinted polymers for explosives detection", 2010.
[34] M. E. Hankus, B. M. Cullum, "SERS nano-imaging probes for characterizing extracellular surfaces", 2007.
[35] M. E. Hankus, G. J. Gibson, B. M. Cullum, "Characterization and optimization of novel surface-enhanced Raman scattering (SERS)-based nanoimaging probes for chemical imaging", 2005.
[36] M. E. Hankus, H. G. Li, G. J. Gibson, B. M. Cullum, *Anal Chem* **2006**, *78*, 7535.
[37] J. Sun, M. E. Hankus, B. M. Cullum, "SERS based immuno-microwell arrays for multiplexed detection of foodborne pathogenic bacteria", 2009.
[38] S. Efrima, L. Zeiri, *J Raman Spectrosc* **2009**, *40*, 277.
[39] A. A. Guzelian, J. M. Sylvia, J. A. Janni, S. L. Clauson, K. M. Spencer, "SERS of whole-cell bacteria and trace levels of biological molecules", 2002.
[40] R. M. Jarvis, R. Goodacre, *Chem Soc Rev* **2008**, *37*, 931.
[41] R. A. Tripp, R. A. Dluhy, Y. P. Zhao, *Nano Today* **2008**, *3*, 31.

[42] J. Guicheteau, L. Argue, D. Emge, A. Hyre, M. Jacobson, S. Christesen, *Appl Spectrosc* **2008**, *62*, 267.
[43] J. D. Driskell, S. Shanmukh, Y. J. Liu, S. Hennigan, L. Jones, Y. P. Zhao, R. A. Dluhy, D. C. Krause, R. A. Tripp, *Ieee Sens J* **2008**, *8*, 863.
[44] F. T. Docherty, P. B. Monaghan, C. J. McHugh, D. Graham, W. E. Smith, J. M. Cooper, *Ieee Sens J* **2005**, *5*, 632.
[45] K. Kneipp, H. Kneipp, I. Itzkan, R. R. Dasari, M. S. Feld, *Chem Phys* **1999**, *247*, 155.
[46] S. Nie, S. R. Emory, *Science* **1997**, *275*, 1102.
[47] K. Kneipp, H. Kneipp, H. G. Bohr, *Top Appl Phys* **2006**, *103*, 261.
[48] J. Kneipp, H. Kneipp, K. Kneipp, *Chem Soc Rev* **2008**, *37*, 1052.
[49] S. M. Nie, S. R. Emery, *Science* **1997**, *275*, 1102.
[50] H. Ko, S. Singamaneni, V. V. Tsukruk, *Small* **2008**, *4*, 1576.
[51] Y. W. C. Cao, R. C. Jin, C. A. Mirkin, *Science* **2002**, *297*, 1536.
[52] K. Kneipp, A. S. Haka, H. Kneipp, K. Badizadegan, N. Yoshizawa, C. Boone, K. E. Shafer-Peltier, J. T. Motz, R. R. Dasari, M. S. Feld, *Appl Spectrosc* **2002**, *56*, 150.
[53] M. C. Daniel, D. Astruc, *Chem Rev* **2004**, *104*, 293.
[54] S. Eustis, M. A. El-Sayed, *Chem Soc Rev* **2006**, *35*, 209.
[55] J. Kneipp, H. Kneipp, M. McLaughlin, D. Brown, K. Kneipp, *Nano Lett* **2006**, *6*, 2225.
[56] R. G. Freeman, K. C. Grabar, K. J. Allison, R. M. Bright, J. A. Davis, A. P. Guthrie, M. B. Hommer, M. A. Jackson, P. C. Smith, D. G. Walter, M. J. Natan, *Science* **1995**, *267*, 1629.
[57] K. C. Grabar, R. G. Freeman, M. B. Hommer, M. J. Natan, *Anal Chem* **1995**, *67*, 735.
[58] R. M. Jarvis, R. Goodacre, *Anal Chem* **2004**, *76*, 40.
[59] W. E. Doering, S. M. Nie, *J Phys Chem B* **2002**, *106*, 311.
[60] M. Moskovits, *J Raman Spectrosc* **2005**, *36*, 485.
[61] C. E. Talley, J. B. Jackson, C. Oubre, N. K. Grady, C. W. Hollars, S. M. Lane, T. R. Huser, P. Nordlander, N. J. Halas, *Nano Lett* **2005**, *5*, 1569.
[62] Z. Q. Tian, B. Ren, D. Y. Wu, *J Phys Chem B* **2002**, *106*, 9463.
[63] C. L. Haynes, R. P. Van Duyne, *J Phys Chem B* **2003**, *107*, 7426.
[64] A. D. McFarland, M. A. Young, J. A. Dieringer, R. P. Van Duyne, *J Phys Chem B* **2005**, *109*, 11279.
[65] L. D. Qin, S. L. Zou, C. Xue, A. Atkinson, G. C. Schatz, C. A. Mirkin, *P Natl Acad Sci USA* **2006**, *103*, 13300.
[66] H. Li, C. E. Baum, J. Sun, B. M. Cullum, "Multilayer enhanced SERS active materials: fabrication, characterization, and application to trace chemical detection", 2006.
[67] J. C. Hulteen, M. A. Young, R. P. Van Duyne, *Langmuir* **2006**, *22*, 10354.
[68] P. L. Stiles, J. A. Dieringer, N. C. Shah, R. R. Van Duyne, *Annu Rev Anal Chem* **2008**, *1*, 601.
[69] M. Litorja, C. L. Haynes, A. J. Haes, T. R. Jensen, R. P. Van Duyne, *J Phys Chem B* **2001**, *105*, 6907.
[70] N. Felidj, S. L. Truong, J. Aubard, G. Levi, J. R. Krenn, A. Hohenau, A. Leitner, F. R. Aussenegg, *J Chem Phys* **2004**, *120*, 7141.
[71] C. L. Haynes, C. R. Yonzon, X. Y. Zhang, R. P. Van Duyne, *J Raman Spectrosc* **2005**, *36*, 471.
[72] Y. Lu, G. L. Liu, L. P. Lee, *Nano Lett* **2005**, *5*, 5.
[73] C. R. Yonzon, D. A. Stuart, X. Y. Zhang, A. D. McFarland, C. L. Haynes, R. P. Van Duyne, *Talanta* **2005**, *67*, 438.
[74] G. Braun, S. J. Lee, M. Dante, T. Q. Nguyen, M. Moskovits, N. Reich, *J Am Chem Soc* **2007**, *129*, 6378.
[75] C. K. Klutse, H. Li, B. M. Cullum, "Optimization of multilayer surface-enhanced Raman scattering (SERS) immuno-nanosensors via self-assembled monolayer spacers", 2009.
[76] H. Li, C. E. Baum, B. M. Cullum, "Characterization of novel gold SERS substrates with multilayer enhancements", 2006.
[77] B. M. Cullum, H. Li, M. E. Hankus, M. V. Schiza, *Nanobiotechnol* **2007**, *3*, 1.
[78] A. P. Malshe, K. Virwani, K. P. Rajurkar, D. Deshpande, *Cirp Ann-Manuf Techn* **2005**, *54*, 175.
[79] R. S. Golightly, W. E. Doering, M. J. Natan, *ACS Nano* **2009**, *3*, 2859.
[80] J. Homola, *Chem Rev* **2008**, *108*, 462.
[81] X. Fang, S. R. Ahmad, *Appl Phys B-Lasers O* **2009**, *97*, 723.

[82] K. Hering, D. Cialla, K. Ackermann, T. Dorfer, R. Moller, H. Schneidewind, R. Mattheis, W. Fritzsche, P. Rosch, J. Popp, *Anal Bioanal Chem* **2008**, *390*, 113.
[83] M. E. Stewart, C. R. Anderton, L. B. Thompson, J. Maria, S. K. Gray, J. A. Rogers, R. G. Nuzzo, *Chem Rev* **2008**, *108*, 494.
[84] A. Gole, C. J. Murphy, *Langmuir* **2008**, *24*, 266.
[85] K. S. Lee, M. A. El-Sayed, *J Phys Chem B* **2005**, *109*, 20331.
[86] V. V.Tsukruk, S. Singamaneni, *Scanning Probe Microscopy of Soft Matter: Fundamentals and Practices (Wiley-VCH)* **2012**.
[87] P. H. C. Camargo, C. M. Cobley, M. Rycenga, Y. N. Xia, *Nanotechnology* **2009**, *20*.
[88] T. E. Bridges, M. P. Houlne, J. M. Harris, *Anal Chem* **2004**, *76*, 576.
[89] S. Rüttinger, V. Buschmann, B. Krämer, R. Erdmann, R. Macdonald, F. Koberling, "Determination of the confocal volume for quantitative fluorescence correlation spectroscopy", 2007.
[90] M. J. Banholzer, J. E. Millstone, L. D. Qin, C. A. Mirkin, *Chem Soc Rev* **2008**, *37*, 885.
[91] J. P. Camden, J. A. Dieringer, J. Zhao, R. P. Van Duyne, *Accounts Chem Res* **2008**, *41*, 1653.
[92] H. Im, K. C. Bantz, N. C. Lindquist, C. L. Haynes, S. H. Oh, *Nano Lett* **2010**, *10*, 2231.
[93] P. Tessier, O. D. Velev, A. T. Kalambur, A. M. Lenhoff, J. F. Rabolt, E. W. Kaler, *Adv Mater* **2001**, *13*, 396.
[94] A. Tao, F. Kim, C. Hess, J. Goldberger, R. R. He, Y. G. Sun, Y. N. Xia, P. D. Yang, *Nano Lett* **2003**, *3*, 1229.
[95] S. H. Chang, H. H. Ko, S. Singamaneni, R. Gunawidjaja, V. V. Tsukruk, *Anal Chem* **2009**, *81*, 5740.
[96] A. G. Brolo, E. Arctander, R. Gordon, B. Leathem, K. L. Kavanagh, *Nano Lett* **2004**, *4*, 2015.
[97] H. Ko, S. Chang, V. V. Tsukruk, *Acs Nano* **2009**, *3*, 181.
[98] D. S. Moore, *Rev Sci Instrum* **2004**, *75*, 2499.
[99] D. Martinak, A. Rudolph, *Proc. IEEE 31st Annual 1997 International Conference on Security Technology* **1997**, 2.
[100] D. Wu, Y. Fang, *J Colloid Interf Sci* **2003**, *265*, 234.
[101] L. M. Cabalin, J. J. Laserna, *Anal Chim Acta* **1995**, *310*, 337.
[102] M. A. El-Sayed, *Accounts Chem Res* **2001**, *34*, 257.
[103] C. D. Chen, S. F. Cheng, L. K. Chau, C. R. C. Wang, *Biosens Bioelectron* **2007**, *22*, 926.
[104] M. A. S. A. Samir, F. Alloin, A. Dufresne, *Biomacromolecules* **2005**, *6*, 612.
[105] R. Derda, A. Laromaine, A. Mammoto, S. K. Y. Tang, T. Mammoto, D. E. Ingber, G. M. Whitesides, *P Natl Acad Sci USA* **2009**, *106*, 18457.
[106] A. W. Martinez, S. T. Phillips, M. J. Butte, G. M. Whitesides, *Angew Chem Int Edit* **2007**, *46*, 1318.
[107] W. A. Zhao, A. van den Berg, *Lab Chip* **2008**, *8*, 1988.
[108] C. M. Cheng, A. W. Martinez, J. L. Gong, C. R. Mace, S. T. Phillips, E. Carrilho, K. A. Mirica, G. M. Whitesides, *Angew Chem Int Edit* **2010**, *49*, 4771.
[109] A. W. Martinez, S. T. Phillips, G. M. Whitesides, E. Carrilho, *Anal Chem* **2010**, *82*, 3.
[110] M. W. Rutland, J. L. Parker, *Langmuir* **1994**, *10*, 1110.
[111] H. Y. Koo, W. S. Choi, D. Y. Kim, *Small* **2008**, *4*, 742.
[112] Y. Habibi, L. A. Lucia, O. J. Rojas, *Chem Rev* **2010**, *110*, 3479.
[113] S. H. Cho, H. S. Han, D. J. Jang, K. Kim, M. S. Kim, *J Phys Chem-Us* **1995**, *99*, 10594.
[114] S. W. Joo, S. W. Han, K. Kim, *J Colloid Interf Sci* **2001**, *240*, 391.
[115] T. Chen, H. Wang, G. Chen, Y. Wang, Y. H. Feng, W. S. Teo, T. Wu, H. Y. Chen, *Acs Nano* **2010**, *4*, 3087.
[116] Y. J. Lee, T. C. Jeon, W. K. Paik, K. Kim, *Langmuir* **1996**, *12*, 5830.
[117] K. L. Kelly, E. Coronado, L. L. Zhao, G. C. Schatz, *J Phys Chem B* **2003**, *107*, 668.
[118] A. M. Alkilany, C. J. Murphy, *J Nanopart Res* **2010**, *12*, 2313.
[119] H. Takahashi, Y. Niidome, T. Niidome, K. Kaneko, H. Kawasaki, S. Yamada, *Langmuir* **2005**, *22*, 2.
[120] A. W. Martinez, S. T. Phillips, G. M. Whitesides, *P Natl Acad Sci USA* **2008**, *105*, 19606.
[121] A. Campion, P. Kambhampati, *Chem. Soc. Rev.* **1998**, *27*, 241.
[122] R. M. Jarvis, R. Goodacre, *Chem Soc Rev* **2008**, *37*, 931.
[123] M. Moskovits, *J. Raman Spectrosc.* **2005**, *36*, 485.
[124] J. Homola, *Chem. Rev.* **2008**, *108*, 462.
[125] X. Fang, S. R. Ahmad, *Appl. Phys. B* **2009**, *97*, 723.

[126] K. Hering, D. Cialla, K. Ackermann, T. Dörfer, R. Möller, H. Schneidewind, R. Mattheis, W. Fritzsche, P. Rösch, J. Popp, *Anal. Bioanal.Chem.* **2008**, *390*, 113.
[127] M. Quinten, A. Leitner, J. R. Krenn, F. R. Aussenegg, *Opt Lett* **1998**, *23*, 1331.
[128] S. A. Maier, M. L. Brongersma, P. G. Kik, S. Meltzer, A. A. G. Requicha, H. A. Atwater, *Adv Mater* **2001**, *13*, 1501.
[129] J. R. Krenn, A. Dereux, J. C. Weeber, E. Bourillot, Y. Lacroute, J. P. Goudonnet, G. Schider, W. Gotschy, A. Leitner, F. R. Aussenegg, C. Girard, *Physical Review Letters* **1999**, *82*, 2590.
[130] S. A. Maier, P. G. Kik, H. A. Atwater, *Appl Phys Lett* **2002**, *81*, 1714.
[131] Q. H. Wei, K. H. Su, S. Durant, X. Zhang, *Nano Lett* **2004**, *4*, 1067.
[132] J. C. Hulteen, R. P. Vanduyne, *J Vac Sci Technol A* **1995**, *13*, 1553.
[133] J. C. Hulteen, D. A. Treichel, M. T. Smith, M. L. Duval, T. R. Jensen, R. P. Van Duyne, *J Phys Chem B* **1999**, *103*, 3854.
[134] C. P. Collier, R. J. Saykally, J. J. Shiang, S. E. Henrichs, J. R. Heath, *Science* **1997**, *277*, 1978.
[135] S. Paul, C. Pearson, A. Molloy, M. A. Cousins, M. Green, S. Kolliopoulou, P. Dimitrakis, P. Normand, D. Tsoukalas, M. C. Petty, *Nano Lett* **2003**, *3*, 533.
[136] H. W. Liu, L. Zhang, X. Y. Lang, Y. Yamaguchi, H. S. Iwasaki, Y. S. Inouye, Q. K. Xue, M. W. Chen, *Sci Rep-Uk* **2011**, *1*.
[137] A. Tittl, X. H. Yin, H. Giessen, X. D. Tian, Z. Q. Tian, C. Kremers, D. N. Chigrin, N. Liu, *Nano Letters* **2013**, *13*, 1816.
[138] E. C. Le Ru, P. G. Etchegoin, *Annual Review of Physical Chemistry, Vol 63* **2012**, *63*, 65.
[139] C. H. Lee, L. M. Tian, A. Abbas, R. Kattumenu, S. Singamaneni, *Nanotechnology* **2011**, *22*.
[140] D.-F. Zhang, Q. Zhang, L.-Y. Niu, L. Jiang, P.-G. Yin, L. Guo, *J Nanopart Res* **2011**, *13*, 3923.
[141] F. L. Yap, P. Thoniyot, S. Krishnan, S. Krishnamoorthy, *Acs Nano* **2012**, *6*, 2056.
[142] N. Gandra, A. Abbas, L. Tian, S. Singamaneni, *Nano Lett* **2012**, *12*, 2645.
[143] J. Ye, F. Wen, H. Sobhani, J. B. Lassiter, P. V. Dorpe, P. Nordlander, N. J. Halas, *Nano Lett* **2012**, *12*, 1660.
[144] L. Li, T. Hutter, U. Steiner, S. Mahajan, *Analyst* **2013**, *138*, 4574.
[145] Y. Li, N. Koshizaki, H. Q. Wang, Y. Shimizu, *Acs Nano* **2011**, *5*, 9403.
[146] N. Gandra, S. Singamaneni, *Adv Mater* **2013**, *25*, 1022.
[147] J. J. Mock, R. T. Hill, A. Degiron, S. Zauscher, A. Chilkoti, D. R. Smith, *Nano Letters* **2008**, *8*, 2245.
[148] C. C. Li, K. L. Shuford, Q. H. Park, W. P. Cai, Y. Li, E. J. Lee, S. O. Cho, *Angew Chem Int Edit* **2007**, *46*, 3264.
[149] S. E. Skrabalak, L. Au, X. D. Li, Y. N. Xia, *Nat Protoc* **2007**, *2*, 2182.
[150] P. N. Sisco, C. J. Murphy, *The Journal of Physical Chemistry A* **2009**, *113*, 3973.
[151] K. S. Yee, *IEEE Trans. Antennas Propag.*, *14*, 302.
[152] E. D. Palik, Ed. *Handbook of Optical Constantsof Solids*, MA: Academic, Boston 1985.
[153] S. E. Skrabalak, J. Chen, Y. Sun, X. Lu, L. Au, C. M. Cobley, Y. Xia, *Accounts Chem Res* **2008**, *41*, 1587.
[154] X. Xia, J. Zeng, L. K. Oetjen, Q. Li, Y. Xia, *J Am Chem Soc* **2011**, *134*, 1793.
[155] R. A. Alvarez-Puebla, D. S. Dos Santos, R. F. Aroca, *Analyst* **2004**, *129*, 1251.
[156] N. Gandra, C. Portz, S. Singamaneni, *Adv Mater* **2014**, *26*, 424.
[157] J. M. McLellan, Z. Y. Li, A. R. Siekkinen, Y. N. Xia, *Nano Lett* **2007**, *7*, 1013.
[158] C. H. Lee, L. M. Tian, S. Singamaneni, *Acs Appl Mater Inter* **2010**, *2*, 3429.
[159] C. H. Lee, M. E. Hankus, L. Tian, P. M. Pellegrino, S. Singamaneni, *Analytical Chemistry* **2011**, *83*, 8953.
[160] A. Abbas, A. Brimer, J. M. Slocik, L. M. Tian, R. R. Naik, S. Singamaneni, *Anal Chem* **2013**, *85*, 3977.
[161] S. Z. Nergiz, N. Gandra, M. E. Farrell, L. M. Tian, P. M. Pellegrino, S. Singamaneni, *J Mater Chem A* **2013**, *1*, 6543.
[162] W. W. Yu, I. M. White, *Anal Chem* **2010**, *82*, 9626.
[163] W. W. Yu, I. M. White, *Analyst* **2013**, *138*, 1020.
[164] I. Pastoriza-Santos, J. Perez-Juste, L. M. Liz-Marzan, *Chem Mater* **2006**, *18*, 2465.
[165] H. M. F. Freundlich, *J. Phys. Chem.* **1906**, *57* 385.
[166] K. Y. Foo, B. H. Hameed, *Chem Eng J* **2010**, *156*, 2.
[167] A. P. G. A.W. Adamson, **1997**.

[168] M. E. Hankus, D. N. Stratis-Cullum, P. M. Pellegrino, *ARL-TR-4957 September* **2009**.
[169] A. W. Martinez, S. T. Phillips, G. M. Whitesides, E. Carrilho, *Anal Chem* **2010**, *82*, 3.
[170] A. W. Martinez, S. T. Phillips, E. Carrilho, S. W. Thomas, H. Sindi, G. M. Whitesides, *Anal Chem* **2008**, *80*, 3699.
[171] A. K. Ellerbee, S. T. Phillips, A. C. Siegel, K. A. Mirica, A. W. Martinez, P. Striehl, N. Jain, M. Prentiss, G. M. Whitesides, *Anal Chem* **2009**, *81*, 8447.
[172] Z. Nie, C. A. Nijhuis, J. Gong, X. Chen, A. Kumachev, A. W. Martinez, M. Narovlyansky, G. M. Whitesides, *Lab Chip* **2010**, *10*, 477.
[173] S. Ge, L. Ge, M. Yan, X. Song, J. Yu, J. Huang, *Chemical Communications* **2012**, *48*, 9397.
[174] N. Godino, R. Gorkin, K. Bourke, J. Ducree, *Lab Chip* **2012**, *12*, 3281.
[175] L. Wang, W. Chen, D. Xu, B. S. Shim, Y. Zhu, F. Sun, L. Liu, C. Peng, Z. Jin, C. Xu, N. A. Kotov, *Nano Lett* **2009**, *9*, 4147.
[176] L. Ge, S. Wang, X. Song, S. Ge, J. Yu, *Lab Chip* **2012**.
[177] F. Xiao, Y. Li, X. Zan, K. Liao, R. Xu, H. Duan, *Advanced Functional Materials* **2012**, *22*, 2487.
[178] W. W. Yu, I. M. White, *Analytical chemistry* **2010**, *82*, 9626.
[179] C. H. Lee, L. Tian, S. Singamaneni, *ACS Appl Mater Interfaces* **2010**, *2*, 3429.
[180] W. W. Yu, I. M. White, *Analyst* **2012**.
[181] B. R. Lutz, P. Trinh, C. Ball, E. Fu, P. Yager, *Lab Chip* **2011**, *11*, 4274.
[182] J. L. Osborn, B. Lutz, E. Fu, P. Kauffman, D. Y. Stevens, P. Yager, *Lab Chip* **2010**, *10*, 2659.
[183] E. Fu, B. Lutz, P. Kauffman, P. Yager, *Lab Chip* **2010**, *10*, 918.
[184] T. Songjaroen, W. Dungchai, O. Chailapakul, C. S. Henry, W. Laiwattanapaisal, *Lab Chip* **2012**.
[185] L. Tian, J. J. Morrissey, R. Kattumenu, N. Gandra, E. D. Kharasch, S. Singamaneni, *Anal Chem* **2012**, *84*, 9928.
[186] J. Yu, L. Ge, J. Huang, S. Wang, S. Ge, *Lab Chip* **2011**, *11*, 1286.
[187] H. Liu, Y. Xiang, Y. Lu, R. M. Crooks, *Angew Chem Int Ed Engl* **2012**, *51*, 6925.
[188] A. W. Martinez, S. T. Phillips, M. J. Butte, G. M. Whitesides, *Angewandte Chemie International Edition* **2007**, *46*, 1318.
[189] K. Abe, K. Suzuki, D. Citterio, *Anal Chem* **2008**, *80*, 6928.
[190] G. Aragay, H. Monton, J. Pons, M. Font-Bardia, A. Merkoci, *Journal of Materials Chemistry* **2012**, *22*, 5978.
[191] S. M. Z. Hossain, J. D. Brennan, *Anal Chem* **2011**, *83*, 8772.
[192] J. C. Jokerst, J. A. Adkins, B. Bisha, M. M. Mentele, L. D. Goodridge, C. S. Henry, *Anal Chem* **2012**, *84*, 2900.
[193] X. Wu, H. Kuang, C. Hao, C. Xing, L. Wang, C. Xu, *Biosensors and Bioelectronics* **2012**, *33*, 309.
[194] H. Hwang, S.-H. Kim, T.-H. Kim, J.-K. Park, Y.-K. Cho, *Lab Chip* **2011**, *11*, 3404.
[195] X. H. Huang, S. Neretina, M. A. El-Sayed, *Adv Mater* **2009**, *21*, 4880.
[196] L. Vigderman, B. P. Khanal, E. R. Zubarev, *Adv Mater* **2012**, *24*, 4811.
[197] A. Abbas, L. Tian, J. Morrissey, E. D. Kharasch, S. Singamaneni, *Advanced Functional Materials* **2012**.
[198] A. Abbas, M. Fei, L. Tian, S. Singamaneni, *Plasmonics* **2012**.
[199] N. Gandra, A. Abbas, L. M. Tian, S. Singamaneni, *Nano Lett* **2012**, *12*, 2645.
[200] P. L. Stiles, J. A. Dieringer, N. C. Shah, R. P. Van Duyne, *Annu Rev Anal Chem* **2008**, *1*, 601.
[201] J. Kneipp, H. Kneipp, K. Kneipp, *Chem Soc Rev* **2008**, *37*, 1052.
[202] K. Kneipp, H. Kneipp, I. Itzkan, R. R. Dasari, M. S. Feld, *Chem. Phys.* **1999**, *247*, 155.
[203] R. Botta, G. Upender, R. Sathyavathi, D. N. Rao, C. Bansal, *Mater Chem Phys* **2013**, *137*, 699.
[204] W. E. Doering, S. Nie, *J. Phys. Chem. B* **2001**, *106*, 311.
[205] C. E. Talley, J. B. Jackson, C. Oubre, N. K. Grady, C. W. Hollars, S. M. Lane, T. R. Huser, P. Nordlander, N. J. Halas, *Nano Lett.* **2005**, *5*, 1569.
[206] K. A. Willets, R. P. Van Duyne, *Annu. Rev. Phys. Chem.* **2007**, *58*, 267.
[207] C. L. Haynes, R. P. Van Duyne, *J. Phys. Chem. B* **2003**, *107*, 7426.
[208] A. D. McFarland, M. A. Young, J. A. Dieringer, R. P. Van Duyne, *J. Phys. Chem. B* **2005**, *109*, 11279.
[209] L. Qin, S. Zou, C. Xue, A. Atkinson, G. C. Schatz, C. A. Mirkin, *Proc. Natl. Acad. Sci. U.S.A.* **2006**, *103*, 13300.
[210] R. Kattumenu, C. H. Lee, L. M. Tian, M. E. McConney, S. Singamaneni, *Journal of Materials Chemistry* **2011**, *21*, 15218.

[211] N. Gandra, A. Abbas, L. M. Tian, S. Singamaneni, *Nano Lett* **2012**, *12*, 2645.
[212] K. Bhatt, S. S. Tan, S. Karumuri, A. K. Kalkan, *Nano Lett.* **2010**, *10*, 3880.
[213] A. Y. Panarin, S. N. Terekhov, K. I. Kholostov, V. P. Bondarenko, *Appl Surf Sci* **2010**, *256*, 6969.
[214] S. Y. Baik, Y. J. Cho, Y. R. Lim, H. S. Im, D. M. Jang, Y. Myung, J. Park, H. S. Kang, *Acs Nano* **2012**, *6*, 2459.
[215] S. Z. Nergiz, N. Gandra, M. E. Farrell, L. Tian, P. M. Pellegrino, S. Singamaneni, *J. Mater. Chem. A* **2013**, *1*, 6543.
[216] A. Abbas, A. Brimer, J. M. Slocik, L. Tian, R. R. Naik, S. Singamaneni, *Anal Chem* **2013**, *85*, 3977.
[217] Z. Nie, C. A. Nijhuis, J. Gong, X. Chen, A. Kumachev, A. W. Martinez, M. Narovlyansky, G. M. Whitesides, *Lab Chip* **2010**, *10*, 477.
[218] S. Ge, L. Ge, M. Yan, X. Song, J. Yu, J. Huang, *Chem. Commun.* **2012**, *48*, 9397.
[219] C. Parolo, A. Merkoci, *Chem. Soc. Rev.* **2013**, *42*, 450.
[220] A. W. Martinez, S. T. Phillips, G. M. Whitesides, E. Carrilho, *Anal. Chem.* **2009**, *82*, 3.
[221] L. M. Tian, J. J. Morrissey, R. Kattumenu, N. Gandra, E. D. Kharasch, S. Singamaneni, *Anal Chem* **2012**, *84*, 9928.
[222] K. Kim, H. B. Lee, J. K. Yoon, D. Shin, K. S. Shin, *The Journal of Physical Chemistry C* **2010**, *114*, 13589.
[223] C. H. Lee, M. E. Hankus, L. Tian, P. M. Pellegrino, S. Singamaneni, *Anal. Chem.* **2011**, *83*, 8953.
[224] A. Abbas, L. Tian, J. J. Morrissey, E. D. Kharasch, S. Singamaneni, *Advanced Functional Materials* **2013**, *23*, 1789.
[225] W. W. Yu, I. M. White, *Analyst* **2012**, *137*, 1168.
[226] L. Tian, S. Tadepalli, S. Hyun Park, K. K. Liu, J. J. Morrissey, E. D. Kharasch, R. R. Naik, S. Singamaneni, *Biosens Bioelectron* **2014**, *59C*, 208.
[227] I. Pastoriza-Santos, J. Perez-Juste, L. M. Liz-Marzan, *Chem Mater* **2006**, *18*, 2465.
[228] G. J. Nusz, A. C. Curry, S. M. Marinakos, A. Wax, A. Chilkoti, *Acs Nano* **2009**, *3*, 795.
[229] L. M. Tian, M. Fei, R. Kattumenu, A. Abbas, S. Singamaneni, *Nanotechnology* **2012**, *23*.
[230] A. Abbas, L. M. Tian, R. Kattumenu, A. Halim, S. Singamaneni, *Chemical Communications* **2012**, *48*, 1677.
[231] A. Abbas, L. M. Tian, J. J. Morrissey, E. D. Kharasch, S. Singamaneni, *Advanced Functional Materials* **2013**, *23*, 1789.
[232] C. J. Orendorff, C. J. Murphy, *J. Phys. Chem. B* **2006**, *110*, 3990.
[233] X. H. Huang, S. Neretina, M. A. El-Sayed, *Adv Mater* **2009**, *21*, 4880.
[234] A. Abbas, L. Tian, R. Kattumenu, A. Halim, S. Singamaneni, *Chem. Commun.* **2012**, *48*, 1677.
[235] H. Gostony, S. L. Schneider, *Schiffer Publishing, PA, USA* **1998**.
[236] A. Russo, B. Y. Ahn, J. J. Adams, E. B. Duoss, J. T. Bernhard, J. A. Lewis, *Adv. Mater.* **2011**, *23*, 3426.
[237] M. Z. Si, Y. P. Kang, Z. G. Zhang, *Appl Surf Sci* **2009**, *255*, 6007.
[238] T. Vosgröne, A. J. Meixner, *ChemPhysChem* **2005**, *6*, 154.
[239] M. S. Maier, *Plasmonics: Fundamentals and Applications (1st ed., Springer: New York)* **2007**.
[240] E. Ozbay, *Science* **2006**, *311*, 189.
[241] B. M. Reinhard, M. Siu, H. Agarwal, A. P. Alivisatos, J. Liphardt, *Nano Lett* **2005**, *5*, 2246.
[242] B. Liedberg, I. Lundström, E. Stenberg, *Sensors and Actuators B: Chemical* **1993**, *11*, 63.
[243] O. Kedem, A. B. Tesler, A. Vaskevich, I. Rubinstein, *Acs Nano* **2011**, *5*, 748.
[244] C. Yu, J. Irudayaraj, *Biophys J* **2007**, *93*, 3684.
[245] C. Wang, J. Irudayaraj, *Small* **2008**, *4*, 2204.
[246] C. X. Yu, H. Nakshatri, J. Irudayaraj, *Nano Lett* **2007**, *7*, 2300.
[247] H. Huang, C. C. He, Y. L. Zeng, X. D. Xia, X. Y. Yu, P. G. Yi, Z. Chen, *Biosens Bioelectron* **2009**, *24*, 2255.
[248] H. Takahashi, Y. Niidome, S. Yamada, *Chemical Communications* **2005**, 2247.
[249] E. C. Dreaden, A. M. Alkilany, X. H. Huang, C. J. Murphy, M. A. El-Sayed, *Chem Soc Rev* **2012**, *41*, 2740.
[250] A. M. Alkilany, L. B. Thompson, S. P. Boulos, P. N. Sisco, C. J. Murphy, *Adv Drug Deliver Rev* **2012**, *64*, 190.
[251] T. R. Kuo, V. A. Hovhannisyan, Y. C. Chao, S. L. Chao, S. J. Chiang, S. J. Lin, C. Y. Dong, C. C. Chen, *J Am Chem Soc* **2010**, *132*, 14163.

[252] S. E. Lee, D. Y. Sasaki, T. D. Perroud, D. Yoo, K. D. Patel, L. P. Lee, *J Am Chem Soc* **2009**, *131*, 14066.
[253] A. K. Salem, P. C. Searson, K. W. Leong, *Nat Mater* **2003**, *2*, 668.
[254] E. T. Castellana, R. C. Gamez, D. H. Russell, *J Am Chem Soc* **2011**, *133*, 4182.
[255] G. W. Lu, L. Hou, T. Y. Zhang, W. Q. Li, J. Liu, P. Perriat, Q. H. Gong, *J Phys Chem C* **2011**, *115*, 22877.
[256] W. Ni, X. Kou, Z. Yang, J. F. Wang, *Acs Nano* **2008**, *2*, 677.
[257] C. J. Orendorff, C. J. Murphy, *J Phys Chem B* **2006**, *110*, 3990.
[258] R. Gans, *Annalen der Physik* **1915**, *352*, 270.
[259] B. H. Yan, Y. Yang, Y. C. Wang, *J Phys Chem B* **2003**, *107*, 9159.
[260] S. Link, M. B. Mohamed, M. A. El-Sayed, *J Phys Chem B* **1999**, *103*, 3073.
[261] A. Brioude, X. C. Jiang, M. P. Pileni, *J Phys Chem B* **2005**, *109*, 13138.
[262] S. Z. Nergiz, S. Singamaneni, *Acs Appl Mater Inter* **2011**, *3*, 945.
[263] S. Malynych, I. Luzinov, G. Chumanov, *J Phys Chem B* **2002**, *106*, 1280.
[264] A. A. Antipov, G. B. Sukhorukov, H. Mohwald, *Langmuir* **2003**, *19*, 2444.
[265] G. Decher, *Science* **1997**, *277*, 1232.
[266] J. Park, L. D. Fouche, P. T. Hammond, *Adv Mater* **2005**, *17*, 2575.
[267] S. T. Dubas, J. B. Schlenoff, *Langmuir* **2001**, *17*, 7725.
[268] G. Decher, J. D. Hong, J. Schmitt, *Thin Solid Films* **1992**, *210*, 831.
[269] V. W. Jones, J. R. Kenseth, M. D. Porter, C. L. Mosher, E. Henderson, *Anal Chem* **1998**, *70*, 1233.
[270] O. Ouerghi, A. Touhami, A. Othmane, H. Ben Ouada, C. Martelet, C. Fretigny, N. Jaffrezic-Renault, *Sensor Actuat B-Chem* **2002**, *84*, 167.
[271] N. Howlader, A. M.Noone, M. Krapcho, N. Neyman, R. Aminou, S. F. Altekruse, C. L. Kosary, J. Ruhl, Z. Tatalovich, H. Cho, A. Mariotto, M. P. Eisner, D. R. Lewis, H. S. Chen, E. J. Feuer, e. K. A. Cronin, *SEER Cancer Statistics Review, 1975-2009 (Vintage 2009 Populations), National Cancer Institute. Bethesda, MD*.
[272] J. J. Morrissey, A. N. London, J. Q. Luo, E. D. Kharasch, *Mayo Clin Proc* **2010**, *85*, 413.
[273] N. A. Cinel, S. Butun, E. Ozbay, *Opt Express* **2012**, *20*, 2587.
[274] S. Kim, J. M. Jung, D. G. Choi, H. T. Jung, S. M. Yang, *Langmuir* **2006**, *22*, 7109.
[275] C. Parolo, A. Merkoci, *Chemical Society Reviews* **2013**, *42*, 450.
[276] X. Li, D. R. Ballerini, W. Shen, *Biomicrofluidics* **2012**, *6*.
[277] X. Li, J. F. Tian, W. Shen, *Cellulose* **2010**, *17*, 649.
[278] M. J. Uddin, F. Cesano, D. Scarano, F. Bonino, G. Agostini, G. Spoto, S. Bordiga, A. Zecchina, *J Photoch Photobio A* **2008**, *199*, 64.
[279] X. Geng, C. Filipe, R. Pelton, *Appita J* **2008**, *61*, 456.
[280] W. A. Zhao, M. M. Ali, S. D. Aguirre, M. A. Brook, Y. F. Li, *Anal Chem* **2008**, *80*, 8431.
[281] C. H. Lee, L. Tian, S. Singamaneni, *Acs Appl Mater Inter* **2010**, *2*, 3429.
[282] R. Tankhiwale, S. K. Bajpai, *Colloids and Surfaces B: Biointerfaces* **2009**, *69*, 164.
[283] K.-S. Lee, M. A. El-Sayed, *The Journal of Physical Chemistry B* **2005**, *109*, 20331.
[284] A. Gole, C. J. Murphy, *Langmuir* **2007**, *24*, 266.
[285] O. Ouerghi, A. Touhami, A. Othmane, H. Ben Ouada, C. Martelet, C. Fretigny, N. Jaffrezic-Renault, *Sensors and Actuators B: Chemical* **2002**, *84*, 167.
[286] C.-D. Chen, S.-F. Cheng, L.-K. Chau, C. R. C. Wang, *Biosensors and Bioelectronics* **2007**, *22*, 926.
[287] *Product data sheet of ImmunoPure Goat Anti-Ribbit IgG, Thermo Scientific.*
[288] J. J. Morrissey, E. D. Kharasch, *Unpublished*.
[289] X. Li, D. R. Ballerini, W. Shen, *Biomicrofluidics* **2012**, *6*, 011301.
[290] X. Li, J. Tian, W. Shen, *Cellulose* **2010**, *17*, 649.
[291] A. W. Martinez, S. T. Phillips, M. J. Butte, G. M. Whitesides, *Angew. Chem. Int. Ed.* **2007**, *46*, 1318.
[292] H. Chen, X. Kou, Z. Yang, W. Ni, J. Wang, *Langmuir* **2008**, *24*, 5233.
[293] C.-M. Cheng, A. W. Martinez, J. Gong, C. R. Mace, S. T. Phillips, E. Carrilho, K. A. Mirica, G. M. Whitesides, *Angew. Chem. Int. Ed.* **2010**, *49*, 4771.
[294] L. Tian, J. J. Morrissey, R. Kattumenu, N. Gandra, E. D. Kharasch, S. Singamaneni, *Anal. Chem.* **2012**, *84*, 9928.

[295] J. Huang, H. Zhu, Y. Chen, C. Preston, K. Rohrbach, J. Cumings, L. Hu, *Acs Nano* **2013**, *7*, 2106.
[296] S. Z. Nergiz, N. Gandra, M. E. Farrell, L. Tian, P. M. Pellegrino, S. Singamaneni, *Journal of Materials Chemistry A* **2013**, *1*, 6543.
[297] G. G. Lewis, M. J. DiTucci, S. T. Phillips, *Angew. Chem. Int. Ed.* **2012**, *51*, 12707.
[298] E. Carrilho, A. W. Martinez, G. M. Whitesides, *Anal. Chem.* **2009**, *81*, 7091.
[299] D. A. Bruzewicz, M. Reches, G. M. Whitesides, *Anal. Chem.* **2008**, *80*, 3387.
[300] J. L. Osborn, B. Lutz, E. Fu, P. Kauffman, D. Y. Stevens, P. Yager, *Lab Chip* **2010**, *10*, 2659.
[301] H. Noh, S. T. Phillips, *Anal. Chem.* **2010**, *82*, 4181.
[302] K. Abe, K. Suzuki, D. Citterio, *Anal. Chem.* **2008**, *80*, 6928.
[303] J. Olkkonen, K. Lehtinen, T. Erho, *Anal. Chem.* **2010**, *82*, 10246.
[304] L.-L. Qu, D.-W. Li, J.-Q. Xue, W.-L. Zhai, J. S. Fossey, Y.-T. Long, *Lab Chip* **2012**, *12*, 876.
[305] B. Sepúlveda, P. C. Angelomé, L. M. Lechuga, L. M. Liz-Marzán, *Nano Today* **2009**, *4*, 244.
[306] A. J. Haes, R. P. Van Duyne, *J. Am. Chem. Soc.* **2002**, *124*, 10596.
[307] J. C. Riboh, A. J. Haes, A. D. McFarland, C. Ranjit Yonzon, R. P. Van Duyne, *J. Phys. Chem. B* **2003**, *107*, 1772.
[308] A. J. Haes, L. Chang, W. L. Klein, R. P. Van Duyne, *J. Am. Chem. Soc.* **2005**, *127*, 2264.
[309] M. Svedendahl, S. Chen, A. Dmitriev, M. Käll, *Nano Lett.* **2009**, *9*, 4428.
[310] C. R. Yonzon, E. Jeoung, S. Zou, G. C. Schatz, M. Mrksich, R. P. Van Duyne, *J. Am. Chem. Soc.* **2004**, *126*, 12669.
[311] N. L. Rosi, C. A. Mirkin, *Chem. Rev.* **2005**, *105*, 1547.
[312] S. A. Maier, H. A. Atwater, *J. Appl. Phys.* **2005**, *98*, 011101.
[313] J. N. Anker, W. P. Hall, O. Lyandres, N. C. Shah, J. Zhao, R. P. Van Duyne, *Nat. Mater.* **2008**, *7*, 11.
[314] K. M. Mayer, J. H. Hafner, *Chem. Rev.* **2011**, *111*, 3828.
[315] P. Englebienne, *Analyst* **1998**, *123*, 1599.
[316] R. Kattumenu, C. H. Lee, L. Tian, M. E. McConney, S. Singamaneni, *Journal of Materials Chemistry* **2011**, *21*, 15218.
[317] I. Pastoriza-Santos, J. Pérez-Juste, L. M. Liz-Marzán, *Chem. Mater.* **2006**, *18*, 2465.
[318] L. Tian, E. Chen, N. Gandra, A. Abbas, S. Singamaneni, *Langmuir* **2012**, *28*, 17435.
[319] L. Tian, M. Fei, R. Kattumenu, A. Abbas, S. Singamaneni, *Nanotechnology* **2012**, *23*, 255502.
[320] X. Huang, S. Neretina, M. A. El-Sayed, *Adv. Mater.* **2009**, *21*, 4880.
[321] A. Abbas, A. Brimer, J. M. Slocik, L. Tian, R. R. Naik, S. Singamaneni, *Anal. Chem.* **2013**, *85*, 3977.
[322] E. Dulkeith, A. C. Morteani, T. Niedereichholz, T. A. Klar, J. Feldmann, S. A. Levi, F. C. J. M. van Veggel, D. N. Reinhoudt, M. Möller, D. I. Gittins, *Phys. Rev. Lett.* **2002**, *89*, 203002.
[323] K. Kang, J. Wang, J. Jasinski, S. Achilefu, *J Nanobiotechnology* **2011**, *9*, 16.
[324] M. Rycenga, M. R. Langille, M. L. Personick, T. Ozel, C. A. Mirkin, *Nano Lett.* **2012**, *12*, 6218.
[325] J. H. Wiley, R. H. Atalla, *Carbohyd Res* **1987**, *160*, 113.
[326] G. Socrates, *Wiley: New York* **2001**.
[327] R. A. Alvarez-Puebla, D. S. Dos Santos Jr, R. F. Aroca, *Analyst* **2004**, *129*, 1251.
[328] J. Wang, B. Yiu, J. Obermeyer, C. D. M. Filipe, J. D. Brennan, R. Pelton, *Biomacromolecules* **2012**, *13*, 559.

Supporting Information: **Paper based Flexible and Conformal SERS Susbstrate for Rapid Trace Detection on Real-world Surfaces**

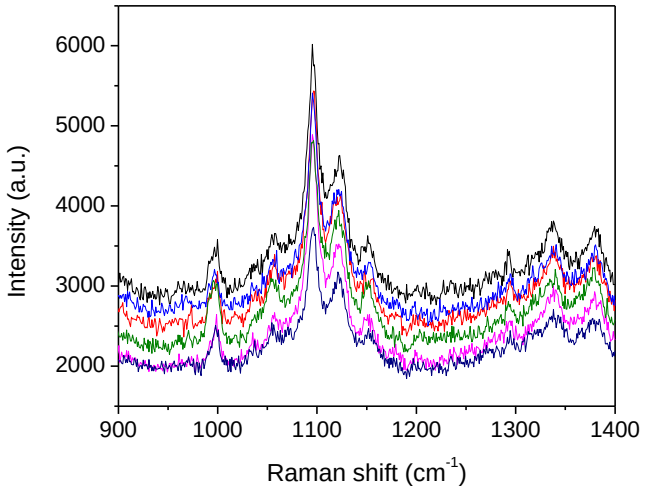

Figure S1.1: Raman spectra of filter paper (Whatman No. 1 grade) collected at six different locations showing the remarkable uniformity of paper

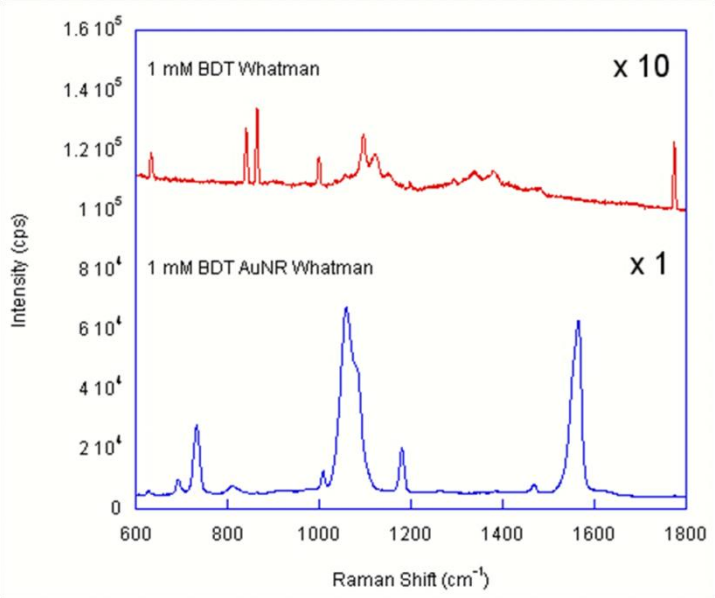

Figure S1.2: Raman spectra of pristine filter paper and that loaded with AuNRs, both treated with 1 mM of 1,4-BDT. Pristine paper shows no Raman enhancement while that loaded with AuNRs show very strong Raman enhanced 1,4-BDT peaks.

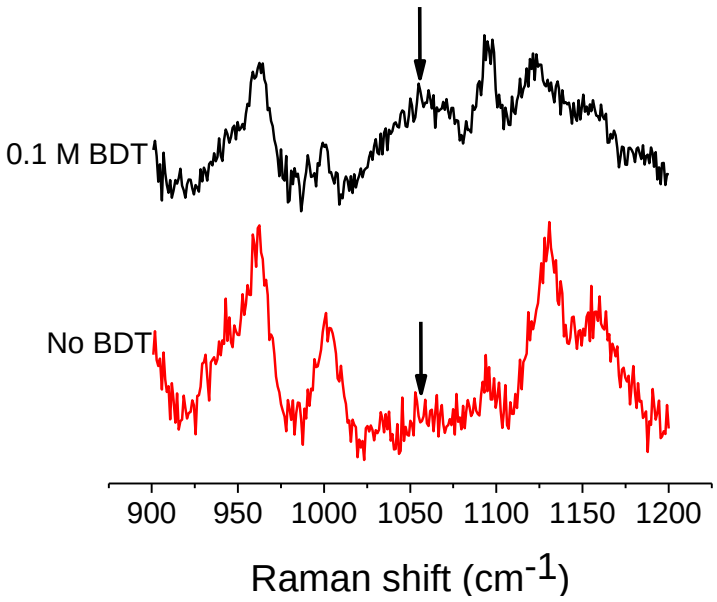

Figure S1.3: Higher resolution SERS spectra obtained from paper substrates exposed to 0.1 M of 1,4-BDT and the control sample (without 1,4-BDT) showing that the 1058 cm^{-1} band of 1,4-BDT can be clearly distinguished with a SNR of ~3.

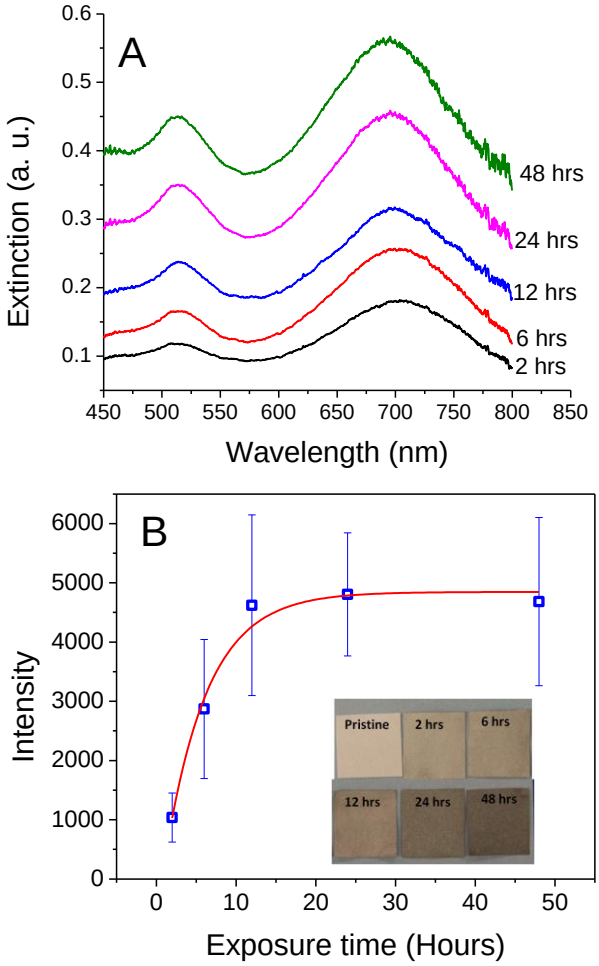

Figure S1.4: (A) Extinction spectra obtained from paper substrates exposed to AuNR solution for different durations (2, 6, 12, 24, 48 hrs) (B) Intensity of the SERS spectra obtained from the same substrates following the exposure to 1 mM 1,4-BDT (Inset shows the photograph of the paper substrates with progressively deepening of the color).

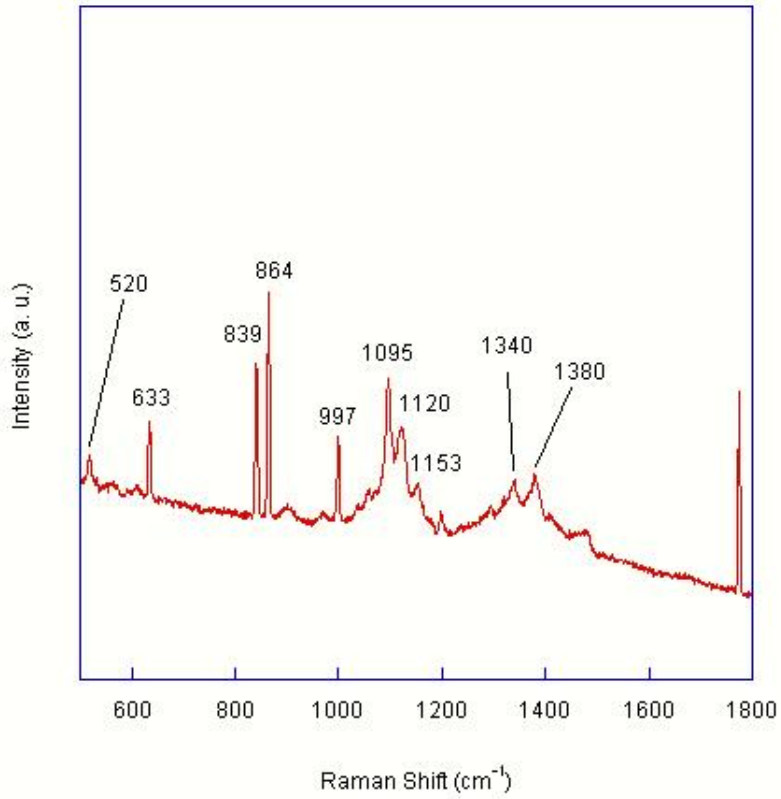

Figure S1.4: Raman peak assignments for pristine Whatman No. 1 paper. 520: some heavy atom bending and stretching. 839, 864: CH_2 deformation vibration. 997, 1120: HCC and HCO bending at C6 heavy atom (CC and CO) stretching. 1153: heavy atom stretching plus HCC and HCO bending. 1340: OH deformation vibration. 1380: CH deformation vibration.[325, 326]

Supporting Information: **Plasmonic nanorattles with intrinsic Hot Spots for Surface Enhanced Raman Scattering**

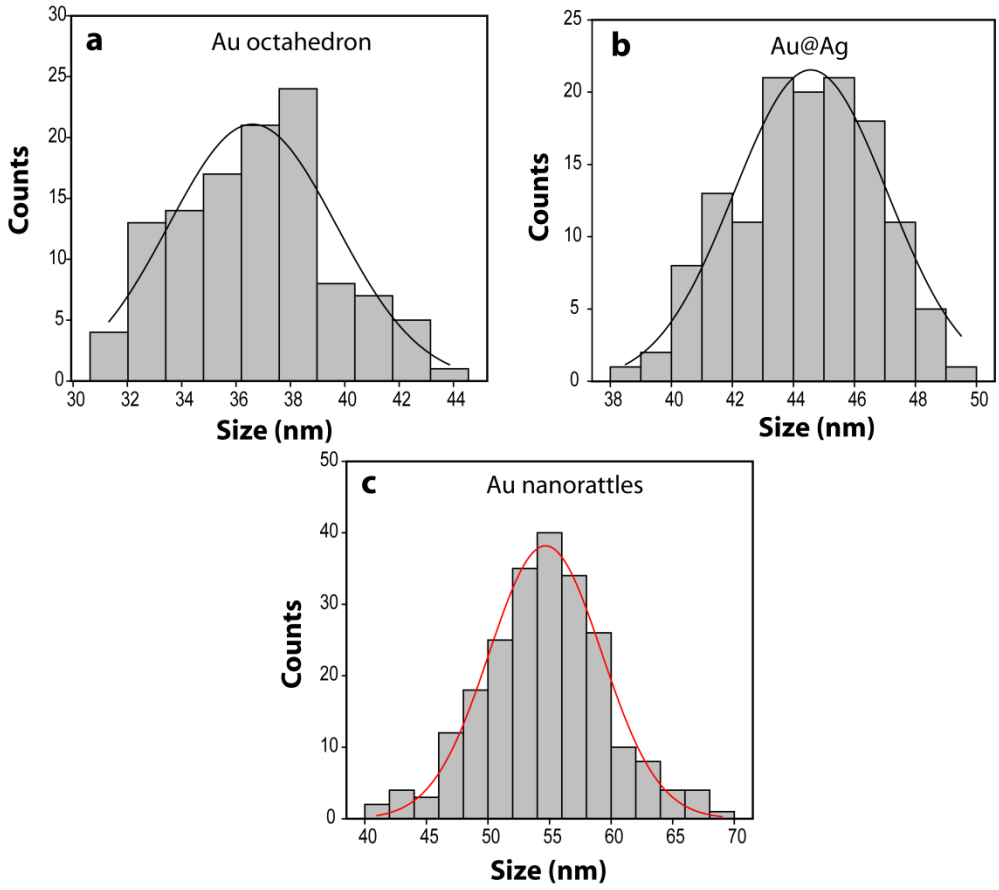

Figure S2.1. Particle size distribution of a) Au core, b) Au@Ag and c) Au nanorattles as obtained from the corresponding TEM images.

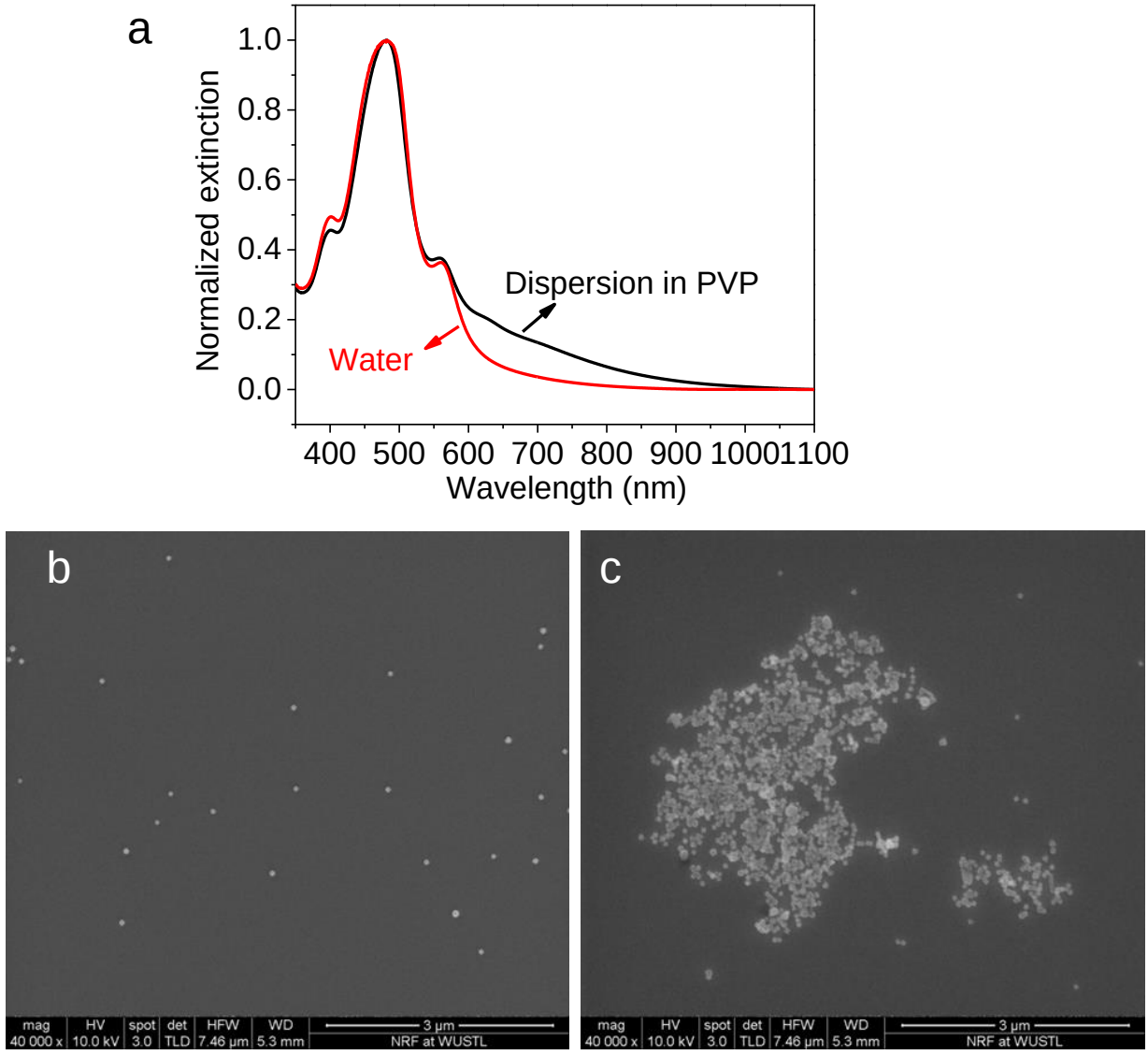

Figure S2.2. (a) Extinction spectra of Ag@Au nanoparticles dispersed in water and PVP solution, and corresponding SEM images obtained from the samples prepared from Ag@Au nanoparticles in water (b) and in PVP solution (c).

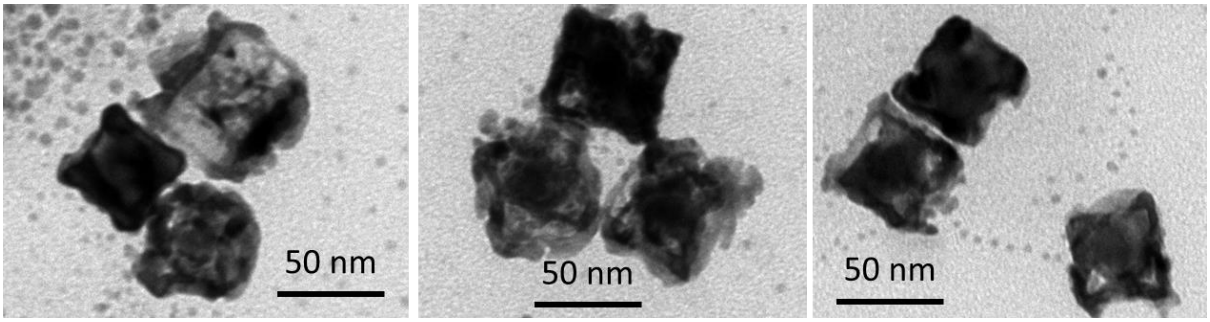

Figure S2.3. TEM images of nanorattles synthesized in the absence of PVP

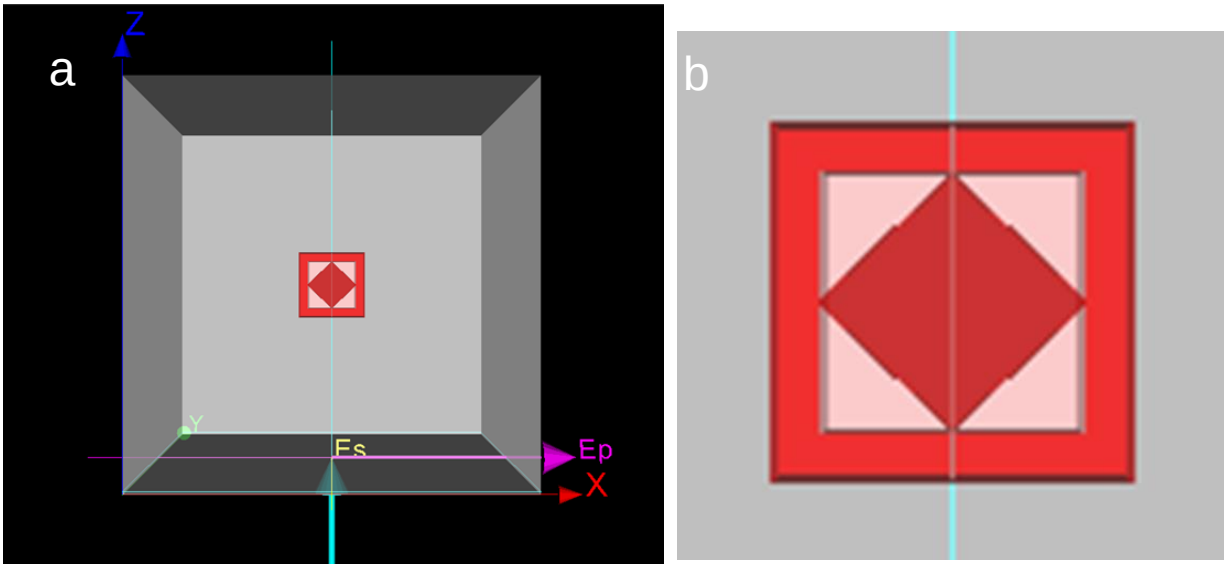

Figure S2.4. (a) Nanorattle structure employed in the FDTD simulation (b) Zoom-in showing that the core is connected to shell.

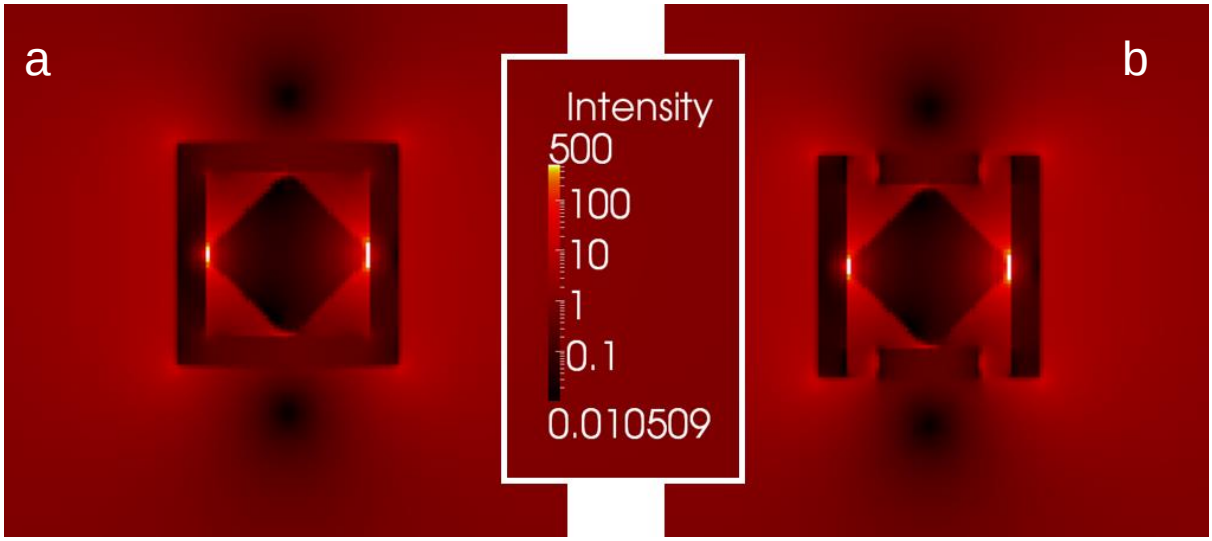

Figure S2.5. The EM field distribution of nanorattle without pores (a) and with pores (b).

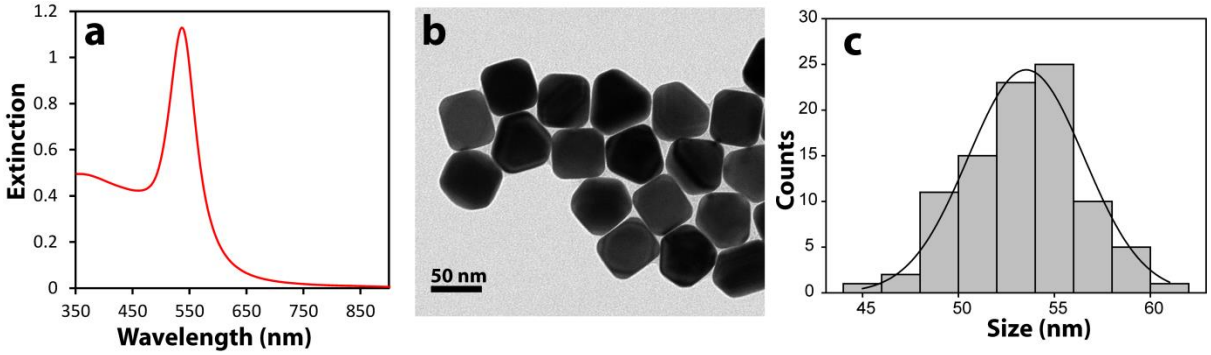

Figure S2.6. (a) Extinction spectrum, (b) TEM image and (c) Particle size distribution of Au nanocubes.

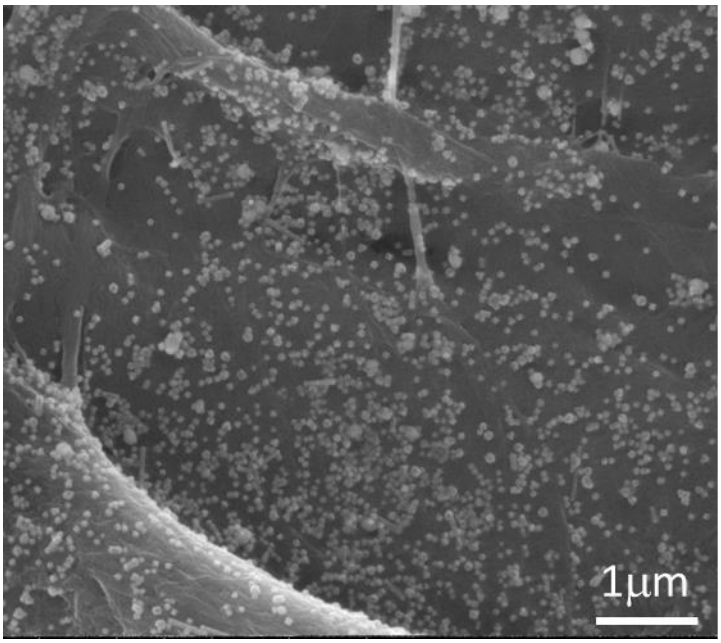

Figure S2.7. SEM image showing the uniform adsorption of Au nanorattles on a paper substrate with an inset Vis-NIR extinction spectra obtained from paper substrates adsorbed with Au nanorattles.

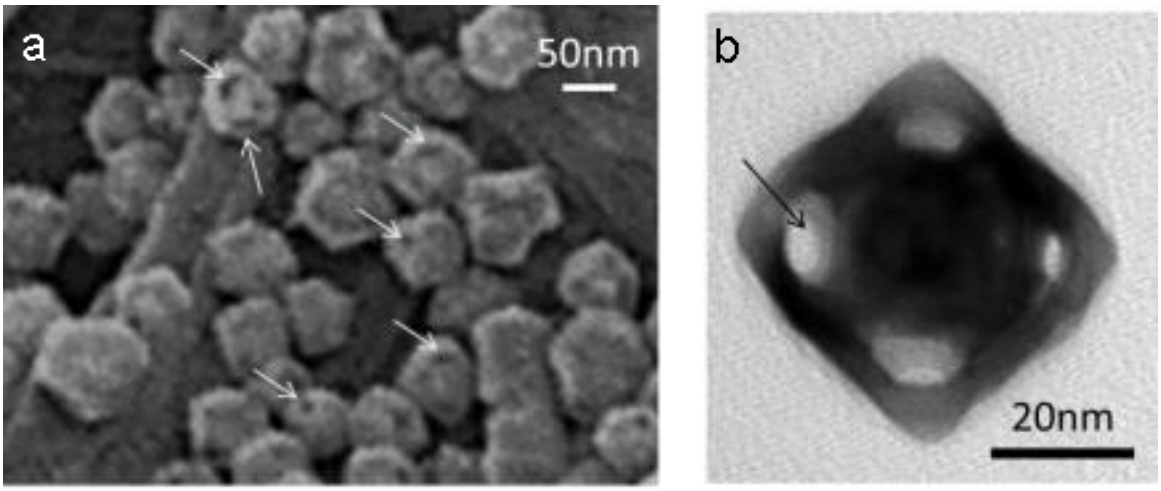

Figure S2.8. Representative magnified SEM image (a) and TEM image (b) showing the tiny pores on the Au nanorattle surface.

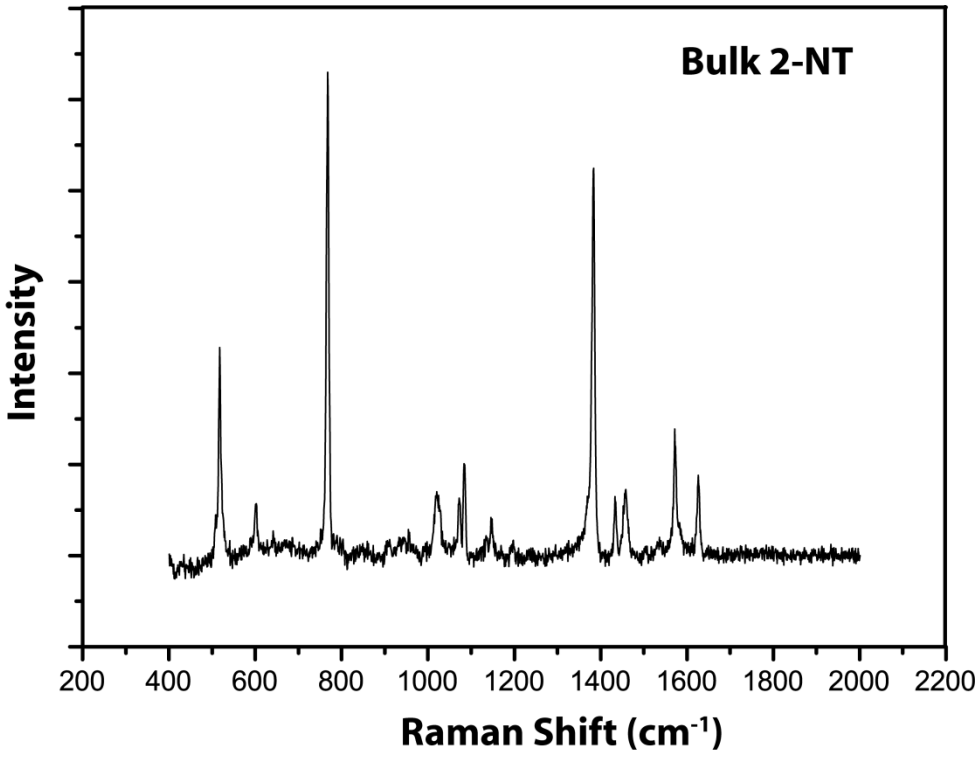

Figure S2.9. Raman spectrum of bulk 2-NT.

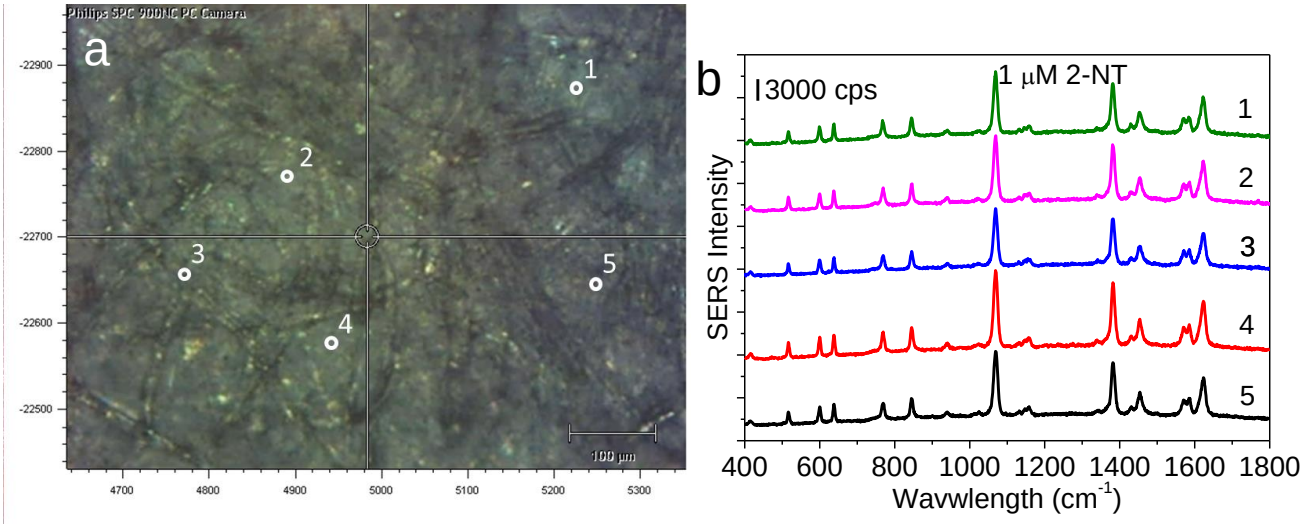

Figure S2.10. (a) Optical microscopy image showing the SERS data collection spot on the paper substrate adsorbed with Au nanorattles exposed to 1 µM of 2-NT, and (b) corresponding SERS spectra with a standard deviation (~15%).

Appendix 3

Supporting information: Multifunctional Analytical Platform on a Paper Strip: Separation, Pre-concentration and Sub-Attomolar Detection

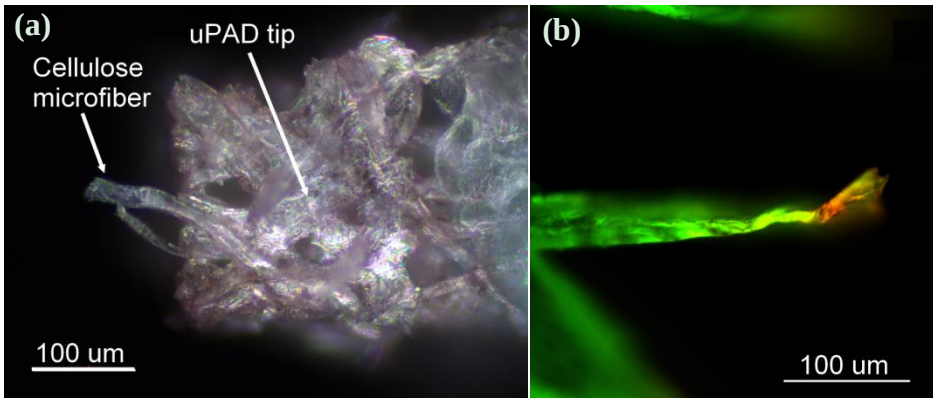

Figure S3.1. Sample pre-concentration at a single cellulose microfiber. (a) Dark field optical image of the µPAD fingertip. A single cellulose microfiber can be seen at the very tip. (b) Pre-concentration of R6G molecules at the tip of a single microfiber.

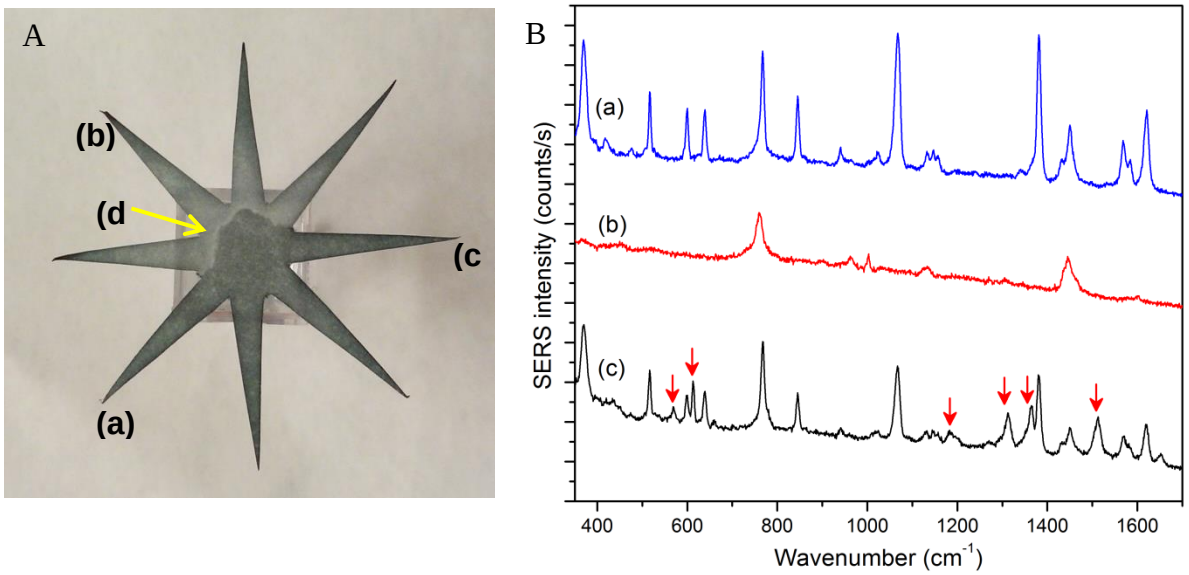

Figure S3.2: Detection of 2-naphtalenethiol in tap water. (a) SERS spectrum of 2-naphtalenethiol obtained at the paper fingertip functionalized with 2% PAH, with all the characteristic aromatic peaks reported in literature.[327] (b) SERS spectrums obtained on the paper finger functionalized with 1 % PSS. It shows 2 peaks due to CTAB molecules (nanorods capping ligands). (c) SERS spectrum obtained in the paper finger functionalized with 0.25% PAH solution. In addition to 2-naphtalenethiol peaks, other peaks are observed at frequencies 570 cm^{-1}, 612 cm^{-1}, 1183 cm^{-1}, 1312 cm^{-1}, 1364 cm^{-1}, 1512 cm^{-1} (red arrows), indicating the presence of other aromatic or saturated components. (d) The white color indicated by an arrow in panel A is caused by the accumulation of different ions (Na, K, Mg, Cl,..) present in tap water at the four fingers functionalized with PSS.

Table S1. Detection limit of microfluidic paper-based analytical devices reported in literature.

Limit of Detection	Analyte	Ref.
0.46 uM	human serum albumin	[189]
0.1 ppb	Hg (II)	[190]
1.0 ng/mL, 0.4 ng/mL, 0.06 U/mL, 0.02 ng/mL	AFP, CA 153, CA 199, CEA	[176]
1 ppb	Hg (II)	[191]
0.01 ug/mL, 0.23 ug/mL, 0.12 ug/mL	B-galactosidase, esterase, PI-PLC	[192]
0.5 nM	BPE	[159]
1 ppb	Pb (II)	[172]
0.6 nM	MC-LR	[328]
0.04 ng/mL	neomycin	[175]
1 uM	Pt-Mn02/rGOP	[193]
0.14 mM, 0.52 mM	Glucose, uric acid	[177]

Supporting information: Multiplexed Charge-Selective Surface Enhanced Raman Scattering based on Plasmonic Calligraphy

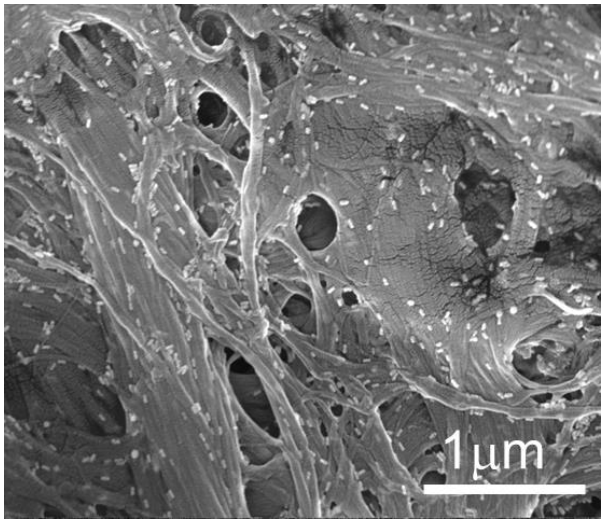

Figure S4.1: SEM images of PAH@AuNRs adsorbed on paper substrates by plasmonic calligraphy approach.

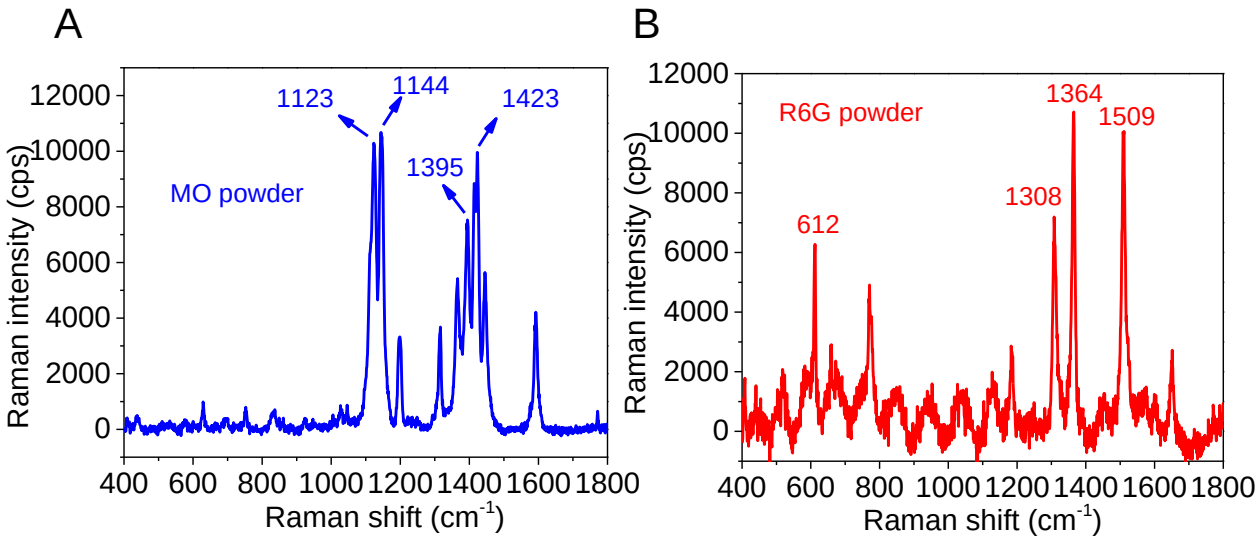

Figure S4.2: Raman spectra of bulk form of methyl orange (MO) and rhodamine 6G (R6G) powder.

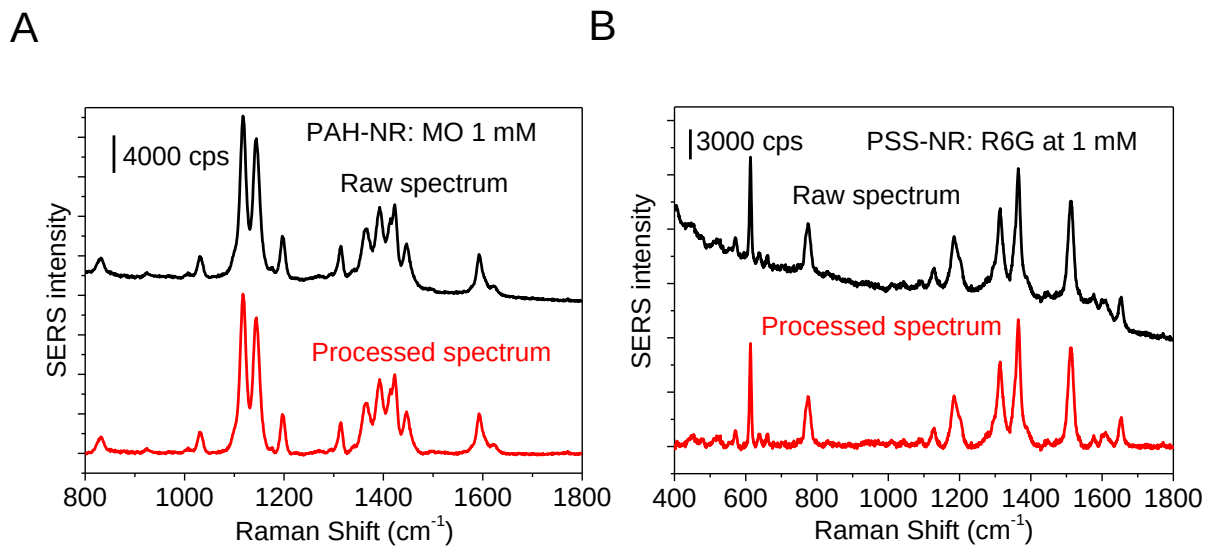

Figure S4.3: Representative SERS spectra (A) before and (B) after background removal.

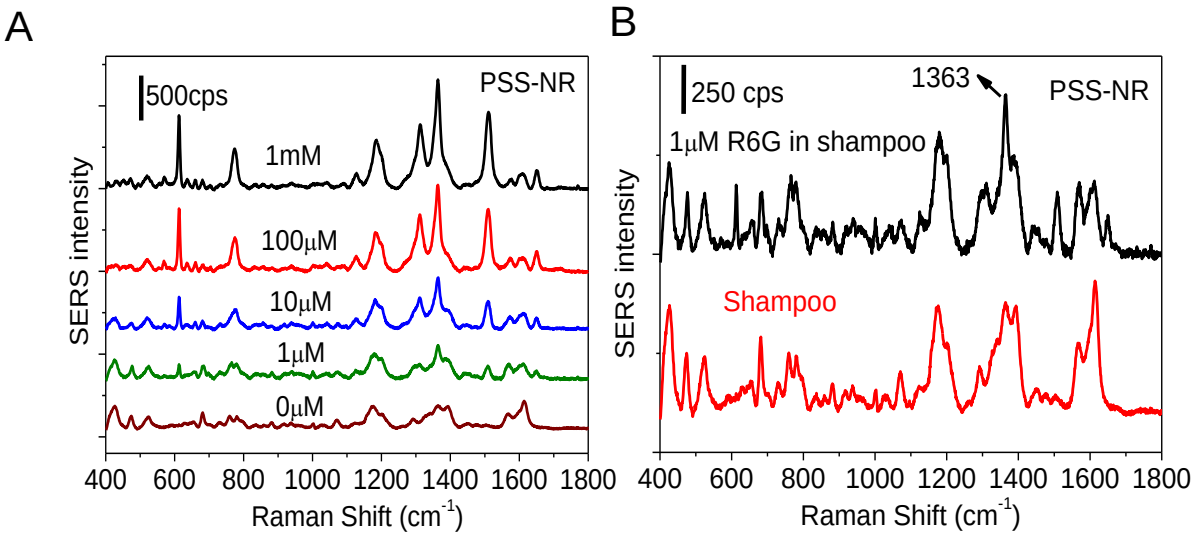

Figure S4.4: (A) SERS spectra obtained from PSS-AuNRs test domain after exposure to different concentration of R6G in 1 mg/ml shampoo solution (D) Zoom in SERS spectra for low concentration of R6G compared with PSS-AuNRs control sample.

Appendix 5

Support information: Gold Nanorods as Plasmonic Nanotransducers: Distance-dependent Refractive Index Sensitivity

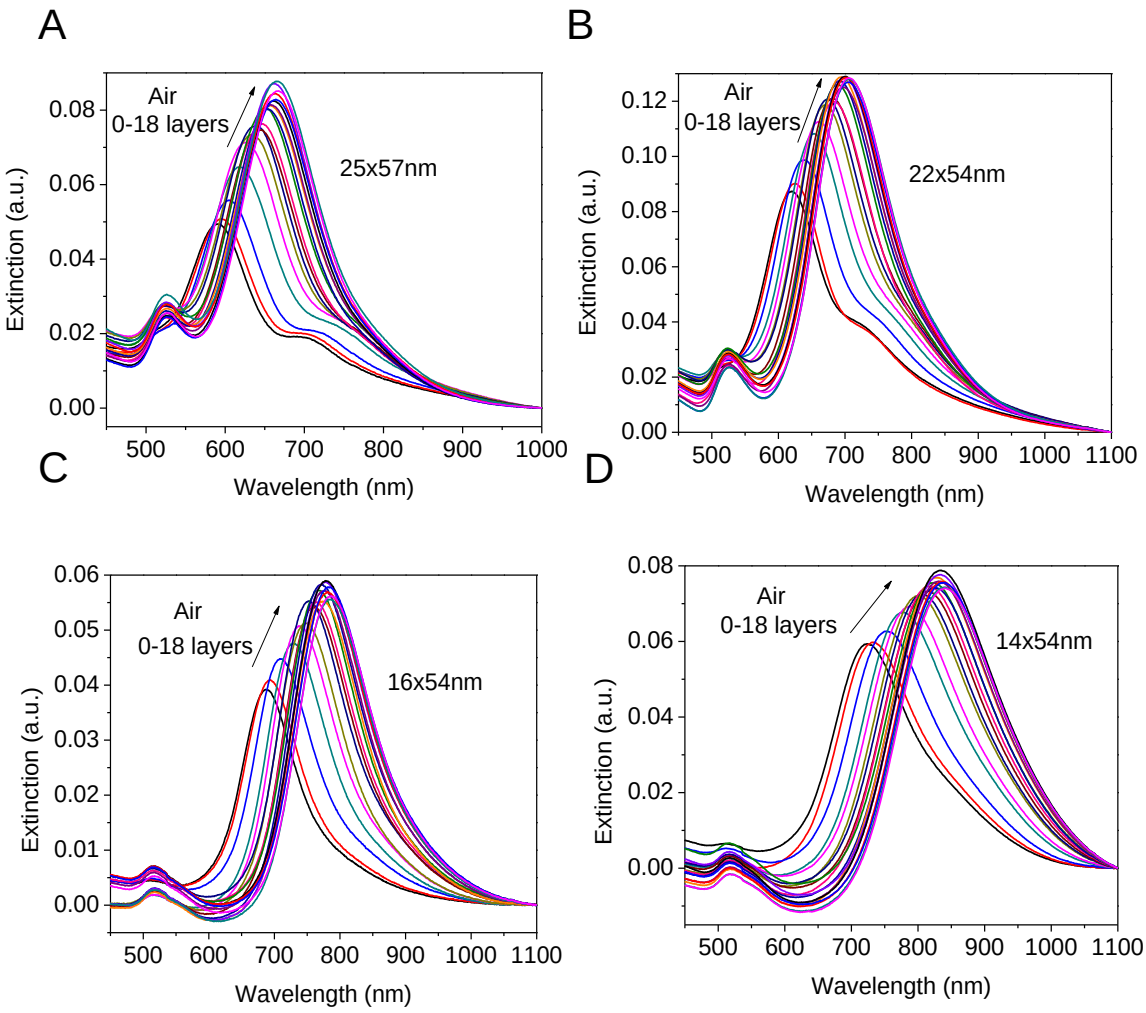

Figure S5.1: UV-vis extinction spectra of AuNR with different dimensions following the deposition each polyelectrolyte layer showing a progressive red-shift and increase in the intensity of the longitudinal plasmon band.

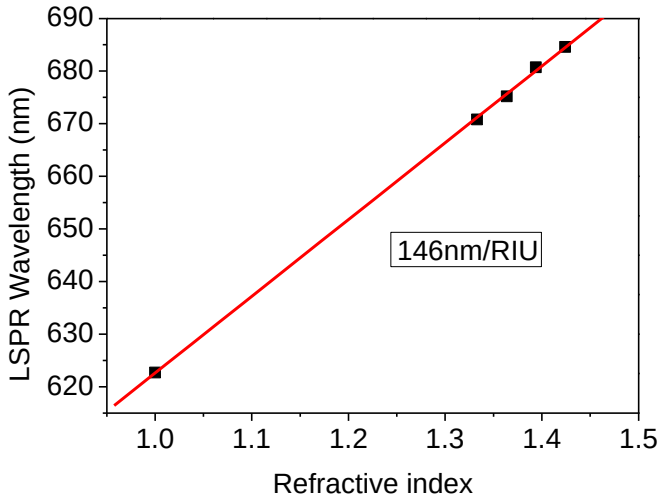

Figure S5.2: Plot showing the LSPR wavelength of the nanorods adsorbed on glass substrates and the refractive index of the surrounding medium. The refractive index was altered by using aqueous sucrose solutions of different concentrations.

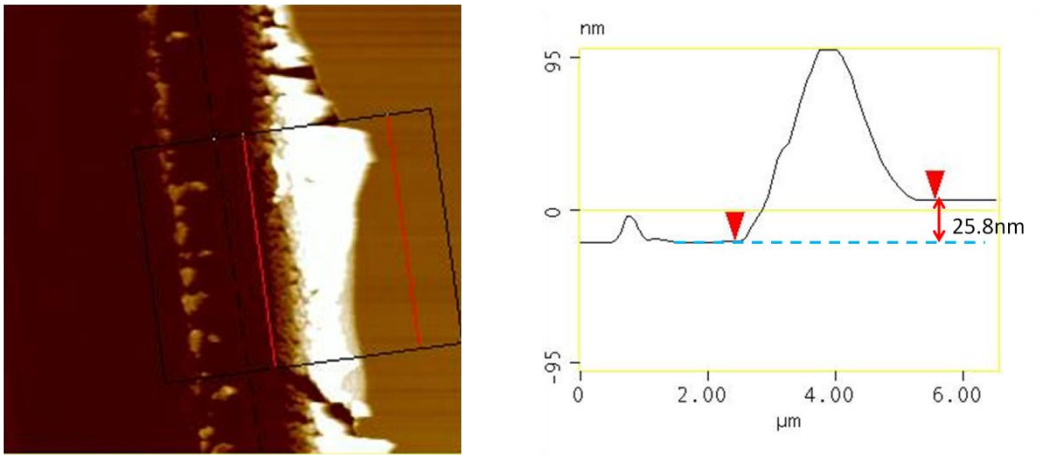

Figure S5.3: AFM image and the corresponding cross-sectional profile along the edge of an intentional scratch in polyelectrolyte multilayer film comprised of 8 bilayers.

Appendix 6

Supporting information: Bioplasmonic Paper as a Platform for Detection of Kidney Cancer Biomarkers

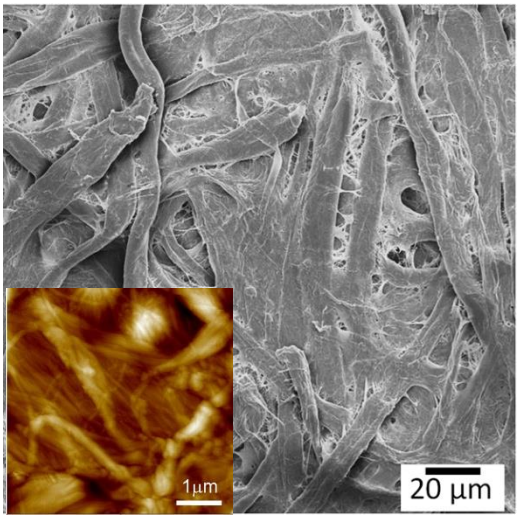

Figure S6.1: SEM image of the filter paper (Whatman #1). Inset: the higher magnification AFM image of the hierarchical fibrous morphology of the filter paper with cellulose nanofibers braided into microfibers (average diameter of ~ 0.4 μm).

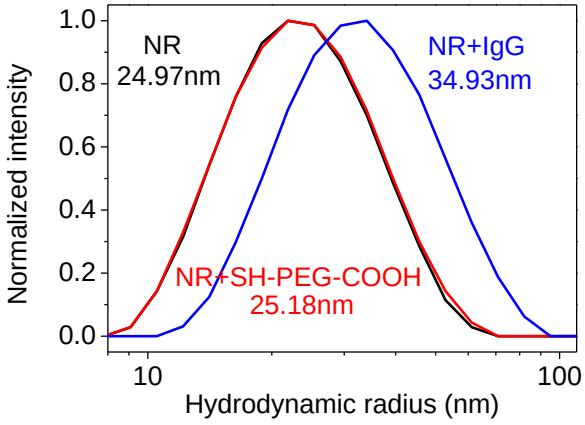

Figure S6.2: Dynamic light scattering (DLS) measurements showing the hydrodynamic diameter of AuNRs, AuNRs-PEG-COOH, and AuNRs-PEG-IgG. The size distribution confirmed the conjugation of SH-PEG-IgG on AuNRs, and the increase in hydrodynamic diameter mainly contributed from IgG (Mw=150KDa), but not PEG (Mw=5KDa) due to their significant difference in molecular weight.

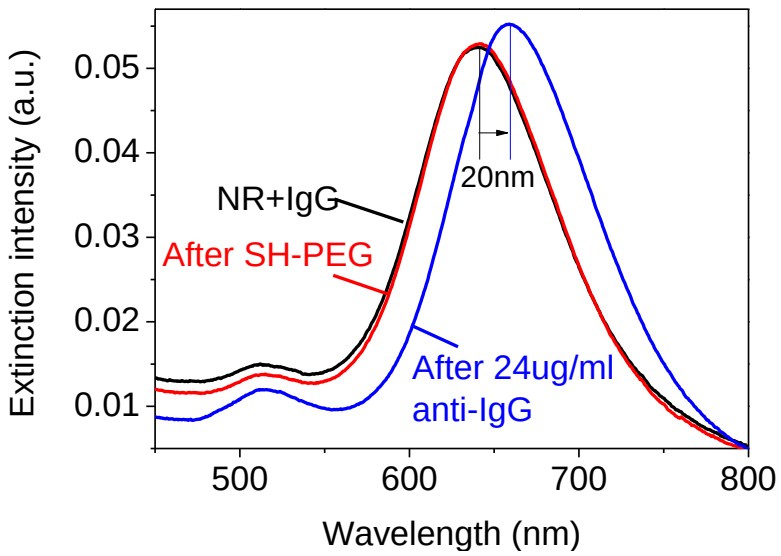

Figure S6.3: LSPR spectra of AuNR-IgG conjugates on a glass substrate (black), after SH-PEG nonspecific blocking step(red), and after binding of anti-IgG (blue).

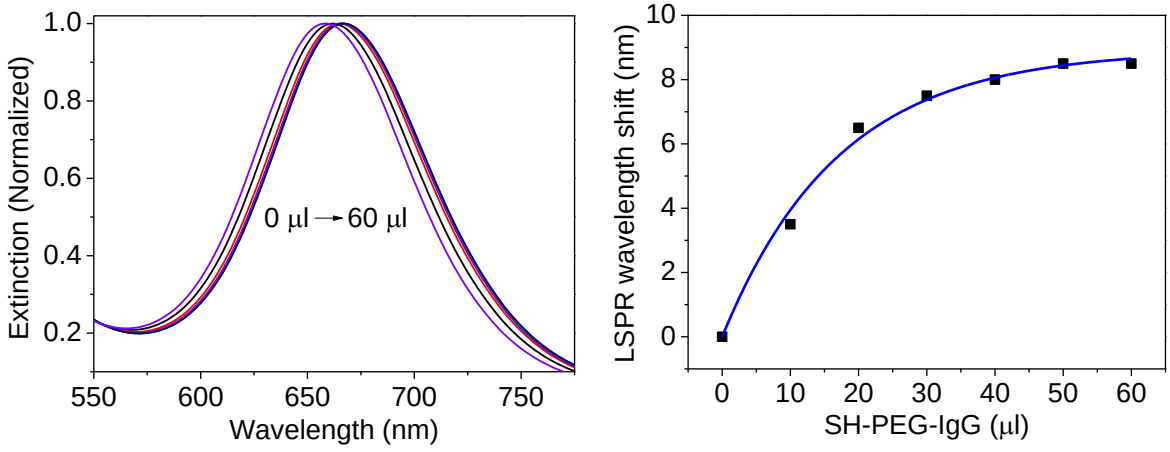

Figure S6.4: Extinction spectra of AuNR solution after adding different amount of SH-PEG-IgG to optimize the coverage of IgG on AuNR surface.

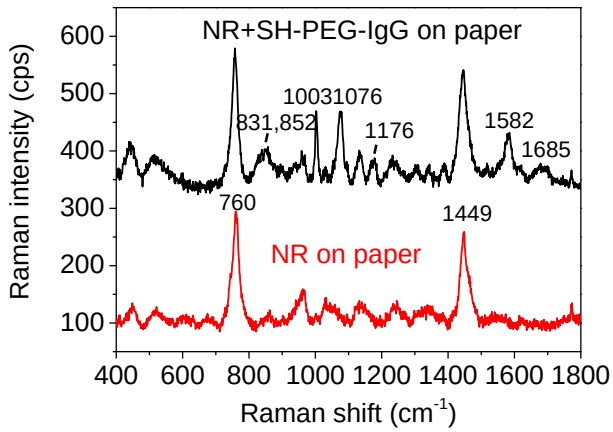

Figure S6.5: Raman spectra confirmed AuNR+IgG conjugates on paper substrates after incubation. The presence of IgG is evidenced by specific bands at 831 cm^{-1}, 852 cm^{-1} and 1176 cm^{-1} , 1004 cm^{-1} and 1582 cm^{-1} , 1076 cm^{-1} , and 1685 cm^{-1} due to tyrosine, phenylalanine, symmetric stretching vibration of $v3PO_4^{3-}$, and Amide I, respectively.

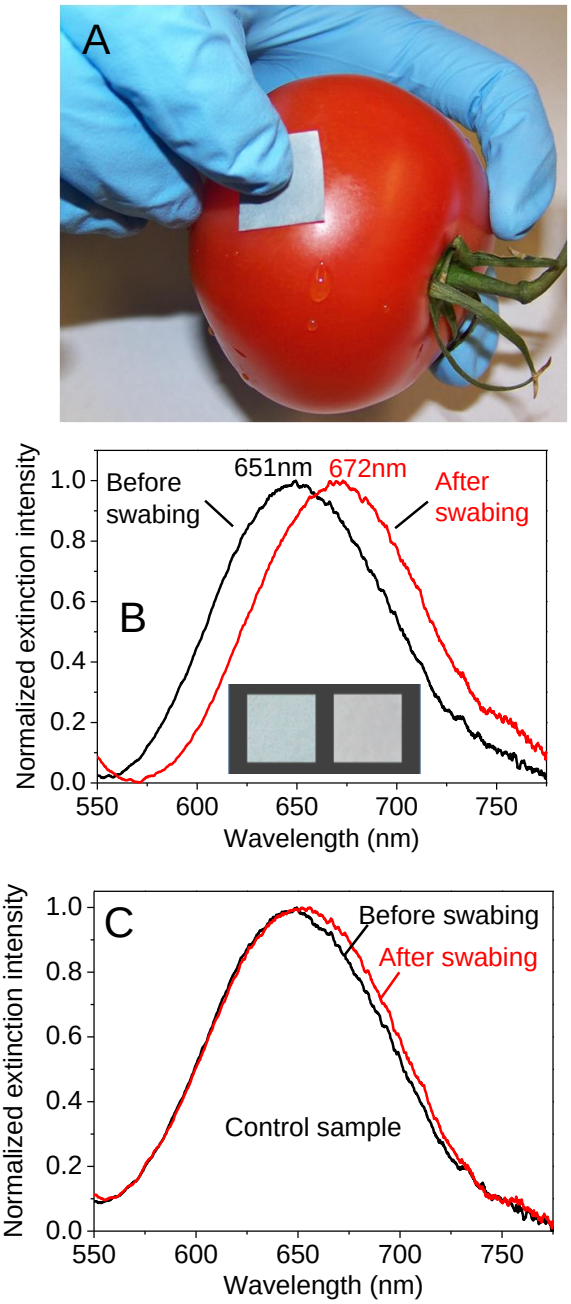

Figure S6.6: (A) Photograph depicting the flexibility of bioplasmonic paper as it is being swabbed on a tomato to collect 12 µg anti-IgG spread on the surface. (B) LSPR spectra of AuNR-IgG conjugates paper before and after collecting anti-IgG (inset: shows photographs of the NR+IgG paper before (left) and after swabbing (right)). (C) LSPR spectra of AuNR-IgG conjugates paper before and after swabbing on the region without anti-IgG.

Supporting Information: Bioplasmonic Calligraphy for Multiplexed Label-free Biodetection

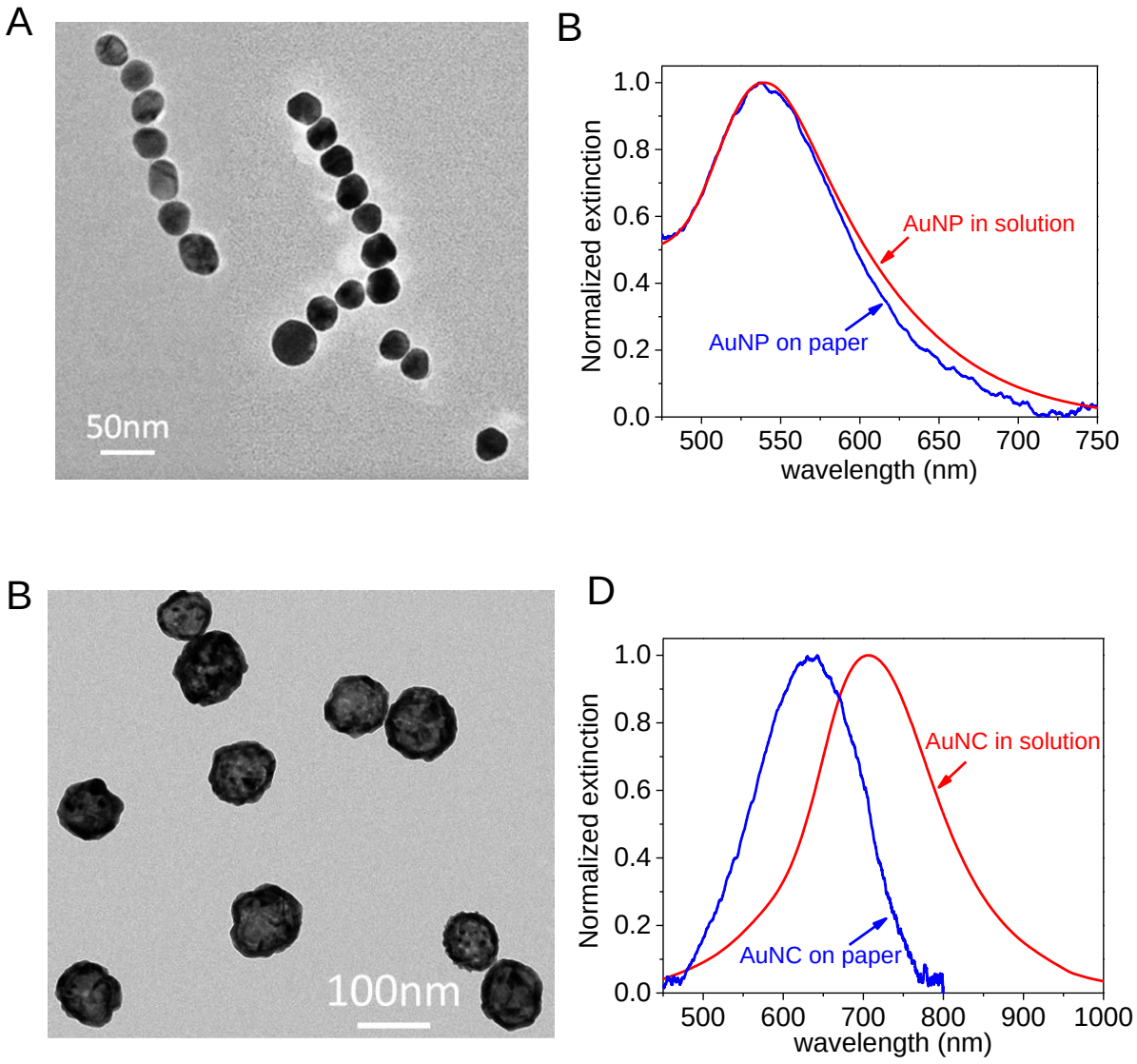

Figure S7.1: (A) TEM of gold nanospheres. (B) Extinction spectra of gold nanospheres stabilized with citrate ions measured in aqueous solution and on paper substrate. (C) TEM of gold nanoshells. (D) Extinction spectra of gold nanshells coated with PVP measured in aqueous solution and on paper substrate.

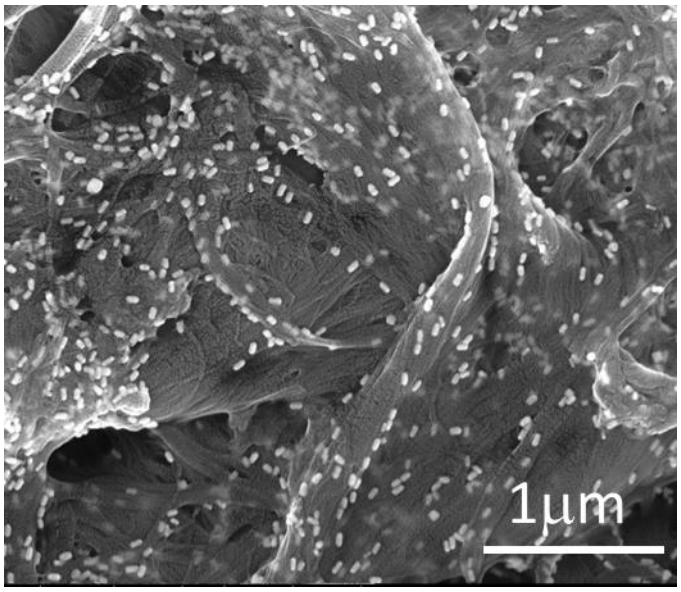

Figure S7.2: Magnified SEM image of biofunctionalized gold nanorods on paper.

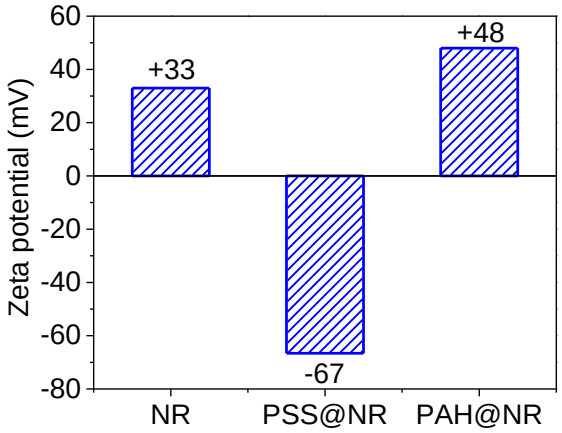

Figure S7.3: Magnified SEM image of biofunctionalized gold nanorods on paper.

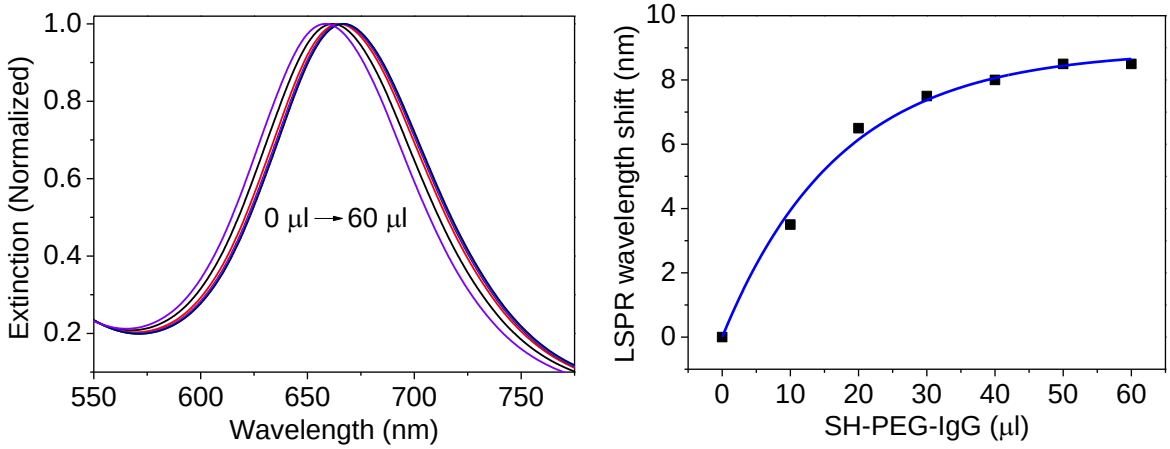

Figure S7.4: Extinction spectra of AuNR solution after adding different amount of SH-PEG-IgG to optimize the coverage of IgG on AuNR surface.

SDS-PAGE was performed to compare affinity and final concentrations of the non-modified Ab (Rabbit IgG showed as control) and modified one (PEGylated Rabbit IgG).

Rabbit IgG was diluted from 5 µg per gel slot by half each slot. The last 6 dilutions of rabbit IgGs solution represent 156-4.9 ng Control or PEGylated Rabbit IgG. After SDS gel (nonreducing), the diluted IgGs were transferred to nitrocellulose and blocking membrane and then the membrane was incubated with goat anti-rabbit IgG at 1µg/ml for 30 min, followed by 3X washes with PBS-0.5% Tween20. After that, the membrane was incubated with Donkey anti-goat IgG 800 from LICOR 1/3000 in LICOR blocking buffer-0.5% TW20 for 30min, followed by 3X washes in PBS-0.5%TW20 and then imaged on a LICOR Odyssey at 800 nm (Figure S5A). After this imaging, the membrane incubated with Donkey anti-rabbit IgG 680 from LICOR 1/3000 in LICOR blocking buffer-0.5% TW20 for 30 min followed by 3X washes in PBS-0.5%TW20 and then imaged on a LICOR Odyssey at 680 nm (Figure S5B).

In conclusion, pegylation did not change rabbit IgGs recognition by two different antibodies. The goat anti-rabbit IgG sees both non-modified rabbit IgGs and modified ones essentially equally well. Furthermore, another anti-rabbit IgG (Donkey) sees both non-modified rabbit IgGs and modified ones essentially equally well.

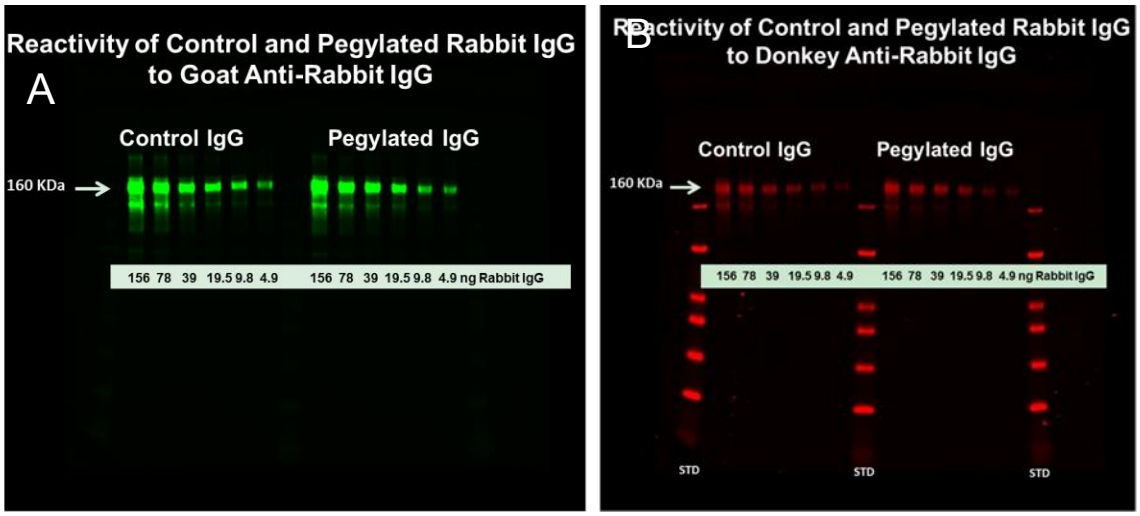

Figure S7.5: SDS-PAGE plots showing the comparison of affinity and final concentrations of the non-modified Ab (Rabbit IgG showed as control) and modified one (PEGylated Rabbit IgG). (A) Goat anti-rabbit IgG sees both non-modified rabbit IgGs and modified ones essentially equally well. (B) Donkey anti-rabbit IgG sees both non-modified rabbit IgGs and modified ones essentially equally well.

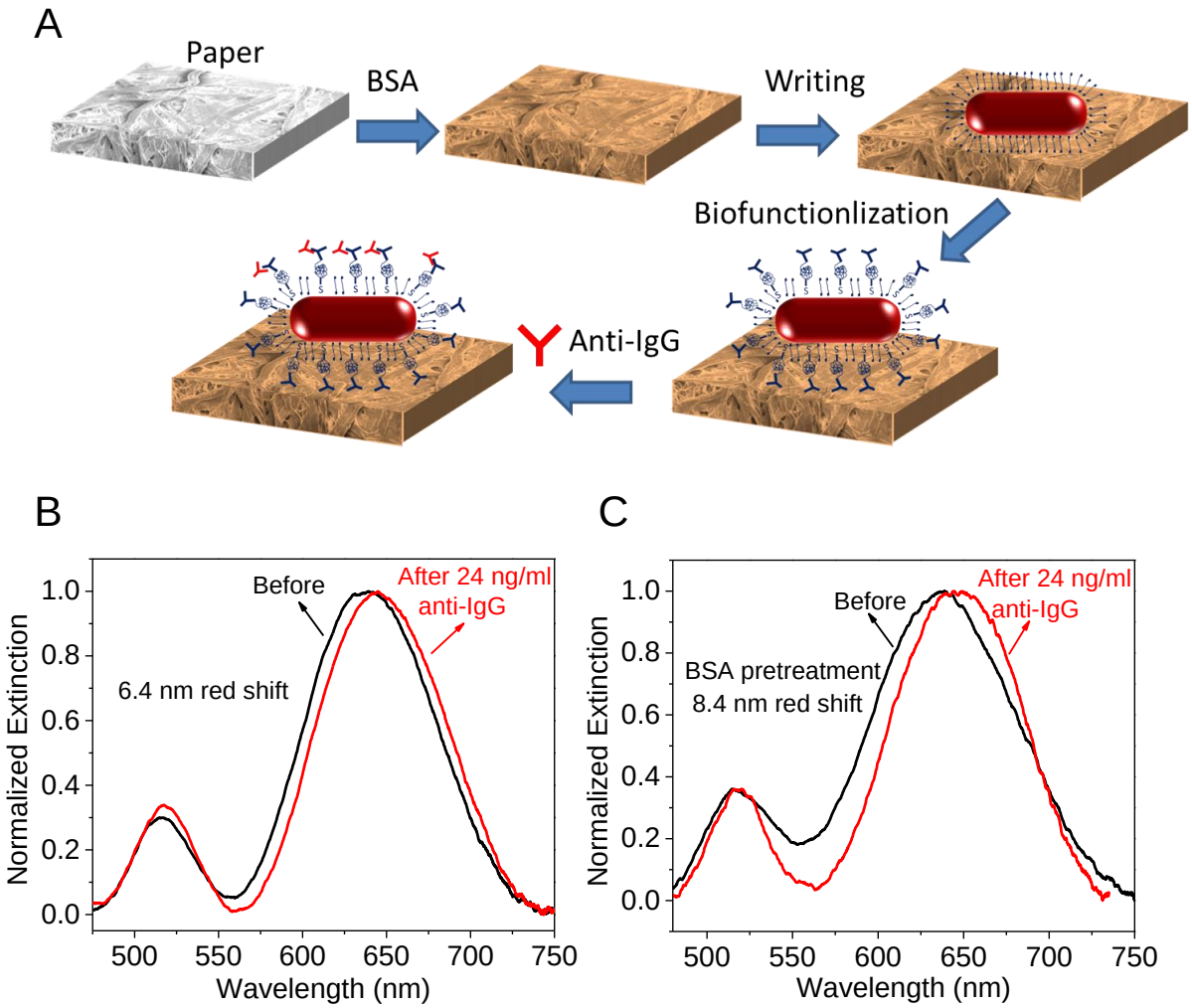

Figure S7.5: (A) Schematic illustration representing the fabrication steps involved in the fabrication of bioplasmonic paper with BSA blocking step for anti-IgG detection. (B-C) Extinction spectra of AuNR paper before and after 24 ng/ml of anti-IgG binding with/without BSA blocking step.

Curriculum Vita

Limei Tian

Education

PhD: Mechanical Engineering, Washington University in St. Louis, August 2014

Dissertation: Plasmonic Paper as a Novel Chem/Bio Detection Platform

Advisor: Dr. Srikanth Singamaneni

Master of Science: Structural Engineering, Shan Dong University, China, July 2009

Thesis: Numerical Simulation of Fluid-Structure Interaction for Wind-induced Dynamic Response of Low-rise Lightweight Buildings

Advisor: Dr. Zhenhua Liu

Bachelor of Science: Civil Engineering, Shan Dong University, China, July 2006

Thesis: The Design of a High-rise Steel Structure Residence

Referred publications directly related to this dissertation

(1) Jaiswal, A.;* **Tian, L.;*** Tadepalli, S.; Liu, K.; Farrell, M. E.; Pellegrino, P. M.; Singamaneni, S. Plasmonic Nanorattles with Intrinsic Electromagnetic Hot-Spots for Surface Enhanced Raman Scattering. *Small* **2014** (In press, DOI: 10.1002/smll.201401278).

(2) **Tian, L.;** Nergiz, S. Z.; Singamaneni, S. Plasmonic Paper: Emerging Analytical and Trace Detection Platform. *J. Mater. Chem. B,* Invited Review (In Preparation)

(3) **Tian, L.;** Tadepalli, S.; Hankus, M. E.; Liu, K.; Gandra, N.; Pellegrino, P. M.; Singamaneni, S. Charge-Selective Surface-Enhanced Raman Scattering using Calligraphy-based Plasmonic Paper. *J. Mater. Chem. C*, **2014**, 2, 5438-5446.

(4) **Tian, L.;** Nergiz, S. Z.; Hankus, M. E.; Pellegrino, P. M.; Slocik, J. M.; Naik, R. R.; Singamaneni, S. Plasmonic Paper: An Emerging Trace Detection Platform, SPIE Newsroom. **2014,** (DOI: 10.1117/2.1201405.005468)

(5) Gandra, N.; **Tian, L.;** Nergiz, S. Z.; Singamaneni, S. Migration of Plasmonics from Static to Dynamic Surfaces. *J. Nanosci. Lett.* **2014**, 4, 23.

(6) **Tian, L.;** Tadepalli, S.; Park, S. H.; Liu, K.; Morrissey, J. J.; Kharasch, E. D.; Naik, R. R.; Singamaneni, S. Bioplasmonic Calligraphy for Multiplexed Label-free Biodetection. *Biosensor and Bioelectronics,* **2014**, 59, 208–215.

(7) Abbas, A.; Brimer, A.; Slocik, J. M.; **Tian, L.;** Naik, R. R.; Singamaneni, S. All-in-one Chemosensor on a Paper Strip: Separation, Pre-concentration and Sub-Attomolar Detection. *Anal. Chem.* **2013**, 85, 3977.

(8) **Tian, L.;** Chen, E.; Gandra, N.; Abbas, A.; Singamaneni, S. Gold Nanorods as Plasmonic Nanotransducers: Distance-dependent Refractive Index Sensitivity. *Langmuir*, **2012,** 28, 17435.

(9) **Tian, L.;** Morrissey, J. J.; Kattumenu, R.; Gandra, N.; Kharasch, E. D.; Singamaneni, S. Bioplasmonic Paper as a Platform for Detection of Kidney Cancer Biomarkers. *Anal. Chem.* **2012**, 84, 9928.

(10) Lee, C. H.; Hankus, M. E.; **Tian, L.;** Pellegrino, P. M.; Singamaneni, S. Highly Sensitive SERS Substrates Based on Filter Paper Loaded with Plasmonic Nanostructures. *Anal. Chem.* **2011**, 83, 8953–8958.

(11) Lee, H. C; **Tian, L.;** Singamaneni, S. Paper based SERS Swab for Rapid Trace Detection on Real-world Surfaces. ACS *Appl. Mater. Interface,* **2010**, 2, 3429.

Publications from related studies

(12) Zhuo, Y.; Hu, H.; Chen, W.; Lu, M.; **Tian, L.;** Yu, H.; Long, K. D.; Chow, E.; King, W. P.;

Singamaneni, S.; Cunningham B. T. Single Nanoparticle Detection Using Photonic Crystal Enhanced Microscopy. *Analyst,* **2014**,139, 1007-1015.

(13) Gandra, N.; Portz, C.; **Tian, L.;** Tang, R.; Xu, B.; Achilefu, S.; Singamaneni, S. Probing Distance-Dependent Plasmon Enhanced Near-infrared Fluorescence using Polyelectrolyte Multilayers as Dielectric Spacers. *Angew. Chem. Int. Ed.* **2014**, 53, 866–870.

(14) **Tian, L.;** Liu, K.; Morrissey, J. J.; Gandra, N.; Kharasch, E. D.; Singamaneni, S. Gold Nanocages with Built-in Artificial Antibodies for Kidney Injury Detection. *J. Mater. Chem. B,* **2014**, 2, 167-170.

(15) Wu, F.; **Tian, L.;** Kanjolia, R.; Singmaneni, S. Banerjee, P. Plasmonic Metal-to-Semiconductor Switching in Au Nanorod-ZnO nanocomposite films. *ACS Appl. Mater. Interface,* **2013**, 5, 7693–7697.

(16) **Tian, L.;** Gandra, N.; Singamaneni, S. Monitoring Controlled Release of Payload from Gold Nanocages using Surface Enhanced Raman Scattering. *ACS Nano*, **2013**, 7, 4252–4260.

(17) Nergiz, S. Z.; Gandra, N.; Farrell, M. E.; **Tian, L.;** Pellegrino, P. M.; Singamaneni, S. Biomimetic SERS substrate: Peptide Recognition Elements for Highly Selective Chemical Detection in Chemically Complex Media. *J. Mater. Chem. A*, **2013**, 1, 6543-6549.

(18) Abbas, A.; Kattumenu, R.; **Tian L.;** Singamaneni, S. Molecular Linker-Mediated Self-assembly of Gold Nanoparticles: Understanding and Controlling the Dynamics. *Langmuir*, **2013**, 29, 56.

(19) Abbas, A.; Brimer, A.; **Tian, L.;** d'Avignon, D. A.; Hameed,Â A. S.; Vittal, J. J.; Singamaneni, S. From Single Molecules to Macroscale structures: Growing by Vesicle Walk and Fusion. *Small,* **2013**, 9, 2611-8.

(20) Abbas, A.; **Tian, L.;** Morrissey, J.; Kharasch, E. D.; Singamaneni, S. Hot-spot Localized Artificial Antibodies for Label-free Plasmonic Biosensing. *Adv. Funct. Mat,* **2013**, 23, 1789.

(21) Abbas, A.; Fei, M.; **Tian, L.;** Singamaneni, S. Trapping proteins within gold nanoparticle assemblies: dynamically tunable hot-spots for nanobiosensing. Plasmonics. **2013**, 8, 537-544.

(22) **Tian, L.;** Fei, M.; Kattumenu, R.; Abbas A.; Singamaneni. S. Gold nanorods as nanotransducers to monitor the growth and swelling of ultrathin polymer films. *Nanotechnology,* **2012**, 23, 255502.

(23) Abbas, A.; **Tian, L.;** Kattumenu, R.; Halim, A.; Singamaneni. S. Freezing the self-assembly process of gold nanocrystals. *Chem. Commun.,* **2012**, 48, 1677–1679.

(24) Gandra, N.; Abbas, A.; **Tian, L.;** Singamaneni, S. Plasmonic Planet-Satellite Analogues: Hierarchical Self-Assembly of Gold Nanostructures. *Nano Lett.,* **2012**, 12, 2645–2651.

(25) Abbas, A.; Kattumenu, R.; **Tian, L.;** Nergiz, Z. S., Singamaneni, S. Self-assembly of plasmonic nanostructures. *J. Nanosci. Lett.,* **2012**, 2, 1-17.

(26) Kattumenu, R.; Lee, H. C.; **Tian, L.;** McConney, E. M.; Singamaneni, S. Nanorod decorated nanowires as highly efficient SERS-active hybrids. *J. Mater. Chem.* **2011**, 21, 15218-15223.

(27) Lee, H. C.; **Tian, L.;** Abbas, A.; Kattumenu, R.; Singamaneni, S. Directed assembly of gold nanorods using aligned electrospun polymer nanofibers for highly efficient SERS substrates. *Nanotechnology,* **2011**, 22, 275311.

Conference Presentations on Dissertation Topic

(1) **Tian, L.;** Tadepalli, S.; Park, S. H.; Liu, K.; Naik, R. R.; Singamaneni, S. Bioplasmonic Calligraphy for Multiplexed Label-free Biodetection. Materials Research Society-Fall Meeting, 2013, Boston, Massachusetts, USA **(Oral Presentation)**

(2) **Tian, L.;** Kattumenu, R.; Gandra, N.; Singamaneni, S. Paper Based Localized Surface Plasmon Resonance Biosensor. Materials Research Society-Fall Meeting, 2012, Boston, Massachusetts, USA (**Oral Presentation)**

(3) **Tian, L.;** Kattumenu, R.; Fei, M.; Abbas, A.; Gandra, N.; Singamaneni, S.

Distance-dependent Refractive Index Sensitivity of Gold Nanorods. Materials Research Society-Fall Meeting, 2012, Boston, Massachusetts, USA **(Poster)**

(4) **Tian, L.**; Kattumenu, R.; Singamaneni, S. Plasmonic Paper as a Novel Biosensing Platform. Materials Research Society-Fall Meeting, 2011, Boston, Massachusetts, USA **(Oral Presentation)**

(5) Singamaneni, S.; Lee, C. H.; **Tian, L**. Paper based Flexible and Conformal SERS Substrate for Rapid Trace Detection on Real-world Surfaces. 2011 APS March meeting. **(Poster)**

(6) Lee, C. H.; **Tian, L**.; Singamaneni, S. Paper-Based SERS Swab for Rapid Trace Detection on Real-World Surfaces. 16th WU Annual Graduate Research Symposium, 2011. St. Louis, USA **(Poster)**